Solution-Based Two-Step Deposition Routes for Perovskite Thin-Film Formation in Photovoltaics

Zur Erlangung des akademischen Grades einer

DOKTORIN DER INGENIEURWISSENSCHAFTEN
(Dr.-Ing.)

von der KIT-Fakultät für Elektrotechnik und Informationstechnik des
Karlsruher Instituts für Technologie (KIT)

angenommene

DISSERTATION

von

M.Sc. Ronja Pappenberger
geb. in Singen (Hohentwiel)

Tag der mündlichen Prüfung:	21.04.2026
Hauptreferent:	Prof. Dr. Ulrich W. Paetzold, KIT
Korreferent:	Prof. Dr. Robby Peibst, Universität Hannover

This document is licensed under a Creative Commons
Attribution-ShareAlike 4.0 International License (CC BY-SA 4.0):
https://creativecommons.org/licenses/by-sa/4.0/deed.en

Kurzfassung

Um dem Klimawandel entgegenzuwirken, ist ein rascher Übergang zu erneuerbaren Energietechnologien erforderlich. Die Photovoltaik spielt dabei eine entscheidende Rolle, da sie kohlenstoffdioxidarmen Strom zur Deckung des weltweit steigenden Energiebedarfs bereitstellt. Silizium-Solarzellen dominieren heutzutage den Markt und zeichnen sich durch hohe Zuverlässigkeit aus; sie nähern sich jedoch zunehmend ihrer praktischen Wirkungsgradgrenze. Eine vielversprechende Strategie, diese Grenze zu überwinden, besteht darin, Silizium mit einem Weitbandlückenabsorber in einer Tandemarchitektur zu kombinieren, um das Sonnenspektrum effizienter zu nutzen. Unter den Photovoltaiktechnologien der nächsten Generation haben sich Metallhalogenid-Perowskite aufgrund ihrer herausragenden optoelektronischen Eigenschaften – einschließlich einer einstellbaren Bandlücke, eines hohen Absorptionskoeffizienten und einer langen Ladungsträgerdiffusionslänge – sowie ihrer raschen Wirkungsgradsteigerung in den vergangenen Jahren als besonders aussichtsreiche Kandidaten erwiesen. Darüber hinaus bieten Perowskite typische Vorteile von Dünnschichttechnologien wie ihre Verarbeitung bei niedrigen Temperaturen und kostengünstige Herstellungsverfahren.

Die Herstellung hochwertiger Perowskit-Dünnschichten mit Dicken von mehreren Hundert Nanometern auf mikrometerstrukturierten industriellen Siliziumwafern bleibt jedoch herausfordernd und erfordert skalierbare und reproduzierbare Herstellungsverfahren. Die bislang effizientesten Perowskit-Solarzellen im Labormaßstab wurden mittels einer einstufigen Rotationsbeschichtung hergestellt. Die dabei eingesetzte schnelle Antilösungsmittelbehandlung führt jedoch zu rascher Kristallbildung, was die Schichthomogenität beeinträchtigen kann und nicht mit großflächiger industrieller Herstellung vereinbar ist. Eine vielversprechende Alternative ist das lösungsbasierte Zweischrittverfahren, bei dem zunächst die anorganischen Materialien – entweder lösungs- oder gasphasenbasiert – und anschließend die organischen Kationen lösungsbasiert aufgebracht werden. Das Eindringen der organischen Materialien von oben ermöglicht eine verbesserte Kontrolle über Kristallisationskinetik und Schichtmorphologie bei gleichzeitiger Kompatibilität mit industriell relevanten Herstellungsmethoden.

Diese Arbeit untersucht sowohl vollständig lösungsbasierte als auch hybride Zweischrittverfahren, um bestehende Herausforderungen in der Dünnschichtbildung auf texturierten Substraten, an Grenzflächen, der Bauteilstabilität und der Prozessreproduzierbarkeit anzugehen. Vor Beginn dieser Arbeit wurden nur wenige Perowskite mit einer weiten Bandlücke ($E_\mathrm{g} \approx 1{,}65\text{-}1{,}75\,\mathrm{eV}$) mittels eines vollständig lösungsbasierten Zweischrittverfahrens hergestellt, obwohl sie für leistungsstarke monolithische Perowskit/Silizium-Tandemsolarzellen essenziell sind. In dieser Arbeit wird daher eine neue Strategie zum Bromeinbau entwickelt, um die Bandlücke auf 1,68 eV einzustellen. In Kombination mit Kompositionsoptimierung sowie fortgeschrittener Perowskitschicht- und Oberflächenpassivierung führt diese Strategie zu Perowskitsolarzellen mit Wirkungsgraden von 20,9%, die damit zu den besten mittels Zweischrittverfahren hergestellten Perowskit-Solarzellen mit weiter Bandlücke zählen. Integriert in monolithische Perowskit/Silizium-Tandemarchitekturen werden Wirkungsgrade von 28,0% auf planaren, 26,2% auf submikrometerstrukturierten und 24,1% auf mikrometerstrukturierten Siliziumsolarzellen erreicht – jeweils im oberen Bereich der für dieses Herstellungsverfahren bisher veröffentlichten Wirkungsgrade. Eine dünne, gasphasenabgeschiedene CsCl-Keimschicht an der Grenzfläche zwischen Lochtransportschicht und Perowskit-Dünnschicht reduziert die Bildung von Kurzschlüssen auf mikrometertexturierten Substraten und verbessert die Ausbeute funktionierender Tandemsolarzellen deutlich. Dafür sind keine Anpassungen im etablierten Herstellungsverfahren notwendig.

Zur weiteren Verbesserung der Kompatibilität mit industriellen Herstellungsverfahren und zur Gewährleistung konformer Beschichtung auf mikrometerstrukturierten Substraten wird ein vollständig sequenzielles hybrides

Zweischrittverfahren eingeführt. Im Vergleich zur konventionellen Co-Abscheidung der anorganischen Materialien verbessert die sequenzielle Abscheidung die Prozessreproduzierbarkeit und ermöglicht Weitbandlücken-Perowskitsolarzellen mit Wirkungsgraden bis zu 20,3%, womit sie zu den effizientesten Hybrid-Zweischritt-Perowskitsolarzellen zählen. Das Wachstum der sequenziell hergestellten anorganischen Schicht ist weitgehend unabhängig von der zugrunde liegenden Substrattextur, wodurch sich dieses Herstellungsverfahren besonders gut für die industrielle Integration monolithischer Perowskit/Silizium-Tandemsolarzellen eignet.

Durch die gezielte Auseinandersetzung mit zentralen Herausforderungen hinsichtlich Defektbildung, Grenzflächenqualität und Prozessreproduzierbarkeit leistet diese Arbeit einen wichtigen Beitrag zur Entwicklung lösungsbasierter Zweischrittverfahren für eine zuverlässige Integration von Perowskit-Dünnschichten auf texturierten Siliziumzellen – ein wesentlicher Schritt in Richtung industrieller Perowskit/Silizium-Tandemphotovoltaik.

Abstract

Addressing climate change requires a rapid transition to renewable energy technologies. Photovoltaics play a central role in this transition by providing low-carbon electricity to meet growing global energy demand. Silicon solar cells dominate today's market and are highly reliable; however, they are approaching their practical efficiency limit. A promising strategy to surpass this limit is to combine silicon with a wide-bandgap absorber in a tandem architecture, enabling more efficient use of the solar spectrum. Among next-generation photovoltaic technologies, metal halide perovskites have emerged as strong candidates due to their outstanding optoelectronic properties – including a tunable bandgap, a high absorption coefficient, and a long charge-carrier diffusion length – as well as their rapid efficiency improvements over the past decade. In addition, perovskites offer key advantages typical of thin-film technologies, such as low-temperature processing and low-cost fabrication.

However, fabricating high-quality perovskite thin films several hundred nanometers thick on micron-textured industrial silicon wafers remains challenging and requires deposition methods that are scalable and highly repeatable. To date, the most efficient laboratory-scale perovskite solar cells have been fabricated using an one-step spin-coating method. However, the fast antisolvent quenching used in this method leads to rapid nucleation, which can compromise film uniformity and is not compatible with large-area industrial manufacturing. A promising alternative is the solution-based two-step deposition method, in which the inorganic precursors are deposited first – either solution- or vapor-based – and are then followed by a solution-based deposition of the organic cation precursors. The top-down penetration of the organic precursors enables improved control over crystallization kinetics and film morphology while remaining compatible with industrially relevant deposition techniques.

This thesis explores both fully solution-based and hybrid two-step deposition routes to address persistent challenges in perovskite thin-film formation on textured substrates, interface quality, device stability, and process repeatability. Prior to this work, wide-bandgap perovskite thin films ($E_g \approx 1.65\text{-}1.75\,\text{eV}$) had only rarely been fabricated using a fully solution-based two-step deposition route, despite being essential for high-performance two-terminal perovskite/silicon tandem solar cells. In response, a novel bromide incorporation strategy is developed to tune the perovskite bandgap to the target of 1.68 eV. Combined with compositional engineering and advanced bulk and surface passivation, this strategy yields perovskite solar cells with efficiencies up to 20.9%, placing them among the highest-performing wide-bandgap perovskite solar cells fabricated *via* a solution-based two-step deposition route. Integrated into two-terminal perovskite/silicon tandem architectures, efficiencies of 28.0% for planar, 26.2% for submicron-textured, and 24.1% for micron-textured silicon bottom cells are achieved – among the highest reported for this fabrication method. Introducing a thin, vapor-deposited CsCl seed layer at the hole transport layer/perovskite interface reduces shunt formation on micron-textured substrates, significantly improving fabrication yield without requiring adjustments to the established fabrication process.

To further enhance compatibility with industrial manufacturing and ensure conformal coverage on micron-textured surfaces, a fully sequential hybrid two-step deposition method is introduced. Compared to conventional co-deposition of inorganic precursors, sequential deposition improves process repeatability and enables wide-bandgap perovskite solar cells with efficiencies up to 20.3%, ranking among the highest-performing hybrid two-step processed perovskite solar cells reported to date. The inorganic scaffold growth for sequential deposition is largely texture-independent, making this method particularly well suited for industrial two-terminal perovskite/silicon tandem integration.

By addressing key challenges in defect formation, interface quality, and process repeatability, this work advances solution-based two-step deposition routes for reliable integration of perovskite thin films on textured silicon bottom cells – an essential step toward industrial perovskite/silicon tandem photovoltaics.

Contents

List of Abbreviations

AFM	Atomic force microscopy
ALD	Atomic layer deposition
AM	Air mass
BAI	n-Butylammonium iodide
BCP	Bathocuproine
C_{60}	Fullerene-C_{60}
CB	Conduction band
CTL	Charge transport layer
DB	Detailed balance
DC	Double-cation
DI	Deionized
DJ	Dion-Jacobson
DMF	N,N-dimethylformamide
DMSO	Dimethyl sulfoxide
E_g	Bandgap energy
EQE	External quantum efficiency
ETL	Electron transport layer
EtOH	Ethanol
FA	Formamidinium
FF	Fill factor
FWHM	Full width at half maximum
GIWAXS	Grazing-incidence wide-angle X-ray scattering
HTL	Hole transport layer
IPA	Isopropanol
ITO	Indium tin oxide
IZO	Indium zinc oxide
J_{SC}	Short-circuit current density

J-V	Current density-voltage
LCOE	Levelized cost of electricity
LiF	Lithium fluoride
MA	Methylammonium
MgF_2	Magnesium fluoride
MPP	Maximum power point
NiO_x	Nickel oxide
n_{id}	Ideality factor
PCE	Power conversion efficiency
$PDAI_2$	Propane-1,3-diammonium iodide
PLQY	Photoluminescence quantum yield
PSC	Perovskite solar cell
PV	Photovoltaic
QCM	Quartz crystal microbalance
QFLS	Quasi-Fermi level splitting
RH	Relative humidity
RMS	Root mean square
RP	Ruddlesden-Popper
SEM	Scanning electron microscopy
Si	Silicon
SJ	Single-junction
SnO_x	Tin oxide
SR	Spectral response
ST	Semitransparent
TC	Triple-cation
TCO	Transparent conductive oxide
ToF-SIMS	Time-of-flight secondary ion mass spectrometry
TSC	Tandem solar cell
UV/Vis	Ultraviolet-visible
VB	Valence band
V_{OC}	Open-circuit voltage
$V_{OC\text{-}imp}$	Implied open-circuit voltage

XRD	X-ray diffraction
XPS	X-ray photoelectron spectroscopy
2PACz	[2-(9H-carbazol-9-yl)ethyl]phosphonic acid
2D	Two-dimensional
2T	Two-terminal
3D	Three-dimensional
4T	Four-terminal

1 Introduction

1.1 Motivation

Energy production is one of the cornerstones of modern society, powering industries, transportation, and daily life. However, the way energy is generated has profound implications for the environment and climate. In 2024, fossil fuels such as coal, natural gas, and oil accounted for nearly 60% of global electricity generation.[1] Despite their current abundance and historical cost advantages, fossil fuels are the primary source of carbon dioxide emissions (Figure 1.1a), driving global warming and its associated ecological and societal consequences.[1,2] Therefore, decarbonizing electricity generation is the most effective path to a low-carbon, sustainable energy future.[1,3,4] While nuclear power offers a low-carbon alternative, it faces persistent challenges related to safety, health, waste management, public acceptance, and high capital costs.[5] Consequently, renewable energy technologies – such as wind, hydro, and solar power – play a central role in global decarbonization efforts, and, in 2025, collectively generated more electricity worldwide than coal.[6] Among these technologies, solar power stands out due to the abundance and universal availability of solar energy. In roughly one hour, the sun delivers far more energy to the Earth than humanity consumes annually, giving solar power the potential to replace fossil fuels at large scale.[7] Photovoltaic (PV) technology, which converts solar energy directly into electrical energy, has become a driving force in this transition.[8] Over the past few decades, PV technology has experienced remarkable growth (Figure 1.1b), driven by technological advancements and substantial cost reductions. Nowadays, it is one of the most cost-effective options for generating new electricity worldwide.[1,4,9]

At the heart of PV technology advancements lies the semiconductor industry. For more than half a century, semiconductors have shaped technological progress, enabling devices ranging from transistors – the fundamental building blocks of modern electronic devices such as computers and smartphones – to light-emitting diodes and solar cells. Their electronic properties and efficient control of charge transport underpin innovations across a wide range of applications. In PV devices specifically, the absorber layer responsible for converting incident light into electrical charge carriers is a semiconductor.

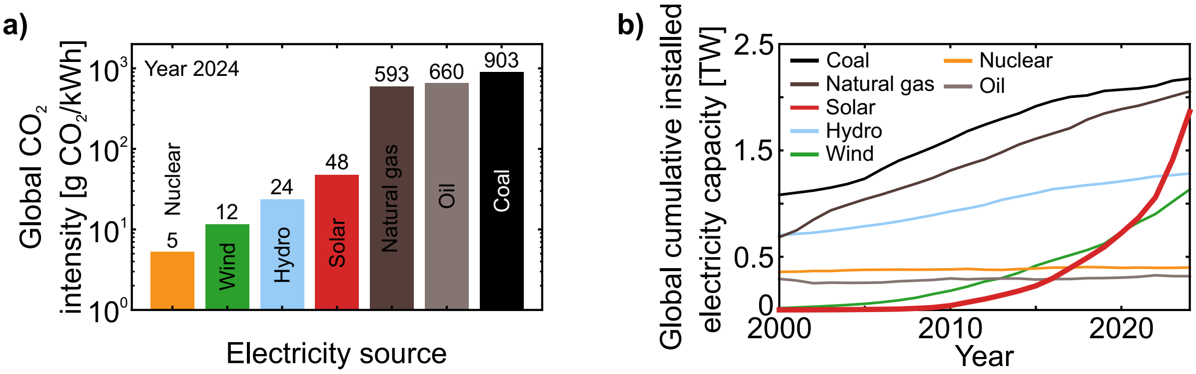

Figure 1.1: a) Global CO_2 intensity by electricity source in 2024, and b) evolution of global cumulative installed electricity capacity from 2000 to 2024, categorized by major electricity generation technologies such as fossil fuels (coal, natural gas, oil), renewable energy technologies (solar, hydro, and wind), and nuclear power, highlighting photovoltaic (PV) technology as the fastest growing energy source. Based on data sets from EMBER[10].

Currently, silicon (Si) solar cells dominate the PV market, accounting for over 95% of global production. Their rapid technological advancements and scalability have made PV systems economically competitive, with levelized cost of electricity (LCOE) falling below that of conventional fossil fuel power plants.[4,8,11] However, crystalline Si solar cells are approaching their practical efficiency limit of $\approx 29.4\%$,[12,13] with current power conversion efficiency (PCE) records at 27.9%.[14] Furthermore, the energy-intensive purification of raw Si significantly contributes to the environmental footprint of PV manufacturing.[15]

To meet future energy demands and accelerate the transition to a low-carbon economy, innovative solar cell concepts capable of surpassing the theoretical efficiency limit of single-junction (SJ) solar cells (approximately 33.7%, detailed balance limit, $E_g = 1.34\,\text{eV}$[16]) are required.[17,18] A promising concept is the development of multi-junction solar cells, in which two or more absorbers with different bandgaps are stacked on top of each other to more effectively utilize the solar spectrum and reduce thermalization losses.[9,19] To balance the trade-off between performance gains and complexity with an increasing number of junctions, tandem solar cells (TSCs) – which stack two subcells – have emerged as one of the most promising multi-junction architectures.[19,20] A variety of material systems have been explored for tandem integration, including III-V (combining Group III and Group V elements), CI(G)S ($CuIn_xGa_{(1\text{-}x)}Se_2$), organic, and dye-sensitized solar cells.[21–24] Currently, III-V/Si TSCs have the highest reported PCE of 36.1%;[14] however, their exceptionally high manufacturing costs and limited material availability restrict their use primarily to space and concentrated solar power applications.[21] Organic and dye-sensitized solar cells offer low-cost and mechanically flexible alternatives but remain constrained by comparatively low efficiencies and limited operational stability.[22,25] These limitations highlight the need for a tandem technology that simultaneously combines high performance, scalability, and low-cost manufacturing.

In recent years, organic-inorganic hybrid metal halide perovskite solar cells (PSCs) have attracted enormous attention as a next-generation PV technology. PCEs have risen impressively from 3.8%[26] in 2009 to 27.3%[14] in 2025, narrowing the gap to the highest reported PCEs of market-dominating Si solar cells (Figure 1.2). Perovskites are an emerging class of thin-film semiconductors, offering outstanding optoelectronic characteristics, including high absorption coefficients, long charge-carrier diffusion lengths, and a high defect tolerance.[9,18,27–30] Perovskite thin films can be processed at low temperatures and require only small material quantities, reducing energy consumption during fabrication.[31] Moreover, perovskites benefit from transferable expertise established in related thin-film technologies such as organic semiconductors, and the material costs contribute only marginally to the overall component cost.[32] Through compositional engineering, the perovskite bandgap can be tuned over a wide spectral range (≈ 1.2-$3.6\,\text{eV}$), making perovskites not only suitable for high-efficiency SJ solar cells but also excellent candidates for multi-junction PV, including combinations with Si and CI(G)S as well as all-perovskite configurations.[18,33–37] Wide-bandgap perovskite top cells ($E_g \approx 1.65$-$1.75\,\text{eV}$) are the perfect partner for Si bottom cells ($E_g \approx 1.12\,\text{eV}$) in a two-terminal (2T) perovskite/Si tandem configuration. This combination of technologies capitalizes on the maturity of Si technology and the unique properties of perovskite semiconductors, making perovskite/Si tandems

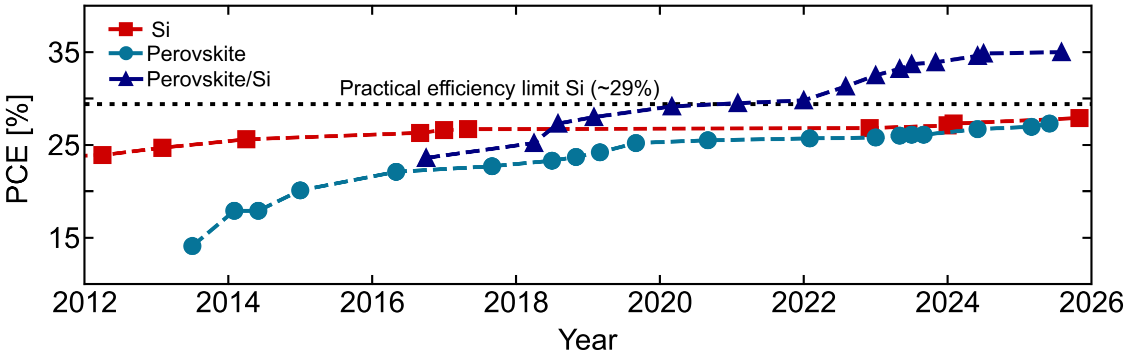

Figure 1.2: Best research-cell power conversion efficiency (PCE) chart of single-junction (SJ) silicon (Si) solar cells, SJ perovskite solar cells (PSCs), and 2T perovskite/Si tandem solar cells (TSCs), highlighting the rapid advances and the potential of perovskite-based photovoltaics (PV) to complement market-dominating Si solar cells. Based on data sets from NLR[14].

among the most promising candidates for mass-market tandem PV.[17,33,38] This tandem concept theoretically enables efficiencies of up to 45.1%,[39] with current laboratory-scale 2T perovskite/Si TSCs achieving efficiencies of 35% (Figure 1.2).[14]

Developing high-efficiency 2T perovskite/Si TSCs requires optimized perovskite compositions and fabrication techniques capable of producing uniform, defect-free perovskite thin films on commercial Si wafers, which typically feature micron-sized pyramidal textures.[40] While this surface texturing is crucial for enhanced light trapping and high device efficiency, it simultaneously introduces a substantial risk of shunting when depositing perovskite thin films with thicknesses of several hundred nanometers.[41–46] To date, the most efficient laboratory-scale SJ PSCs have been fabricated using one-step spin-coating processes.[46–51] However, the rapid nucleation induced by antisolvent quenching often results in poor film uniformity, and the method is not compatible with large-area industrial solar cell manufacturing.[52–56] A promising alternative is the two-step deposition method, comprising the subsequent deposition of the inorganic lead halide precursor in the first step, followed by the organic cation precursor.[57,58] Originally developed by Mitzi *et al.*[59] in 1998 and adapted for PSCs by Grätzel *et al.*[60,61] from 2013 onwards, this method enables – due to the top-down penetration of the organic precursors – improved control over film morphology, resulting in uniform, dense, and pinhole-free perovskite thin films with improved surface coverage. These characteristics make the two-step deposition method suitable for coating on Si bottom cells,[57,58,61–65] while offering flexibility in perovskite composition and compatibility with scalable perovskite deposition techniques such as vapor deposition, inkjet printing, and slot-die coating.[55,57,63,66–70]

Building on the versatility of the fully solution-based two-step process, hybrid two-step deposition methods have emerged, combining vapor deposition of the inorganic precursors with a subsequent solution-based deposition of the organic cations. This deposition method utilizes the conformal coverage provided by vapor deposition – even on micron-scale textures – and its established use in other industrial thin-film manufacturing processes,[71–75] while retaining the fast deposition of solution processing for organic components. The hybrid two-step deposition method allows for enhanced compositional flexibility, facile introduction of additives and the use of environmentally friendly solvents,[76–81] while being compatible with industrial-scale manufacturing. Hybrid two-step deposition has been successfully demonstrated in both SJ PSCs[80,82–86] and 2T perovskite/Si TSCs, with reported efficiencies of $\approx 31\%$ on micron-scale textured Si bottom cells.[87–89]

For a solar cell technology to reach mass production, it must meet several technological, economic, and social criteria. These include cost competitiveness, the use of environmentally friendly materials, scalability, high efficiency, and long-term operational stability.[90,91] For PSCs, this entails addressing challenges related to solvent use, lead content, and end-of-life management. If long-term operational stability and scalable fabrication are attained, perovskite/Si tandems have the potential to become a commercially viable, high-efficiency PV technology.[92,93] In wide-bandgap PSCs – essential for high-performance 2T perovskite/Si TSCs[39] – both efficiency and stability are notably limited by open-circuit voltage (V_{OC}) losses.[94–96] These are induced by non-radiative recombination,[97–99] halide phase segregation under continuous illumination,[100,101] and an inappropriate energy-level alignment at the perovskite/charge transport layer (CTL) interfaces.[102,103] Since the V_{OC} represents the driving force of the device, achieving values as close as possible to the radiative limit is critical to unlock the full potential of perovskite/Si TSCs (detailed balance V_{OC}: Si solar cell ≈ 0.86 V, PSC with 1.68 eV bandgap ≈ 1.38 V, $\rightarrow$ perovskite/Si TSC ≈ 2.24 V).[104,105] Although recent 2T perovskite/Si TSCs have demonstrated V_{OC} values exceeding 2 V,[89] the majority of reported devices remain below 1.9 V.[33,47] Therefore, minimizing non-radiative recombination losses at perovskite/CTL interfaces and within the perovskite bulk is essential.[97–99] To address these losses and improve long-term operational stability, advanced passivation strategies have gained attention.[106,107] One effective strategy involves incorporating two-dimensional (2D) perovskites based on long-chain organic cations at the surface or within the bulk of the three-dimensional (3D) perovskite thin film.[34,97,108–112]

Combining advanced passivation strategies with scalable two-step deposition methods has the potential to enable high-performance, stable SJ PSCs and 2T perovskite/Si TSCs suitable for industrial manufacturing.

1.2 Research Questions

A key challenge in the development of highly efficient 2T perovskite/Si TSCs is the deposition of high-quality perovskite films on textured Si bottom cells. While textured surfaces are important for light management and are standard in industrial Si manufacturing, they present significant challenges for conventional solution-based deposition methods. Uniform coverage is essential to minimize defect formation, ensure efficient charge-carrier transport, suppress non-radiative recombination, and fully exploit the performance potential of wide-bandgap perovskite top cells. Addressing these challenges requires deposition routes capable of forming dense, crystalline, and defect-free perovskite thin films while remaining compatible with industrial manufacturing. This work focuses on thin-film formation and material engineering of wide-bandgap perovskite thin films ($E_g \approx 1.68\text{-}1.70\,\mathrm{eV}$) fabricated *via* solution-based two-step deposition routes – either fully solution-based or as a hybrid route combining vapor- and solution-based deposition – by addressing the following research questions:

I: Bandgap engineering
How can the perovskite bandgap be tuned to a target of 1.68 eV for application in two-terminal perovskite/silicon tandem solar cells using a fully solution-based two-step deposition route?

II: Thin-film formation
How do perovskite composition and deposition route influence the microstructure and optoelectronic properties of perovskite thin films fabricated *via* a fully solution-based or hybrid two-step deposition route?

III: Additive and interface engineering
Which additive and interface engineering strategies can enhance perovskite film quality and thereby improve device performance and fabrication yield using a fully solution-based two-step deposition route?

IV: Tandem integration
How does the surface texture of the silicon bottom cell influence the integration of perovskite thin films in two-terminal perovskite/silicon tandem solar cells fabricated *via* a fully solution-based or hybrid two-step deposition route?

V: Stability
How stable are the fully solution-based two-step processed perovskite solar cells under relevant operational and stress conditions?

The research questions are addressed within the motivation and summary sections of the respective chapters. The concluding summary in Chapter 8 reviews the results of this work in relation to the defined research questions, evaluates the degree to which they have been achieved, and outlines possible future research objectives.

1.3 Outline

Chapter 1 positions perovskite PV within the broader context of renewable energy technologies. It outlines the motivation behind this work, highlights the current challenges in the field, and presents the overarching research questions that guide the thesis.
Chapter 2 provides the theoretical background, including the fundamental properties of hybrid metal halide perovskite semiconductors, the operating principles of PV devices, and technological concepts such as perovskite/Si TSCs.
Chapter 3 presents the experimental methods used throughout the thesis, covering the fabrication of thin films and PSCs with a focus on the solution-based two-step method – encompassing both fully solution-based deposition and hybrid deposition routes – as well as the material and device characterization methods used to evaluate structural,

optical, and electronic properties.

Chapter 4 addresses **research question I** by investigating a novel bromide incorporation strategy to engineer the bandgap of fully solution-based two-step processed perovskite thin films to 1.68 eV. Through a systematic evaluation, different bromide incorporation strategies are examined with respect to their influence on film morphology, crystallization, and optoelectronic properties. These findings provide valuable insights into **research question II**.

Chapter 5 investigates additives and interface passivation strategies to improve perovskite film quality and device stability of fully solution-based two-step processed PSCs, addressing **research questions III & V**. The resulting perovskite films are thoroughly characterized to assess improvements in microstructure and device performance, further contributing to **research question II**. Following the optimization of the perovskite film, the absorber is integrated into a 2T perovskite/Si tandem architecture, addressing the challenges outlined in **research question IV**.

Chapter 6 introduces a thin, vapor-deposited CsCl seed layer strategy to enhance film formation in fully solution-based two-step processed perovskite thin films. Motivated by deposition challenges on textured Si bottom cells, the influence of the CsCl seed layer on the microstructure of the inorganic scaffold and the final perovskite thin film is investigated, addressing **research questions II & III**. The impact of the CsCl seed layer on device performance and operational stability is further examined, contributing to **research question V**. Finally, the implementation of this strategy in 2T perovskite/Si tandem architectures – particularly on textured Si substrates – is evaluated with respect to fabrication yield, thereby addressing **research question IV**.

Chapter 7 develops a fully sequential hybrid two-step deposition route for the inorganic scaffold to enhance process repeatability and industrial compatibility. Comprehensive microstructural and elemental characterization of the sequentially deposited inorganic scaffolds and the resulting perovskite films addresses **research question II**. Beyond materials-level insights, the integration of the sequential deposition route at the device level and its compatibility with Si bottom cells with different surface textures is evaluated, directly addressing **research question IV**.

Chapter 8 summarizes the key findings of this thesis and outlines potential directions for future research on solution-based two-step processed perovskite PV.

2 Fundamentals

This chapter provides the theoretical background required to understand and evaluate the results presented in this thesis. It introduces metal halide perovskites, the material class used as the absorber layer in perovskite solar cells, covering their crystal structure, semiconductor properties, and morphology. The fundamental working principle of a perovskite solar cell is explained, including the equivalent circuit model, current-voltage characteristics, and key performance parameters. Finally, the chapter discusses device architectures of single-junction and tandem solar cells and concludes with the basic concepts underlying tandem integration.

2.1 Hybrid Metal Halide Perovskite Semiconductors

The perovskite crystal structure was discovered in 1839 by the German mineralogist G. Rose,[113] who observed it in a calcium titanate ($CaTiO_3$) compound and named it "perovskite" after the Russian mineralogist L. Perovski.[114] Hybrid metal halide perovskites were first synthesized in 1893, primarily as cesium (Cs) and potassium (K) lead halides with the formula $APbX_3$, where A denotes Cs or K and X represents iodide (I), bromide (Br), or chloride (Cl).[115] Detailed studies of their crystallographic and physical properties followed several decades later, with D. Weber publishing the first comprehensive report in 1978.[116,117] In recent years, hybrid metal halide perovskite semiconductors have gained significant attention in the field of PV technologies due to their exceptional optoelectronic properties.
In this work, only hybrid metal halide perovskite semiconductors are considered. These are hereafter denoted as "perovskite".

2.1.1 Crystal Structure

Perovskites exhibit a crystal structure described by the general chemical formula ABX_3, where A is a monovalent cation, B is a divalent cation, and X is a monovalent anion.[118] In the cubic unit cell, the B cation occupies the body center, the A cations the cube corners, and the X anions the face centers (Figure 2.1a). This arrangement places the B cation at the center of an octahedron formed by six surrounding X anions, and the periodic stacking of these unit cells results in a 3D crystal lattice (Figure 2.1b).[119] The electronic band structure is predominantly determined by the electronic orbitals of B^{2+} and X^-, while the A-site cations primarily ensure charge neutrality and lattice cohesion.[120] The formation of a cubic perovskite structure depends on the ionic radii of the atoms and molecules involved in the crystal lattice. The structural stability of a 3D perovskite structure can be estimated by the Goldschmidt tolerance factor t given by:

$$t = \frac{r_\mathrm{A} + r_\mathrm{X}}{\sqrt{2}(r_\mathrm{B} + r_\mathrm{X})}, \tag{2.1}$$

where r_A, r_B and r_X are the ionic radii of the corresponding ions.[121] The perovskite phase is formed when $0.8 < t < 1$.[33] A tolerance factor between 0.9-1.0 results in a cubic structure, which is well suited for solar cell application. Values in the range $0.8 < t < 0.9$ lead to lower-symmetry phases such as tetragonal, orthorhombic, or rhombohedral. For $t < 0.8$ or $t > 1.0$, the structure becomes non-perovskite, characterized by a distorted lattice due to tilted BX_6 octahedra, decreasing the symmetry of the structure.[56,122] For this reason, only a narrow range of organic and

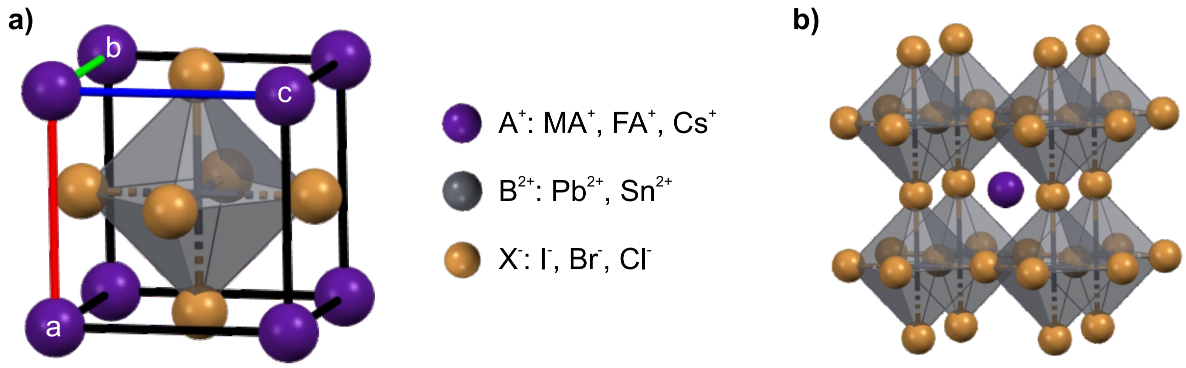

Figure 2.1: Schematic illustration of the perovskite crystal structure. a) The cubic perovskite unit cell with the general chemical formula ABX_3, where A is a monovalent cation, B is a divalent cation, and X is a monovalent anion. The B cation is located at the body center, the A cations at the corners of the cube, and the X anions at the face centers. b) Corner-sharing network of BX_6 octahedra forming the 3D crystal lattice.

inorganic A-site cations such as methylammonium ($\mathrm{CH_3NH_3^+}$, $\mathrm{MA^+}$), formamidinium ($\mathrm{NH_2CH=NH_2^+}$, $\mathrm{FA^+}$), or cesium ($\mathrm{Cs^+}$) have a suitable size to form a stable 3D lattice.[123] If the size of the A-site cation is too large to fit within the crystal lattice ($t > 1$), the perovskite lattice transitions from a bulk 3D structure to lower-dimensional phases with altered optoelectronic properties (Section 2.1.4).[111,124–126] The B-site cations are composed of metal cations such as lead ($\mathrm{Pb^{2+}}$) or tin ($\mathrm{Sn^{2+}}$), while the X-site anions are halides such as chloride ($\mathrm{Cl^-}$), bromide ($\mathrm{Br^-}$) and iodide ($\mathrm{I^-}$).[119,127]

2.1.2 Optoelectronic Properties

Perovskites exhibit exceptional optoelectronic properties that make them highly attractive for a broad range of applications, including PV, light-emitting diodes (LEDs), and lasers. The individual optoelectronic properties are discussed below, and a comparison to other semiconductor materials can be found in Table 2.1.

1. High absorption coefficient: As expected for direct-bandgap semiconductors, perovskites exhibit exceptionally high absorption coefficients (typically $\alpha > 10^4\,\mathrm{cm^{-1}}$), comparable to other thin-film semiconductors such as GaAs and about an order of magnitude higher than crystalline Si.[32,128] This outstanding absorption capability, combined with their direct bandgap, allows efficient light harvesting even in thin absorber layers of a few hundred nanometers. Consequently, perovskite solar cells (PSCs) require substantially less absorber material compared to conventional Si solar cells, which rely on thicknesses of several hundred micrometers.[56,129]

2. Low exciton binding energy: In perovskites, photogenerated excitons (Coulombically bound electron-hole pairs) have a low binding energy of around 10-60 meV, which is below the thermal energy at room temperature ($k_\mathrm{B}T \approx 25\,\mathrm{meV}$, with the Boltzmann constant k_B). As a result, they can easily dissociate into free charge carriers upon light absorption, enabling efficient charge separation and extraction.[32,56,130] In low-dimensional perovskite systems, the enlarged bandgap results in a higher exciton binding energy, causing excitonic effects to become more pronounced.[131]

3. Long charge-carrier lifetimes and diffusion lengths: In perovskites, free charge carriers exhibit high charge-carrier mobilities ($\mu \approx 10\,\mathrm{cm^2V^{-1}s^{-1}}$) and long charge-carrier lifetimes that can exceed 1 µs, resulting in diffusion lengths of several micrometers. Combined with their high absorption coefficients – which translate into absorption lengths of only a few tens to hundreds of nanometers, well below the diffusion length – and their remarkable intrinsic defect tolerance, charge carriers can travel significant distances before recombining, increasing the probability of charge-carrier extraction.[27,132–134]

4. Tunable bandgap: One of the most distinctive characteristics of perovskites is their tunable bandgap, which can be adjusted over a wide spectral range ($\approx$ 1.2-3.6 eV) by compositional engineering. This tunability is primarily achieved by varying the elemental composition at the halide (X) or metal (B) sites within the $\mathrm{ABX_3}$ crystal structure. Substituting $\mathrm{I^-}$ with smaller halides such as $\mathrm{Br^-}$ or $\mathrm{Cl^-}$ increases the bandgap to 2.3 eV and 3.6 eV, respectively. Partial or complete replacement of $\mathrm{Pb^{2+}}$ with $\mathrm{Sn^{2+}}$ reduces the bandgap, enabling absorption closer to the near-infrared region. Density functional theory studies attribute this bandgap tunability to changes in orbital coupling between the B-site cation and the halide anion. The valence band (VB) maximum originates from antibonding coupling between the B-site cation s-orbitals and the X-site anion p-orbitals, making its energetic position sensitive to the electronegativity χ of the constituent elements ($\chi(\mathrm{Pb}) < \chi(\mathrm{Sn})$ and $\chi(\mathrm{I}) < \chi(\mathrm{Br}) < \chi(\mathrm{Cl})$). Consequently, a change in metal or halide component leads to a shift in the VB maximum. The conduction band (CB) minimum involves an antibonding coupling between the B-site cation p-orbitals and the X-site anion s-orbitals. Because the orbital overlap is smaller for the CB, hybridization is not as pronounced, leading to a more ionic bond in which the CB is dominated by the metal state.[37,120,135] Consequently, compositional modifications at the B- or X-sites in the perovskite structure alter the B-X bond length and the orbital overlap, with larger bond distances narrowing the bandgap and shorter distances widening it.[136]

Table 2.1: Comparison of fundamental optoelectronic properties of Si, GaAs, organic and perovskite semiconductors.[32]

Property	Si[137,138]	GaAs[137–139]	Organic semiconductor[140]	Perovskite[56,141]
Crystal form	monocrystalline	monocrystalline	amorphous	polycrystalline
Electron mobility μ [$cm^2V^{-1}s^{-1}$]	1400	8500	10^{-6}-10^0	10-100
Bandgap [eV]	1.12 (indirect)	1.42 (direct)	1.1 - > 3	1.2-3.6
Absorption coefficient α at 650 nm [cm^{-1}]	$2{\cdot}10^3$	10^4	10^4-10^5	$4{\cdot}10^4$ ($MAPbI_3$)
Exciton binding energy [meV]	15	4	several hundred	10 ($MAPbI_3$) - 60 ($MAPbCl_3$)

2.1.3 Electronic Structure and Defect Tolerance

Perovskites exhibit remarkable morphological versatility owing to their soft ionic crystal structure and can be fabricated as colloidal nanocrystals (quantum dots), bulk single crystals, and polycrystalline thin films. While nanocrystals and single crystals are widely used in LEDs and detector applications, polycrystalline thin films are the predominant morphology in PV devices.

In contrast to single crystals with a continuous crystal lattice, polycrystalline thin films consist of numerous crystallites of varying size and orientation. Grain sizes typically range from tens of nanometers to several micrometers, depending on nucleation and crystallization kinetics during film formation. Grain boundaries and surfaces can host structural disorder and point defects, including atomic vacancies, interstitials, and anti-site substitutions, which introduce electronic states within the bandgap, shift the position of the Fermi level, and trap or release charge carriers. Shallow traps, with defect levels close to the band edges, primarily slow down the charge-carrier transport *via* trapping-detrapping processes, whereas deep traps, with defect levels inside the bandgap, act as efficient

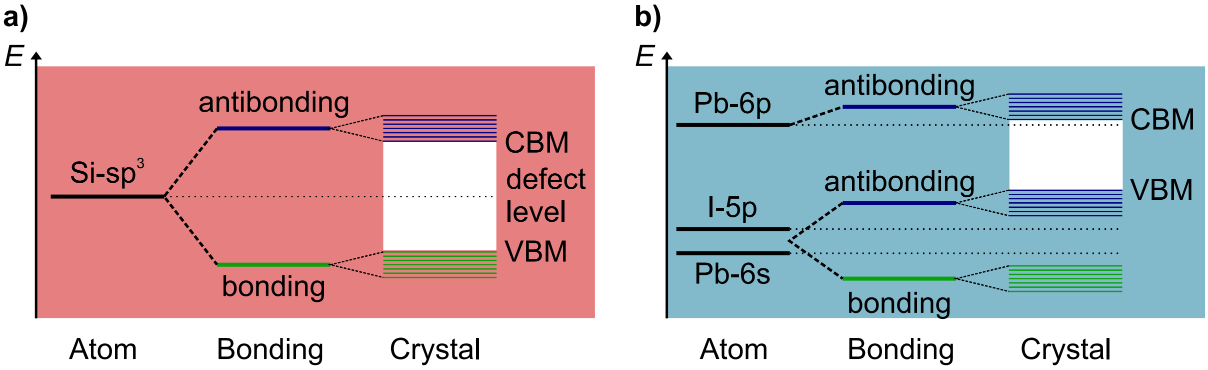

Figure 2.2: Schematic illustration of the electronic structure of a crystal formed by the overlap of atomic orbitals, shown for a) silicon (Si) and for b) the perovskite composition $MAPbI_3$. Defect levels resulting from unsaturated bonds can lie within or outside the bandgap (light area) between the conduction band minimum (CBM) and the valence band maximum (VBM).

non-radiative recombination centers and strongly reduce charge-carrier lifetimes.[37,142] Conventional semiconductors such as Si or GaAs are highly sensitive to such defects and therefore require defect densities $< 10^8 - 10^{10}$ cm^{-3}.[143–145] In contrast, polycrystalline perovskite thin films exhibit a comparatively high tolerance toward structural imperfections, with trap densities in the order of $\approx 10^{13} - 10^{18}$ cm^{-3}.[146]

This high defect tolerance is closely linked to the electronic structure of perovskites. In conventional inorganic semiconductors such as Si, the hybridization of the sp^3-orbitals of two Si atoms results in a bonding orbital and an antibonding orbital. When defects are present, such as undercoordinated atoms or dangling bonds, these atoms cannot fully hybridize and the corresponding unpaired orbitals remain as deep trap states (Figure 2.2a). In contrast, perovskites have an antibonding valence band maximum (VBM), originating from the covalent bonding between the metal s-orbitals (Pb-6s or Sn-5s) and the halide p-orbitals (I-5p, Br-4p, Cl-3p). Consequently, uncoordinated atoms or unsaturated bonds generate states within the VB that do not markedly affect charge carriers (Figure 2.2b). The antibonding conduction band minimum (CBM) has metal p-character (Pb-6p or Sn-5p) and hybridizes with the significantly lower-energy halide s-orbital (not shown in the figure). Due to the relatively small energetic splitting, the CBM remains close in energy to the metal p-states. As a result, defects lead to shallow traps, which only marginally affect charge-carrier transport. The A-site cations do not participate in covalent bonding in the perovskite lattice. Therefore, A-site vacancies usually do not introduce defect states within the bandgap, further contributing to the defect tolerance characteristic of perovskites.[32,147–149] As a result, polycrystalline perovskite thin films can retain long charge-carrier diffusion lengths and sharp absorption onsets, exhibiting optoelectronic properties surprisingly close to those of high-quality single crystals despite their higher defect densities.[32,150]

Because perovskite thin-film morphology strongly influences crystallization kinetics, defect formation, phase stability, and interface quality, controlling the microstructure is essential. Parameters such as compositional and structural uniformity, film thickness, surface roughness, and grain-size distribution directly affect charge-carrier transport and recombination. While larger grains reduce the grain-boundary density, effective defect passivation at grain boundaries and interfaces remains equally important. Ultimately, minimizing electronically active defects is crucial for maximizing both efficiency and long-term operational stability of PSCs.[150–152]

2.1.4 Low-Dimensional Perovskites

Low-dimensional perovskites are formed when bulky organic cations are incorporated at the A-site of the perovskite crystal, disrupting the 3D lattice and resulting in 2D (sheet), 1D (wire), or 0D (dot) structures. Among these, 2D Dion-Jacobson (DJ)[126] and Ruddlesden-Popper (RP)[111,124] phase perovskites have attracted particular interest for optoelectronic applications due to their tunable electronic properties and superior environmental stability. 2D perovskites follow the general crystal structure $\mathrm{R_mA_{n-1}B_nX_{3n+1}}$ with $\mathrm{n} = 1, 2, 3, \ldots, \infty$. Here, R represents a long-chain aliphatic or aromatic alkylammonium organic cation spacer between the 3D perovskite layers. The parameter n defines the number of 3D perovskite layers sandwiched between two organic cation spacer layers, ranging from 2D ($\mathrm{n} = 1$), quasi-2D ($\mathrm{n} =$ 2-5), and 3D ($\mathrm{n} \to \infty$) perovskite phases (Figure 2.3a).[125,131] DJ perovskite phases use single organic cations ($\mathrm{m} = 1$) with two functional groups, and the adjacent layers are connected *via* hydrogen bonding.[150,153–155] In contrast, 2D RP perovskite phases use two bulky organic spacer cations ($\mathrm{m} = 2$) per formula unit, and the 2D layers are held together by weak van der Waals interactions.[126,150,153,156,157]

Compared to their 3D counterparts, 2D perovskite structures exhibit enhanced moisture and thermal stability. The hydrophobic organic spacer layers, together with strong interlayer interactions, effectively protect the perovskite surface from humidity-induced degradation.[158,159] In addition, the low volatility of the long-chain organic cations further enhances the thermal robustness of the devices.[160]

Despite these advantages, the PV performance of 2D PSCs remains inferior to that of 3D perovskites. The insulating nature of the organic spacer cations hinders efficient charge transport. Furthermore, the large dielectric mismatch between the inorganic layers and the bulky organic spacers – combined with the difference in bandgap – induces pronounced quantum confinement of the charge carriers. This confinement substantially increases the exciton binding energy, causing excitonic effects to become increasingly pronounced in low-dimensional perovskite

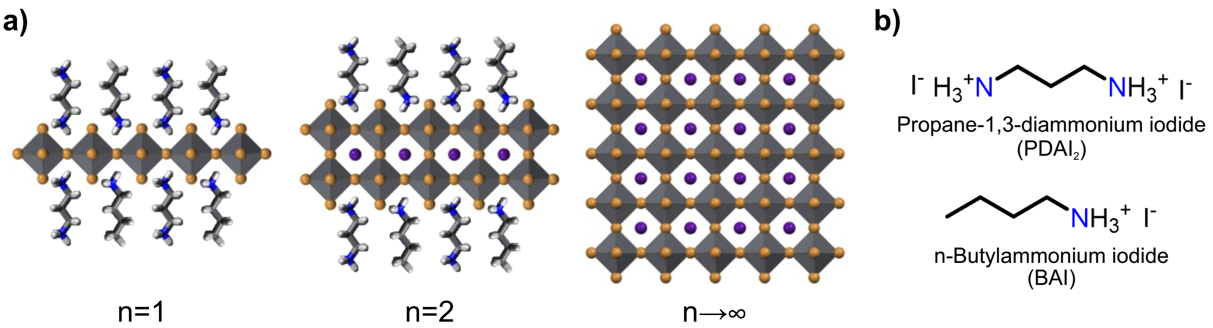

Figure 2.3: a) Schematic illustration of low-dimensional perovskites, showing the transition from 2D ($\mathrm{n} = 1$) through quasi-2D ($\mathrm{n} =$ 2-5) to 3D ($\mathrm{n} \to \infty$) perovskite phases. b) Molecule structures of propane-1,3-diammonium iodide ($PDAI_2$) and n-butylammonium iodide (BAI).

systems.[131] These factors limit charge-carrier separation and migration to the electrode contacts, ultimately reducing the device performance of 2D PSCs.[161–163]

Incorporating an ultrathin 2D layer at perovskite/charge transport layer (CTL) interfaces or within the bulk of a 3D perovskite increases the activation energy for ion migration, while the resulting 2D/3D heterojunction introduces an energy offset that suppresses interfacial recombination. Together, these effects efficiently passivate defects of the 3D perovskite surface and bulk, thereby enhancing device stability and reducing non-radiative recombination losses.[110,164–169] This positions low-dimensional perovskites as an effective passivation strategy for wide-bandgap PSCs. In this work, propane-1,3-diammonium iodide ($PDAI_2$), forming a DJ phase, and n-butylammonium iodide (BAI), forming an RP phase, are used as passivation agents (Figure 2.3b).

2.2 Perovskite Solar Cells

2.2.1 Working Principle

PSCs operate based on the photovoltaic effect, converting the energy of incident solar radiation into electrical energy through a series of fundamental physical processes. The energy conversion mechanism can be summarized in five fundamental steps (Figure 2.4a): (1) absorption of incident photons in the absorber, (2) generation of electron-hole pairs, (3) spatial separation of free charge carriers (electrons and holes), (4) selective extraction of free charge carriers at charge transport layers (CTLs), and (5) extraction of free charge carriers at respective electrode contacts. In a closed electrical circuit, the transport of charge carriers through the external load constitutes the photocurrent, while the photovoltage arises from the potential difference between the two electrode contacts.[137,170,171]

To provide a deeper understanding of the underlying processes, these five fundamental steps are discussed in more detail below:

1. Absorption of incident photons: Incident photons with an energy equal to or greater than the perovskite bandgap ($E_\gamma \geq E_\mathrm{g}$) are absorbed by the perovskite thin film, exciting electrons from the valence band (VB) to the conduction band (CB). Photons with an energy below the bandgap ($E_\gamma < E_\mathrm{g}$) pass through the material without interaction. For photons with an energy exceeding the bandgap ($E_\gamma > E_\mathrm{g}$), the additional energy is rapidly dissipated as heat as excited carriers relax to the band edges, resulting in thermalization losses.

2. Generation of electron-hole pairs: The excitation of an electron from the VB to the CB generates an electron-hole pair. At room temperature, photogenerated electron-hole pairs readily dissociate into free negative (electrons, e) and positive (holes, h) charge carriers.

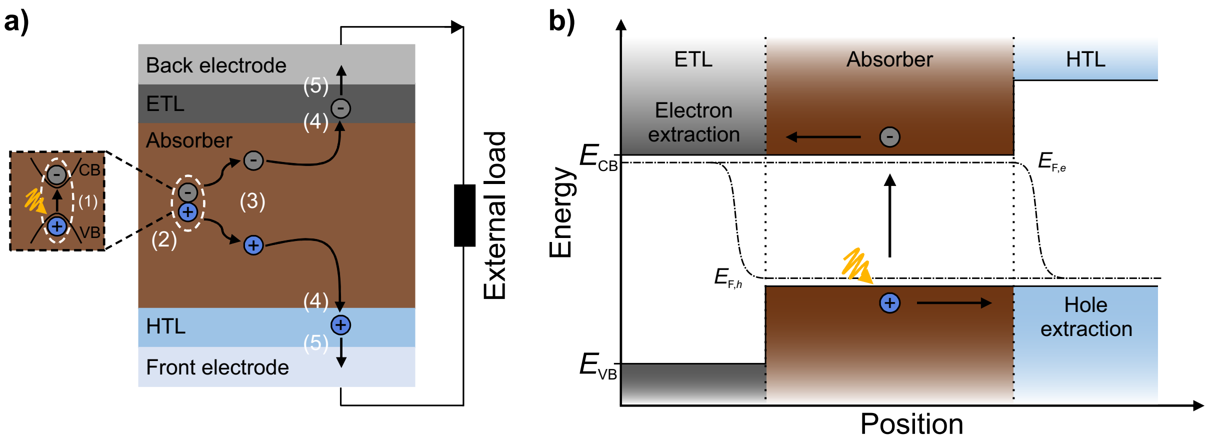

Figure 2.4: Working principle of a perovskite solar cell (PSC). a) Schematic illustration of the fundamental physical processes in a *p-i-n* PSC, where the perovskite thin film is sandwiched between an electron transport layer (ETL) and a hole transport layer (HTL), each connected to its respective electrode contact. The process sequence comprises: (1) absorption of incident photons in the absorber, (2) generation of electron-hole pairs, (3) spatial separation of free charge carriers (electrons and holes), (4) selective extraction of free charge carriers at charge transport layers (CTLs), and (5) extraction of free charge carriers at respective electrode contacts. b) Idealized energy band diagram of a PSC under illumination and at open-circuit condition. Electrons accumulate at the conduction band minimum (CB, E_{CB}), and holes accumulate at the valence band maximum (VB, E_{VB}). The quasi-Fermi level splitting (QFLS) into electron ($E_{\mathrm{F},e}$) and hole ($E_{\mathrm{F},h}$) quasi-Fermi levels generates a potential difference between the electrode contacts. The selective ETL and HTL enable efficient charge-carrier separation and extraction.

3. Spatial separation of free charge carriers: The free charge carriers propagate within the VB (holes) and CB (electrons) under the influence of two principal transport mechanisms: (i) drift, driven by a gradient in the electrical potential (electric field), and (ii) diffusion, governed by a gradient in the chemical potential (charge-carrier concentration).[170,172] To derive the total charge-carrier current of electrons (e) and holes (h) considering both driving transport mechanisms within the material, their individual contributions are first presented.

(i) If charge transport occurs only under the influence of an electric field E, the resulting charge-carrier drift current ($J_{\mathrm{drift},i}$) for carrier type i can be expressed as:

$$J_{\mathrm{drift},i} = z_i^2 e n_i \mu_i E = \sigma_i E = -\frac{\sigma_i}{z_i e}\mathrm{grad}(z_i e \varphi), \tag{2.2}$$

with e being the elementary charge (with $z_e = -1$ for electrons and $z_h = 1$ for holes), n_i the concentration of charge carriers, μ_i their mobility and σ_i their electrical conductivity. $E = -\,\mathrm{grad}(\varphi)$ represents the driving electric field acting on the charge carriers, with φ denoting the electrical potential.

(ii) When the electrical potential is the same at every location ($\mathrm{grad}(\varphi) = 0$), only a diffusion current acts on the charge carriers caused by a gradient in the charge-carrier concentration. The resulting charge-carrier diffusion current ($J_{\mathrm{diff},i}$) is given by Fick's law:

$$J_{\mathrm{diff},i} = z_i e(-D_i \mathrm{grad}(n_i)) = -\frac{\sigma_i}{z_i e}\mathrm{grad}(\Phi_{\mathrm{chem},i}), \tag{2.3}$$

using the Einstein relation $D_i = \frac{\mu_i k_{\mathrm{B}} T}{e}$ between the diffusion coefficient D_i and the mobility μ_i. Here, k_{B} is the Boltzmann constant and T the temperature. $\Phi_{\mathrm{chem},i}$ is the chemical potential.

Both driving transport mechanisms – drift and diffusion – act simultaneously, and their combined contribution determines the total charge-carrier current ($J_{\mathrm{total},i}$):

$$J_{\mathrm{total},i} = -\frac{\sigma_i}{z_i e}\mathrm{grad}(z_i e \varphi + \Phi_{\mathrm{chem},i}) = -\frac{\sigma_i}{z_i e}\mathrm{grad}(\eta_i), \tag{2.4}$$

where η_i is the electrochemical potential of the charge carriers.[172]

In the dark, a semiconductor is in thermodynamic equilibrium and the Fermi level (E_F) is identical with the electrochemical potential. According to the Fermi-Dirac distribution, the Fermi level is defined as the energy at which the occupation probability of an electronic state equals 50%. Therefore, electronic states below E_F are more likely to be occupied than those above it.

Under illumination, the generation of electron-hole pairs disturbs this equilibrium. The increased electron density in the CB shifts E_F closer to the CB minimum, whereas the increased hole density in the VB simultaneously pushes E_F closer to the VB maximum. Since a single Fermi level cannot describe both conditions, this contradiction is resolved by introducing two separate quasi-Fermi levels: $E_{\mathrm{F},e}$ for electrons, and $E_{\mathrm{F},h}$ for holes. This phenomenon, known as quasi-Fermi level splitting (QFLS), reflects the nonequilibrium steady state under continuous illumination (Figure 2.4b). The energy difference between these quasi-Fermi levels corresponds to the maximum achievable open-circuit voltage (V_OC) of the solar cell.[173]

The electrochemical potential of electrons in the CB is directly represented by their quasi-Fermi level ($\eta_e = E_{\mathrm{F},e}$), while the electrochemical potential of holes corresponds to their quasi-Fermi level ($\eta_h = E_{\mathrm{F},h}$), describing the occupation of states in the CB or VB, respectively. Consequently, the resulting charge-carrier currents are determined by the gradients of the quasi-Fermi levels ($E_{\mathrm{F},i}$) and the respective electrical conductivities (σ_i):

$$J_{total,i} = -\frac{\sigma_i}{z_i e}\mathrm{grad}(E_{\mathrm{F},i}). \tag{2.5}$$

4. Selective extraction of free charge carriers at charge transport layers: Efficient solar cell operation requires selective extraction of photogenerated electrons and holes at opposite contacts. In contrast to classical, heavily doped *p-n* junctions, PSCs operate as heterostructure devices in which an intrinsic perovskite film is sandwiched between two carrier-selective contacts: an electron transport layer (ETL) and a hole transport layer (HTL). Although this device architecture is frequently labeled as *n-i-p* or *p-i-n*, such notation should not be interpreted as classical doping profiles. Instead, PSCs are more accurately described as flatband heterostructure solar cells, emphasizing that charge-carrier extraction is primarily determined by interfacial energy-level alignment of the charge transport layers (CTLs).

Energy-level alignment is central to contact selectivity. The ETL must provide a CB minimum closely aligned with that of the perovskite to enable efficient electron transfer, while its VB maximum must be sufficiently offset to block holes. Conversely, the HTL requires a VB maximum aligned with that of the perovskite for efficient hole transfer and a large CB offset to block electrons. Proper energy-level alignment between the perovskite and CTLs minimizes interfacial recombination and maximizes QFLS, which is critical for achieving high V_OC.

Beyond energy-level alignment, the ETL and HTL must exhibit high conductivity for their respective charge-carrier type and low conductivity for the opposite type. This selective conductivity ensures directional transport toward the electrode contacts while preventing back-injection. Given the long charge-carrier lifetimes and diffusion lengths in perovskites, nearly all photogenerated electrons and holes are efficiently extracted from the absorber through the ETL and HTL, respectively. In such flatband heterostructures, the direction of the net charge-carrier current is opposite to the maximum gradient of the quasi-Fermi levels.[170,174,175]

5. Extraction at electrode contacts: The charge carriers are extracted at their respective electrode contacts, enabling current flow through the external load. Under short-circuit conditions, the potential difference between the contacts vanishes ($V = 0$), and charge carriers are collected at their respective electrode contacts, generating a short-circuit current (I_SC). Under open-circuit conditions, no net current flows, and the difference between the quasi-Fermi levels at the electrode contacts defines the open-circuit voltage (V_OC). During normal operation under illumination with an external load, the device operates between these two extremes, producing both photocurrent and photovoltage, thereby generating electrical power.

To calculate the steady-state current generated by a solar cell under continuous illumination, the net contribution of all generated and recombined charge carriers across the absorber must be considered. The resulting charge current density is given by:

$$J = e \int_0^d (G(x) - R(x))\, dx, \tag{2.6}$$

where d is the absorber thickness, G the generation rate and R the recombination rate. The sign convention is defined such that a positive current density represents charge being extracted from the illuminated solar cell toward the external load. The generation rate is divided into G_0 under dark conditions and ΔG under illumination, corresponding to the absorption of photons with $E_\gamma \geq E_\mathrm{g}$:

$$G(x) = G_0(x) \,+\, \Delta G(x). \tag{2.7}$$

The recombination rate is given by:

$$R(x) = R_0(x)\, \exp\left(\frac{E_{\mathrm{F},e}(x) - E_{\mathrm{F},h}(x)}{k_\mathrm{B}T}\right) = R_0(x)\, \exp\left(\frac{eV}{k_\mathrm{B}T}\right), \tag{2.8}$$

where R_0 describes the recombination rate under dark conditions, and the energy difference $E_{\mathrm{F},e}(x) - E_{\mathrm{F},h}(x)$ can be expressed as eV, where V represents the voltage drop between the respective electrode contacts.
In equilibrium, the generation rate and the recombination rate are equal ($G_0 = R_0$). Thus, the current density in Equation 2.6 can be expressed as follows:

$$\begin{aligned} J &= -e \int_0^d \left[G_0 \left(\exp\left(\frac{eV}{k_\mathrm{B}T}\right) - 1\right) - \Delta G(x)\right] dx \\ &= -e \left(\exp\left(\frac{eV}{k_\mathrm{B}T}\right) - 1\right) \int_0^d G_0(x)\, dx \,+\, e \int_0^d \Delta G(x)\, dx. \end{aligned} \tag{2.9}$$

To identify the individual contributions to the current density, two limiting cases of the governing equation are considered. Under illumination and short-circuit conditions ($V = 0$), the voltage-dependent term vanishes, and the remaining integral $e \int_0^d \Delta G(x)\, dx$ corresponds to the short-circuit current density (J_SC). Conversely, in the dark ($\Delta G = 0$) and under large negative bias ($\exp\left(\frac{eV}{k_\mathrm{B}T}\right) \ll 1$), the current is dominated by recombination, yielding the dark saturation current density (J_0). Therefore, the current-voltage characteristic of an ideal solar cell can be formulated as:

$$J = J_\mathrm{SC} - J_0 \left(\exp\left(\frac{eV}{k_\mathrm{B}T}\right) - 1\right). \tag{2.10}$$

This derivation relies on several simplifying assumptions. Only radiative generation and radiative recombination are considered, while non-radiative recombination pathways are neglected. The QFLS is assumed to be spatially uniform across the absorber, implying ideal transport without resistive losses or interfacial recombination. The transport layers and contacts are treated as perfectly selective and loss-free, and carrier extraction is assumed to occur without limitations from series resistance or space-charge effects. These idealizations correspond to the radiative limit and do not fully describe the behavior of a real solar cell.[16,170,175]

2.2.2 Photovoltaic Characteristics

2.2.2.1 Current Density-Voltage Characteristics

The electrical behavior of a solar cell can be described using an equivalent circuit based on the ideal diode equation. Although this equation is often derived for classical *p-n* junctions, its validity is not restricted to

doped homojunction devices. More generally, the exponential current-voltage dependence arises from the voltage-dependent recombination rate governed by the QFLS within the absorber.[170]
In the dark, the current is dominated by the diode current I_{diode}, representing radiative recombination losses:

$$I_{\mathrm{diode}}(V) = I_0 \left(\exp\left(\frac{eV}{n_{\mathrm{id}} k_{\mathrm{B}} T} \right) - 1 \right), \tag{2.11}$$

where I_0 is the dark saturation current and n_{id} the ideality factor (for more detail on n_{id}, see Section 3.2.2).
Under illumination, the solar cell generates a photocurrent I_{photo}, which increases with illumination intensity and is represented in the equivalent circuit as a current source in parallel with the diode. For an ideal solar cell, the output current $I(V)$ is therefore given by:

$$I(V) = I_{\mathrm{photo}} - I_0 \left(\exp\left(\frac{eV}{n_{\mathrm{id}} k_{\mathrm{B}} T} \right) - 1 \right). \tag{2.12}$$

To enable a meaningful comparison of solar cell performance, several fundamental parameters are derived from the current density-voltage (*J*-*V*) characteristics. These parameters quantify the electrical behavior under standard test conditions (AM1.5G spectrum) and provide insight into efficiency and loss mechanisms.
The short-circuit current (I_{SC}) represents the maximum current of the solar cell and is measured under short-circuit conditions ($V = 0$):

$$I_{\mathrm{SC}} = I(V = 0) \approx I_{\mathrm{photo}}. \tag{2.13}$$

For comparability across solar cells with different active areas (A), the short-circuit current is normalized to the short-circuit current density (J_{SC}):

$$J_{\mathrm{SC}} = \frac{I_{\mathrm{SC}}}{A}. \tag{2.14}$$

The open-circuit voltage (V_{OC}) is the maximum achievable voltage when no current flows ($I(V) = 0$). Using the diode equation, it is expressed as:

$$V_{\mathrm{OC}} = \frac{n_{\mathrm{id}} k_{\mathrm{B}} T}{e} \ln\left(\frac{I_{\mathrm{photo}}}{I_0} + 1 \right). \tag{2.15}$$

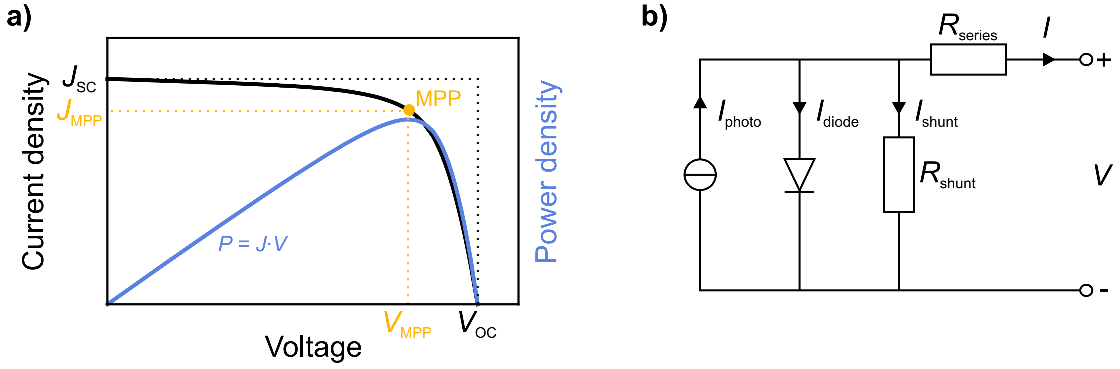

Figure 2.5: Photovoltaic (PV) and electrical characteristics of a perovskite solar cell (PSC). a) Current density *versus* voltage (*J*-*V*) characteristic under illumination, highlighting the key PV performance metrics: short-circuit current (J_{SC}) and open-circuit voltage (V_{OC}). The corresponding power density curve identifies the maximum power point (MPP), defined by J_{MPP} and V_{MPP}. From these parameters, the fill factor (FF) and the power conversion efficiency (PCE) are determined. b) Equivalent circuit of a PSC based on the one-diode model, representing the electrical response of the device. The model includes the photocurrent (I_{photo}), the diode current (I_{diode}) and resistive losses described by series (R_{series}) and shunt (R_{shunt}) resistances. The one-diode model represents the simplest model for describing a real solar cell. To account for non-radiative recombination losses, a second diode is added in parallel, resulting in the two-diode model.

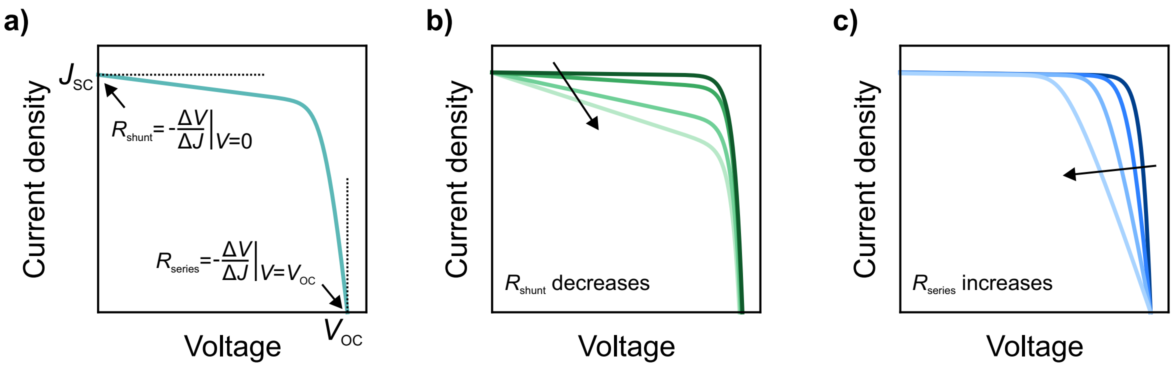

Figure 2.6: Influence of shunt (R_{shunt}) and series (R_{series}) resistances on the current density *versus* voltage (*J*-*V*) characteristics of a perovskite solar cell (PSC). a) Extraction of R_{shunt} and R_{series} from the slope of the *J*-*V* characteristic at short-circuit ($V = 0$) and open-circuit ($V = V_{\text{OC}}$) conditions, respectively. b) Effect of decreasing R_{shunt} on the *J*-*V* characteristic, leading to reduced fill factor (FF) and, for sufficiently low R_{shunt}, a noticeable reduction in V_{OC}. c) Effect of increasing R_{series} on the *J*-*V* characteristic, which similarly reduces the FF. Therefore, both – a low R_{shunt} and a high R_{series} – result in a reduced power conversion efficiency (PCE).

The product of current and voltage reaches its maximum at the maximum power point (MPP), defined by:

$$P_{\text{MPP}} = I_{\text{MPP}} V_{\text{MPP}}, \tag{2.16}$$

indicating the maximum power P_{MPP}. A characteristic current density *versus* voltage (*J*-*V*) curve of a PSC and the corresponding generated power output density is shown in Figure 2.5a.

The fill factor (FF) quantifies how closely the *J*-*V* curve approaches an ideal rectangular shape and is calculated as:

$$\text{FF} = \frac{P_{\text{MPP}}}{J_{\text{SC}} V_{\text{OC}}}. \tag{2.17}$$

Finally, the power conversion efficiency (PCE), the most important performance metric, is defined as the ratio of the electrical power at the MPP (P_{MPP}) to the incident light power density (P_{in}):

$$\text{PCE} = \frac{P_{\text{MPP}}}{P_{\text{in}}} = \frac{\text{FF} J_{\text{SC}} V_{\text{OC}}}{1000\,\text{Wm}^{-2}}, \tag{2.18}$$

assuming standard testing conditions (AM1.5G spectrum) with P_{in} of 1000 Wm^{-2}.

In a real solar cell, apart from radiative recombination losses, resistive losses have to be accounted for and cannot be neglected. The shunt resistance R_{shunt} represents unwanted leakage current paths due to imperfections in the absorber, while losses due to limited charge-carrier transport through the solar cell are described with the series resistance R_{series}. Both – shunt and series resistance – have to be added to the equivalent circuit, resulting in the one-diode model of a real solar cell (Figure 2.5b):

$$\begin{aligned} I(V) &= I_{\text{photo}} - I_{\text{diode}} - I_{\text{shunt}} \\ &= I_{\text{photo}} - I_0 \left(\exp\left(\frac{e(V + IR_{\text{series}})}{n_{\text{id}} k_{\text{B}} T} \right) - 1 \right) - \frac{V + IR_{\text{series}}}{R_{\text{shunt}}}, \end{aligned} \tag{2.19}$$

where I_{shunt} corresponds to the shunt resistance current.

The impact of R_{shunt} and R_{series} on solar cell performance can be extracted from the *J*-*V* characteristics at $V = 0$ and $V = V_{\text{OC}}$, respectively (Figure 2.6a):[137]

$$R_{\text{shunt}} = -\frac{\Delta V}{\Delta I}\Big|_{V=0} \; ; \; R_{\text{series}} = -\frac{\Delta V}{\Delta I}\Big|_{V=V_{\text{OC}}} \tag{2.20}$$

Low R_{shunt} results, for instance, from short-circuits caused by defects and grain boundaries in the bulk, considerably affecting FF and V_{OC} (Figure 2.6b). High R_{series} is caused by limited layer conductivity in the adjacent layers (ETL/HTL, electrode contact) in the device architecture, limiting the FF of the solar cell (Figure 2.6c).
The one-diode model represents the simplest model for describing a real solar cell. To account for non-radiative recombination losses, a second diode is added in parallel, resulting in the two-diode model.[137,170,176]

2.2.2.2 External Quantum Efficiency

The external quantum efficiency (EQE) is the fraction of photons incident on the solar cell that generate electron-hole pairs in the absorber and are successfully collected. The EQE is wavelength-dependent and is usually measured by illuminating the solar cell with monochromatic light of wavelength λ (known radiant photon flux $\Phi_{\mathrm{ph}}(\lambda)$) and measuring the photocurrent J_λ through the solar cell.[176] This can be calculated using the following equation:

$$\mathrm{EQE}(\lambda) = \frac{\text{collected charge carriers}}{\text{incident photons}} = \frac{J(\lambda)}{e\,\Phi_{\mathrm{ph}}(\lambda)}, \tag{2.21}$$

where e is the elementary charge. The J_{SC} can be calculated from the EQE using the following relationship:

$$J_{\mathrm{SC}} = e \int_{\lambda_1}^{\lambda_2} \mathrm{EQE}(\lambda)\,\Phi_{\mathrm{ph},\lambda}^{\mathrm{AM1.5}}\,d\lambda, \tag{2.22}$$

with the spectral photon flux of the AM1.5G spectrum $\Phi_{\mathrm{ph},\lambda}^{\mathrm{AM1.5}}$.[176]
Since the EQE quantifies the ratio of collected charge carriers to incident photons as a function of wavelength, it provides information about losses in the short-circuit current of a solar cell. For example, low quantum yields at small wavelengths typically indicate increased recombination at the front surface, whereas low quantum yields at longer wavelengths point to increased recombination at the back surface of the absorber. This is due to the wavelength dependence of the absorption coefficient: blue light is absorbed within a much shorter penetration depth than red light. In addition to recombination losses, optical losses such as parasitic absorption and reflected light also reduce the EQE signal. Taken together, these effects make the interpretation of EQE spectra inherently complex.[176]

2.2.3 Device Architecture of Single-Junction Perovskite Solar Cells

A typical single-junction (SJ) PSC consists of a photoactive perovskite thin film sandwiched between two CTLs – an ETL and an HTL – and adjacent electrode contacts. The front electrode, facing the incoming light, must be transparent and is typically made of a transparent conductive oxide (TCO) such as indium tin oxide (ITO) or indium zinc oxide (IZO). The rear electrode is usually a metal layer (e.g., Au, Ag, Cu).
Two main device architectures are distinguished based on the order of the CTLs with respect to the incident light: the "regular" architecture (*n-i-p*) shown in Figure 2.7a, and the "inverted" architecture (*p-i-n*) shown in Figure 2.7b. Although the terms *n*, *i* and *p* are commonly used to describe perovskite device architectures, they should not be interpreted as classical doping profiles. Historically, the *n-i-p* architecture dominated early perovskite PV research due to already established fabrication methods and initially higher efficiencies. With rapid material and process improvements, both architectures now achieve comparable PCEs. However, the *p-i-n* architecture has become attractive for practical applications due to improved stability, scalability, and simple integration into tandem devices.[177] For 2T perovskite/Si tandem solar cells (TSCs), the *p-i-n* architecture offers clear advantages: The layer stack minimizes parasitic absorption at the front side compared to *n-i-p* devices. For example, the thin n-type interface layer in *p-i-n* architecture (e.g., fullerene-C_{60}) introduces less optical loss than the thick, highly absorbing HTL commonly used in *n-i-p* architecture (e.g., Spiro-OMeTAD).[18]

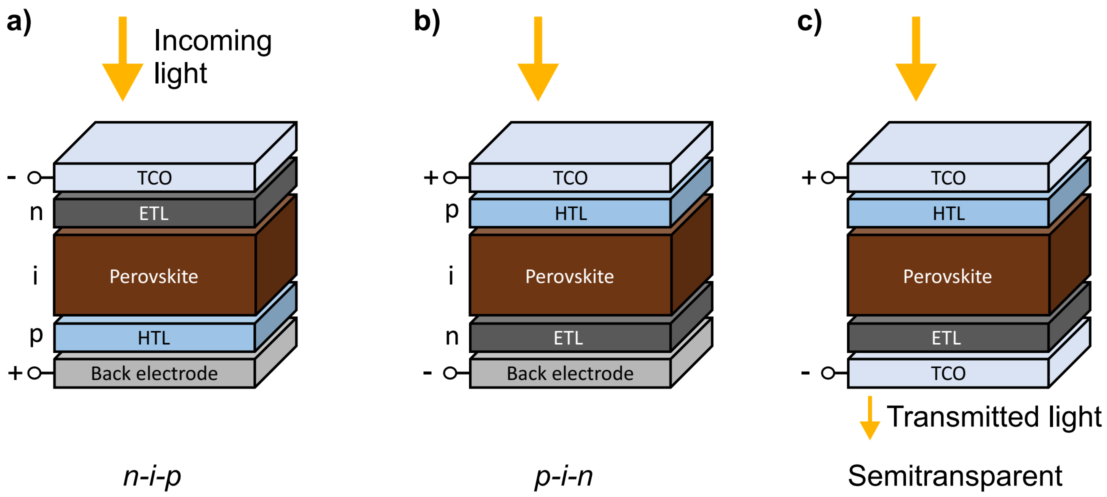

Figure 2.7: Schematic illustration of device architectures for single-junction (SJ) perovskite solar cells (PSCs). The perovskite thin film is sandwiched between an electron transport layer (ETL) and a hole transport layer (HTL), which guide electrons and holes, respectively, to the corresponding electrodes or transparent conductive oxides (TCOs). a) Layer stack of a *n-i-p* PSC, where incident light first enters through the ETL before reaching the perovskite thin film. b) Layer stack of a *p-i-n* PSC, where incident light first enters through the HTL before reaching the perovskite thin film. Although the terms *n*, *i* and *p* are commonly used to describe perovskite device architectures, they should not be interpreted as classical doping profiles. c) Semitransparent (ST) PSC layer stack, in which the rear electrode is replaced by a transparent electrode or TCO, allowing non-absorbed light to transmit through the entire layer stack.

Replacing the metal rear electrode with a second TCO enables semitransparent (ST) device architectures (Figure 2.7c), which are essential for multi-junction solar cells where light must pass through multiple absorbers to subsequent subcells. Consequently, optimizing ST *p-i-n* PSCs is critical for high-performance tandem applications.[178]

2.3 Perovskite-Based Tandem Solar Cells

2.3.1 Theoretical Efficiency Limit of Single-Junction Solar Cells

As discussed in Section 2.2.1, the maximum achievable efficiency of a SJ solar cell is fundamentally constrained by the band structure of the absorber material (Figure 2.8a). In semiconductors, only photons with an energy equal to or greater than the bandgap ($E_\gamma \geq E_\mathrm{g}$) can generate electron-hole pairs, while photons with lower energy pass through the absorber without contributing to photocurrent (transmission losses). Conversely, photons with energy significantly above the bandgap ($E_\gamma > E_\mathrm{g}$) lose their excess energy as heat (thermalization losses), where excited carriers relax to the band edges by emitting phonons. These two mechanisms – transmission and thermalization – represent the dominant intrinsic loss channels in SJ devices.[137,170,179]

For crystalline Si solar cells ($E_\mathrm{g} \approx 1.12\,\mathrm{eV}$) under the AM1.5G solar spectrum, these losses are substantial (Figure 2.8b): Approximately 32% of the incident solar power is lost due to transmission and 19% due to thermalization, leaving only about 49% theoretically usable for electricity generation.[137] This fraction is referred to as the ultimate efficiency η_ult, which can be expressed as:

$$\eta_\mathrm{ult} = \frac{J_\mathrm{max} V_\mathrm{max}}{P_\mathrm{in}}, \tag{2.23}$$

where J_max and V_max denote the maximum achievable current density and voltage, respectively, and P_in is the incident light power density ($1000\,\mathrm{W\,m^{-2}}$). For Si, $J_\mathrm{max} \approx 44\,\mathrm{mA\,cm^{-2}}$ and $V_\mathrm{max} = E_\mathrm{g}/e = 1.12\,\mathrm{V}$, resulting in an ultimate efficiency of about 49%.

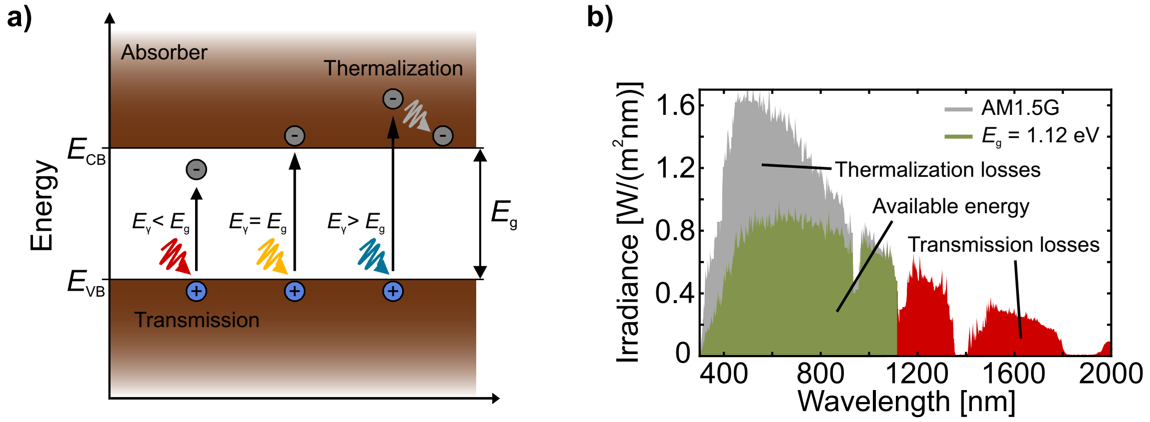

Figure 2.8: a) Schematic energy band diagram of a semiconductor illustrating the conduction band minimum (CB, E_{CB}), the valence band maximum (VB, E_{VB}) and the resulting bandgap E_{g}. Incoming photons with energy $E_\gamma \geq E_{\mathrm{g}}$ are absorbed and can generate electron-hole pairs, whereas photons with $E_\gamma < E_g$ are transmitted, contributing to transmission losses. For photons with $E_\gamma > E_{\mathrm{g}}$, the excess energy above the bandgap is dissipated as heat through carrier thermalization, referred to as thermalization losses. b) Schematic illustration of the solar spectrum (AM1.5G) utilization of a silicon (Si) solar cell with a bandgap of 1.12 eV, indicating the fraction of usable photon energy (green) and the associated thermalization (grey) and transmission (red) losses.

In 1961, Shockley and Queisser introduced the detailed balance (DB) limit,[16] which accounts for radiative recombination and thermodynamic constraints, reducing the theoretical efficiency below the ultimate limit. Their model assumes:

1. 100% absorption for photons with $E_\gamma \geq E_{\mathrm{g}}$
2. 0% absorption for photons with $E_\gamma < E_{\mathrm{g}}$
3. One electron-hole pair per absorbed photon
4. Perfect selective contacts with negligible series resistance
5. Absence of non-radiative recombination

Under these assumptions and standard test conditions ($T = 298\,\mathrm{K}$, AM1.5G spectrum), the maximum theoretical efficiency for Si solar cells is reduced to 32.6%. The maximum theoretical efficiency of SJ solar cells depends heavily on the bandgap of the absorber, with the highest efficiencies achieved for bandgaps in the range of 1-1.4 eV (Figure 2.9d), with a maximum of approximately 33.7% at 1.34 eV.[16,90] For perovskite thin films with $E_{\mathrm{g}} \approx 1.68$ eV, the corresponding theoretical efficiency limit is about 28.4%.[104] In practice, additional loss mechanisms – such as non-radiative and Auger recombination, parasitic free-carrier absorption, and optical or resistive losses – further reduce the achievable efficiency.[16,137] For example, including Auger recombination and parasitic free-carrier absorption decreases the practical efficiency limit for Si solar cells to 29.4%.[12,13] Under typical one sun illumination, Auger recombination is negligible in PSCs compared to radiative and trap-assisted recombination. However, it becomes relevant at high carrier densities, such as under concentrated illumination or in transient optical experiments.[180]

2.3.2 The Concept of Tandem Solar Cells

To overcome the theoretical efficiency limit of SJ solar cells, multi-junction architectures have been developed. By stacking absorbers with different bandgaps, thermalization losses are reduced, enabling more efficient utilization of the solar spectrum (Figure 2.9a).[39,137,170,181] Although the theoretical efficiency limit increases with the number of junctions,[19] the added complexity and the risk of damaging underlying layers must be weighed against performance gains.[20] Consequently, TSCs – which stack two subcells – have emerged as one of the most promising multi-junction architectures.

In a tandem architecture, high-energy photons are absorbed in the wide-bandgap top cell, while lower-energy photons pass through and are absorbed in the narrow-bandgap bottom cell. This configuration minimizes both transmission and thermalization losses, thereby enhancing overall energy conversion.[137,170]

Two main device architectures currently dominate tandem PV design: (i) two-terminal (2T) and (ii) four-terminal (4T) configurations.[39,182] In the 2T configuration (Figure 2.9b), both subcells are monolithically integrated and electrically connected in series, with the top cell fabricated directly on the bottom cell. This design reduces optical losses and offers lower LCOE but introduces fabrication challenges, such as processing compatibility with textured Si bottom cells and minimizing recombination losses at the interconnection layer (typically a thin TCO or tunnel junction).[18] Due to the series connection of the two subcells, the total power output is given by:

$$P_{\text{tot}} = I_{\text{lim}}(V_{\text{top}} + V_{\text{bot}}), \tag{2.24}$$

where the current I_{lim} is limited by the subcell generating the lower current. As a result, for optimal device performance, current matching is essential, which requires adjusting the layer thickness and tuning the bandgap of the perovskite thin film.[39,176,182] In the 4T configuration (Figure 2.9c), the subcells are mechanically stacked and operate electrically independently. This configuration simplifies fabrication and avoids current-matching constraints

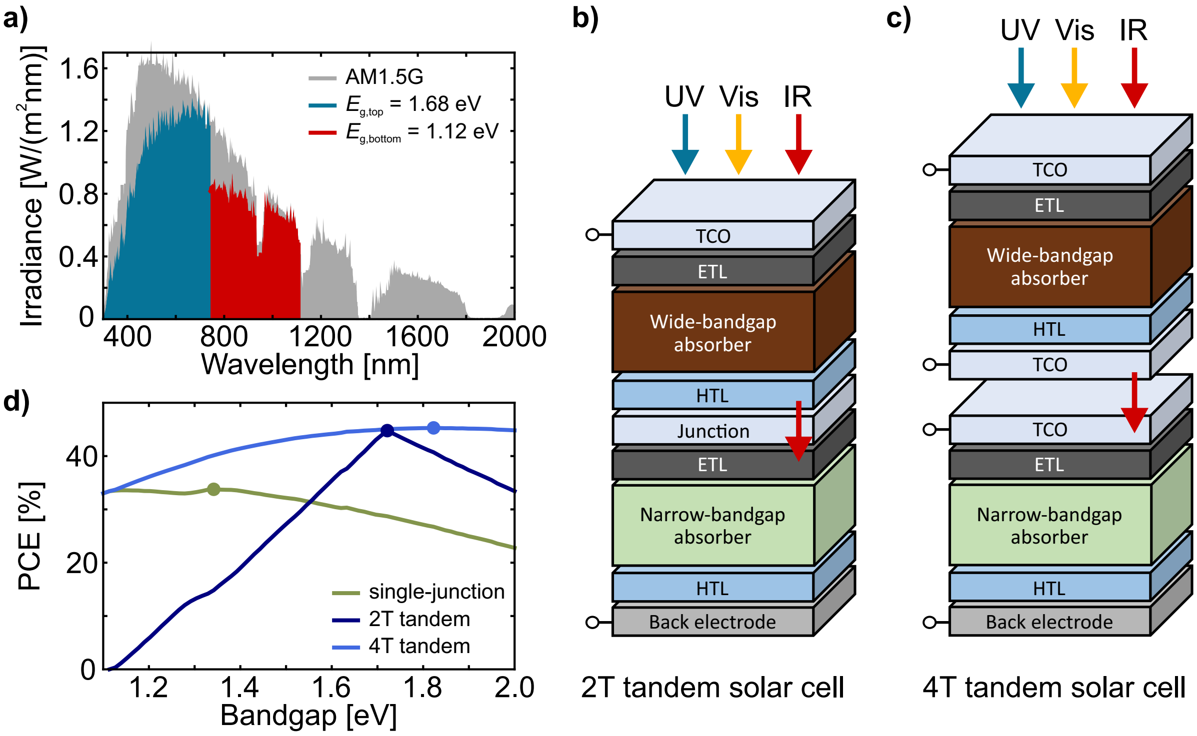

Figure 2.9: a) Schematic spectral response of a tandem device comprising a top absorber with $E_{\text{g,top}} = 1.68\,\text{eV}$ and a bottom absorber with $E_{\text{g,bot}} = 1.12\,\text{eV}$ under the AM1.5G solar spectrum. Ultraviolet (UV) and visible (Vis) light are predominantly absorbed in the top cell, while infrared (IR) light is primarily absorbed in the bottom cell. b) Two-terminal (2T) tandem architecture, in which the two subcells are optically and electrically connected in series *via* an interconnecting junction layer. c) Four-terminal (4T) tandem architecture, where the subcells are optically stacked (with air gap in between) but operate electrically independently. The front electrodes of both subcells typically consist of a transparent conductive oxide (TCO). d) Maximum theoretical power conversion efficiency (PCE) of single-junction (SJ) solar cells and 2T/4T tandem solar cells as a function of the (top-cell) bandgap under the AM1.5G solar spectrum, calculated from the detailed balance (DB) limit. Silicon (Si, $E_{\text{g}} \approx 1.12\,\text{eV}$) is used as the bottom cell material in both tandem configurations.

but suffers from additional optical losses due to additional TCO layers and reflection at interfaces. Furthermore, scaling to larger modules requires lateral series connections for each junction type, which can lead to significant optical and resistive losses at the module level.[18,34,183]

Due to their easily tunable bandgap, perovskite semiconductors are highly promising for tandem applications, particularly in combination with crystalline Si. For 2T perovskite/Si TSCs, the optimal perovskite bandgap is around 1.65-1.75 eV, while a wider bandgap range is possible for 4T configurations (Figure 2.9d).[39,90,176,182] This tandem concept theoretically enables efficiencies of up to 45.1%.[39] Recent progress has resulted in certified record efficiencies of 35% for 2T and 30.24% for 4T perovskite/Si tandem architectures, surpassing the best Si solar cells (27.9%) and SJ PSCs (27.3%).[14,184]

3 Methods

This chapter presents the experimental methods used for the fabrication and characterization of perovskite thin films and solar cells. The fabrication section encompasses the deposition processes for all functional layers involved in the fabrication of both opaque and semitransparent perovskite solar cells, including their integration into a 2T tandem architecture. Particular focus is placed on spin coating and thermal sublimation, as both deposition methods are essential for the production of perovskite thin films in this work. The characterization section discusses the working principles and implementation of the characterization methods used to evaluate both thin-film quality and device performance.

3.1 Fabrication Methods

The fabrication of the individual functional layers required for PSC production primarily relies on two thin-film deposition techniques: solution-based deposition and vapor deposition.[71] Both methods are discussed in detail in the following section, with particular emphasis on spin coating and thermal sublimation – key processes used in this work for the deposition of perovskite thin films. These thin films are fabricated using either a fully solution-based two-step process or a hybrid route that combines both deposition methods. The section then outlines the subsequent fabrication steps for opaque and semitransparent (ST) PSCs, as well as the 2T perovskite/Si TSCs investigated in this thesis.

3.1.1 Solution-Based Deposition

Solution-based deposition is a widely adopted technique in perovskite PV research due to its simplicity, low cost, and minimal equipment requirements. In this method, precursor materials are dissolved in a solvent system to form a solution, which is then deposited onto a substrate. Upon solvent removal *via* thermal annealing or quenching, the desired thin film forms. Depending on the intended application and desired scalability, various deposition techniques can be used to apply the precursor solution, such as spin coating, blade coating, slot-die coating, spray coating, and inkjet printing.[71] Among these, spin coating remains the most commonly used method for laboratory-scale research, as it enables rapid prototyping and facilitates experimentation.[185] Consequently, the majority of high-efficiency PSCs reported in the literature have been fabricated using spin coating.

Spin Coating

In the spin-coating method, the precursor solution is dispensed using a pipette onto a substrate fixed by vacuum on a rotating chuck. Upon rotation at high speeds, centrifugal forces spread the solution evenly across the surface, while excess material is expelled. In most cases, a heating step – referred to as "annealing" – is necessary to evaporate remaining solvent. The resulting film thickness and morphology can be tuned by adjusting parameters such as solution concentration, spin speed, spin acceleration, spin duration, and solvent volatility.[186–189]
To promote rapid crystallization and improve the uniformity of perovskite films during spin coating, an antisolvent or vacuum quenching step is typically introduced shortly after the start of rotation. In the antisolvent method, a non-polar solvent is dispensed onto the rotating substrate, displacing the host solvent and inducing the formation of an intermediate phase. Subsequent thermal annealing converts the intermediate phase into a crystalline perovskite layer. This spin coating technique is commonly referred to as one-step spin coating.[190–192]

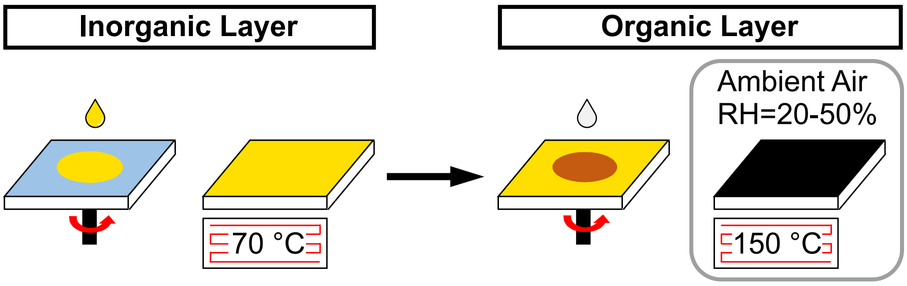

Figure 3.1: Schematic illustration of the fully solution-based two-step spin-coating process used in this work for fabricating perovskite thin films. An inorganic precursor solution is first deposited, followed by deposition of the organic precursor solution, and the perovskite thin film is subsequently annealed under ambient conditions with a relative humidity (RH) of ≈ 20-50%.

The growth of high-quality perovskite layers is essential for achieving high-performance PSCs. Therefore, solution-based two-step deposition methods have emerged. In these methods (Figure 3.1), an inorganic precursor solution – typically containing PbI_2 and $PbBr_2$ dissolved in a N,N-dimethylformamide (DMF)/dimethylsulfoxide (DMSO) solvent mixture – is first deposited onto the substrate, followed by a short thermal annealing step. Subsequently, an organic cation solution – commonly containing methylammonium (MA)- and formamidinium (FA)-based organic cations dissolved in isopropanol (IPA) – is deposited on the inorganic scaffold. This second precursor solution acts similarly to an antisolvent, inducing crystallization upon contact with the inorganic scaffold. Therefore, the choice of solvent represents one of the most influential variables in fully solution-based two-step deposition methods.[193] A final annealing step under ambient conditions with a relative humidity (RH) of $\approx$ 20-50% facilitates the conversion of the precursors into a crystalline perovskite film. Compared to one-step spin coating, the two-step spin coating method offers improved control and reproducibility of the perovskite crystallization process, as the reaction between the inorganic and organic precursors is decoupled from the film-deposition step. This separation allows for finer regulation of nucleation, crystal growth, and film thickness, consistently yielding smoother and pinhole-free perovskite layers.[61,66,177,193–196] The solution-based two-step deposition method is used in the present work due to its compatibility with scalable industrial processes and its ability to yield uniform, high-quality perovskite films.

In this thesis, spin coating is utilized to produce the 2PACz hole transport layer (HTL), the fully solution-based two-step processed perovskite layers, the organic cation solution in the hybrid route, and the $PDAI_2$+BAI surface passivation layer.

3.1.2 Vapor Deposition

In contrast to solution-based deposition, vapor deposition is a dry and solvent-free method in which precursor materials are converted into vapor under vacuum conditions and subsequently deposited onto a substrate to form a uniform thin film. This method eliminates the need for toxic solvents and offers enhanced control over deposition parameters, which enables reproducible processes and scalable fabrication for large-area applications.[71]

Vapor-deposition techniques can be categorized into two main types: physical vapor deposition (PVD) and chemical vapor deposition (CVD). PVD involves the physical transfer of material from a condensed phase into the vapor phase, followed by condensation onto the substrate without any chemical reaction occurring in the vapor phase.[197] Common PVD methods used in this thesis include thermal sublimation and sputtering. In contrast, CVD relies on chemical reactions of gaseous precursors near or directly on the substrate surface to form the desired thin film.[198] In this work, CVD is implemented in the form of atomic layer deposition (ALD).

Thermal Sublimation

Thermal sublimation, also known as thermal or resistive evaporation depending on the phase transition of the material used, is a PVD technique performed under high vacuum conditions (typically around 10^{-6} mbar) to ensure a long mean free path for the gas-phase particles and to prevent unwanted reactions with residual gases. In this process, solid precursor materials such as powders are heated close to their sublimation/boiling point in a resistively heated metal boat or crucible. The resulting vapor is emitted isotropically and condenses on the cooler substrate surface, forming a uniform thin film. The sublimation/evaporation rate therefore depends on the vapor pressure of the material at the applied temperature and is typically monitored using quartz crystal microbalances (QCMs).[199] These sensors detect changes in resonant frequency caused by mass accumulation, allowing precise control of deposition rate and film thickness, resulting in reproducible processes. Rotating the substrate during deposition enhances film uniformity by promoting even material distribution. Structured layers, such as patterned metal electrodes, are defined using shadow masks.

To overcome the respective limitations of fully solution-based and vapor-deposition methods for perovskite layer

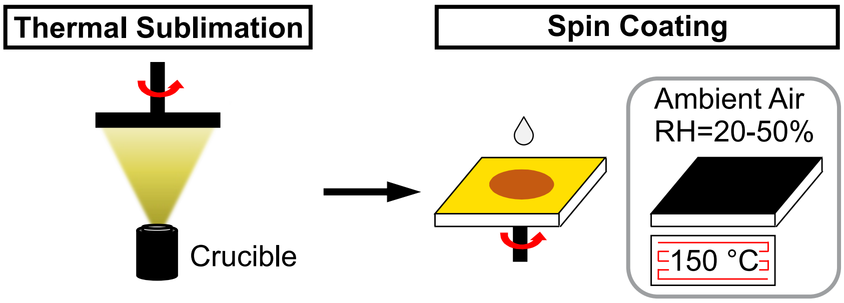

Figure 3.2: Schematic illustration of the hybrid two-step deposition route for fabricating perovskite thin films in this work. This method combines thermal sublimation of the inorganic precursors with spin coating of the organic cation solution. The perovskite film is subsequently annealed under ambient conditions with a relative humidity (RH) of ≈ 20-50%.

fabrication, hybrid two-step deposition routes have emerged as a promising alternative (Figure 3.2). These methods combine the conformal and uniform deposition of the inorganic precursors *via* thermal sublimation with a subsequent solution-based deposition of the organic cations – implemented *via* spin coating in this thesis. The hybrid method offers several advantages, including enhanced compositional flexibility, facile introduction of additives in the solution step and the use of environmentally friendly solvents.[76–81]

In this thesis, different thermal sublimation/evaporation systems are used depending on the material and application. An Angstrom evaporation system (Angstrom Engineering, Inc, Kitchener, Canada) is used for the deposition of the electron transport layers (ETLs) C_{60} and BCP, for LiF surface passivation, and for the MgF_2 antireflective coating. For the CsCl seed layer and for the inorganic scaffold in the hybrid fabrication route, a PEROvap system (M. Braun Inertgas-Systeme GmbH, Dresden, Germany) is used. Metallic contacts, specifically Ag and Au, are deposited using a Coat 340 system (Vactec B.V., KJ Heinenoord, The Netherlands).

Sputtering

Sputtering is a vacuum-based deposition method in which a process gas – typically argon – is ionized by an electric field between an anode and a cathode, generating a plasma. The resulting argon ions are accelerated toward a target material, ejecting atoms from its surface. The ejected atoms then travel through the vacuum chamber and deposit on the substrate, forming a uniform thin film.[200] Substrate rotation during deposition enhances thickness uniformity. The process is conducted under vacuum conditions to reduce particle collisions and ensure efficient material transfer.

Unlike thermal sublimation, sputtering does not require heating the target to its sublimation point, making it suitable for materials with high melting points or complex compositions. Deposition parameters such as plasma power, pressure, and magnetic field strength can be tuned to optimize film quality. Radio frequency sputtering enables the deposition of insulating materials by alternating the voltage polarity, preventing charge buildup. Reactive sputtering, achieved by introducing gases like oxygen or nitrogen, allows for the formation of compound films such as transparent conductive oxides (TCO, e.g., indium zinc oxide (IZO)).

In this thesis, a Pro Line PVD 75 sputtering system (Kurt J. Lesker Company, Dresden, Germany) is used to deposit the NiO_x HTL and IZO TCO.

Atomic Layer Deposition

Atomic Layer Deposition (ALD) is a CVD technique that enables the formation of ultrathin, conformal films with atomic-scale thickness control. The process relies on alternating, self-limiting surface reactions between gaseous precursors and the substrate, allowing for precise layer-by-layer growth. Each ALD cycle consists of alternating

pulses of precursor gases, separated by purge steps that remove excess reactants and byproducts, ensuring high film purity and uniformity.[201]
In this thesis, a GemStar XT thermal ALD system (Arradiance, Littleton, USA) is used to deposit the SnO_x buffer layer.

Throughout this work, unless stated otherwise, the term "vapor deposition" refers to thermal sublimation.

3.1.3 Perovskite Thin-Film Formation in Solution-Based Two-Step Deposition

Perovskite thin-film formation in solution-based two-step deposition routes is primarily governed by the diffusion of the organic halides into the pre-deposited inorganic scaffold and the interfacial perovskite conversion, which progresses through a characteristic top-down infiltration process. The diffusion process follows Fick's law, whereas the perovskite conversion is determined by the chemical reactivity of the precursors, local stoichiometry, and the associated thermodynamic driving forces. In particular, the concentration of the organic halides is a critical factor controlling both the kinetics and completeness of the conversion. While both fully solution-based and hybrid two-step deposition routes rely on the same overall chemical reaction ($\mathrm{PbX_2 + AX \rightarrow APbX_3}$), their film-formation pathways differ substantially due to differences in inorganic scaffold permeability, intermediate solvate phases, and ion-transport mechanisms.[61,196]

Fully Solution-Based Two-Step Deposition

In the fully solution-based two-step deposition method, a porous, solvate-containing inorganic scaffold is formed first, followed by the infiltration of an organic halide solution. The Lewis-base character of coordinating solvents such as DMSO in the inorganic precursor solution promotes the formation of intermediate solvate complexes (e.g. $\mathrm{PbX_2 \cdot DMSO}$), which stabilize the wet precursor film and retard crystallization. These complexes strongly impact the porosity of the inorganic scaffold and the chemical reactivity between the inorganic and organic components.[66,202]
Mild thermal annealing ($T < 100\,°C$) partially removes coordinated solvent molecules, yielding a polycrystalline inorganic scaffold. The evaporation rate of the solvent determines the grain size, residual solvate content, and permeability of the inorganic scaffold, all of which affect the subsequent organic cation diffusion.
Upon deposition of the organic halide solution, A-site cations diffuse into the permeable inorganic scaffold driven by concentration gradients and destabilization of residual PbX_2-solvate complexes.[196] Conversion typically initiates at grain boundaries and defect-rich regions, where ion transport is enhanced, propagating inward as a diffusion-reaction front. The resulting microstructure is determined by the interplay between nucleation density and crystal growth rate.[203]
Post-deposition annealing promotes complete conversion and grain growth *via* Ostwald ripening, leading to larger and more thermodynamically stable domains.[203] Optimizing the annealing temperature and duration is essential to reduce shallow trap states associated with halide vacancies and undercoordinated Pb species. Humidity (RH $\approx$ 20-50%) during the annealing step has been reported to enhance conversion kinetics and crystallinity, possibly by facilitating organic cation diffusion, although the detailed mechanisms remain under investigation.[167,196]

Hybrid Two-Step Deposition

In the hybrid two-step deposition method, a compact inorganic scaffold is formed by thermal sublimation of PbX_2, followed by deposition of an organic halide solution. In contrast to solution-processed inorganic scaffolds, thermally sublimated PbX_2 forms dense, non-porous inorganic scaffolds without solvate intermediates.[204] As a result, infiltration of the organic halides is limited, and perovskite formation proceeds through a surface-initiated reaction in which a perovskite layer forms at the top interface and gradually propagates into the film. Compared to fully solution-based two-step processes, reaction kinetics are slower and primarily governed by thermally activated ion diffusion through the growing perovskite phase. Consequently, a post-deposition annealing step is essential to promote diffusion and complete conversion to the perovskite phase. As in the fully solution-based two-step method, annealing in a humid environment has been reported to improve perovskite film quality.[205,206]

Despite significant progress, some challenges remain in the perovskite thin-film formation in solution-based two-step deposition routes. First, precise control over the final perovskite composition is difficult because the inorganic and organic precursors exhibit different reaction kinetics and diffusivities. Second, vertical compositional gradients of halides and A-site cations may exist in the final perovskite film. Since organic cations with different diffusivities infiltrate the pre-deposited inorganic scaffold from the top, spatial variations in stoichiometry can arise, often resulting in an organic-rich upper region and an organic-deficient lower region. Such gradients can induce bandgap inhomogeneity and spatial variations in optoelectronic properties.[196]
To tackle these challenges, various additive and solvent engineering strategies, as well as process modifications, have been developed.[66,207]

3.1.4 List of Materials

Because the performance of PSCs is highly dependent on the materials used, and efficiency can vary even when materials of the same specified purity are sourced from different manufacturers, it is essential to report the materials used along with their purities and suppliers. A summary of the materials used in this work is provided in Table A.1.

3.1.5 Device Architecture

The following section presents the device architecture and fabrication process of the PSCs and 2T perovskite/Si TSCs used in this thesis.
PSCs can be configured in "regular" (*n-i-p*) or "inverted" (*p-i-n*) architecture, depending on whether the perovskite thin film is contacted by the ETL or the HTL on the illuminated side. In this work, all PSCs are fabricated in the *p-i-n* architecture due to its superior compatibility with Si bottom cells in a 2T tandem configuration. Figure 3.3 presents the general device architecture for both opaque and semitransparent (ST) single-junction (SJ) PSCs, as

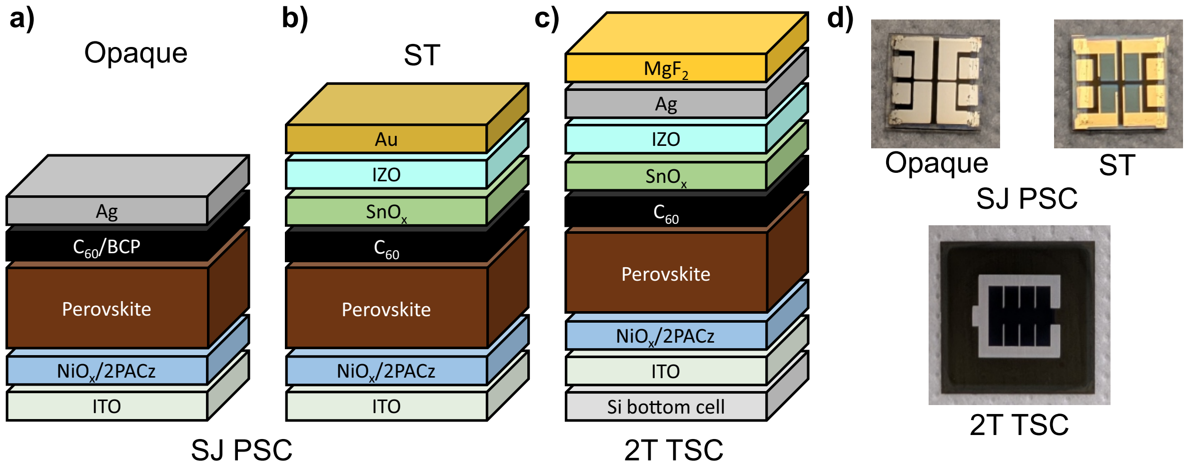

Figure 3.3: Schematic representation of the general device architecture for a) opaque and b) semitransparent (ST) *p-i-n* single-junction (SJ) perovskite solar cells (PSCs), and c) two-terminal (2T) perovskite/Si tandem solar cells (TSCs) fabricated in this thesis. d) Optical photographs of opaque and ST SJ PSCs and 2T perovskite/Si TSCs used in this thesis. Deviations in the layer sequence are indicated in the text. Dimensions shown are approximate and not to scale.

well as for 2T perovskite/Si TSCs.

Designing the layer stack requires careful consideration of deposition compatibility to avoid damaging underlying layers. This can be achieved through the use of orthogonal solvent systems or buffer layers. Additionally, the energy levels of the electron and hole transport layers must be aligned with those of the perovskite thin film to ensure efficient charge extraction or provide sufficient blocking barriers. Finally, optimizing the thickness of each layer is essential to minimize electrical transport losses and optical reflection.

The device fabrication for each PSC and TSC used in this thesis is presented in the following. Figure 3.4 illustrates a typical fabrication process for opaque *p-i-n* SJ PSCs, while Figure 3.5 depicts the process for 2T perovskite/Si TSCs.

Perovskite Solution Preparation

For the fully solution-based two-step deposition method of the perovskite thin film, two separate precursor solutions are prepared: an inorganic solution and an organic cation solution. In contrast, the hybrid deposition route requires only the organic cation solution, as the inorganic precursors are deposited *via* thermal sublimation. The reference narrow-bandgap perovskite solution (labeled as Ref) is prepared according to Gutierrez-Partida et al.[208] All nominal perovskite compositions are presented in the chapters in which they are first introduced. Details on the preparation of the inorganic precursor solution are provided in Table 3.1, while the preparation of the organic cation solution is outlined in Table 3.2.

Table 3.1: Preparation of the inorganic precursor solution for all perovskite thin films used in the fabrication of perovskite solar cells (PSCs) in this thesis. PbI_2 and $PbBr_2$ are dissolved in a 9:1 (vol%) mixture of N,N-dimethylformamide (DMF) and dimethyl sulfoxide (DMSO), and the solution is heated to 130 °C for 30 min to ensure complete dissolution. For perovskites containing CsI, the inorganic precursor solution is prepared similarly but with reduced DMSO content, as the CsI solution is added separately. After cooling, 70 µL CsI solution (7 mol%, 390 mg mL^{-1} in DMSO) is added to the inorganic precursor solution.

Perovskite name	PbI_2 [M]	$PbBr_2$ [M]	CsI [M]
Ref	1.5	-	-
$PbBr_2$	1.07	0.43	-
FABr	1.5	-	-
$PbBr_2$+FABr/Control	1.275	0.225	-
CsI/CsI+LiF/TC/DC/DC opt./CsCl	1.275	0.225	0.105

Table 3.2: Preparation of the organic cation precursor solution for all perovskite thin films used in the fabrication of perovskite solar cells (PSCs) in this thesis. For the fully solution-based two-step deposition method, organic cations are dissolved in isopropanol (IPA). In the hybrid deposition route, ethanol (EtOH) is used as the solvent for the organic cations. For the optimized double-cation (DC opt.) perovskite, $PDAI_2$ and BAI are used as bulk passivation agents and dissolved in IPA. The addition of MACl enhances perovskite film crystallization but evaporates during the final annealing step.[209]

Perovskite name	FAI [M]	FABr [M]	MAI [M]	MACl [M]	$PDAI_2$ [mM]	BAI [mM]
Ref	0.523	-	0.04	0.113	-	-
$PbBr_2$	0.523	-	0.04	0.113	-	-
FABr	0.113	0.41	0.04	0.113	-	-
$PbBr_2$+FABr/Control/CsI/CsI+LiF/TC	0.3	0.223	0.04	0.113	-	-
DC	0.34	0.223	-	0.113	-	-
DC opt./CsCl	0.34	0.223	-	0.113	0.303	0.497
Co (0.65 M)	0.228	0.423	-	0.065	-	-
Seq (0.75 M)	0.263	0.488	-	0.075	-	-

Single-Junction Perovskite Solar Cells

This part contains a detailed description of the fabrication steps for opaque and ST SJ PSCs fabricated *via* the fully solution-based and the hybrid two-step deposition method. The layer stack of opaque *p-i-n* SJ PSCs consists of the glass substrate, the transparent electrode, the HTL, the perovskite thin film, the surface passivation (if applicable), the ETL, and the metal electrode. In the case of ST PSCs, a transparent electrode and a buffer layer between the ETL and the transparent electrode are added.

Sample preparation and cleaning:
Glass substrates coated with a 120 nm thick, pre-patterned indium tin oxide (ITO) layer (sheet resistance $15\,\Omega\,sq^{-1}$, Luminescence Technology, CAS: 50926-11-9) are used as substrate material, where ITO serves as the bottom electrode, offering both electrical conductivity and optical transparency. The glass substrates are cut to $16\times16\,mm^2$ and cleaned in an ultrasonic bath using deionized (DI) water with glass cleaner, followed by acetone and IPA, each for 10 min, to eliminate potential contaminants. This is followed by 3 min of oxygen plasma treatment prior to the deposition of the HTL. The plasma treatment effectively removes residual organic compounds, such as solvent residues, and enhances surface wettability for subsequent liquid-based processes like spin coating.[210]

Hole transport layer (HTL):
A 5 nm thick nickel oxide (NiO_x) film is sputtered onto the ITO substrate using a NiO_x target (4 inch, 99.99% pure, Kurt J. Lesker Company) with 100 W power ($7.95\,W\,in^{-2}$ power density) and pure Ar at 1 mTorr. Subsequently, a thin layer of [2-(9H-carbazol-9-yl)ethyl]phosphonic acid (2PACz) is deposited on the ITO/NiO_x substrate in a N_2-filled glovebox by dispensing 70-75 µL 2PACz solution on the substrate with a resting time of 5 s followed by rotation at 3000 rpm (acceleration: $1000\,rpm\,s^{-1}$) for 30 s. The solution concentration is $0.375\,mg\,mL^{-1}$ in anhydrous EtOH for the fully solution-based two-step method, and $0.5\,mg\,mL^{-1}$ for the hybrid two-step route and the prepared solution is placed in an ultrasonic bath for at least 20 min before use. The substrates are then annealed at 100 °C for 10 min. For the hybrid two-step route and samples with CsCl seed layer, an additional washing step is used to remove unbound molecules. In this step, 150 µL of pure EtOH is dynamically dispensed onto the substrate within 2 s at 3000 rpm (acceleration: $1000\,rpm\,s^{-1}$) for 30 s of total rotation time. A final annealing step at 100 °C for 10 min follows. This process was first introduced by Al-Ashouri et al.[211]. The NiO_x/2PACz bilayer serves as the *p*-selective contact, which has been shown to improve both hole extraction and perovskite film quality compared to

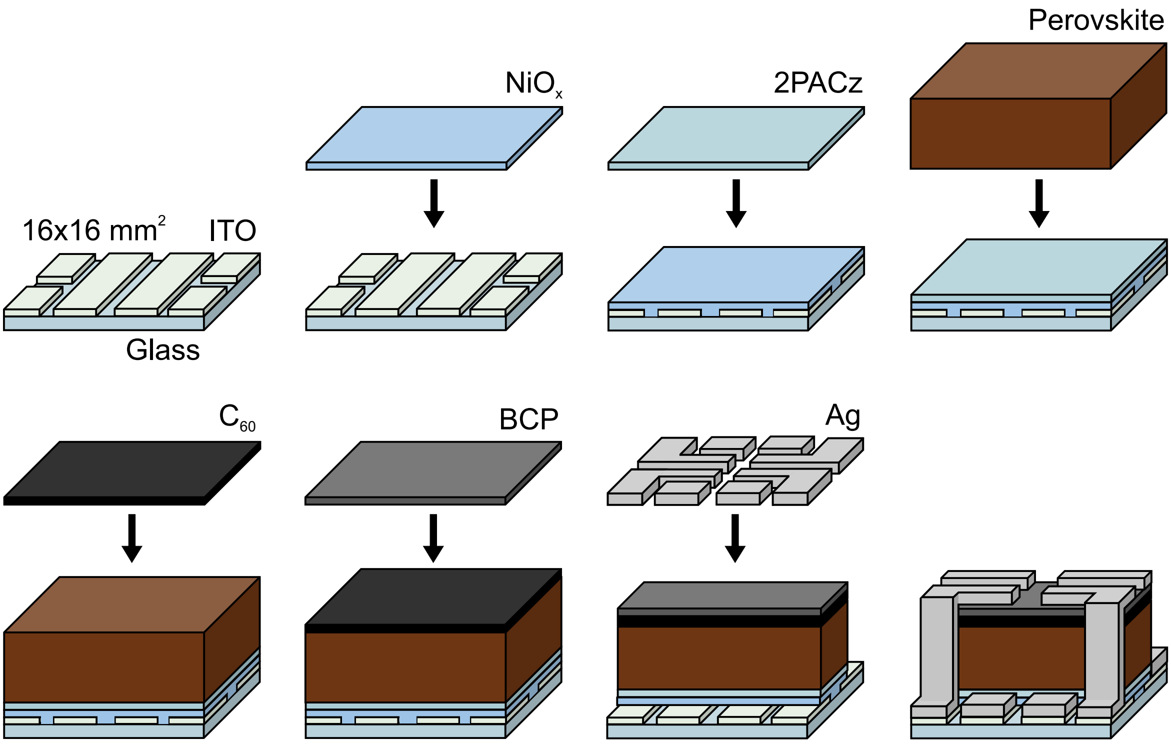

Figure 3.4: Schematic representation of the layer-by-layer fabrication of the opaque *p-i-n* single-junction (SJ) solar cell architecture, starting with a glass substrate (16×16 mm^2) with pre-patterned indium tin oxide (ITO) electrode, followed by sputtering of nickel oxide (NiO_x) hole transport layer (HTL), spin coating of [2-(9H-carbazol-9-yl)ethyl]phosphonic acid (2PACz) HTL, solution-based two-step processing of the perovskite thin film, thermal sublimation of fullerene-C_{60} (C_{60}) electron transport layer (ETL), bathocuproine (BCP) ETL, and thermal evaporation of the silver (Ag) electrode. Deviations in the layer sequence are indicated in the text. Dimensions shown are approximate and not to scale.

devices using 2PACz alone.[212]

Perovskite deposition *via* the fully solution-based two-step method:

The deposition begins with the inorganic scaffold, formed by dispensing 60 µL of the inorganic precursor solution onto the substrate and spin coating at 1500 rpm (acceleration: 2000 rpm s^{-1}) for 30 s. The resulting film is annealed at 70 °C for 1 min, yielding a yellow-transparent layer. Perovskite formation is initiated by applying 80 µL of the organic cation solution onto the inorganic scaffold, followed immediately by spin coating at 2500 rpm (acceleration: 2000 rpm s^{-1}) for 30 s, producing a red film. This is followed by annealing at 150 °C for 15 min under ambient conditions (relative humidity (RH): 20-50%), converting the film into the desired black perovskite phase. The spin-coating process is conducted inside a N_2-filled glovebox. For the final annealing step, samples are transferred using a sealed transport box to maintain a N_2 atmosphere until just before placement on the preheated hotplate. Upon opening the box, crystallization and phase transformation begin immediately, and rapid transfer to the hotplate is crucial for optimal device performance.[208]

For the samples with CsCl seed layer, thermal sublimation of CsCl is performed in a PEROvap system (M. Braun Inertgas-Systeme GmbH, Dresden) integrated into a N_2-filled glovebox. A cooled inner surface, surrounding all sublimation sources, is set to -20 °C. Prior to the heating process, the system is evacuated, with a standard base pressure at the start of heating below $3 \cdot 10^{-6}$ mbar. The substrate temperature (18 °C) is kept constant for all experiments. The source-to-substrate setup uses a 300 mm vertical distance and 165 mm lateral distance between the sublimation source and the substrate. The final thickness of CsCl is 5 nm with a static sublimation rate of 0.1 Å s^{-1}. For all experiments, cylindrical 10 cm^3 crucibles are used, filled with ≈ 5 g of CsCl.

Perovskite deposition *via* the hybrid two-step method:

The thermal sublimation of the inorganic precursor materials is carried out using a PEROvap system (M. Braun Inertgas-Systeme GmbH, Dresden), integrated within a N_2-filled glovebox. Individual QCMs monitor the deposition rate of each material. A cooled inner surface surrounding all sublimation sources is maintained at -20 °C. Prior to heating, the chamber is evacuated to a base pressure below $3 \cdot 10^{-6}$ mbar. The sublimation rates are controlled automatically and kept constant throughout each process. The substrate temperature is maintained at 18 °C for all experiments. The source-to-substrate configuration includes a vertical distance of 300 mm and a lateral offset of 165 mm. For both sequential and co-deposition of the inorganic scaffold, static deposition rates of 1.0 and 0.1 Å s^{-1} are used for PbI_2 and CsCl, respectively. In co-deposition, the process is terminated upon reaching a PbI_2 film thickness of 300 nm, resulting in a final CsCl thickness of $30 \pm 2\,\mathrm{nm}$. In sequential deposition, 30 nm of CsCl is deposited first, followed by 300 nm of PbI_2. All depositions utilize cylindrical crucibles with a volume of 10 cm^3, filled with 5 g of either PbI_2 or CsCl. The organic cation solution is deposited *via* spin coating in a N_2-filled glovebox. A volume of 100 µL is dynamically dispensed onto the substrate within 5 s at a spin speed of 4000 rpm for Batch A and at 5500 rpm for Batch B–F (acceleration: 1000 rpm s^{-1}) for 35 s. The change in rotation speed resulted from maintenance of the PEROvap system. The substrates are subsequently annealed at 150 °C for 20 min under ambient conditions (relative humidity (RH): 20-50%).

Surface passivation:

For samples with LiF as surface passivation, 1 nm LiF is thermally evaporated on the perovskite film at an evaporation rate of 0.1-0.2 Å s^{-1} at a pressure of around 10^{-6} mbar.

For samples with propane-1,3-diammonium iodide ($PDAI_2$) and butylammonium iodide (BAI) as surface passivation, 100 µL of the bimolecular passivation is dispensed onto the perovskite film with a resting time of 5 s followed by rotation of 4500 rpm (acceleration: 1000 rpm s^{-1}) for 30 s in a N_2-filled glovebox. This is followed by thermal annealing at 100 °C for 5 min. The solution concentration is 1.25 mg mL^{-1} $PDAI_2$ and 1.25 mg mL^{-1} BAI in IPA for the fully solution-based two-step method, and 0.3 mg mL^{-1} $PDAI_2$ and 0.3 mg mL^{-1} BAI in EtOH for the hybrid two-step method.

Electron transport layer (ETL):

For opaque PSCs, 20 nm of fullerene-C_{60} (C_{60}) and 5 nm of bathocuproine (BCP) are thermally sublimated and deposited using an Angstrom evaporation system at a sublimation rate of 0.1-0.2 Å s^{-1} at a pressure of around 10^{-6} mbar.

For ST PSCs, the C_{60} is followed by a 20 nm thick tin oxide (SnO_x) layer prepared by ALD. The TDMASn source is heated to 70 °C while the TDMASn carrier line is maintained at 125 °C during operation. SnO_x films are deposited over 200 ALD cycles. The chamber temperature is set to 90 °C. Subsequently, 90 nm indium zinc oxide (IZO) is sputtered from an IZO target (4 inch, In_2O_3/ZnO 90/10 wt%, 99.99% pure, Kurt J. Lesker Company) using 190 W power (15.10 W in^{-2} power density) and a mixture of argon and oxygen (1.3%) at a process pressure of 1.1 mTorr as transparent conductive layer. For the opaque PSCs fabricated in Chapter 6, a 20 nm thick SnO_x layer is used instead of BCP.

Top contact:

To enable electrical contact to both the cathode and anode, the contact areas are exposed by carefully removing the top layers locally using a scalpel. This method avoids the use of solvents that could damage the perovskite layer. The exposed strip must remain narrower than 4 mm to preserve the active area. Subsequently, metal electrodes are thermally evaporated through a shadow mask to define the active area to 10.5 mm^2 and complete the PSCs with four pixels per substrate. For opaque PSCs, 100 nm of silver (Ag) is deposited, while for ST PSCs, 75 nm of gold (Au) is used.

2T Perovskite/Si Tandem Solar Cells

This part contains a detailed description of the fabrication steps for the 2T perovskite/Si TSCs fabricated *via* the fully solution-based two-step deposition method and the hybrid two-step deposition method with the layer stack Si bottom cell/ITO/NiO_x/2PACz/perovskite/$PDAI_2$+BAI/C_{60}/SnO_x/IZO/Ag/MgF_2. The fabrication process follows similar steps to that of SJ PSCs described in the section before, with variations primarily in the layer thicknesses.
Before depositing the HTL layer, the Si bottom cells (25×25 mm^2) are cleaned with acetone and IPA in a spin coater process (150 µL, 1800 rpm for 15 s) to remove possible impurities.
For the HTL layer, a NiO_x film (5 nm for planar Si bottom cells, and 15 nm for textured Si bottom cells, as well as for the hybrid two-step processed perovskite thin film on all types of Si bottom cells) is sputtered from a NiO_x

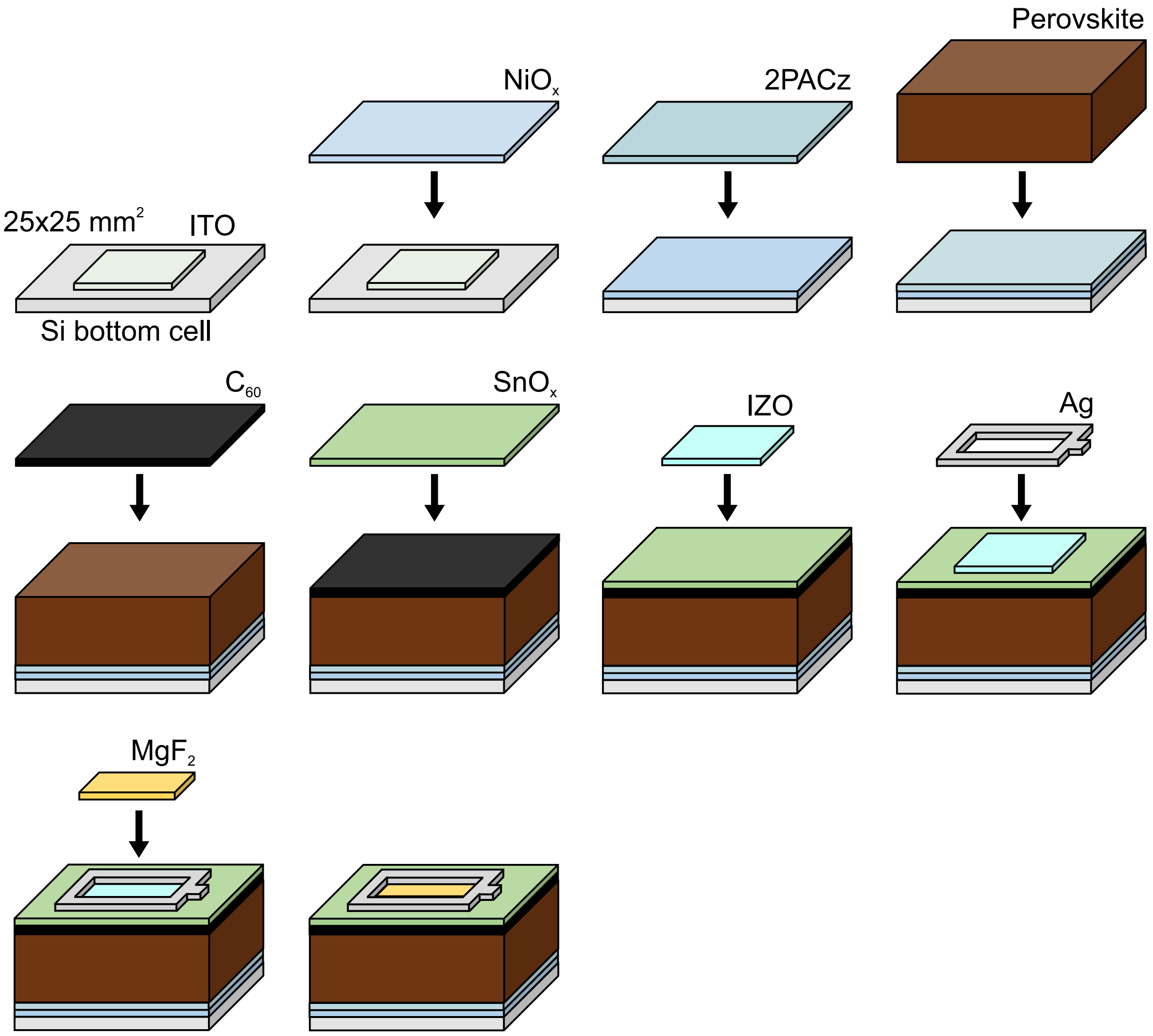

Figure 3.5: Schematic representation of the general sequential layer-by-layer fabrication of the two-terminal (2T) tandem solar cell (TSC) architecture, starting with a silicon (Si) bottom cell (25×25 mm^2) with pre-deposited indium tin oxide (ITO) electrode, followed by sputtering of nickel oxide (NiO_x) hole transport layer (HTL), spin coating of [2-(9H-carbazol-9-yl)ethyl]phosphonic acid (2PACz) HTL, solution-based two-step processing of the perovskite thin film, thermal sublimation of fullerene-C_{60} (C_{60}) electron transport layer (ETL), atomic layer deposition of tin oxide (SnO_x) buffer layer, sputtering of indium zinc oxide (IZO) transparent electrode, and thermal evaporation of the silver (Ag) electrode and the magnesium fluoride (MgF_2) antireflective coating. Deviations in the layer sequence are indicated in the text. Dimensions shown are approximate and not to scale.

target using 100 W power with pure Ar at 1 mTorr onto the Si bottom cell with ITO layer. This is followed by a thin 2PACz layer deposited as mentioned before (dispensing 180 µL 2PACz solution) using a more highly concentrated 2PACz solution with 0.475 mg mL^{-1} (1 mg mL^{-1} for the hybrid two-step method). For the hybrid two-step method, an additional washing step is used to remove unbound molecules.

The fully solution-based two-step processed perovskite thin film is fabricated as previously described, using the same solution concentration (1.5 M) for planar Si bottom cells and higher concentrated solutions of 1.7 M for small-textured and 1.9 M for large-textured Si bottom cells. The concentration refers to the inorganic solution, while the organic cation solution is adjusted accordingly to match the intended stoichiometry. Bulk passivation follows the same procedure as for the SJ PSCs, with modifications to align with the respective perovskite solution molarity. In the spin-coating process, 130 µL of the inorganic solution and 150 µL of the organic cation solution are dispensed. The hybrid two-step processed perovskite thin film is fabricated as described before, using either co- or sequential deposition of the inorganic precursors (50 nm CsCl, 500 nm PbI_2). The organic cation solution has a molarity of 0.75 M and is deposited with a spin speed of 4000 rpm.

For fully solution-based two-step processed perovskite thin films on planar or small-textured Si bottom cells, the concentration of the surface passivation is the same as for SJ PSCs. For large-textured Si bottom cells, the concentration is reduced to 0.3 mg mL^{-1} for $PDAI_2$ and 0.3 mg mL^{-1} for BAI. For hybrid two-step processed perovskite thin films on all kinds of Si bottom cells, the concentration of the surface passivation is the same as for SJ PSCs.

For the ETL layer, 20 nm of C_{60} is thermally evaporated. A 20 nm SnO_x layer prepared by ALD is used as buffer layer. Subsequently, 90 nm sputtered IZO (45 nm IZO for large-textured Si bottom cells and hybrid two-step processed perovskite/Si TSCs) from an IZO target (4 inch, In_2O_3/ZnO 90/10 wt%, 99.99% pure, Kurt J. Lesker Company) using 190 W power (15.10 W in^{-2} power density) and a mixture of argon and oxygen (1.3%) at a process pressure of 1.1 mTorr is used as a transparent electrode and the active area of 1.04 cm^2 is defined by the thermally evaporated Ag electrode (300 nm for small-textured and planar Si bottom cells, 600 nm with 3x100 µm gridfingers for large-textured Si bottom cells and for hybrid two-step processed perovskite/Si TSCs). In order to reduce reflection losses, 100 nm MgF_2 (125 nm MgF_2 for hybrid two-step processed perovskite/Si TSCs) as an antireflection layer is evaporated on top of the active area.

3.2 Characterization Methods

Compared to Si solar cells, gaining a comprehensive physical understanding of the working mechanisms in PSCs is much more challenging. In crystalline Si solar cells, charge transport is primarily governed by the diffusion of minority carriers. In PSCs, charge transport occurs through drift, driven by an electric field, and diffusion, driven by gradients in charge-carrier concentration. Both electron and hole densities vary spatially and contribute significantly to the device performance, making the system more complex. As a result, a wide range of characterization methods is required to thoroughly investigate the performance and underlying physics of PSCs.[213]

In the following section, experimental measurement methods used to probe and characterize the properties of perovskite thin films and PSCs are discussed.

3.2.1 Characterization of Thin Films

X-ray Diffraction

X-ray diffraction (XRD) is a fundamental technique to characterize the crystallographic structure of materials. When X-rays with a wavelength in the order of interatomic spacings interact with a material that has a periodic lattice, they elastically scatter and interfere constructively if the Bragg condition is fulfilled:

$$2d\,\sin(\Theta) = n\lambda, n = 1, 2, 3, \ldots \tag{3.1}$$

where d is the spacing between crystal lattice planes, λ is the X-ray wavelength, and Θ is the incident angle (Figure 3.6a). By measuring the intensity of diffracted X-rays as a function of the scattering angle (2Θ), the electron density distribution can be inferred, allowing determination of atomic positions within the crystal. Each material produces a unique diffraction pattern, which can be used to identify unknown materials and determine their crystallographic structure.

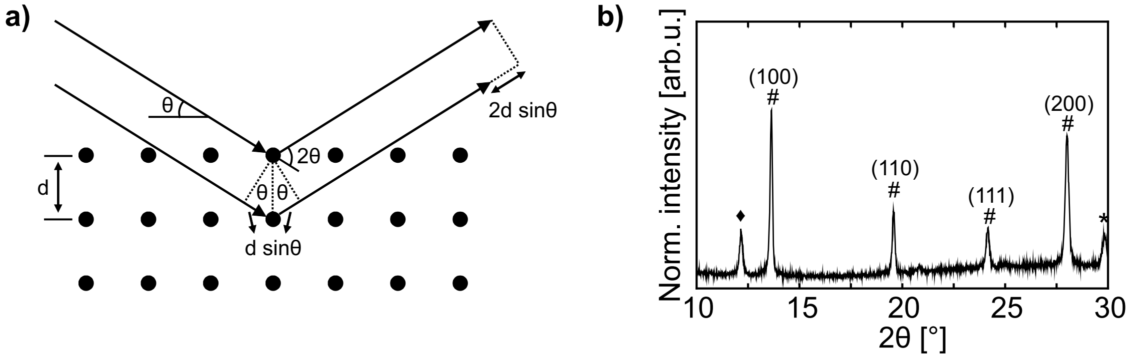

Figure 3.6: a) Working principle of X-ray diffraction (XRD) using Bragg's law, with the diffraction order n, the wavelength of the incident X-rays λ, the interplanar spacing d, and the incident angle Θ. b) A representative XRD pattern of a perovskite thin film fabricated on glass/indium tin oxide (ITO)/NiO_x/2PACz. ♦ denotes the PbI_2 phase, # the perovskite phase and $*$ the ITO phase.

In this thesis, XRD measurements are performed to determine the crystallinity and crystal orientation of the inorganic scaffold and the perovskite thin film. The observed perovskite diffraction peaks are indexed to the cubic space group $\mathrm{Pm\overline{3}m}$.[214] The Miller indices (hkl) denote the crystallographic planes responsible for the corresponding diffraction peaks.[215] To calibrate the diffraction pattern, an ITO reference peak at around 30° is used to align the spectra.[216] Crystallinity is further assessed by analyzing peak area ratios and the full width at half maximum (FWHM). A reduction in the FWHM is commonly associated with enhanced crystallinity and improved crystal quality of the perovskite layer according to the Scherrer equation.[217,218] Measurements are carried out using a Bruker D2Phaser system with Cu-K_α radiation (λ = 1.5405 Å) in Bragg-Brentano configuration, utilizing a LynxEye detector. The detector measures the angle-dependent diffraction with a 0.01° step size within a 2Θ range from 10 to 30°. A representative XRD pattern of a perovskite thin film fabricated on glass/ITO/NiO_x/2PACz is shown in Figure 3.6b, where ♦ denotes the PbI_2 phase, # the perovskite phase and $*$ the ITO phase.

Grazing-Incidence Wide-Angle X-Ray Scattering

Grazing-incidence wide-angle X-ray scattering (GIWAXS) is an advanced characterization technique used to probe the crystallographic structure of thin films. In GIWAXS, X-rays are incident at a shallow angle and the scattered X-rays are collected over a wide angular range, allowing simultaneous analysis of both in-plane and out-of-plane crystallographic orientations (Figure 3.7a). Highly isotropic samples, consisting of randomly oriented crystallites

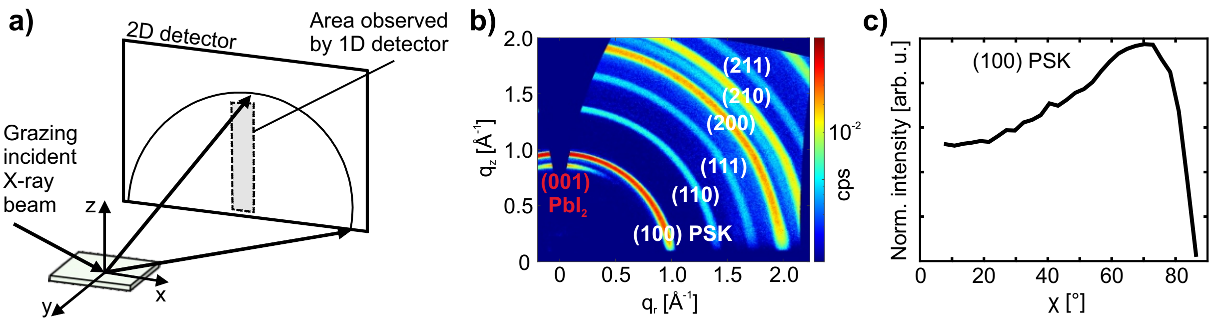

Figure 3.7: a) Schematic illustration of grazing-incidence wide-angle X-ray scattering (GIWAXS). b) A representative GIWAXS pattern of a perovskite thin film with denoted PbI_2 and perovskite (PSK) phases fabricated on glass/indium tin oxide (ITO)/NiO_x/2PACz. c) Extracted pole figure of the (100) perovskite phase from the GIWAXS pattern.

with no preferential orientation, produce symmetric ring-like scattering patterns. In contrast, samples with highly oriented crystals exhibit discrete spots or arcs, reflecting the alignment of crystallographic planes relative to the substrate. In this thesis, GIWAXS measurements are used to examine the preferred crystal orientation of the inorganic scaffolds and the perovskite layers, as well as to identify possible 2D phases. A representative GIWAXS pattern of a perovskite thin film is shown in Figure 3.7b. The ring-like scattering pattern indicates the respective crystal phases and their preferred orientations, as determined by the position of the intensity maxima. By integrating the measured intensity along each ring over the incident angle, so-called pole figures can be derived, enabling a comparison of crystal orientations for different crystal phases (Figure 3.7c). The χ angle is the polar angle between the scattering vector q and the $\mathrm{q_z}$ direction perpendicular to the sample surface, with low χ values indicating out-of-plane orientation and high χ values indicating in-plane orientation.
All GIWAXS measurements in this thesis are performed by Dr. Tonghan Zhao at the Institute of Microstructure Technology (IMT) at KIT, using a Bruker D8 Advance diffractometer. The system is equipped with a Cu X-ray source (40 kV, 40 mA), a Goebel mirror, a 0.5 mm micro mask and a 0.3 mm snout on the primary track. Scattered X-rays are detected using an Eiger2 R 500K 2D detector mounted on the secondary track. The incidence angle is fixed at 1.5° (1.0° for inorganic/perovskite layers on Si bottom cells in Chapter 6), which allows analysis of the entire perovskite film. Initially, all acquired scattering images are projected onto a virtual detector positioned directly behind the real goniometer circle using a custom MATLAB program developed in-house.[219] For transforming the experimentally acquired data into 2D diffractograms in reciprocal space, the open-source software GIXSGUI is used.[220]

X-ray Photoelectron Spectroscopy

X-ray photoelectron spectroscopy (XPS) is a highly surface-sensitive technique used to investigate the chemical and electronic structure of materials. The typical characteristic attenuation length λ is $\approx$ 1-3 nm. In XPS, an X-ray beam irradiates the sample, exciting electrons from a core level into the vacuum (Figure 3.8a). The kinetic energy (E_{kin}) of the emitted photoelectrons is measured, and their binding energy (E_{bin}) is calculated using the photoelectric equation:

$$E_{\mathrm{bin}} = h\nu - E_{\mathrm{kin}}, \tag{3.2}$$

where $h\nu$ is the X-ray photon energy. The spectrometer is calibrated such that $E_{\mathrm{bin}} = 0$ corresponds to the Fermi level (E_{F}). Since the binding energies of core-level electrons are element-specific and sensitive to the chemical environment, XPS provides detailed information about the surface composition and chemical bonding at the surface. In this thesis, XPS is used to investigate changes in the surface composition of the perovskite thin film upon deposition of different surface treatments. A representative XPS survey spectrum of a perovskite thin film is shown in Figure 3.8b, in which the intensity of the detected photoelectrons is plotted as a function of binding

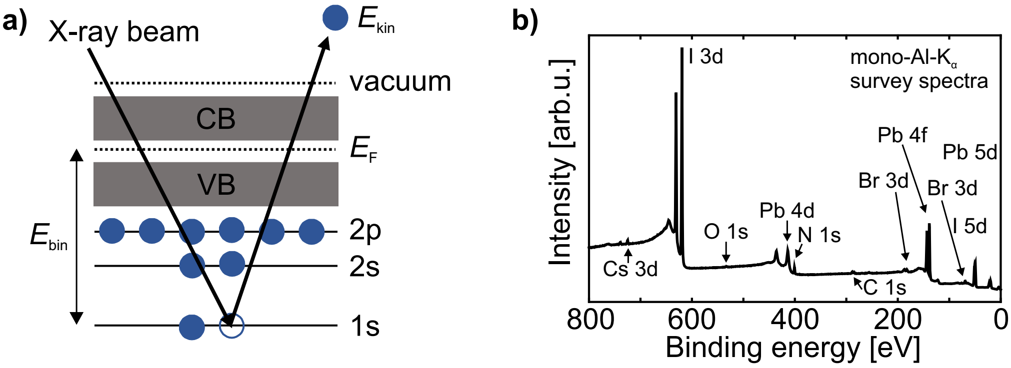

Figure 3.8: a) Schematic illustration of X-ray photoelectron spectroscopy (XPS), with the valence band (VB), the conduction band (CB), the Fermi level (E_F), as well as the binding energy (E_bin) and the kinetic energy (E_kin) of the emitted photoelectrons. b) A representative XPS survey spectrum of a perovskite thin film fabricated on glass/indium tin oxide (ITO)/NiO_x/2PACz.

energy. Each element exhibits a distinct set of XPS peaks correlated to the electron's configuration, e.g., 1s, 2s, 2p, etc.

The XPS measurements are carried out by Dr. Dirk Hauschild in the Materials for Energy (MFE) laboratory at the Institute for Photon Science and Synchrotron Radiation (IPS) at KIT. For this purpose, a monochromatic Al-K_α X-ray source (MECS SIGMA Surface Science) and a hemispherical electron analyzer (Omicron Argus CU) are used. The samples are processed at the Light Technology Institute (LTI, KIT, Campus South) and transferred into the MFE ultra-high vacuum system at IPS (Campus North) without air exposure. The successful sample transfer is indicated by a low oxygen content (O 1s core-level signal). An upper limit of approximately two hours of continuous X-ray exposure for a specific sample spot is determined in this study until beam-induced changes are visible in the spectra. Hence, each measurement spot is exposed for less than 30 min, chosen to minimize radiation-induced changes to the sample.

Scanning Electron Microscopy

Scanning electron microscopy (SEM) is a key technique to examine the surface morphology and microstructure of perovskite films with high spatial resolution.

In SEM, a focused electron beam (energy in the keV range) is scanned across the sample surface, generating various effects at different depths through electron-sample interactions. Primarily, low-energy secondary electrons emitted from the top few nanometers of the sample are collected to produce detailed images that reveal surface features such as grain boundaries and defects. To minimize charging effects and enhance image quality, samples are coated with a thin conductive layer prior to imaging.

In this thesis, top-view SEM images (Figure 3.9a) are acquired by Dr. Alexander Diercks at the Laboratory

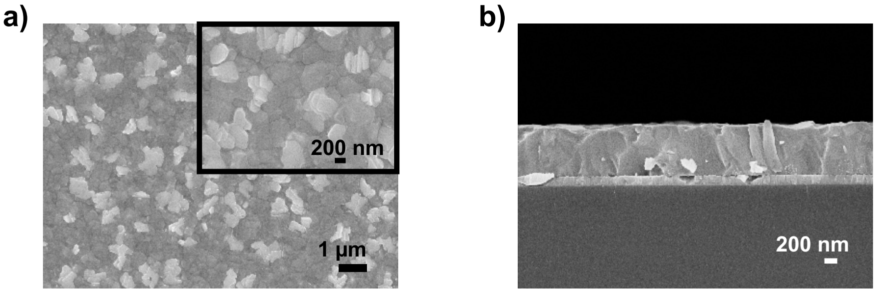

Figure 3.9: Representative a) top-view and b) cross-sectional scanning electron microscopy (SEM) images of a perovskite thin film fabricated on glass/indium tin oxide (ITO)/NiO_x/2PACz.

for Electron Microscopy (LEM) at KIT and by Raphael Pesch at the IMT at KIT with a Zeiss LEO Gemini 1530 microscope with an in-lens detector and an aperture size of 20-30 µm. For cross-sectional analysis (Figure 3.9b), the cross sections are covered with a 3 nm thick platinum layer deposited by sputtering to prevent charging. Acceleration voltages between 5-10 kV are applied for both surface and cross-sectional imaging. Grain size distributions are calculated using a data evaluation program based on StarDist. As an example, pristine perovskite films prepared *via* the fully solution-based two-step method exhibit a mean grain size of around 360 nm.

Atomic Force Microscopy

Atomic force microscopy (AFM) is used to analyze the surface morphology and roughness of perovskite films with nanometer-scale resolution. Measurements are conducted in intermittent contact mode (tapping mode), where a cantilever with a sharp tip oscillates near its resonance frequency while scanning the surface at minimal distance. To maintain a constant oscillation amplitude, the cantilever height is actively regulated during scanning. This mode is preferred for soft materials like perovskites, as it significantly reduces lateral shear forces that can damage the sample. Force interactions between the tip and the sample modulate the oscillation amplitude, which is optically detected *via* a laser beam reflected onto a photodiode. Assuming a uniform chemical composition of the surface, variations in the signal are primarily attributed to differences in tip-sample distance, allowing precise topographical mapping. All AFM measurements in this thesis are performed using a NanoWizard II (JPK Instruments AG). Images are typically acquired over a 5 µm × 5 µm scanning area at a 512×512 pixel resolution and processed using Gwyddion software. For each parameter, two to three measurements are taken, and the average root-mean-square (RMS) value is calculated. As an example, pristine perovskite films prepared *via* the hybrid two-step deposition method with sequential deposition of the inorganic scaffold exhibit an RMS surface roughness of around 27 nm (Figure 3.10b).

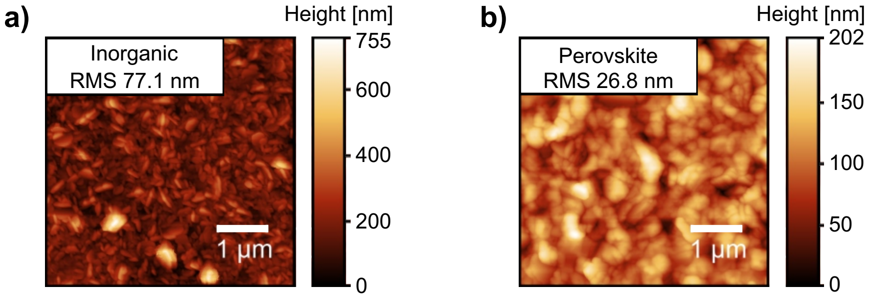

Figure 3.10: Representative atomic force microscopy (AFM) images of a) an inorganic scaffold and b) a perovskite thin film fabricated on glass/indium tin oxide (ITO)/NiO$_x$/2PACz. For each parameter, two to three measurements are taken, and the average root-mean-square (RMS) value is calculated.

Ultraviolet-Visible Spectroscopy

To optically characterize perovskite thin films and solar cells, ultraviolet-visible (UV/Vis) spectroscopy is performed. Light from a deuterium lamp (UV range) and a tungsten halogen lamp (visible to near-infrared range) is split by a monochromator, allowing wavelength-dependent measurements. The light spot is focused on the sample, and either the reflectance or the transmittance of the sample is measured. The central component in both measurements is the integrating sphere, where its interior is an almost perfectly diffuse reflecting body. For transmittance measurements, the sample is placed directly in front of the sphere, with the exit side closed by a white reference disc. For reflectance measurements, the sample is positioned behind the sphere. The transmitted or reflected light is collected inside the integrating sphere and detected with a Si/InGaAs photodiode. For calibration, a reference measurement without

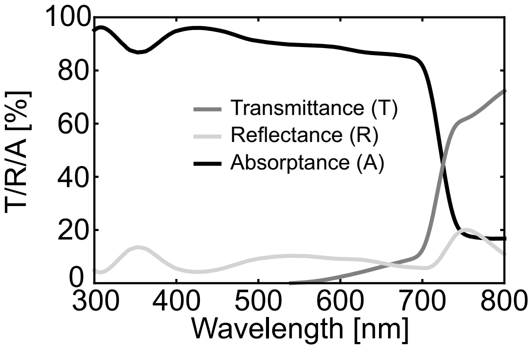

Figure 3.11: Representative transmittance (T) and reflectance (R) spectra, along with the derived absorptance (A), of a perovskite thin film fabricated on glass/indium tin oxide (ITO)/NiO_x/2PACz. The spectra are smoothed using a Savitzky-Golay filter (window length = 51, polynomial order = 3) for noise reduction.

sample is performed to determine the baseline transmission. The absorptance (A) is calculated from reflectance (R) and transmittance (T) using:

$$A(\lambda) = 1 - R(\lambda) - T(\lambda). \tag{3.3}$$

In this thesis, transmittance and reflectance measurements are conducted using a PerkinElmer Lambda1050 spectrophotometer equipped with a dual-monochromator, a 150 mm diameter integrating sphere, and a dual lamp system (deuterium and tungsten halogen). A chopper frequency of 46 Hz is applied. The studied spectral range extends from ultraviolet to near-infrared, typically covering 300-850 nm for PSCs, and 300-1200 nm for 2T perovskite/Si TSCs, with a step size of 2 nm. The illumination spot is maximized to average out film inhomogeneities. A representative UV/Vis measurement of a perovskite thin film fabricated on glass/ITO/NiO_x/2PACz is shown in Figure 3.11.

Time-of-Flight Secondary Ion Mass Spectrometry

Time-of-flight secondary ion mass spectrometry (ToF-SIMS) is a powerful analysis technique providing detailed elemental and molecular information with high lateral resolution. In ToF-SIMS, a focused high-energy ion beam bombards the sample surface, causing the ejection of secondary ions. These secondary ions are accelerated into a time-of-flight mass spectrometer, where their mass-to-charge ratios are determined based on their travel time to the detector. This enables precise identification of both elemental and molecular species, including organic fragments, with high mass resolution and sensitivity. The depth of analysis depends on the energy of the sputter ion beam: Higher-energy ions allow for deeper sputtering and depth profiling, but may induce damage or intermixing, while low-energy ions are preferred for surface-sensitive measurements. In this thesis, ToF-SIMS is used to study the elemental distribution and diffusion processes within the inorganic scaffolds and perovskite thin films. A representative ToF-SIMS measurement of a PSC with the layer stack ITO/NiO_x/2PACz/perovskite/$PDAI_2$+BAI/C_{60}/SnO_x/Ag is shown in Figure 3.12.

All ToF-SIMS measurements in this thesis are carried out in collaboration with the Karlsruhe Nano Micro Facility (KNMFi) at KIT by Dr. Alexander Welle on a TOF.SIMS5 instrument (ION-TOF GmbH, Münster, Germany). For depth profiling, a dual-beam analysis is performed. Depth-resolved mass spectra are recorded by eroding the sample with a secondary ion beam during data acquisition. In negative secondary ion polarity, signals from halogens and cluster ions such as $\mathrm{PbI_3^-}$ and $\mathrm{PbIBr_2^-}$ are detected. In contrast, positive polarity enables the detection of metals such as Pb, Na, Sn, Si, Ni, and In. The implantation of sputter ions into the substrate at the bottom of the resulting crater increases the secondary ion yield in positive polarity, while reducing it in negative polarity. This effect is particularly desirable, as it is the only way to reduce the extremely high secondary ion yield of iodide, which could otherwise lead to detector saturation. Detailed measurement parameters are provided in Table 3.3 for fully

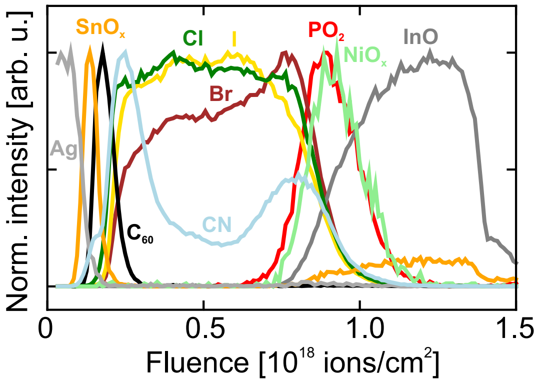

Figure 3.12: Representative time-of-flight secondary ion mass spectrometry (ToF-SIMS) measurement (negative polarity) of a perovskite solar cell (PSC) with the layer stack indium tin oxide (ITO)/NiO_x/2PACz/perovskite/$PDAI_2$+BAI/C_{60}/SnO_x/Ag.

solution-based two-step processed PSCs and in Table 3.4 for hybrid two-step processed inorganic scaffolds and perovskite layers. The short primary ion pulse length of 1.5 ns allows for high mass resolution (6500 $m\,(\Delta m)^{-1}$ for $^{208}Pb^{+}$). The applied sputter ion fluence is used as an arbitrary depth scale. However, this scale might not be linear due to different erosion speeds of the different deposited layers. Secondary ion intensities are normalized to their respective maximum values, which may introduce increased noise in signals with lower absolute intensities. It is ensured that signals showing secondary ion detector saturation are omitted.

Table 3.3: Parameters for time-of-flight secondary ion mass spectrometry (ToF-SIMS) measurements of fully solution-based two-step processed perovskite solar cells (PSCs) presented in Chapter 6. The base pressure during analysis is below $7\cdot10^{-8}$ mbar.

	Positive polarity	Negative polarity
Primary ion source	Bi_3^+, 25 keV, pulse bunching, 1.5 ns pulse length, 100 µs cycle time	
Target current [pA]	0.4	0.1
Field of view [µm^2]	100×100	
Lateral resolution [pixel]	64×64	
Mass scale calibration	^{23}Na, ^{25}Mg, ^{26}Mg, ^{39}K, ^{41}K, ^{113}In, ^{208}Pb	^{12}C, $^{12}C_2$, ^{35}Cl, InO, I_2
Sputter ion	O_2^+, 1 keV, 250 nA	
Crater size [µm^2]	300×300	250×250
Measurement conditions	non-interlaced, 4 s sputter, 1 s pause, charge compensation	non-interlaced, 2 s sputter, 1 s pause, charge compensation

Table 3.4: Parameters for time-of-flight secondary ion mass spectrometry (ToF-SIMS) measurements of inorganic scaffolds and perovskite layers fabricated using the hybrid two-step deposition route presented in Chapter 7. The base pressure during analysis is below $7{\cdot}10^{-8}$ mbar.

	Positive polarity	Negative polarity
Primary ion source	Bi_3^+, 25 keV, pulse bunching, 1.5 ns pulse length, 100 µs cycle time	
Target current [pA]	0.31-0.35, 10 kHz repetition rate	
Field of view [μm^2]	200×200	
Lateral resolution [pixel]	128×128	
Mass scale calibration	Li^+, Na^+, $^{204}\mathrm{Pb}^+$, $^{206}\mathrm{Pb}^+$, Cs_2^+	$^{37}\mathrm{Cl}^-$, PO_2^-, CsI_2^-, PbI_2^-
Sputter ion	Ar_{1500}^+, 10 keV, 7.4-7.5 nA	
Crater size [μm^2]	500×500	
Measurement conditions	interlaced	

3.2.2 Characterization of Perovskite Solar Cells

External Quantum Efficiency

The external quantum efficiency (EQE) characterizes the spectral response (SR) of solar cells and allows calculation of the J_{SC} following Equation 2.22. The integrated J_{SC} over the measured wavelength range is shown in each EQE figure (Figure 3.13a). In this thesis, EQE measurements are conducted in N_2 atmosphere using a PVE300 photovoltaic QE system (Bentham EQE system). Monochromatic light is generated from a dual xenon/quartz halogen source and modulated by an optical chopper operating at a 560-590 Hz. A lock-in amplifier filters this frequency to isolate the signal from background noise (e.g., ambient light). For SJ PSCs, EQE spectra are measured from 300 to 850 nm with a 500 ms integration time and a 0.74×0.74 mm illumination spot. TSCs are measured over a wider spectral range (300-1200 nm) with a 750 ms integration time and a larger 2.0×2.0 mm illumination spot. In 2T perovskite/Si tandem devices, subcells are measured individually using tailored bias lighting: the perovskite top cell with 780 nm and 940 nm LEDs, and the Si bottom cell with a 465 nm LED and a white light source.

Various methods exist in the literature to determine the bandgap of semiconductors.[221] In this thesis, the bandgap of all processed perovskite thin films is calculated from the maximum of the first derivative of the EQE near the absorption edge (d(EQE)/d(E)), following the method by Krückemeier et al.[222] (Figure 3.13b).

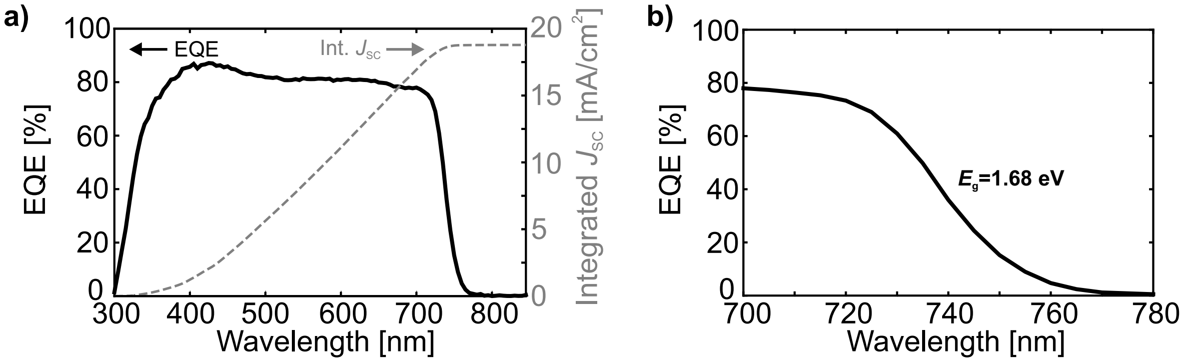

Figure 3.13: a) Representative external quantum efficiency (EQE) spectrum as well as the corresponding integrated short-circuit current density (J_{SC}), and b) optical bandgap (E_g) extracted from the inflection point of the EQE spectrum of a single-junction (SJ) perovskite solar cell (PSC).

Current Density-Voltage Characteristics

Measuring the current density-voltage (*J*-*V*) characteristics is a fundamental method for evaluating solar cell performance, as key PV parameters including the V_{OC}, the FF, the J_{SC} and the PCE can be extracted. To ensure a comparison of PV characteristics within the scientific community, standard test conditions are defined: a solar cell temperature of 25 °C, a solar irradiance of $100\,\mathrm{mW\,cm^{-2}}$ and an air mass (AM) of 1.5G.[223] The AM1.5G spectrum represents the solar spectrum for transmission through 1.5 times the global air mass, corresponding to a solar irradiance angle of 48.2° relative to the surface normal.[170,224]

In this thesis, *J*-*V* measurements of SJ PSCs are performed using a class AAA xenon-lamp solar simulator (Newport Oriel Sol3A) in N_2 atmosphere, with a voltage sweep from -0.2 to 1.2 V. 2T perovskite/Si TSCs are characterized using a class AAA LED-based solar simulator (Wavelabs Sinus-70 Advanced) under ambient conditions, with a voltage range from -0.2 to 2.0 V. The solar simulator irradiation intensity is calibrated using a certified Si reference cell (Fraunhofer ISE), equipped with a KG5 band pass filter for SJ PSCs and without filter for perovskite/Si TSCs.

To account for hysteresis effects in PSCs,[225] both backward ($V_{\mathrm{OC}} \rightarrow J_{\mathrm{SC}}$) and forward ($J_{\mathrm{SC}} \rightarrow V_{\mathrm{OC}}$) scans are performed consecutively at a constant sweep rate of $0.6\,\mathrm{V\,s^{-1}}$ using a Keithley 2400 sourcemeter. For clarity, only backward scans are shown when comparing multiple *J*-*V* curves. The hysteresis index (HI) is calculated from the PCEs of the forward and backward scans as:

$$\mathrm{HI}\ [\%] = \frac{\mathrm{PCE}_{\mathrm{backward}} - \mathrm{PCE}_{\mathrm{forward}}}{\mathrm{PCE}_{\mathrm{backward}}} \cdot 100. \tag{3.4}$$

A representative *J*-*V* measurement of a SJ PSC is shown in Figure 3.14a.

To ensure precise control over the illuminated area during measurements, shadow masks are used: $7.84\,\mathrm{mm^2}$ for fully solution-based two-step processed SJ PSCs (except $9.28\,\mathrm{mm^2}$ for ISOS-D1/D2 stability tests in Chapter 5), no mask for hybrid two-step processed SJ PSCs, and $1.0\,\mathrm{cm^2}$ for perovskite/Si TSCs. Using a shadow mask allows for a more accurate measurement of the J_{SC}. However, it leads to an underestimation of the V_{OC}, because parts of the active area remain unilluminated and exhibit increased recombination.

Box-whisker diagrams are used to visualize the distribution of PV parameters across different sample sets. The box represents the interquartile range (IQR), with the median shown as a black line and individual data points as black diamonds. Whiskers extend to the furthest data points within 1.5 times the IQR, while data points beyond the whiskers are indicated as outliers.

Long-term operational stability is assessed following the International Summit on Organic Photovoltaic Stability (ISOS) protocols adapted for perovskite PV.[226] In this work, three standardized stability tests are used: ISOS-D1 (dark storage, 25 °C, intermittent *J*-*V* measurements) to test dark storage stability, ISOS-D2 (dark storage, 85 °C,

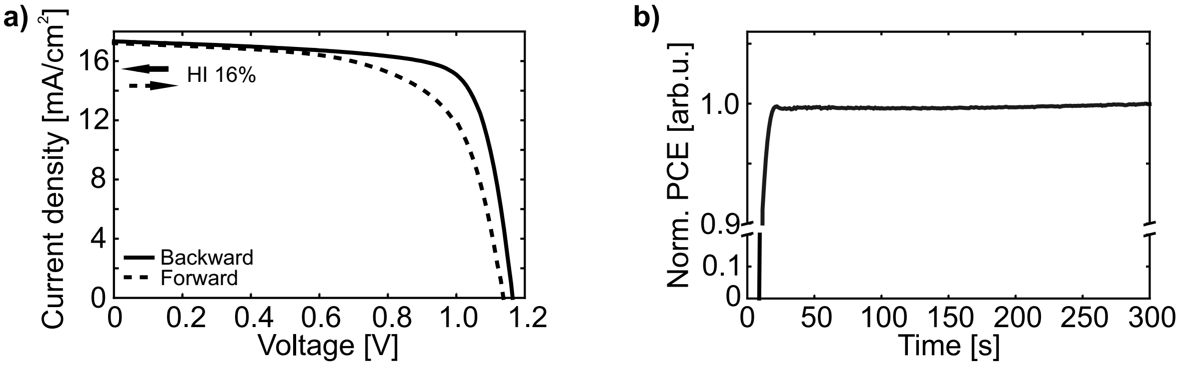

Figure 3.14: a) Representative current density *versus* voltage (*J*-*V*) characteristic measured from short-circuit to open-circuit (forward scan) and from open-circuit to short-circuit (backward scan), showing a pronounced hysteresis index (HI), and b) corresponding stabilized power conversion efficiency (PCE) determined by measuring the photocurrent at the maximum power point (MPP) of a single-junction (SJ) perovskite solar cell (PSC).

intermittent *J-V* measurements) to evaluate thermal stability and ISOS-L1 (100 mW cm^{-2}, 25 °C, MPP tracking) to assess light-induced degradation. All stability measurements are performed under N_2 atmosphere.

The stabilized PCE under continuous AM1.5G illumination is determined by maximum power point (MPP) tracking using a perturb-and-observe algorithm. The voltage is varied by ±0.01 V in 0.1 s intervals, and the corresponding power is calculated at each step. The voltage yielding the highest power is selected, and the current is measured five times and averaged. For short-term stability measurements, this process is repeated every second for 5 min. A representative measurement is shown in Figure 3.14b. Extended MPP tracking for ISOS-L1 stability tests (300-1000 h) in Chapter 5 and Chapter 6 is conducted using a class AAA LED solar simulator (Wavelabs LS-2) in N_2 atmosphere at 25 °C. The simulator spectrum closely matches AM1.5G, with an irradiance of 98 mW cm^{-2}. To enable consistent stability comparisons within the scientific community, the time at which 80% of the initial efficiency remains (T_{80}) is usually considered as a figure of merit for evaluating PSC stability.[226]

Even in A+ class solar simulators, spectral deviations of up to 12.5% per 100 nm interval are not unusual,[227] making mismatch correction essential for accurate device characterization. To correct for spectral mismatch between the solar simulator and the reference spectrum (AM1.5G), a mismatch factor (MM) is calculated using the spectral response (SR), derived from the EQE:

$$\mathrm{SR}(\lambda) = \mathrm{EQE}(\lambda)\frac{e\lambda}{hc}, \tag{3.5}$$

where λ corresponds to the wavelength, e to the elementary charge, h to Planck's constant and c to the speed of light. Using the SR of the reference cell ($\mathrm{SR_{ref}}$) and the PSC ($\mathrm{SR_{pero}}$) along with the spectral irradiance of the reference spectrum (E_0, corresponds to AM1.5G) and the solar simulator spectrum (E_{sim}), the mismatch factor can be calculated:

$$\mathrm{MM} = \frac{\int E_0(\lambda)\cdot \mathrm{SR_{ref}}(\lambda)d\lambda}{\int E_{\mathrm{sim}}(\lambda)\cdot \mathrm{SR_{ref}}(\lambda)d\lambda}\cdot\frac{\int E_{\mathrm{sim}}(\lambda)\cdot \mathrm{SR_{pero}}(\lambda)d\lambda}{\int E_0(\lambda)\cdot \mathrm{SR_{pero}}(\lambda)d\lambda}. \tag{3.6}$$

The measured J_{SC} is corrected:

$$J_{\mathrm{SC,corr}} = \frac{J_{\mathrm{SC,meas}}}{\mathrm{MM}}, \tag{3.7}$$

and $J_{\mathrm{SC,corr}}$ is used to correct the PCE.[228,229]

Photoluminescence Quantum Yield

Photoluminescence quantum yield (PLQY) measurements provide valuable insights into the optoelectronic quality of the perovskite thin film, particularly regarding non-radiative recombination losses within the perovskite bulk and at the perovskite/CTL interfaces. PLQY is defined as the ratio between the emitted photon flux (Φ_{em}) and the absorbed photon flux (Φ_{abs}):[173,230]

$$\mathrm{PLQY} = \frac{\Phi_{\mathrm{em}}}{\Phi_{\mathrm{abs}}} = \frac{J_{\mathrm{rad}}}{J_G} \tag{3.8}$$

J_{rad} denotes the radiative current density, and J_G the photogenerated current density. Under the assumption that all photogenerated carriers recombine radiatively, J_G equals the J_{SC}.[231]

The implied V_{OC} ($V_{\text{OC-imp}}$) distinguishes the radiative open-circuit voltage limit ($V_{\mathrm{OC,rad}}$) from the voltage loss due to non-radiative recombination ($V_{\mathrm{OC,non-rad}}$). Following the procedure described by Stolterfoht *et al.*[232], Kirchartz *et al.*[233], and Fassl *et al.*[234], $V_{\text{OC-imp}}$ is extracted under one sun illumination using the quasi-Fermi level splitting (QFLS, ΔE_{F}):

$$V_{\mathrm{OC,imp}} = \frac{\Delta E_{\mathrm{F}}}{e} = V_{\mathrm{OC,rad}} - V_{\mathrm{OC,non-rad}} = V_{\mathrm{OC,rad}} + \frac{k_BT}{e}\ln(\mathrm{PLQY}) = \frac{k_BT}{e}\ln\left(\frac{\mathrm{PLQY}\ J_G}{J_{0,\mathrm{rad}}}\right) \tag{3.9}$$

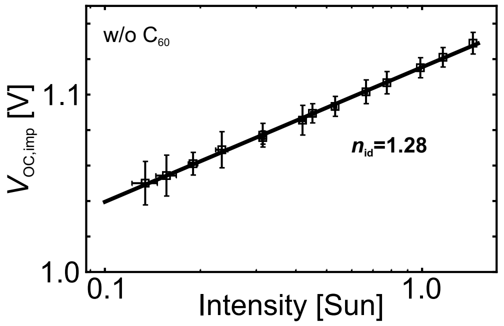

Figure 3.15: Representative ideality factor (n_{id}) extracted from a fit to the implied V_{OC} ($V_{\mathrm{OC\text{-}imp}}$) derived from intensity-dependent photoluminescence quantum yield (PLQY) measurements of a perovskite thin film without C_{60} electron transport layer (ETL) fabricated on glass/indium tin oxide (ITO)/$\mathrm{NiO_x}$/2PACz. PLQY is measured from the hole transport layer (HTL) side.

Here, $V_{\mathrm{OC,rad}}$ represents the maximum achievable voltage assuming purely radiative recombination and perfect photon outcoupling (100% PLQY). k_B is the Boltzmann constant, T the temperature, e the elementary charge, and $J_{0,\mathrm{rad}}$ the radiative saturation current density, which can be calculated as follows:

$$J_{0,\mathrm{rad}} = e \int \mathrm{EQE}(\lambda) \cdot \Phi_{\mathrm{BB}}(\lambda, T)\; d\lambda, \tag{3.10}$$

where Φ_{BB} is the photon flux density emitted by blackbody radiation at the temperature T:

$$\Phi_{\mathrm{BB}}(\lambda, T) = \frac{2\pi c}{\lambda^4} \cdot \frac{1}{\exp\left(\frac{hc}{\lambda k_B T}\right) - 1}, \tag{3.11}$$

with c the speed of light in vacuum and h the Planck's constant.

In addition, intensity-dependent PLQY measurements enable the extraction of the ideality factor (n_{id}), which provides insight into the dominant recombination mechanisms within the solar cell. The n_{id} is obtained from the slope of a logarithmic fit of $V_{\mathrm{OC\text{-}imp}}$ *versus* the light intensity (Figure 3.15). A value of $n_{\mathrm{id}} \approx 1$ typically indicates radiative bimolecular recombination, while values approaching 2 suggest trap-assisted Shockley-Read-Hall recombination.[97,232,234,235] In this thesis, PLQY measurements are performed using a LuQY Pro system (QYB). The samples are mounted inside an integrating sphere and illuminated from the HTL side. Excitation is provided by a green laser (λ = 532 nm) introduced through a small entrance port. All measurements are conducted under ambient conditions.

3.2.3 Statistical Analysis

To assess whether the statistical results of two independent samples differ significantly, *Welch's t test* is used in this thesis. This test is a modification of the traditional *Student's t test*,[236] offering improved reliability when the two samples exhibit unequal variances and/or different sample sizes.[237,238] Such tests are commonly referred to as "independent samples" or "unpaired" *t tests*, as they are applied when the underlying statistics of the two samples are assumed to be distinct. A key assumption is that the sample means of the two samples being compared are normally distributed.[236] The *t* statistic used to evaluate the difference between the two sample means is calculated as:

$$t = \frac{\overline{X} - \overline{Y}}{\sqrt{\frac{S_x^2}{n_x} + \frac{S_y^2}{n_y}}}, \tag{3.12}$$

where $\overline{X}$ and $\overline{Y}$ denote the sample means, S_x and S_y the standard deviations, and n_x and n_y the respective sample sizes.

PSCs with a V_{OC} below 0.8 V and a FF below 60% were excluded to filter out non-representative data. For hybrid two-step processed PSCs, the filter criterion was relaxed to exclude only those with V_{OC} below 0.8 V.

4 Bandgap Engineering of Solution-Based Two-Step Processed Perovskite Thin Films

In two-terminal perovskite/silicon tandem solar cells, precise bandgap engineering of the perovskite top cell to approximately 1.65-1.75 eV is essential for achieving current matching between the subcells and maximizing overall device performance. Bandgap widening can be conveniently realized by partially substituting iodide with bromide in the perovskite lattice. However, perovskites with bandgaps above 1.65 eV often exhibit compositional instability, which can lead to degraded film morphology and increased non-radiative recombination losses, limiting their implementation in high-performance and industrially relevant tandem devices. Although solution-based two-step deposition routes are known to produce uniform and high-quality perovskite films on silicon bottom cells, achieving a bandgap beyond 1.65 eV remains comparatively underexplored. In two-step deposition, the spatial and temporal separation of precursor conversion introduces distinct challenges compared to conventional one-step processing, especially regarding halide distribution and crystallization pathways. This chapter addresses these challenges by introducing a novel bandgap engineering strategy for fully solution-based two-step processed perovskite thin films, targeting a bandgap of 1.68 eV required for high-efficiency two-terminal tandem integration (research question ***I****). The role of bromide incorporation at different stages of the two-step deposition process is systematically investigated. By precisely controlling how and when bromide is introduced, its impact on film morphology, crystallization behavior, and optoelectronic properties is examined (research question* ***II****). The resulting insights enable the fabrication of wide-bandgap perovskite thin films that combine the target bandgap with high perovskite film quality. These findings serve as a general guideline for two-step deposition methods and support the development of industry-relevant perovskite/silicon tandem solar cells.*

Parts of this chapter review the published research article "Bandgap Engineering of Two-Step Processed Perovskite Top Cells for Perovskite-Based Tandem Photovoltaics" in *Advanced Functional Materials* 34.9 (2024) by *R. Pappenberger (R.P.)* as first author, together with *A. Diercks*, *J. Petry*, *S. Moghadamzadeh*, *P. Fassl*, and *U. W. Paetzold*.[239] Some figures in this chapter were adapted from reference[239] with permission from Wiley.
R.P. contributed to this project by conceptualizing the study, leading experimental investigations, data curation, formal analysis, and visualization, as well as writing the original draft of the manuscript. The contributions of all authors involved in this study are listed in Table A.3 according to the CRediT system.
For better consistency in scientific content, the second part of the research article is presented in Chapter 5.

4.1 Motivation

For 2T perovskite/Si TSCs, perovskite thin films with a bandgap of approximately 1.65-1.75 eV – predicted by optical simulations to enable optimal current matching between the subcells – are essential for maximizing device performance.[47,181,240–243] In industrial PV manufacturing, Si solar cells typically feature random pyramidal textures (texture height $\approx$ 2-5 µm) to enhance light-incoupling and reduce reflection losses compared to planar or polished surfaces.[41–46] Therefore, developing high-quality wide-bandgap perovskite thin films using a deposition method that is not affected by the surface texture of the underlying Si bottom cell is a key objective for industrial tandem integration.

Among established solution-based deposition processes, the two-step method – comprising the deposition of the inorganic precursors in the first step, followed by the organic cation precursors in the second step – has emerged as a promising candidate for tandem integration due to its superior control over film formation and reliable surface coverage on Si bottom cells.[57,58,60,61] Despite these advantages, the solution-based two-step deposition method has not been adopted as widely as the solution-based one-step deposition method.[64] While the one-step spin-coating method has yielded most of the record-efficiency devices at laboratory scale so far,[46–51] it relies on an extremely narrow antisolvent quenching window of roughly 3-5 s.[54,244,245] This requires highly skilled technicians to handle the pipette steadily and reproducibly, which can lead to challenges such as rapid crystallization, cracking, and incomplete coverage on textured substrates.[52,53,55] These constraints limit its manufacturability and therefore its industrial relevance.[54] In contrast, the solution-based two-step deposition method provides a more controlled perovskite film formation, as perovskite crystallization is governed by the top-down penetration of the organic cation precursors into the inorganic scaffold in the second deposition step, enabling uniform, dense, and pinhole-free perovskite thin films.[57,58,61–65] Moreover, the two-step method offers flexibility in precursor composition and solvent systems, and is compatible with scalable deposition techniques such as vapor deposition, inkjet printing, slot-die coating, and hybrid combinations thereof, making it a promising deposition technique for industrial fabrication.[55,57,63,66–70]

Despite these advantages, most reports on fully solution-based two-step processed PSCs focus on narrow-bandgap perovskite thin films ($E_g < 1.60$ eV),[167,246,247] while fabricating wider bandgaps ($E_g > 1.65$ eV) – required for high-performance 2T perovskite/Si tandem architecture – remains comparatively underexplored. Prior to the start of this work, only one report had been published on a wide-bandgap ($E_g \geq 1.63$ eV) PSC in the *p-i-n* architecture fabricated *via* a fully solution-based two-step deposition route (Table A.7).[57]

Bandgap tuning in perovskites is commonly achieved by adjusting the halide composition, particularly the bromide-to-iodide ratio ($\mathrm{X} = \mathrm{I}_{1-\gamma}\mathrm{Br}_{\gamma}$).[248–250] However, when the bromide fraction exceeds 20%, wide-bandgap perovskites typically exhibit increased non-radiative recombination and halide phase segregation, where iodide-rich and bromide-rich domains form under illumination or electrical bias. These processes result in reduced V_{OC} and compromise operational stability.[101,251–256]. In addition, the two-step deposition method introduces a spatial and temporal separation of precursor conversion, which leads to challenges distinct from those in one-step processing, especially regarding halide distribution and crystallization pathways.

In hybrid two-step deposition methods – where vapor deposition of the inorganic precursors is combined with solution-based deposition of the organic precursors – CsBr has been successfully incorporated *via* the vapor-deposition step to widen the bandgap.[78,79,87,212] However, CsBr is poorly soluble in conventional two-step inorganic precursor solvents such as DMF or DMSO, preventing direct transfer of this strategy to fully solution-based two-step processes.[257,258]

Prior to this thesis, two main bromide incorporation strategies existed for the fully solution-based two-step deposition method:

1. Introducing $PbBr_2$ to the inorganic precursor solution (PbI_2 in DMF/DMSO) during the first deposition step. However, this strategy results in a compact $PbBr_2$-rich bulk structure that hinders the diffusion of organic cations during the second deposition step, resulting in incomplete conversion and residual PbI_2.[57,58,259,260] Excess interfacial PbI_2, a wide-bandgap semiconductor, is particularly detrimental in *p-i-n* devices. It can impair charge-carrier extraction due to the formation of a counter diode, leading to pronounced hysteresis

and reduced stability of the resulting PSCs.[123,195,206] In addition, uncoordinated Pb-sites act as non-radiative recombination centers, limiting device performance and promoting ionic migration effects.[261–266]

2. Introducing organic bromide salts such as FABr or MABr to the organic cation solution during the second deposition step. This strategy is limited by the intrinsically slow bromide diffusion into the inorganic scaffold, as a higher activation energy is required for the migration of bromide compared to iodide.[267–269] As a result, achieving a homogeneous bromide distribution is challenging, often yielding vertical or lateral composition gradients that impair device performance.[267–269]

Together, these limitations highlight a significant knowledge gap in the existing bromide incorporation strategies for the fully solution-based two-step deposition method, underscoring the need for a reliable bromide incorporation strategy to achieve a target bandgap of ≈ 1.68 eV without compromising the morphology, crystallization behavior, or optoelectronic quality of the perovskite film.

Section 4.2 introduces the fully solution-based two-step method used in this chapter. The following two sections (Section 4.3 and Section 4.4) present a systematic material characterization of perovskite films prepared *via* three different bromide incorporation strategies. To assess the impact of bromide incorporation strategy at the device level, PSCs are fabricated and the results are discussed in Section 4.5. The insights gained in this chapter lay the groundwork for future perovskite film optimizations discussed in Chapter 5 and Chapter 6, as well as their integration into 2T perovskite/Si tandem architecture.

4.2 Fabrication Process

The fully solution-based two-step method used to fabricate the perovskite thin films in this chapter is illustrated in Figure 4.1, following an established recipe introduced by Gutierrez-Partida *et al.*[208]

For bandgap engineering, three bromide incorporation strategies are investigated and compared:

1. Partial substitution of PbI_2 with $PbBr_2$ in the inorganic precursor during the first deposition step (labeled as $PbBr_2$). The perovskite thin film has the nominal composition $MA_{0.07}FA_{0.93}Pb(I_{0.79}Br_{0.21})_3$.

2. Partial substitution of FAI with FABr in the organic cation precursor during the second deposition step (labeled as FABr). The perovskite thin film has the nominal composition $MA_{0.07}FA_{0.93}Pb(I_{0.80}Br_{0.20})_3$.

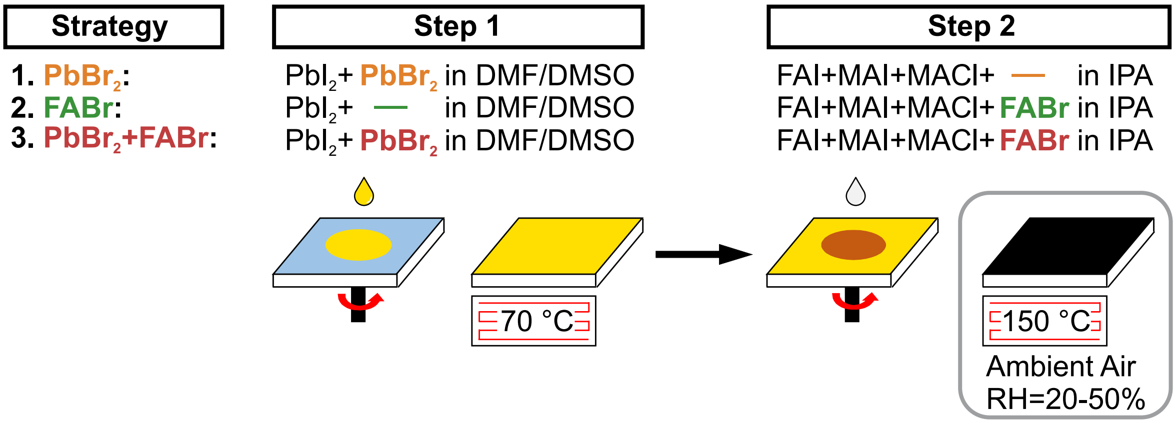

Figure 4.1: Schematic illustration of the fully solution-based two-step deposition method for the fabrication of wide-bandgap perovskite thin films used in this chapter. The bromide is either incorporated *via* $PbBr_2$ in the first deposition step, *via* FABr in the second deposition step or *via* a combination of $PbBr_2$ and FABr in the first and second deposition steps (labeled as $PbBr_2$, FABr and $PbBr_2$+FABr, respectively). The perovskite film is annealed under ambient conditions with a relative humidity (RH) of ≈ 20-50%. Adapted from reference[239] with permission from Wiley.

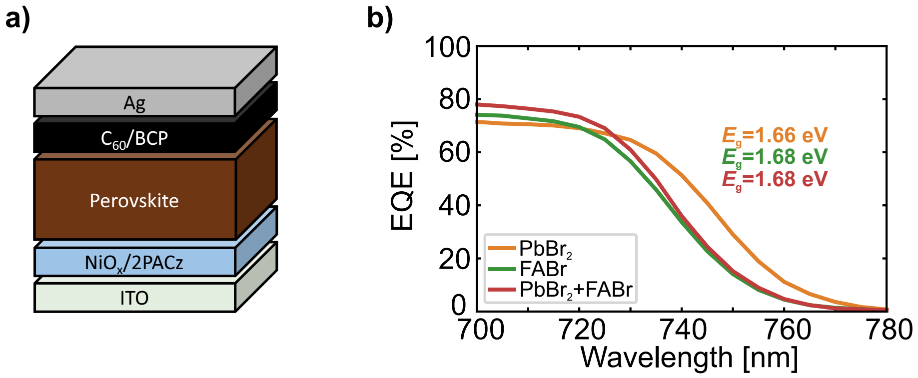

Figure 4.2: a) Schematic of the perovskite solar cell (PSC) structure (*p*-*i*-*n*) used in this chapter. b) Optical bandgap (E_g) extracted from the inflection point of the external quantum efficiency (EQE) spectra for opaque PSCs with bromide added *via* $PbBr_2$ in the first deposition step, FABr in the second deposition step or $PbBr_2$ in the first and FABr in the second deposition step ($PbBr_2$+FABr). Adapted from reference[239] with permission from Wiley.

3. Combined bromide incorporation *via* $PbBr_2$ in the inorganic precursor during the first deposition step and FABr in the organic cation precursor during the second deposition step (labeled as $PbBr_2$+FABr). The perovskite thin film has the nominal composition $MA_{0.07}FA_{0.93}Pb(I_{0.78}Br_{0.22})_3$.

In contrast to previous reports – where rubidium acetate (RbAc) was incorporated during the first deposition step[57] or a Br-rich seeding growth method was introduced[58] – the presented strategies use no additives other than MACl, thereby simplifying the overall process.

The PSCs follow the layer stack ITO/NiO_x/2PACz/perovskite/C_{60}/BCP/Ag (Figure 4.2a). To enable consistent comparisons between the bromide incorporation strategies, the bandgap of each perovskite thin film is specified. Unless stated otherwise, the following characterization focuses on perovskite thin films with bandgaps between 1.66 and 1.68 eV (Figure 4.2b).

4.3 Microstructure Analysis

To investigate how different bromide incorporation strategies influence the perovskite microstructure, XRD and SEM measurements are conducted on half-stacks with the architecture ITO/NiO_x/2PACz/perovskite.

The XRD patterns of the perovskite films (Figure 4.3a) reveal that all three bromide incorporation strategies lead to similar crystal orientations, with dominant diffraction peaks at $\approx 13.3°$ and $\approx 27.6°$, corresponding to the (100) and (200) planes of the cubic perovskite phase. A closer inspection of the peak area ratios (Figure 4.3b) confirms comparable diffraction features across the perovskite films. A preference for the (111) orientation is, however, observed when bromide is introduced *via* $PbBr_2$. In all three perovskite films, a pronounced PbI_2 peak is present, indicating a substantial amount of unreacted PbI_2, consistent with previous reports using the solution-based two-step method.[66,270,271] Reducing the residual PbI_2 fraction will therefore be a key aspect of future optimization. Interestingly, perovskite films prepared with bromide incorporation *via* $PbBr_2$ display a distinct double-peak feature of the PbI_2 peak at $\approx 11.9°$. This splitting points to halide phase segregation and a non-uniform bromide distribution within the perovskite layer.[272]

Examination of the full width at half maximum (FWHM) of the (100) perovskite peak (Figure 4.3c) highlights the impact of the bromide incorporation strategy. Perovskite films prepared with combined bromide incorporation in both deposition steps ($PbBr_2$+FABr) exhibit the narrowest peak (0.19°), compared to $PbBr_2$ (0.21°) and FABr (0.36°). This reduction in FWHM indicates improved perovskite crystallinity.

These trends are supported by SEM analysis (Figure 4.3d), and subtle differences in surface morphology are evident. Perovskite films prepared with bromide incorporation *via* $PbBr_2$ show a higher density of pinholes and a

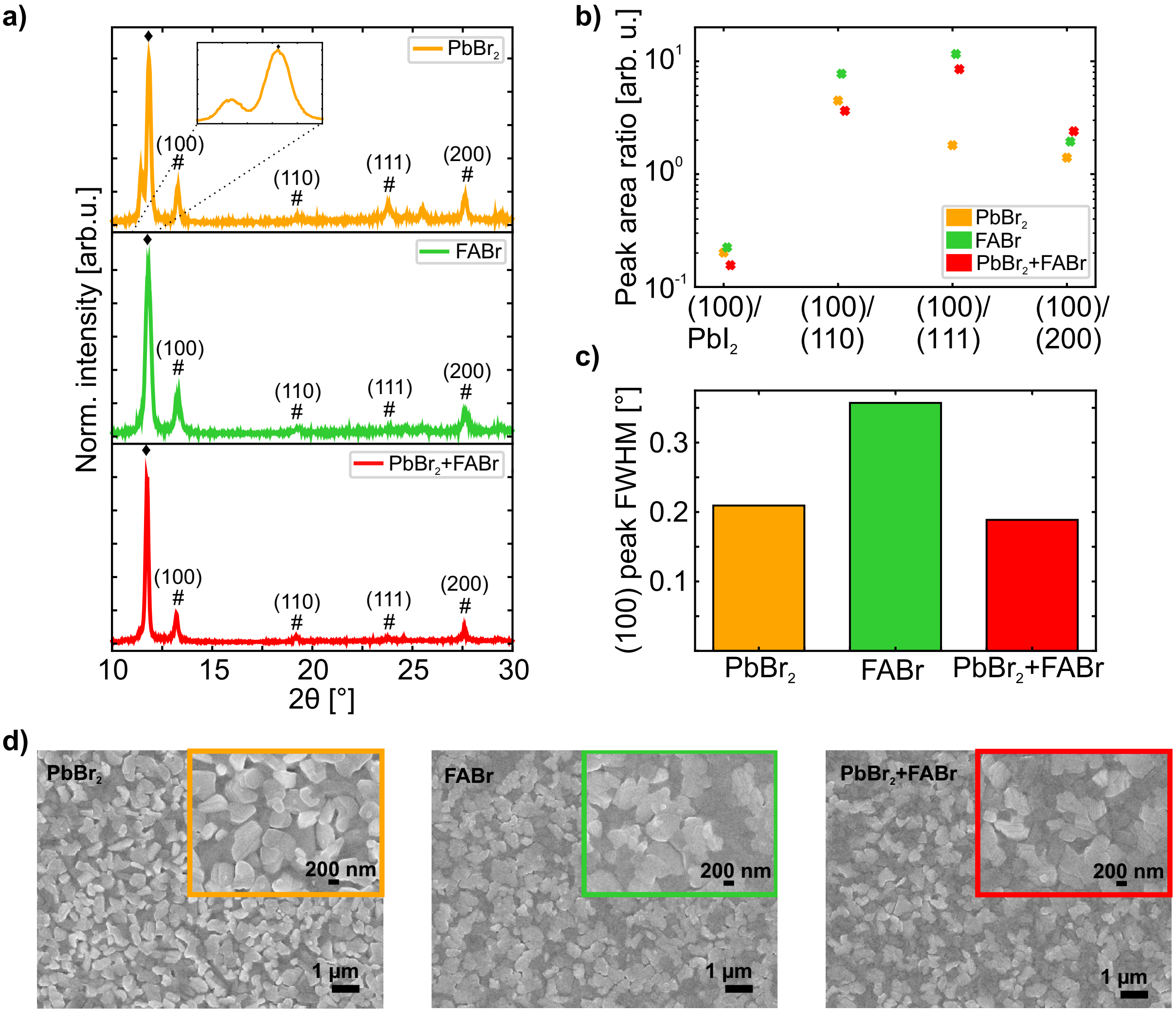

Figure 4.3: a) X-ray diffraction (XRD) patterns (♦ denotes the (001) PbI$_2$ phase and # the perovskite phase), b) peak area ratios, c) the full width at half maximum (FWHM) of the (100) perovskite peak and d) top-view scanning electron microscopy (SEM) images of perovskite films with bromide incorporated *via* PbBr$_2$, FABr or PbBr$_2$+FABr fabricated on glass/indium tin oxide (ITO)/NiO$_x$/2PACz. Adapted from reference[239] with permission from Wiley.

less ordered surface structure. In contrast, bromide incorporation *via* FABr or PbBr$_2$+FABr leads to more uniform perovskite films with reduced surface defects and enhanced crystalline growth. However, FABr perovskite films exhibit additional microwrinkles. Bright features observed in the SEM correspond to residual PbI$_2$, consistent with the XRD results. Within the limits of measurement uncertainty, all three perovskite films exhibit comparable grain sizes in the range of 360-390 nm, with slightly larger grains observed for the FABr films (Figure A.1).

Microstructure analysis shows that, among the three bromide incorporation strategies examined, introducing bromide in both deposition steps yields the highest overall film quality with enhanced grain growth, reduced pinhole density, and improved crystallinity.

4.4 Optoelectronic Properties

To evaluate non-radiative recombination losses in perovskite films fabricated *via* the three different bromide incorporation strategies, PLQY measurements along with internal quasi-Fermi level splitting (QFLS) are performed.

From the QFLS, the implied open-circuit voltage ($V_{\text{OC-imp}}$) can be derived.

Two types of half-stacks are investigated: one without ETL, consisting of ITO/NiO_x/2PACz/perovskite, and one with C_{60} as the ETL (ITO/NiO_x/2PACz/perovskite/C_{60}). Analyzing half-stacks without C_{60} allows the evaluation of non-radiative recombination at the HTL/perovskite interface and within the bulk, and its potential impact on the V_{OC} of the final device. This provides insights into the intrinsic quality of the perovskite layer.[102,232,273] Remarkably high average PLQY values (Figure 4.4a) and high $V_{\text{OC-imp}}$ values (Figure 4.4b) are observed for all three bromide incorporation strategies, exceeding typical values reported for one-step processed perovskite films. These results suggest a high optoelectronic quality of the perovskite thin film and indicate that the 2PACz/perovskite interface does not significantly limit the achievable V_{OC} of the device. Among the bromide incorporation strategies, perovskite films with combined bromide incorporation in both deposition steps ($PbBr_2$+FABr) yield the highest PLQY and an increase in $V_{\text{OC-imp}}$ by more than 10 mV compared to bromide incorporation *via* $PbBr_2$ or FABr alone, pointing to improved bulk properties. However, it should be noted that the high PLQY values may also result from residual PbI_2, which has been shown to enhance PLQY values and can therefore be misleading.[274]

Upon adding C_{60} as the ETL, the PLQY decreases due to interfacial recombination at the perovskite/C_{60} interface, in line with previous studies.[97,100,103,275] However, this fullerene-induced charge-carrier quenching is modest, with PLQY values dropping by less than one order of magnitude and only a slight reduction in $V_{\text{OC-imp}}$ is observed (Figures 4.4a/b). These findings suggest that the perovskite/C_{60} interface is of high quality, even without additional surface passivation, and does not considerably limit the V_{OC}, in contrast to earlier reports for wide-bandgap PSCs.[100] Notably, perovskite films with combined bromide incorporation in both deposition steps ($PbBr_2$+FABr) retain the highest PLQY and $V_{\text{OC-imp}}$ values.

To further investigate recombination mechanisms, intensity-dependent PLQY measurements are performed. The

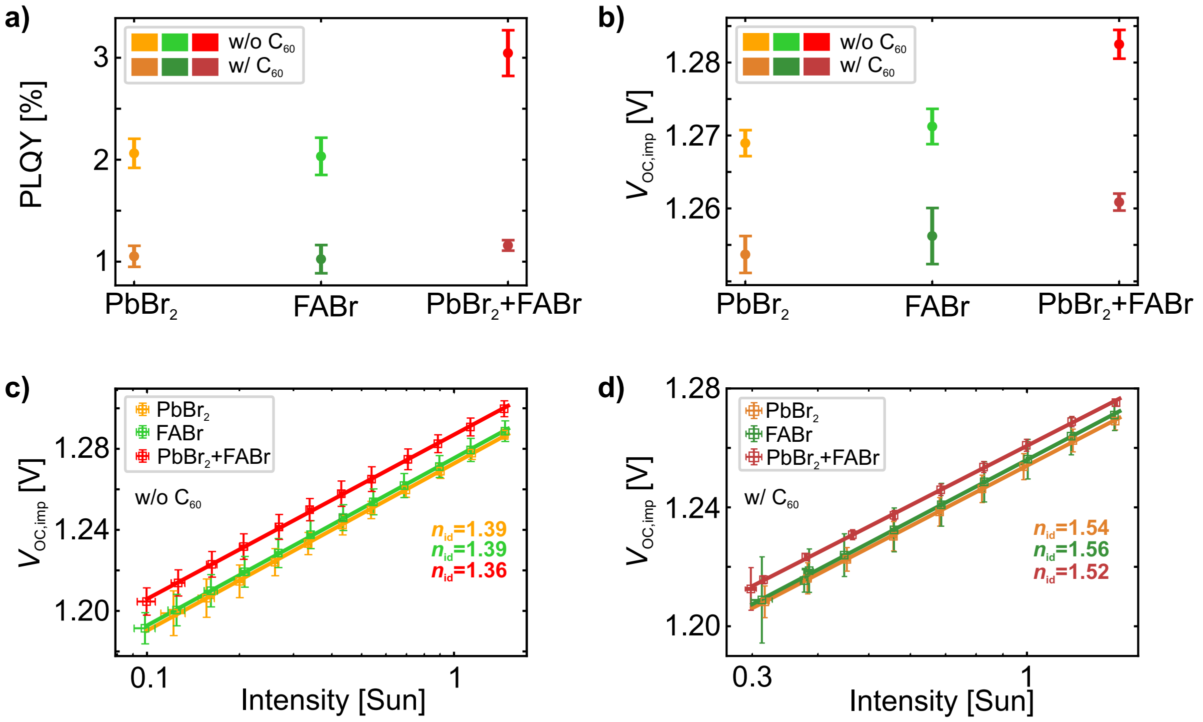

Figure 4.4: a) Photoluminescence quantum yield (PLQY), b) the obtained implied V_{OC} ($V_{\text{OC-imp}}$), and the ideality factor (n_{id}) extracted from a fit to the $V_{\text{OC-imp}}$ (derived from intensity-dependent PLQY measurements) measured c) without and d) with C_{60} electron transport layer (ETL) of the perovskite films with bromide incorporated *via* $PbBr_2$, FABr or $PbBr_2$+FABr fabricated on glass/indium tin oxide (ITO)/NiO_x/2PACz. PLQY is measured from the hole transport layer (HTL) side. For each parameter, several perovskite films are measured, and the corresponding mean and standard deviation are plotted. Adapted from reference[239] with permission from Wiley.

extracted $V_{\text{OC-imp}}$ is used to determine the internal ideality factor (n_{id}), which reflects both bulk and interfacial recombination properties.[47,232,276–278] In high-performance PSCs that are not limited by recombination at one of the perovskite/CTL interfaces, a reduction in n_{id} towards a value of 1 typically indicates dominant bimolecular radiative recombination and reduced trap-assisted Shockley-Read-Hall recombination.[47,232,278,279] There is a direct correlation between n_{id} and FF, which will be further discussed in Section 4.5. For half-stacks without C_{60} (Figure 4.4c), n_{id} decreases from 1.39 for perovskite films with bromide incorporation in one deposition step ($PbBr_2$ or FABr) to 1.36 for combined bromide incorporation in both deposition steps ($PbBr_2$+FABr), consistent with the observed improvements in PLQY and $V_{\text{OC-imp}}$. A similar trend is observed for half-stacks with C_{60}, where n_{id} drops from 1.56 (FABr) and 1.54 ($PbBr_2$) to 1.52 for the combined bromide incorporation in both deposition steps ($PbBr_2$+FABr). These results suggest that combined bromide incorporation in both deposition steps not only enhances bulk properties but also modestly improves the perovskite/C_{60} interface, with minimal losses at both HTL and ETL interfaces.

4.5 Photovoltaic Performance

To gain further insights into the impact of bromide incorporation strategy on device performance, wide-bandgap PSCs are fabricated in *p-i-n* architecture with the layer stack ITO/NiO_x/2PACz/perovskite/C_{60}/BCP/Ag, as schematically illustrated in Figure 4.2a. The current density-voltage (*J-V*) characteristics of the best-performing cells are displayed in Figure 4.5, while detailed PV parameters are summarized in Table 4.1.

The narrow-bandgap reference perovskite thin film ($E_g \approx 1.55$ eV) with a nominal composition of $MA_{0.07}FA_{0.93}PbI_3$ (labeled as Ref) exhibits a champion PCE of 19.4% and 18.9% in the backward and forward scan, respectively (Table 4.1 and Figure A.2).

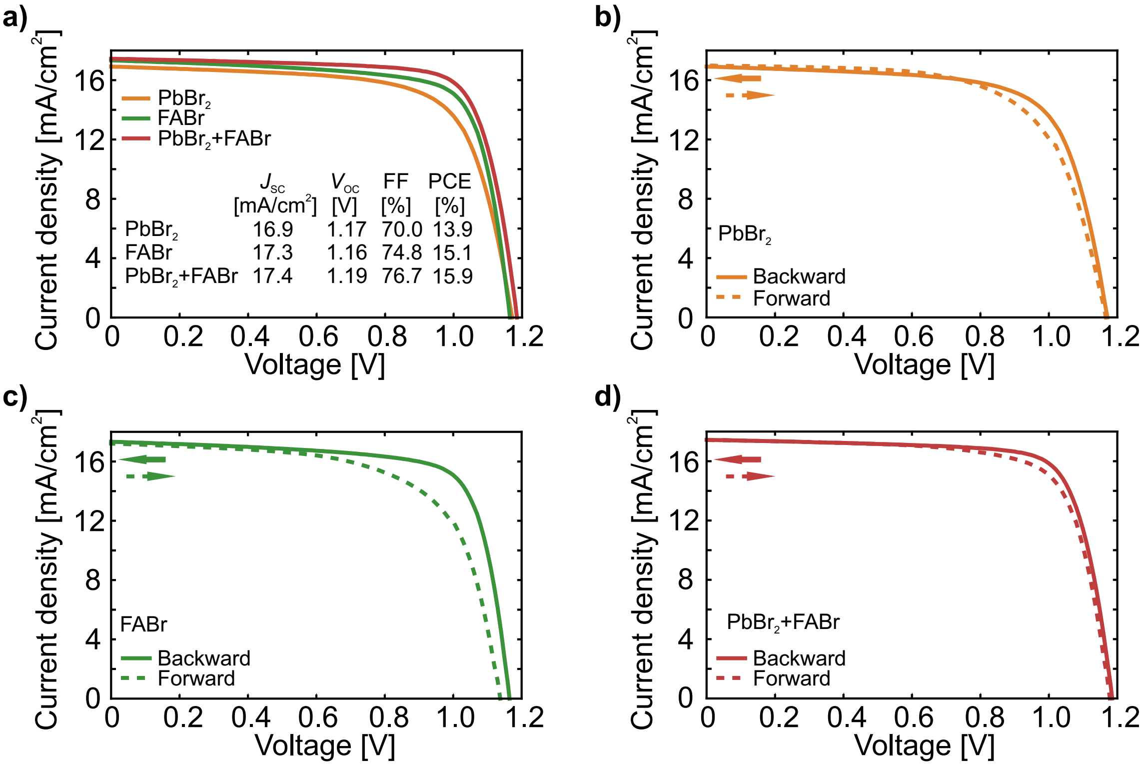

	J_{SC} [mA/cm²]	V_{OC} [V]	FF [%]	PCE [%]
$PbBr_2$	16.9	1.17	70.0	13.9
FABr	17.3	1.16	74.8	15.1
$PbBr_2$+FABr	17.4	1.19	76.7	15.9

Figure 4.5: Current density *versus* voltage (*J-V*) characteristics of the best-performing perovskite solar cells (PSCs) a) for all three bromide incorporation strategies, and with bromide incorporated *via* b) $PbBr_2$, c) FABr, and d) $PbBr_2$ and FABr in both scan directions (backward and forward). Adapted from reference[239] with permission from Wiley.

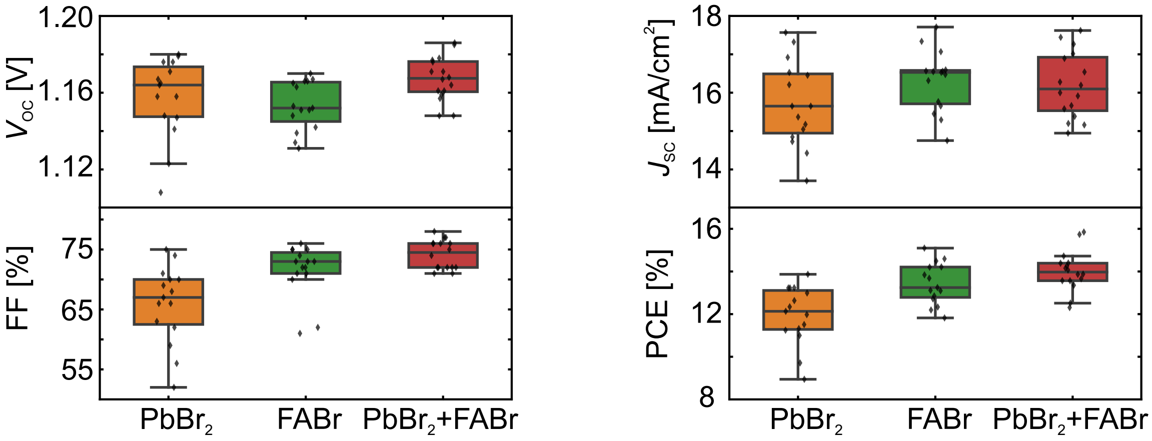

Figure 4.6: Statistical distribution (in total 46 devices) of the open-circuit voltage (V_{OC}), fill factor (FF), short-circuit current density (J_{SC}) and power conversion efficiency (PCE) for opaque perovskite solar cells (PSCs) with bromide incorporated *via* $PbBr_2$, FABr or $PbBr_2$ and FABr. Adapted from reference[239] with permission from Wiley.

Devices fabricated with bromide incorporation *via* $PbBr_2$ in the first deposition step (Figure 4.5b) exhibit the lowest champion efficiency, reaching 13.9% in the backward scan. The corresponding PV parameters are a V_{OC} of 1.17 V, a J_{SC} of 16.9 mA cm^{-2}, and a FF of 70.0%, with slightly reduced values under forward bias. This relatively poor performance is mainly attributed to limited charge-carrier extraction and a moderate FF.

Incorporating bromide *via* FABr in the second deposition step (Figure 4.5c) leads to improvements in FF and J_{SC}, although the V_{OC} shows a slight decrease compared to $PbBr_2$ incorporation in the first deposition step. This results in a champion performance of 15.1% in the backward scan, with corresponding PV values of V_{OC} = 1.16 V, J_{SC} = 17.3 mA cm^{-2}, and FF = 74.8%. However, this bromide incorporation strategy exhibits the most pronounced hysteresis of 16%, which may be attributed to ion migration and defects within the perovskite thin film. These factors can impair charge transport and lead to unstable PSCs, but this hypothesis warrants further study.[280]

Table 4.1: Photovoltaic parameters (open-circuit voltage (V_{OC}), short-circuit current density (J_{SC}), fill factor (FF), power conversion efficiency (PCE) and hysteresis index (HI)) of the champion opaque perovskite solar cells (PSCs) including the reference device ($E_g \approx 1.55$ eV) and the devices with bromide incorporated ($E_g \approx 1.68$ eV) *via* $PbBr_2$, FABr or a combination of $PbBr_2$ and FABr ($PbBr_2$+FABr).

Perovskite name	Scan direction	V_{OC} [V]	J_{SC} [mA cm^{-2}]	FF [%]	PCE [%]	HI [%]
Ref	backward	1.11	22.6	77.8	19.4	2.4
	forward	1.10	22.6	76.1	18.9	
$PbBr_2$	backward	1.17	16.9	70.0	13.9	6.3
	forward	1.17	17.0	65.6	13.0	
FABr	backward	1.16	17.3	74.8	15.1	16.0
	forward	1.14	17.2	64.8	12.7	
$PbBr_2$+FABr	backward	1.19	17.4	76.7	15.9	4.7
	forward	1.18	17.4	73.5	15.1	

The most significant performance improvement is obtained with bromide incorporation in both deposition steps, i.e., *via* $PbBr_2$ in the first and FABr in the second deposition step (Figure 4.5d). This combined bromide incorporation strategy results in the highest device performance, reaching a champion efficiency of 15.9% in the backward scan, with corresponding PV values of V_{OC} = 1.19 V, J_{SC} = 17.4 mA cm^{-2} and FF = 76.7%. Notably, these devices also show reduced hysteresis compared to the other strategies (< 5%), suggesting suppressed defect-assisted ion migration and interfacial charge accumulation. Such hysteresis suppression has been linked to improved long-term operational stability and reduced trap densities at interfaces or within the perovskite bulk.[281] This aspect is not discussed in detail here, but is worth further investigation.

Statistical analysis of the PV parameters across multiple devices (Figure 4.6) confirms the effectiveness of the combined bromide incorporation strategy. Among all PV parameters, the FF shows the most substantial improvement, accompanied by moderate increases in both V_{OC} and J_{SC}. Importantly, the enhancement in V_{OC} cannot be attributed to a shift in the perovskite bandgap, as verified by the derivative of the EQE spectrum (Figure 4.2b). Instead, the increase in V_{OC} is associated with the suppression of non-radiative recombination losses, in agreement with the observed trends in PLQY and $V_{\mathrm{OC\text{-}imp}}$ (Figure 4.4a/b). Additionally, the reduced ideality factor obtained for the combined bromide incorporation strategy (Figure 4.4c/d) correlates strongly with the enhanced FF and V_{OC} in full devices. Despite these advances, the device still exhibits a V_{OC} deficit of approximately 70 mV relative to $V_{\mathrm{OC\text{-}imp}}$ and the J_{SC} remains below 18 mA cm^{-2}. For wide-bandgap PSCs intended for 2T tandem integration, however, achieving a higher V_{OC} – as close as possible to the detailed balance (DB) limit of ≈ 1.38 eV for a bandgap of 1.68 eV – and attaining a J_{SC} exceeding 20 mA cm^{-2} to ensure current matching with the Si bottom cell, are essential for maximizing device performance.[38,39,104] These limitations highlight the need for further improvements through refined compositional engineering and targeted passivation strategies.

A statistical evaluation using *Welch's t test* demonstrates that devices fabricated with bromide incorporation in both deposition steps have a statistically significant increase in FF and PCE compared to those with bromide incorporation in only one deposition step (Table A.8). In addition, the reduced spread in performance metrics for the combined bromide incorporation strategy highlights an improved repeatability and process reliability.

The influence of bromide incorporation strategy on charge-carrier extraction is further examined with EQE and absorption spectra (Figure 4.7). Devices with bromide incorporation in only one deposition step show a significant drop in EQE at short wavelengths compared to the narrow-bandgap reference cells (Figure A.2b), resulting in integrated J_{SC} values of 17.9 mA cm^{-2} ($PbBr_2$) and 17.6 mA cm^{-2} (FABr). This loss is effectively mitigated when bromide is incorporated in both deposition steps ($PbBr_2$+FABr), yielding an enhanced integrated J_{SC} of 18.8 mA cm^{-2}. Given that both the device architecture and the absorption spectra (Figure 4.7b) remain comparable across all bromide incorporation strategies, the observed reduction in EQE for bromide incorporation in one deposition step is likely caused by limited charge-carrier extraction rather than optical losses. The combined bromide incorporation strategy facilitates more efficient charge-carrier extraction, consistent with the high film quality indicated by XRD, SEM, and PLQY analyses. This underscores the role of combined bromide incorporation in mitigating non-radiative recombination losses and improving charge-carrier transport dynamics, ultimately enabling higher device efficiencies.

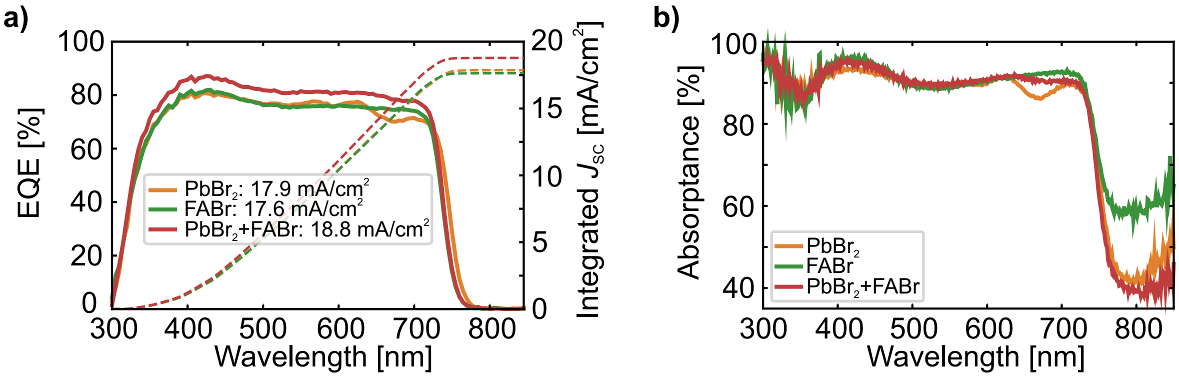

Figure 4.7: a) External quantum efficiency (EQE) spectra as well as the corresponding integrated short-circuit current density (J_{SC}) and b) absorptance spectra for opaque perovskite solar cells (PSCs) with bromide incorporated *via* $PbBr_2$, FABr, or $PbBr_2$ and FABr process. Adapted from reference[239] with permission from Wiley.

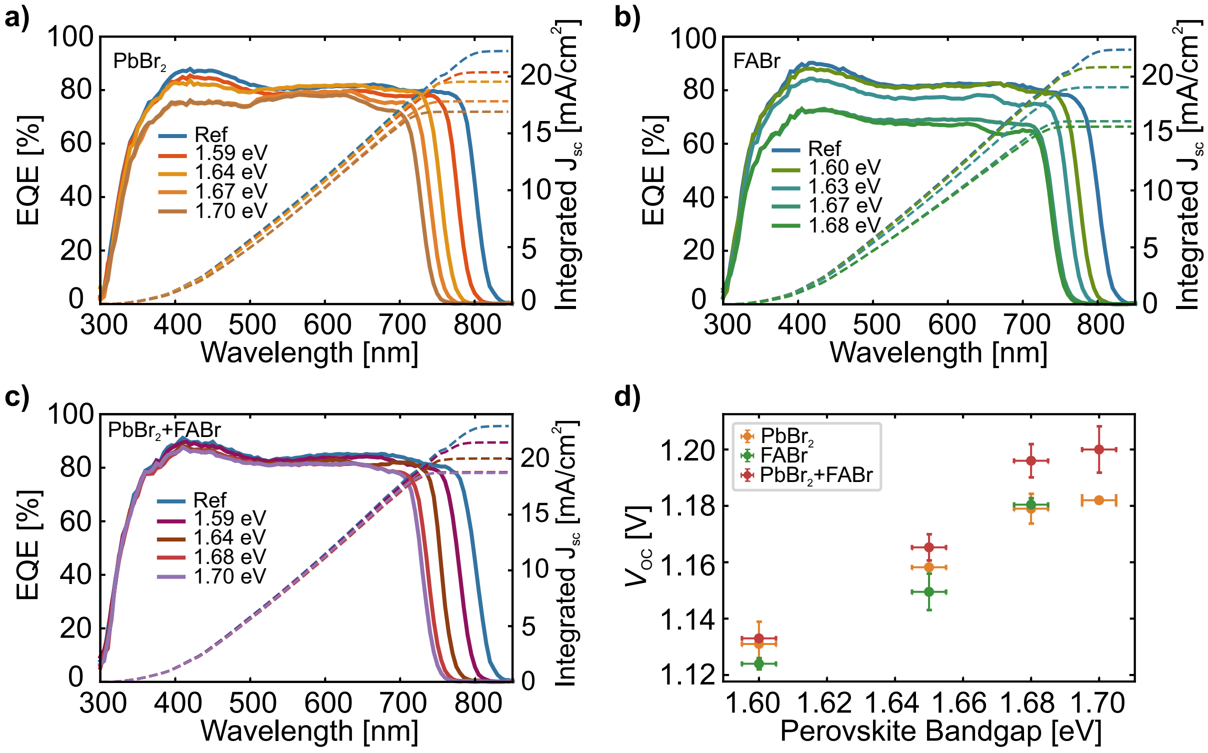

Figure 4.8: External quantum efficiency (EQE) as well as the corresponding integrated short-circuit current density (J_{SC}) of perovskite solar cells (PSCs) with increased bandgap ($E_g \approx 1.59$-$1.70\,\text{eV}$). PSCs without any modification are labeled as Ref ($E_g = 1.55\,\text{eV}$). The bromide is incorporated *via* a) PbBr$_2$, b) FABr or c) PbBr$_2$ and FABr. d) Open-circuit voltage (V_{OC}) as a function of the perovskite bandgap for opaque PSCs with bromide incorporated *via* PbBr$_2$, FABr or PbBr$_2$ and FABr. Adapted from reference[239] with permission from Wiley.

The effect of limited charge-carrier extraction in one-step bromide incorporation becomes even more pronounced when studying devices with bandgaps ranging from 1.55 to 1.70 eV. For bandgaps above 1.6 eV, the EQE loss associated with bromide incorporation in one deposition step becomes increasingly significant. While the incorporation of PbBr$_2$ in the first deposition step primarily reduces the EQE in the short-wavelength region (Figure 4.8a), the incorporation of FABr in the second deposition step leads to a decrease in EQE across the entire spectral range (Figure 4.8b). The short-wavelength EQE drop can be attributed to bromide introduced *via* PbBr$_2$ preferentially integrating in a bulk structure, which may impede the interdiffusion of organic cations during the second deposition step, resulting in incomplete conversion and residual PbI$_2$.[57,58,259,260] In contrast, devices fabricated with the combined bromide incorporation strategy (PbBr$_2$+FABr) maintain high EQE (Figure 4.8c), indicating good charge extraction across the entire spectral range for all bandgaps.

Notably, devices with the combined bromide incorporation strategy also exhibit an improved V_{OC} across all studied bandgaps (1.59 to 1.70 eV) compared to the bromide incorporation in only one deposition step (Figure 4.8d and Figure A.3). This universal trend is attributed to the reduction of non-radiative recombination losses and better energetic alignment of the charge transport interfaces, leading to lower interfacial recombination rates.[102]

Overall, the results show that combined bromide incorporation in both deposition steps significantly improves the device performance. While the achieved efficiency of 15.9% at a bandgap of 1.68 eV remains below state-of-the-art solution-based one-step processed PSCs – with efficiencies exceeding 22% for bandgaps above 1.65 eV[282] – it represented, at the time this study was conducted, one of the highest efficiencies reported for solution-based two-step processed PSCs in the *p-i-n* architecture with a bandgap exceeding 1.65 eV.[57,58,64] It is also worth noting that no additional passivation layers were applied, leaving room for further performance improvements, which will be explored in Chapter 5.

4.6 Summary

This chapter presents the first systematic study of bromide incorporation for fabricating wide-bandgap perovskite thin films using a fully solution-based two-step deposition method. Three distinct bromide incorporation strategies are investigated:

1. Introducing bromide *via* $PbBr_2$ in the first deposition step.
2. Introducing bromide *via* FABr in the second deposition step.
3. A combined bromide incorporation in both deposition steps, i.e., *via* $PbBr_2$ in the first and FABr in the second deposition step.

All three bromide incorporation strategies yield operational PSCs with bandgaps in the target range of 1.66-1.68 eV. Structural and morphological characterization reveals that all bromide incorporation strategies result in perovskite films with comparable crystal orientation and residual PbI_2. However, significant differences emerge in their microstructure and halide distribution. Bromide incorporation *via* $PbBr_2$ induces a more pronounced (111) perovskite crystal orientation and exhibits signs of halide phase segregation, reflected in a double-peak structure of the PbI_2 peak. The combined bromide incorporation strategy leads to the highest film quality, characterized by enlarged grain sizes, reduced pinhole density, and improved crystallinity. Consistently, optoelectronic analysis shows that the combined bromide incorporation strategy improves the quality of the perovskite bulk as well as the interfaces. This is reflected by the highest PLQY and $V_{\text{OC-imp}}$ values and the lowest ideality factor for both with and without ETL. These improvements suggest reduced non-radiative recombination losses in both the bulk and at the interfaces.

Device-level studies in *p-i-n* architecture further confirm the advantages of combined bromide incorporation. While incorporating bromide in only one deposition step results in efficiencies of 13-15%, introducing bromide in both deposition steps yields the best-performing devices, achieving a champion efficiency of 15.9% with minimal hysteresis (HI < 5%). At the time this study was conducted, this efficiency ranked among the highest reported for fully solution-based two-step processed PSCs with bandgaps exceeding 1.65 eV. Statistical analysis validates a significant improvement in FF and V_{OC}, while EQE measurements underline enhanced charge-carrier extraction. Despite these advances, the device still exhibits a V_{OC} deficit of approximately 70 mV relative to $V_{\text{OC-imp}}$ and the J_{SC} remains below 18 mA cm^{-2}. For wide-bandgap perovskite top cells for 2T tandem integration, however, achieving a V_{OC} as close as possible to the DB limit (≈ 1.38 eV for $E_g \approx 1.68$ eV) and reaching a J_{SC} exceeding 20 mA cm^{-2} – to ensure current matching with the Si bottom cell – are essential for maximizing device performance.[38,39,104] To tackle these remaining limitations, refined compositional engineering and targeted passivation strategies are addressed in Chapter 5.

Expanding the analysis across a bandgap range of 1.59 to 1.70 eV reveals that the combined bromide incorporation strategy is universally advantageous, independent of the bandgap. Devices fabricated with this strategy consistently show reduced non-radiative recombination losses and improved charge-carrier extraction. These improvements are likely due to a more effective bromide incorporation and enhanced conversion to the photoactive perovskite phase when bromide is introduced in both deposition steps. However, the mechanistic details require further investigation beyond the scope of this thesis.

In conclusion, this chapter establishes a clear link between bromide incorporation strategy (research question **I**), perovskite film quality (research question **II**), and device performance. Among the bromide incorporation strategies investigated, combined bromide incorporation in both deposition steps emerges as the most effective route for fabricating wide-bandgap perovskite thin films ($E_g \approx 1.68$ eV) with superior optoelectronic properties and reduced non-radiative recombination losses. This strategy provides a solid foundation for future optimizations of wide-bandgap perovskite thin films and its interfaces, and for its integration into 2T perovskite/Si TSCs, which are further explored in Chapter 5. In addition, the understanding of bandgap engineering in two-step deposition methods developed in this chapter underpins subsequent work in the field, including the advancement of a solution-based two-step slot-die coating process by Geistert *et al.*[70] and the further refinement of the perovskite thin film by Cui *et al.*[283] and Luo *et al.*[284] using advanced passivation strategies.

5 Perovskite Thin-Film Optimization for Enhanced Efficiency and Stability toward Tandem Integration

*Wide-bandgap perovskite thin films are crucial for high-efficiency two-terminal perovskite/silicon tandem solar cells, where both current matching between the subcells and high open-circuit voltages are required to reach maximal device performance. Despite rapid progress in tandem photovoltaics, the industrial implementation of wide-bandgap perovskite solar cells remains limited by voltage losses, insufficient long-term operational stability, and challenges associated with reliable film coverage on industrially relevant textured silicon bottom cells. Although the two-step deposition method offers compatibility with textured substrates and scalable processing, voltage losses and device stability issues remain critical and are strongly linked to the microstructural quality of the perovskite thin film and to defect-induced non-radiative recombination losses in the perovskite bulk and at perovskite/charge transport layer interfaces. Building on the wide-bandgap perovskite thin film developed in Chapter 4, this chapter advances additive and interface engineering strategies for a fully solution-based two-step deposition route (research question **III**). Because effective passivation strategies for solution-based two-step processed wide-bandgap perovskite thin films remain comparatively underexplored, particular emphasis is placed on understanding how these strategies influence film crystallization, defect passivation, and charge-carrier extraction (research question **II**). Together, these insights provide a comprehensive understanding of the key parameters that allow the fully solution-based two-step method to be precisely tuned for reliable, high-performance, and stable wide-bandgap perovskite solar cells (research question **V**). Finally, the optimized perovskite thin film is integrated into a two-terminal perovskite/silicon tandem architecture to evaluate its compatibility with different silicon surface textures (research question **IV**). By analyzing surface coverage and optoelectronic properties on both planar and textured silicon bottom cells, this chapter connects fundamental materials engineering to the practical requirements of industrial silicon photovoltaics. In doing so, it strengthens the pathway from laboratory-scale perovskite thin-film optimization toward manufacturable, high-performance two-terminal perovskite/silicon tandem technology.*

Parts of this chapter review the published research article "Bandgap Engineering of Two-Step Processed Perovskite Top Cells for Perovskite-Based Tandem Photovoltaics" in *Advanced Functional Materials* 34.9 (2024) by *R. Pappenberger (R.P.)* as first author, together with *A. Diercks*, *J. Petry*, *S. Moghadamzadeh*, *P. Fassl*, and *U. W. Paetzold*[239] and the published research article "Versatile Two-Step Process for Perovskite-Based Tandem Photovoltaics" in *Solar RRL* 9.13 (2025) by *R. Pappenberger* as first author, together with *R. Singh*, *A. Diercks*, *T. Zhao*, *R. Pesch*, *J. Petry*, *D. Baumann*, *X. Liu*, and *U. W. Paetzold*.[285] Some figures in this chapter were adapted from reference[239] and reference[285] with permission from Wiley.
R.P. contributed to both projects by conceptualizing the study, leading experimental investigations, data curation, formal analysis, and visualization, as well as writing the original draft of the manuscript. The contributions of all authors involved in this study are listed in Table A.3 and Table A.4 according to the CRediT system.

5.1 Motivation

Achieving high-efficiency 2T perovskite/Si TSCs requires wide-bandgap perovskite thin films with sufficiently high J_{SC} for current matching with the silicon bottom cell and minimal non-radiative recombination losses to maximize the V_{OC}. Despite rapid progress in tandem PV, wide-bandgap PSCs continue to face substantial limitations for industrial implementation, including pronounced voltage deficits, restricted long-term operational stability, and challenges associated with reliable and defect-free film coverage on industrially relevant textured silicon bottom cells.[286] Although the two-step deposition method is well suited for improved film coverage and scalable manufacturing, voltage losses and device stability issues remain critical and originate predominantly from defect-assisted non-radiative recombination in the perovskite bulk and at perovskite/CTL interfaces.

Among the perovskite/CTL interfaces, the perovskite/ETL interface is particularly critical in *p-i-n* devices. C_{60}, the most commonly used ETL material, suffers from energy-level mismatch and defect-induced recombination due to dangling bonds.[103,112,287,288] In parallel, bulk defects – often concentrated at grain boundaries – facilitate ion migration and accelerate degradation under illumination and thermal stress.[289–296] Addressing both interfacial and bulk non-radiative recombination pathways is therefore crucial for achieving high V_{OC}, improved long-term operational stability, and overall high tandem performance.

A common strategy to reduce non-radiative recombination losses at the perovskite/C_{60} interface is the post-treatment of the perovskite film.[106,297–299] Thin LiF layers (≈ 1 nm) are among the most widely used physical surface passivation materials due to the compatibility with various perovskite compositions and straightforward implementation *via* thermal evaporation.[47,48,100,102,288,300–304] LiF can act as a field-effect passivator, likely compensating for the high defect density in the first monolayers of C_{60}, thereby enabling a higher V_{OC} and improved device performance.[288] However, recent studies indicate that LiF-based surface passivation can negatively impact the long-term operational stability of PSCs,[47,97,300,305] underscoring the need for alternative passivation strategies that provide high efficiencies without sacrificing stability – still one of the key challenges limiting the commercialization of PSCs.[123,306–308]

In response, various chemical and field-effect passivation strategies have been proposed. Liu *et al.*[112] introduced a bimolecular passivation strategy, combining diammonium ligands and monoammonium ligands. The diammonium ligands provide field-effect passivation: One $-\mathrm{NH}_3^+$ group anchors to the perovskite surface, while the other extends outward, forming a surface dipole that induces n-type doping. This surface dipole repels hole carriers from the interface, thereby effectively suppressing non-radiative recombination losses.[112,309–312] Monoammonium ligands complement this effect by providing chemical passivation, which reduces further surface recombination. While physical passivation suppresses non-radiative recombination by forming energy barriers or insulating interlayers that prevent carriers from reaching defects, chemical passivation directly neutralizes defect sites through specific interactions or bonding, thereby eliminating their electronic activity.[313]

Passivation strategies are not limited to perovskite interfaces. Bulk passivation is equally important for suppressing non-radiative recombination, particularly at grain boundaries. A widely used strategy is the incorporation of large organic cations that induce the formation of 2D perovskite phases within the 3D matrix. Bulky monoammonium cations, for example, form 2D Ruddlesden-Popper (RP) phase perovskites within the 3D perovskite.[97,107,314–322] These 2D layers are held together by weak van der Waals interactions, which, while effective in passivating defects, can compromise structural stability. Moreover, the resulting deep quantum wells hinder efficient charge transport across the 2D layers.[126,153,156,157] By incorporating diammonium cations in the 3D perovskite, 2D Dion-Jacobson (DJ) phase perovskites can be formed, where adjacent layers are connected *via* hydrogen bonding. The stronger interlayer interaction enhances structural stability and facilitates charge transfer.[153–155] However, DJ-type perovskites are less tolerant to lattice distortions, particularly in FA-based perovskite films. The large FA cations distort the Pb-I octahedra and the integration of rigid diammonium spacer cations into the already strained lattice can introduce additional defects.[323] Combining RP- and DJ-type spacer cations provides a strategy to balance defect tolerance, structural rigidity, and structural stability. This strategy leverages the defect passivation benefits of RP-phases with the enhanced stability and charge transport of DJ-phases, offering a promising route toward more robust and efficient perovskite films.[153]

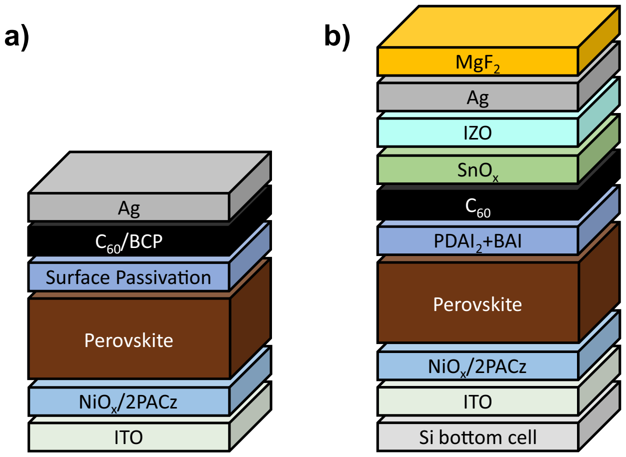

Figure 5.1: Schematic of the a) perovskite solar cell (PSC) architecture (*p-i-n*) and b) two-terminal (2T) perovskite/silicon (Si) tandem solar cell (TSC) architecture used in this chapter. Adapted from reference[285] with permission from Wiley.

While such interface and bulk passivation strategies have demonstrated promising results in conventionally one-step processed perovskite solar cells, their applicability to fully solution-based two-step deposition routes – especially for wide-bandgap perovskite compositions – remains insufficiently explored. Due to the stepwise conversion to the final perovskite phase, the two-step deposition method fundamentally differs from conventional one-step deposition, necessitating a re-evaluation of established passivation concepts.

Beyond interface and bulk passivation, the perovskite composition itself plays a decisive role in long-term device stability. Incorporating Cs – which is smaller than the other commonly used A-site cations MA and FA – into the perovskite lattice enhances both structural and thermal stability by suppressing phase impurities, improving crystallinity, and reducing defect densities.[324,325] In contrast, perovskite compositions containing MA – despite often achieving the highest PCEs – are particularly susceptible to thermal degradation, which compromises long-term operational stability and limits their suitability for industrial applications. These composition-dependent stability constraints have intensified efforts toward developing MA-free perovskite thin films that combine high efficiency with robust thermal and operational stability.[320,326–330]

This chapter presents compositional engineering and passivation strategies for fully solution-based two-step processed wide-bandgap perovskite thin films aimed at improving both the quality of the perovskite bulk and the perovskite/C_{60} interface, building on the wide-bandgap perovskite thin film developed in Chapter 4 with the nominal composition $MA_{0.07}FA_{0.93}Pb(I_{0.78}Br_{0.22})_3$ ($PbBr_2$+FABr).

Section 5.2 of this chapter introduces Cs *via* CsI into the perovskite composition, resulting in a nominal perovskite composition of $Cs_{0.16}MA_{0.06}FA_{0.78}Pb(I_{0.79}Br_{0.21})_3$. In parallel, a surface passivation layer using standard evaporated LiF is applied at the perovskite/C_{60} interface. This section includes a comprehensive material characterization of the resulting perovskite films, examining crystallinity, morphology, and optoelectronic properties. The study concludes with the implementation of the optimized perovskite thin film at the device level, using the following layer stack ITO/NiO_x/2PACz/perovskite/LiF/C_{60}/BCP/Ag (Figure 5.1a). Section 5.3 presents additional compositional engineering and passivation strategies to address long-term operational stability and device performance. This includes adjusting the perovskite composition from a triple-cation to a MA-free double-cation (nominal perovskite composition: $Cs_{0.16}FA_{0.84}Pb(I_{0.79}Br_{0.21})_3$), eliminating MA from the perovskite lattice. In addition, the LiF surface passivation layer is replaced by a dual bimolecular passivation strategy using a combination of propane-1,3-diammonium iodide ($PDAI_2$) – acting as field-effect passivator – and n-butylammonium iodide (BAI) – a commonly used chemical passivating agent.[331,332] These molecules are not only used at the perovskite/C_{60} interface for surface passivation but also incorporated into the organic cation solution to serve as a bulk passivation agents. This dual bimolecular passivation strategy is systematically investigated through material characterization and the section concludes with the integration of the optimized passivation strategy into device architecture (Figure 5.1a) to examine its impact on operational stability and device performance of wide-bandgap PSCs. Section 5.4 advances the material-level analysis by using X-ray photoelectron spectroscopy (XPS) to investigate the impact of LiF and $PDAI_2$+BAI as surface passivation strategies. Finally, Section 5.5 demonstrates the integration of the optimized perovskite thin film into a 2T perovskite/Si tandem architecture (Figure 5.1b). This section explores the compatibility of the fully solution-based two-step deposition method with both planar and textured Si bottom cells, focusing on surface coverage and light management.

5.2 Optimization with CsI and LiF

This section investigates compositional engineering and surface passivation of fully solution-based two-step processed PSCs developed in Chapter 4, targeting high PCEs and a J_{SC} suitable for current matching in 2T tandem integration. Here, wide-bandgap PSCs with combined bromide incorporation in both deposition steps ($PbBr_2$+FABr, now labeled as Control) serve as the baseline perovskite thin film. The data for the Control devices are taken from Chapter 4, and no additional measurements are performed. For compositional engineering, an optimized amount of CsI (7 mol% CsI, Figure A.4) is added to the inorganic precursor solution, thereby modifying the nominal perovskite composition from a double-cation ($MA_{0.07}FA_{0.93}Pb(I_{0.78}Br_{0.22})_3$) to a triple-cation ($Cs_{0.16}MA_{0.06}FA_{0.78}Pb(I_{0.79}Br_{0.21})_3$) perovskite thin film. For surface passivation, a thin layer of evaporated LiF (1 nm) is applied to improve interfacial quality (Figure 5.2).

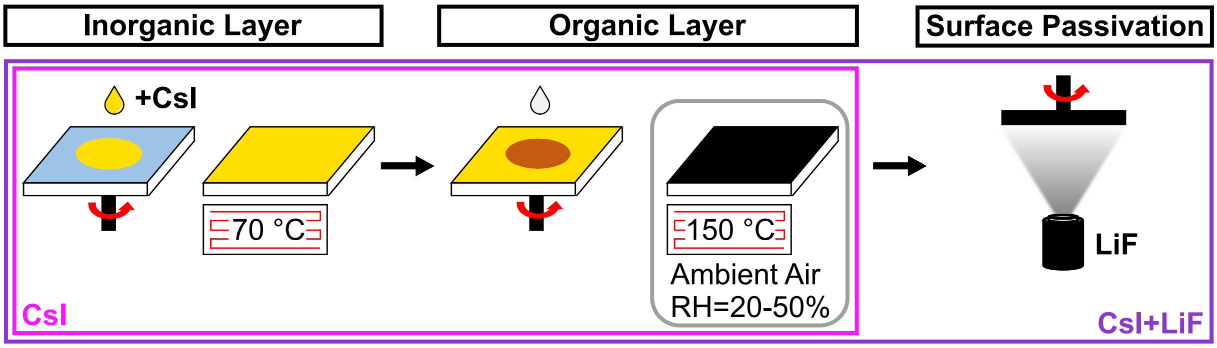

Figure 5.2: Schematic illustration of the fully solution-based two-step deposition method for fabrication of wide-bandgap perovskite films with added CsI in the inorganic precursor solution (labeled as CsI) and with additional LiF as surface passivation (labeled as CsI+LiF) used in this section. All perovskite films are based on the developed recipe with bromide incorporation *via* a combination of $PbBr_2$ and FABr in the first and second deposition step introduced in Chapter 4, now labeled as Control. The perovskite film is annealed under ambient conditions with a relative humidity (RH) of ≈ 20-50%.

5.2.1 Microstructure Analysis

To gain insights into the crystallinity and surface morphology of the perovskite layer, microstructural analysis is performed using XRD and SEM measurements on half-stacks with the architecture ITO/NiO_x/2PACz/perovskite. Even to the naked eye, the Control inorganic scaffold without CsI appears noticeably more reflective than the CsI-containing counterpart, pointing to an increased surface roughness of the CsI-containing inorganic scaffold (Figure A.5a). This observation is supported by AFM measurements (Figure A.6a), which reveal that inorganic scaffolds containing CsI exhibit a root-mean-square (RMS) surface roughness 1.6 times higher than that of the Control films (31.5 nm and 19.9 nm, respectively). Interestingly, the perovskite films display comparable RMS surface roughness values, with 23.0 nm for the Control films and 22.0 nm for the CsI-containing films (Figure A.6b).

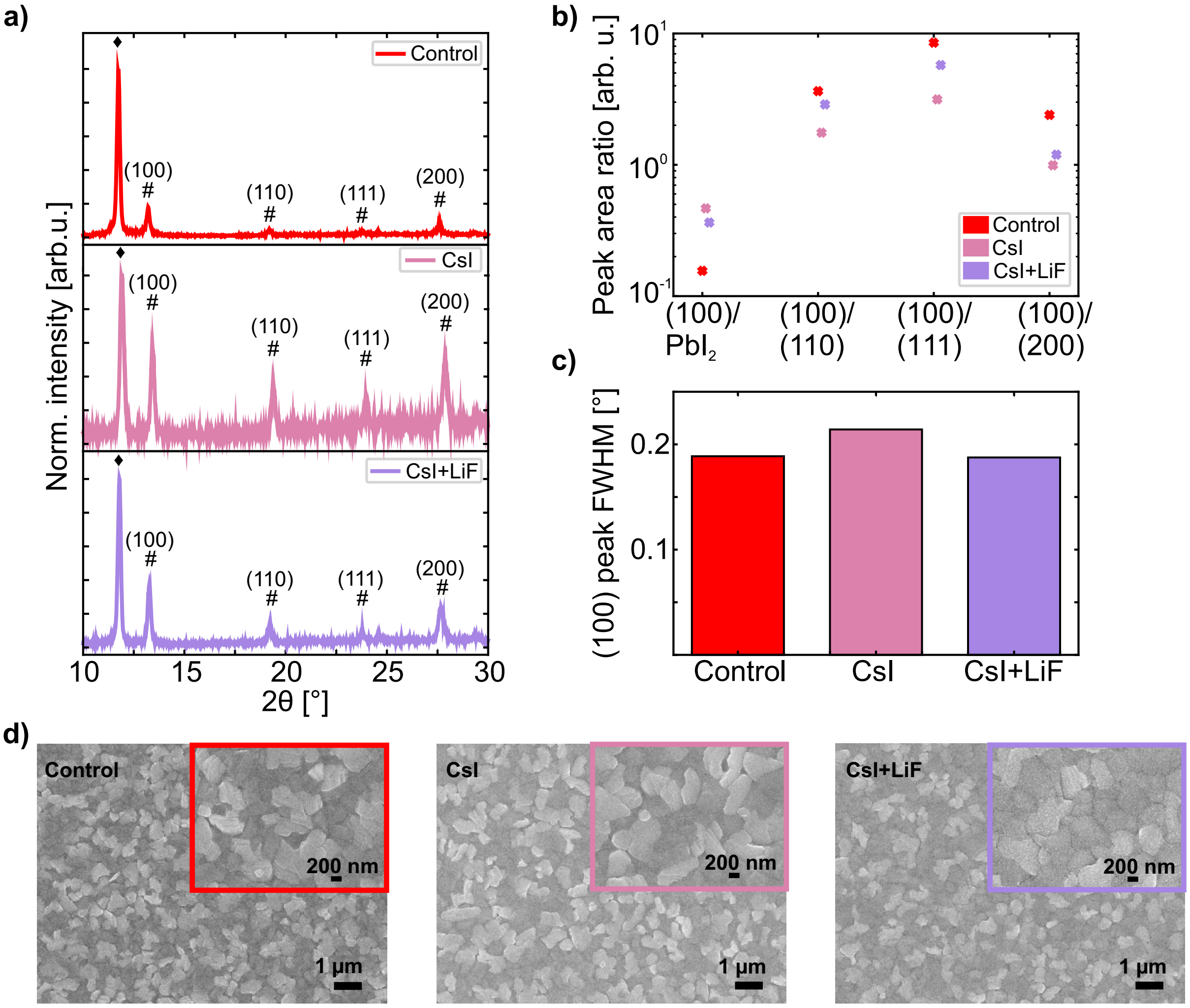

Figure 5.3: a) X-ray diffraction (XRD) patterns (◆ denotes the (001) PbI_2 phase and # the perovskite phase), b) peak area ratios, c) the full width at half maximum (FWHM) of the (100) perovskite peak and d) top-view scanning electron microscopy (SEM) images of the perovskite films (bromide incorporated *via* $PbBr_2$ and FABr) without any further modification (Control), with additional CsI (CsI) and with additional CsI and LiF (CsI+LiF) fabricated on glass/indium tin oxide (ITO)/NiO_x/2PACz. Adapted from reference[239] with permission from Wiley.

The XRD patterns of perovskite films with and without CsI (Figure 5.3a/b) reveal that CsI incorporation slightly modifies the crystal orientation. Diffraction peaks corresponding to the (110), (111), and (200) planes of the cubic perovskite phase become more pronounced relative to the (100) perovskite plane. This trend aligns with literature reports, which indicate that highly Cs-doped perovskites generally favor orientation along the (110) plane.[333,334] Interestingly, this effect appears to be slightly mitigated by surface passivation with LiF. Beyond influencing crystal orientation, CsI incorporation significantly reduces the amount of residual PbI_2, suggesting improved conversion to the photoactive perovskite phase – an observation supported by previous studies.[335–338] Zhou *et al.*[336] attributed this to the formation of a PbX_2-DMSO-CsI intermediate phase, which suppresses PbI_2 crystallization and enhances infiltration of the organic cation solution in the inorganic scaffold, thereby promoting perovskite conversion. This improved perovskite conversion is also visually apparent (Figure A.5b): CsI-containing perovskite films exhibit a darker appearance, while Control films show a reddish color. It is noted that adding LiF as surface passivation does not result in a visible color change, suggesting that its influence on optical properties is minimal.

Analysis of the FWHM of the (100) perovskite diffraction peak (Figure 5.3c) indicates only minor differences in crystallinity among the perovskite films. Compared to the Control films (0.19°), CsI-containing films exhibit a slightly broader peak (0.21°), whereas films with CsI in the bulk and LiF as surface passivation show an FWHM similar to the Control films (0.19°).

SEM images (Figure 5.3d) support the findings from XRD, revealing subtle differences in surface morphology. Addition of CsI leads to a slightly reduced density of bright grains, which are associated with PbI_2-rich crystallites,[97] consistent with the reduced residual PbI_2 observed in XRD. Furthermore, CsI incorporation results in slightly enlarged grain sizes (412 nm, Figure A.7). Applying a thin layer of LiF as surface passivation leads to a more defined surface morphology, with grain sizes similar to the Control films (≈ 360 nm).

Microstructural analysis indicates a change in crystal orientation and improved conversion to the photoactive perovskite phase for perovskite films with incorporated CsI. LiF as surface passivation has only a minor impact on the morphology and crystal structure.

5.2.2 Optoelectronic Properties

To gain deeper insights into non-radiative recombination losses and to evaluate the quality of the perovskite bulk and its interfaces, PLQY measurements along with internal quasi-Fermi level splitting (QFLS) are performed. From the QFLS, the implied open-circuit voltage ($V_{\text{OC-imp}}$) is determined.

Two types of half-stacks are studied: one without ETL, consisting of ITO/NiO_x/2PACz/perovskite, and one with C_{60} as the ETL (ITO/NiO_x/2PACz/perovskite/C_{60}). First, half-stacks without C_{60} are investigated (Figure 5.4a/b), which allow for the evaluation of non-radiative recombination at the HTL/perovskite interface and within the bulk,

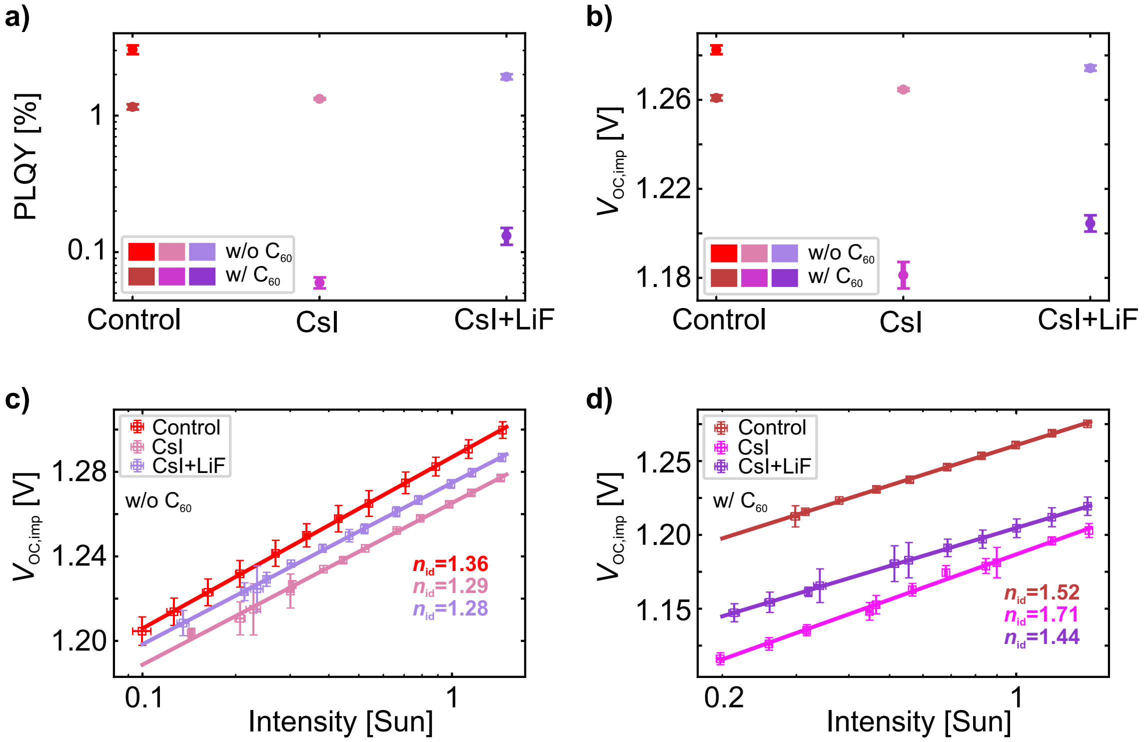

Figure 5.4: a) Photoluminescence quantum yield (PLQY), b) the obtained implied V_{OC} ($V_{\text{OC-imp}}$), and the ideality factor (n_{id}) extracted from a fit to the $V_{\text{OC-imp}}$ (derived from intensity-dependent PLQY measurements) measured c) without and d) with C_{60} electron transport layer (ETL) of the perovskite films (bromide incorporated *via* $PbBr_2$ and FABr) without any further modification (Control), with additional CsI (CsI) and with additional CsI and LiF (CsI+LiF) fabricated on glass/indium tin oxide (ITO)/NiO_x/2PACz. PLQY is measured from the hole transport layer (HTL) side. For each parameter, several perovskite films are measured, and the corresponding mean and standard deviation are plotted. Adapted from reference[239] with permission from Wiley.

and its potential impact on the V_{OC} of the final device. This configuration provides valuable insights into the intrinsic quality of the perovskite layer.[102,232,273] As discussed in Chapter 4, Section 4.4, Control devices exhibit high average PLQY and $V_{OC\text{-imp}}$ values, indicating a high optoelectronic quality of the perovskite thin film. Upon incorporation of CsI, both PLQY and $V_{OC\text{-imp}}$ decrease, indicating less favorable bulk properties. This reduction is only marginally mitigated by the implementation of LiF as surface passivation layer, and the PLQY value is not fully restored.

The PLQY reduction becomes even more pronounced when C_{60} is added as ETL. For CsI-containing perovskite films, the PLQY values drop by more than one order of magnitude and show only a slight improvement with LiF as surface passivation, hinting towards high interfacial recombination losses. Surface passivation with LiF does not substantially enhance the perovskite/C_{60} interface, which is somewhat unexpected.

As previously noted in Chapter 4, PLQY values can be influenced by residual PbI_2.[274] XRD analysis reveals a reduced amount of residual PbI_2 in CsI-containing perovskite films, which may lead to lower PLQY values and thus to potentially misleading interpretations regarding optoelectronic properties.

To address this, the internal ideality factor (n_{id}), extracted from the intensity-dependent $V_{OC\text{-imp}}$, is considered for validation (Figure 5.4c/d), as it remains unaffected by residual PbI_2. For half-stacks without C_{60} (Figure 5.4c), n_{id} is reduced from 1.36 for Control films to 1.29 for CsI films and 1.28 for CsI films with LiF as surface passivation. This suggests improved bulk properties of CsI-containing perovskite films, contrary to the trends observed in PLQY and $V_{OC\text{-imp}}$. A reduction in bulk defect density together with an increase in grain size has been reported in the literature for CsI incorporation into the inorganic precursor solution.[335,336,338] However, upon adding C_{60} as ETL, CsI-containing perovskite films exhibit a significantly increased n_{id} of 1.71 compared to 1.52 of the Control films (Figure 5.4d), indicating deteriorating interface properties with increased non-radiative recombination losses. This can most likely be associated with the increased surface roughness and a modified surface chemistry of the CsI-containing films. Applying a thin layer of LiF as surface passivation improves the properties of the perovskite/C_{60} interface, thus reducing the ideality factor to its lowest obtained value of 1.44.

These findings indicate that while CsI incorporation enhances the bulk properties of the perovskite, it adversely affects the perovskite/C_{60} interface. This detrimental interfacial effect can be mitigated by applying LiF as a surface passivation layer. The data further highlights that relying solely on PLQY values may lead to inaccurate conclusions regarding bulk and interfacial quality, due to their sensitivity to residual PbI_2.

5.2.3 Photovoltaic Performance

In a final step, PSCs are fabricated in *p-i-n* architecture with the layer stack ITO/NiO_x/2PACz/perovskite/LiF/C_{60}/BCP/Ag to investigate the influence of CsI incorporation in combination with LiF as surface passivation (Figure 5.1a). Incorporating an optimized concentration of CsI (7 mol% CsI) into the inorganic precursor solution results in a significant increase in the J_{SC} by an average of 2-3 mA cm^{-2} compared to the Control devices (Figure 5.5 and Figure 5.6a), representing a meaningful improvement according to commonly applied PV performance criteria.[339] This trend is already evident during CsI content optimization (Figure A.4), highlighting that the primary benefit of CsI incorporation lies in the enhancement of the J_{SC}. EQE measurements further support this observation, showing an improved spectral response across the entire wavelength range for CsI-containing PSCs (Figure 5.6d). Notably, the enhancement observed in the EQE spectrum cannot be attributed to increased optical absorption (Figure A.8a), but is associated with improved charge-carrier extraction. This improvement is likely due to the reduced amount of residual PbI_2 (Figure 5.3a/b), which otherwise can act as an insulating layer and hinder charge transport – as observable in the Control devices. Additionally, the enlarged grain sizes in CsI-containing films observed in SEM measurements may further facilitate charge-carrier extraction (Figure A.7b).[340,341] Such improvements in short-circuit current density are particularly beneficial for current matching in 2T perovskite/Si TSCs, where the subcells operate in series and the tandem current is limited by the subcell with the lowest current.[342]

While the incorporation of CsI in the perovskite bulk leads to a notable increase in J_{SC}, it simultaneously results in a significant reduction in V_{OC} by an average of 30-40 mV compared to the Control devices (Figure 5.5 and Figure 5.6a).

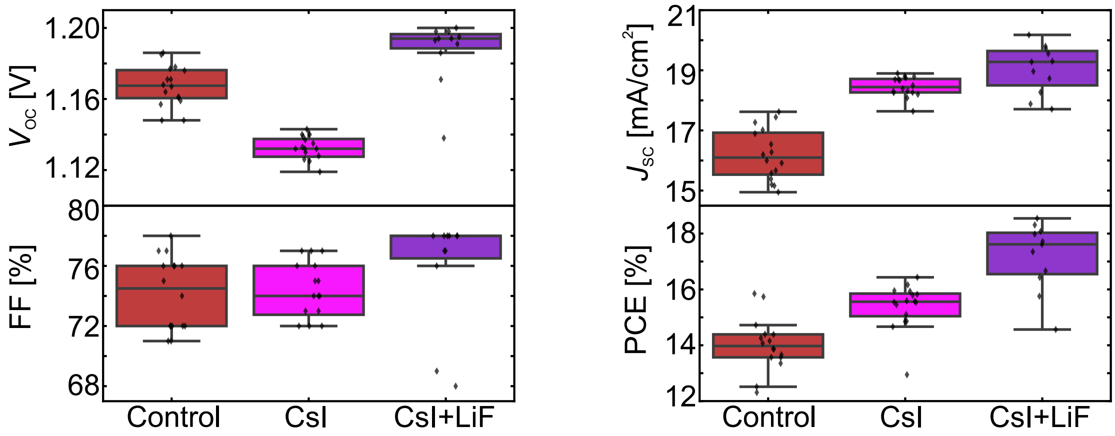

Figure 5.5: Statistical distribution (in total 43 devices) of the open-circuit voltage (V_{OC}), fill factor (FF), short-circuit current density (J_{SC}) and power conversion efficiency (PCE) for opaque perovskite solar cells (PSCs) (bromide incorporated *via* $PbBr_2$ and FABr) without any further modification (Control), with additional CsI (CsI) and with additional CsI and LiF (CsI+LiF). Adapted from reference[239] with permission from Wiley.

This reduction in V_{OC} is consistent with increased non-radiative recombination losses at the perovskite/C_{60} interface observed in PLQY measurements (Figure 5.4d). The observed V_{OC} loss may also be linked to the reduced amount of residual PbI_2, which is known to improve band alignment and passivate interfacial defects, thereby enabling higher V_{OC}. Consequently, an optimal balance of residual PbI_2 appears crucial to achieving the best trade-off between J_{SC} gain and V_{OC} loss.

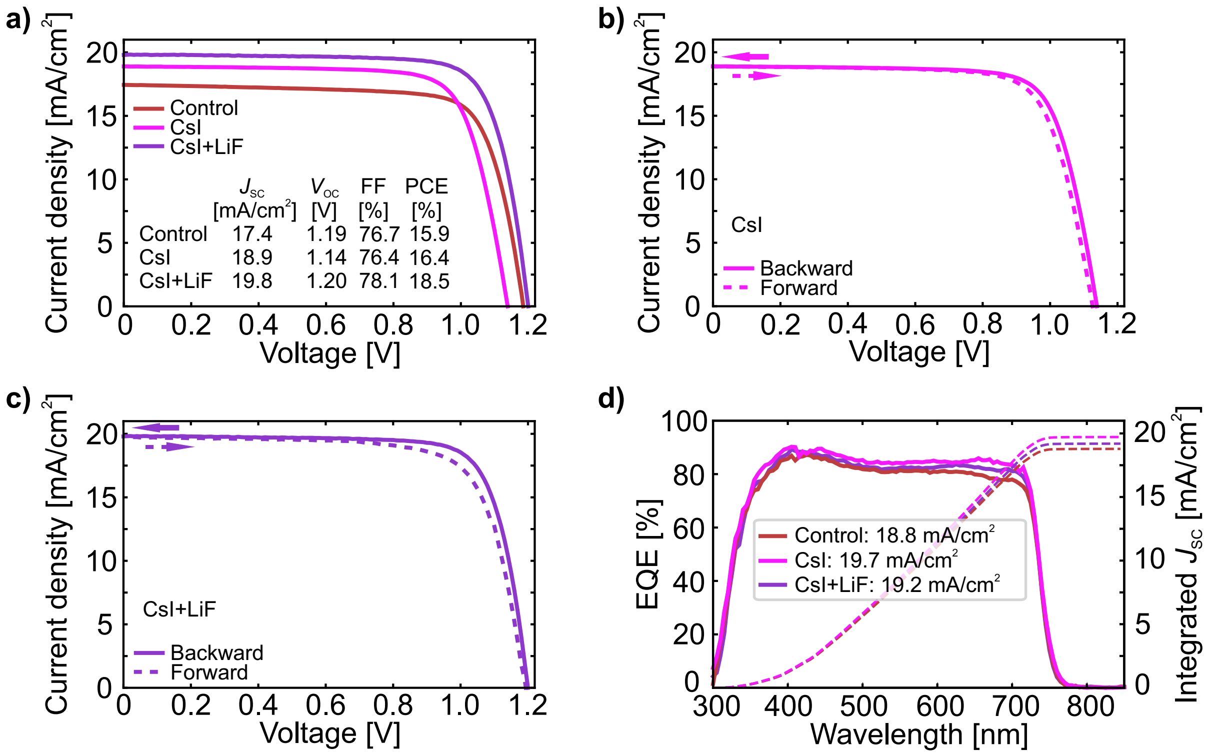

Figure 5.6: Current density *versus* voltage (*J*-*V*) characteristics of the best-performing perovskite solar cells (PSCs) a) for all parameters to facilitate comparison, and b) with additional CsI (CsI), and c) with additional CsI and LiF (CsI+LiF) in both scan directions (backward and forward). d) External quantum efficiency (EQE) spectra as well as the corresponding integrated short-circuit current density (J_{SC}). Adapted from reference[239] with permission from Wiley.

To mitigate the loss in V_{OC} while preserving the improved J_{SC}, 1 nm of LiF is applied as a surface passivation. This strategy successfully recovers and even enhances the V_{OC} by an average of 20-30 mV compared to the Control devices (Figure 5.6a and Figure 5.5). As a result, the PCE of the champion devices increases from 15.9% for the Control PSCs, to 16.4% for the CsI PSCs and to 18.5% for the CsI+LiF PSCs with the exact PV parameters listed in Table 5.1. The enhancement in V_{OC} and FF for the devices with CsI and LiF is consistent with the lowest obtained n_{id} of 1.44 (Figure 5.4d, with ETL interface), indicating improved interfacial properties. It should be noted that the enhancement in V_{OC} does not correspond to an increase in the perovskite bandgap (Figure A.8b).

A short-term stability study (5 min MPP tracking) shows that this combination does not impair short-term operational stability (Figure A.8c). However, literature reports indicate that LiF may negatively affect long-term operational stability.[47,97,305] Therefore, Section 5.3 explores alternative surface passivation strategies that maintain performance without compromising stability.

Table 5.1: Photovoltaic parameters (open-circuit voltage (V_{OC}), short-circuit current density (J_{SC}), fill factor (FF), power conversion efficiency (PCE) and hysteresis index (HI)) of the wide-bandgap ($E_g \approx 1.68$ eV, bromide incorporation *via* $PbBr_2$+FABr) champion opaque perovskite solar cells (PSCs) with added CsI and a combination of CsI and LiF (CsI+LiF).

Perovskite name	Scan direction	V_{OC} [V]	J_{SC} [mA cm^{-2}]	FF [%]	PCE [%]	HI [%]
Control	backward	1.19	17.4	76.7	15.9	4.7
	forward	1.18	17.4	73.5	15.1	
CsI	backward	1.14	18.9	76.4	16.4	3.0
	forward	1.13	18.9	75.0	15.9	
CsI+LiF	backward	1.20	19.8	78.1	18.5	6.1
	forward	1.19	19.8	73.9	17.4	

Performing a *Welch's t test* (Table A.9) confirms a statistically significant improvement in J_{SC} and V_{OC} for the devices with CsI in the bulk and LiF as surface passivation.

Overall, the results demonstrate that PSCs with CsI in the bulk and LiF as a surface passivation layer benefit from both enhanced J_{SC}, due to improved charge-carrier extraction resulting from reduced residual PbI_2 at the HTL/perovskite interface, and an increased V_{OC}, enabled by the passivating effect of LiF at the perovskite/ETL interface. While the achieved efficiency of 18.5% at a bandgap of 1.68 eV remains below state-of-the-art solution-based one-step processed PSCs – with efficiencies exceeding 22% for bandgaps above 1.65 eV[282] – it represented the highest efficiency reported for solution-based two-step processed PSCs in the *p-i-n* architecture with a bandgap beyond 1.65 eV at the time this study was conducted.[57,58,64]

5.3 Dual Bimolecular Passivation Strategy

To improve long-term operational stability, MA is removed from the perovskite lattice, and an alternative surface passivation method to LiF is required. This section therefore investigates compositional engineering, as well as bulk and surface passivation, to improve device performance and long-term operational stability of the fully solution-based two-step processed PSCs developed in Section 5.2.

Here, triple-cation PSCs with CsI in the bulk and LiF as surface passivation serve as the baseline perovskite thin film (CsI+LiF, Figure 5.7a, labeled now as TC). Replacing MAI with FAI in the perovskite organic precursor solution results in a double-cation perovskite film with the nominal composition $Cs_{0.16}FA_{0.84}Pb(I_{0.79}Br_{0.21})_3$ (Figure 5.7b, labeled as DC). The addition of MACl in the organic cation solution improves the crystallization of the perovskite film and evaporates in the final annealing step.[209] For the DC perovskite film, LiF is used as standard surface

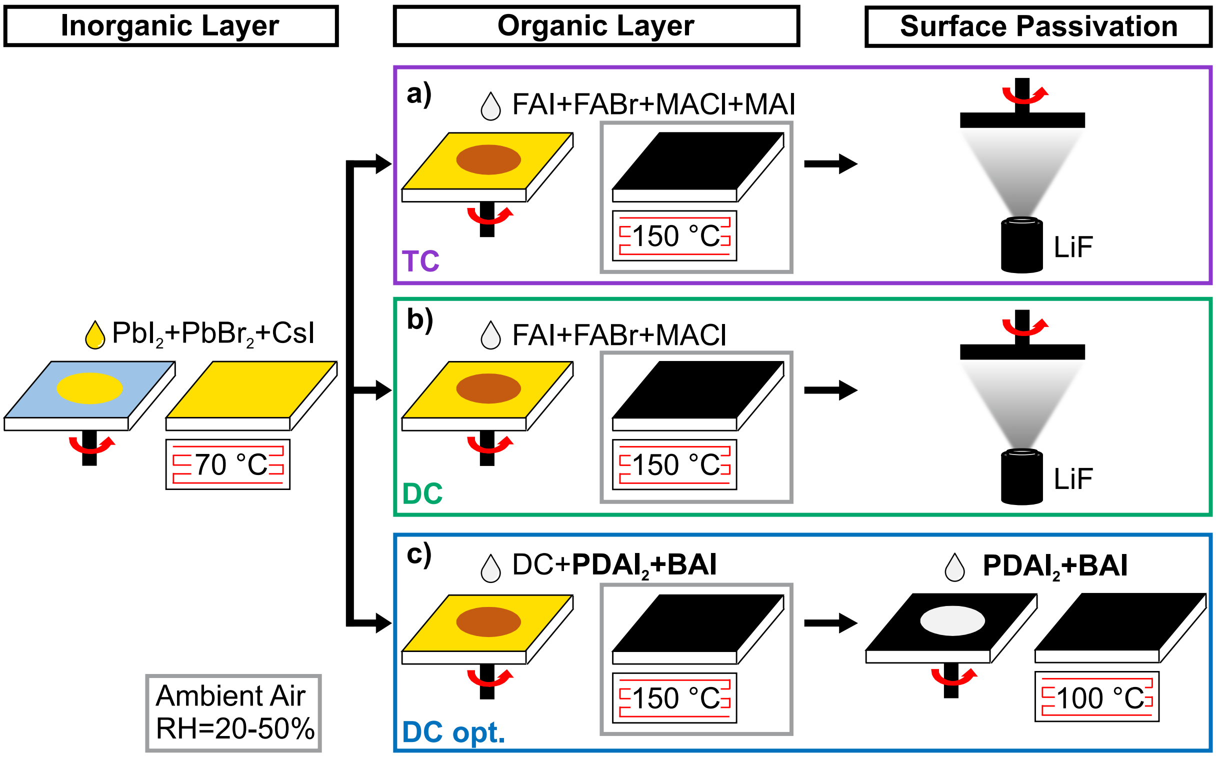

Figure 5.7: Schematic illustration of the fully solution-based two-step deposition method for fabrication of a) triple-cation (labeled as TC), b) double-cation (labeled as DC) and c) optimized double-cation (labeled as DC opt.) perovskite films used in this section. The perovskite film is annealed under ambient conditions with a relative humidity (RH) of ≈ 20-50%. TC and DC perovskite films have a 1 nm layer of LiF as surface passivation. DC opt. perovskite films use a combination of $PDAI_2$+BAI for bulk (0.1 mg mL^{-1}) and surface (1.25 mg mL^{-1}) passivation. Adapted from reference[285] with permission from Wiley.

passivation. To enhance the PSC performance and long-term operational stability of the DC perovskite film, a dual bimolecular passivation strategy is developed. Here, a combination of $PDAI_2$ and BAI is incorporated into the organic precursor solution for bulk passivation and is additionally applied as surface passivation layer to replace LiF (Figure 5.7c, labeled as DC opt.). The concentration of the bimolecular passivation plays a decisive role in achieving highest device performance. For bulk passivation, it is essential to carefully balance the trade-off between V_{OC} loss and improvements in J_{SC} and FF. The optimal concentration is identified as 0.1 mg mL^{-1} dissolved in IPA (Figure A.9). In the case of surface passivation, exceeding the optimal concentration of 1.25 mg mL^{-1} (dissolved in IPA) leads to higher V_{OC} and J_{SC}, but results in a sharp drop in FF – likely due to the insulating nature of a thicker 2D passivation layer at the perovskite/C_{60} interface (Figure A.10).[97,316,317,343–345] Conversely, if the concentration is too low (<1 mg mL^{-1}), no significant improvements in FF or J_{SC} are observed compared to the DC PSCs (Figure A.11). Unless stated otherwise, the optimized DC perovskite uses 0.1 mg mL^{-1} of $PDAI_2$ and BAI as bulk passivation and 1.25 mg mL^{-1} of $PDAI_2$ and BAI as surface passivation.

5.3.1 Microstructure Analysis

To gain insight into the microstructural properties of the perovskite films, XRD, GIWAXS, SEM, and AFM measurements are conducted on half-stacks with the architecture ITO/NiO_x/2PACz/perovskite.

XRD analysis is performed to examine the crystal structure of the perovskite films (Figure 5.8a), revealing distinct changes in the crystal orientation depending on the perovskite composition and passivation strategy. All three perovskite films exhibit characteristic diffraction peaks at ≈ 13.7°, ≈ 19.6°, ≈ 24.2° and ≈ 28.1°, corresponding to

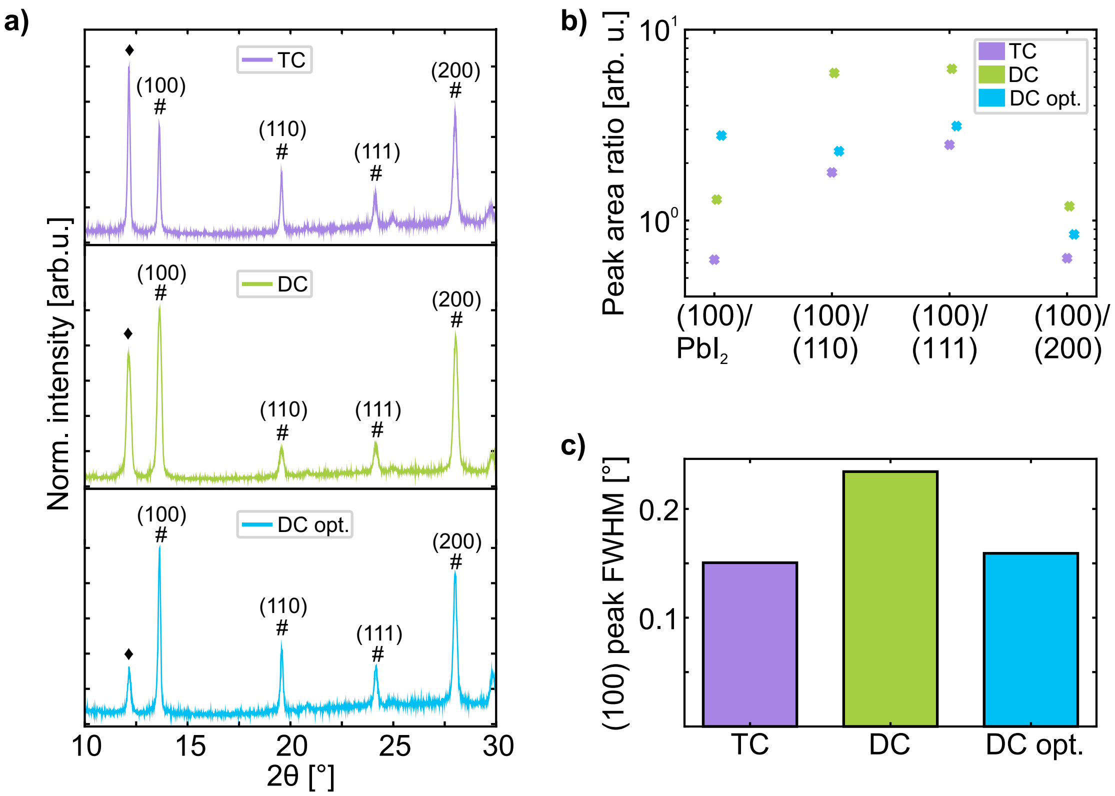

Figure 5.8: a) X-ray diffraction (XRD) patterns (♦ denotes the (001) PbI_2 phase and # the perovskite phase), b) peak area ratios and c) the full width at half maximum (FWHM) of the (100) perovskite peak of triple-cation (TC), double-cation (DC) and optimized double-cation (DC opt.) perovskite films fabricated on glass/indium tin oxide (ITO)/NiO_x/2PACz. Adapted from reference[285] with permission from Wiley.

the (100), (110), (111) and (200) crystal planes of the 3D perovskite, respectively. A distinct peak at around 12.2° is attributed to residual PbI_2, suggesting incomplete precursor conversion.[97,107,346,347] This behavior is typical for two-step deposition methods and was previously discussed in Chapter 4. Compared to TC perovskite films, the DC perovskite films exhibit a higher (100)/PbI_2 peak area ratio (Figure 5.8b), indicating reduced residual PbI_2. The amount of residual PbI_2 is further diminished by implementing the dual bimolecular passivation strategy in the optimized DC films, pointing to the most efficient conversion to the photoactive perovskite phase. Additionally, both DC and optimized DC perovskite films show a more pronounced (100) orientation than TC perovskite films – most prominent for the DC perovskite films, as evidenced by the elevated (100) peak intensity relative to other diffraction peaks. This indicates preferential growth along the (100) crystal plane in the DC and optimized DC perovskite films. Analysis of the FWHM of the (100) perovskite peak (Figure 5.8c) reveals a lower value for the optimized DC perovskite film (0.16°) compared to the DC perovskite film (0.23°), pointing to improved crystallinity with dual bimolecular passivation strategy.

To complement the XRD measurements, GIWAXS measurements provide additional insights into the crystal structure of the perovskite film. The GIWAXS patterns of the TC, DC, bulk-passivated DC and optimized DC perovskite films show no significant differences (Figure A.12). For the bulk-passivated and optimized DC perovskite films, the absence of peaks at low scattering vectors q suggests that the incorporation of $PDAI_2$ and BAI into the perovskite bulk either results in concentrations too low to form a detectable 2D perovskite phase or produces layers too thin to be resolved by GIWAXS.[348,349] Further analysis of the pole figure of the (100) perovskite peak highlights subtle but meaningful differences in crystal orientation among the perovskite films (Figure 5.9). TC perovskite films show pronounced scattering at 10°, while both TC and DC perovskite films predominantly orient around 60°. In contrast, bulk-passivated DC perovskite films display a double peak at 40° and 70°. The introduction of additional surface passivation in the optimized DC perovskite films results in the strongest scattering at 70°, indicating a

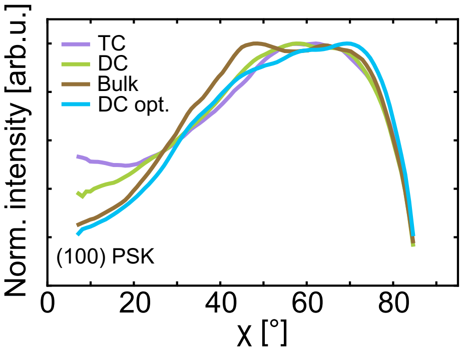

Figure 5.9: Pole figure of the (100) perovskite (PSK) phase for triple-cation (TC), double-cation (DC), bulk-passivated double-cation (Bulk with 0.1 mg mL^{-1} PDAI$_2$+BAI dissolved in IPA) and optimized double-cation (DC opt.) perovskite films fabricated on glass/indium tin oxide (ITO)/NiO$_x$/2PACz. Adapted from reference[285] with permission from Wiley.

stronger preferential vertical crystal orientation of the (100) perovskite phase. This alignment is expected to facilitate more efficient charge-carrier transport, thereby most likely leading to enhanced device performance.[169,350] The surface morphology of the perovskite films is systematically studied by SEM and AFM measurements. SEM measurements (Figure 5.10a and Figure A.13a) reveal a comparable surface morphology for TC and DC perovskite films. Interestingly, introducing bulk passivation reduces the grain size to ≈ 341 nm compared to TC (≈ 402 nm) and DC (≈ 424 nm) perovskite films (Figure A.14). Notably, the brighter regions observed in the SEM image are attributed to residual, unreacted PbI$_2$, in agreement with the XRD analysis. Upon surface passivation of the DC perovskite films with PDAI$_2$ and BAI, a pronounced change in surface morphology is observed. Specifically, the surface-passivated films display a distinctive lamellar structure with less discernible grain boundaries and a marked reduction in the density of bright grains. This morphological change is indicative of the formation of a 2D capping layer atop the 3D perovskite film, which facilitates the conversion of residual PbI$_2$. Such a 2D capping layer has

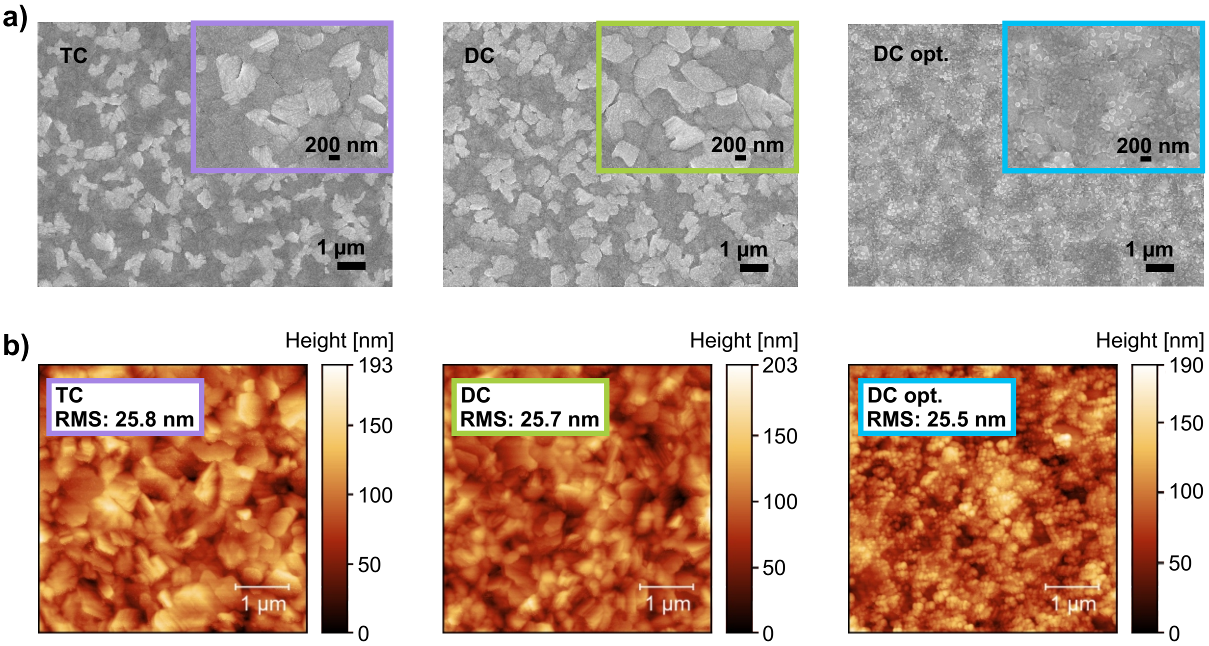

Figure 5.10: a) Top-view scanning electron microscopy (SEM) images and b) atomic force microscopy (AFM) images of triple-cation (TC), double-cation (DC) and optimized double-cation (DC opt.) perovskite films fabricated on glass/indium tin oxide (ITO)/NiO$_x$/2PACz. Two to three measurements are taken for each parameter, and the average root-mean-square (RMS) value is calculated for AFM measurements. Adapted from reference[285] with permission from Wiley.

previously been reported by Niu *et al.*[351] for perovskite films treated with 1,6-diaminohexane ammonium (HDA) or 2,2-(ethylenedioxy)bis(ethylammonium) (EDBE) surface passivation and by Li *et al.*[352] for perovskite films treated with $PDAI_2$ or n-propylammonium iodide (PAI) surface passivation. It is noteworthy that the 2D capping layer does not form a continuous coverage over the underlying layer but preferentially accumulates along the grain boundaries, which potentially enhances charge-carrier transfer.

AFM measurements (Figure 5.10b and Figure A.13b) support the SEM findings, showing no significant variation in the RMS surface roughness among the TC, DC, and optimized DC perovskite films (25.5 to 25.8 nm). Interestingly, bulk-passivated DC perovskite films show a slight reduction in RMS surface roughness (24.1 nm), whereas surface-passivated DC perovskite films exhibit slightly rougher surfaces (27.8 nm). When bulk and surface passivation are applied together, the effects cancel each other out.

Materials characterization reveals that the dual bimolecular passivation strategy effectively reduces residual PbI_2 and subtly shifts the crystal orientation toward a more vertical alignment. Additionally, surface passivation with $PDAI_2$ and BAI results in the formation of a 2D capping layer atop the 3D perovskite film.

5.3.2 Optoelectronic Properties

The optoelectronic properties of the TC, DC, and optimized DC perovskite films are examined using intensity-dependent PLQY measurements. The implied V_{OC} ($V_{OC\text{-imp}}$) is derived from the internal QFLS. By plotting $V_{OC\text{-imp}}$ as a function of light intensity, the internal n_{id} is determined, providing insights into the trap-state density and non-radiative recombination losses (Figure 5.11).[34,232,276–278]

This analysis is essential for understanding the underlying loss mechanisms in PSCs and is key for enhancing both the performance and long-term operational stability of PSCs. As previously noted in Chapter 4, PLQY values can be influenced by residual PbI_2.[274] Therefore, in the following, only the internal ideality factor is considered.

Analysis of half-stacks without a C_{60} layer (ITO/NiO_x/2PACz/perovskite) gives information about the quality of the perovskite bulk (Figure 5.11a). A comparison between TC and DC perovskite films reveals a slight reduction in n_{id} from 1.59 for the TC perovskite films to 1.55 for the DC perovskite films, indicating improved bulk quality due to the modified perovskite composition. The implementation of the dual bimolecular passivation strategy further lowers n_{id} to 1.28 (DC opt.), reflecting a significant reduction in trap-state density. A similar trend is observed upon addition of the C_{60} layer (Figure 5.11b). DC perovskite films exhibit a lower n_{id} factor (1.62) compared to the TC perovskite films (1.65), suggesting less non-radiative recombination centers at the perovskite/C_{60} interface. The optimized DC perovskite films show the lowest n_{id} value (1.39), demonstrating the effectiveness of the dual

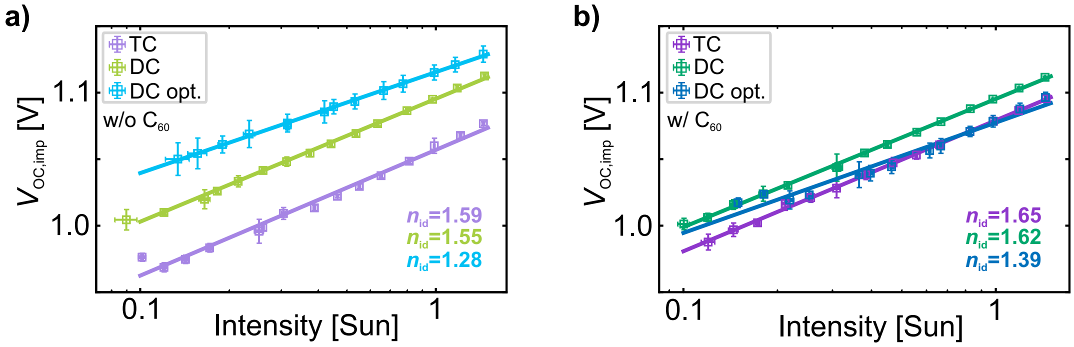

Figure 5.11: Ideality factor (n_{id}) extracted from a fit to the implied V_{OC} ($V_{OC\text{-imp}}$) derived from intensity-dependent photoluminescence quantum yield (PLQY) measurements measured a) without and b) with C_{60} electron transport layer (ETL) of triple-cation (TC), double-cation (DC) and optimized double-cation (DC opt.) perovskite films fabricated on glass/indium tin oxide (ITO)/NiO_x/2PACz. PLQY is measured from the hole transport layer (HTL) side. For each parameter, several perovskite films are measured, and the corresponding mean and standard deviation are plotted. Adapted from reference[285] with permission from Wiley.

bimolecular passivation strategy in suppressing interfacial recombination.

These results clearly demonstrate that the dual bimolecular passivation strategy significantly reduces non-radiative recombination losses both at the perovskite/C_{60} interface and within grain boundaries, thereby enhancing the overall optoelectronic quality of the perovskite film. The improved material properties indicate that the perovskite layers are well suited for integration into complete device architecture, which is part of the next section.

5.3.3 Photovoltaic Performance

To investigate the effect of compositional engineering and dual bimolecular passivation at device level, wide-bandgap PSCs are fabricated in *p-i-n* architecture with the layer stack ITO/NiO_x/2PACz/perovskite/surface passivation/C_{60}/BCP/Ag, as schematically illustrated in Figure 5.1a.

Modifying the perovskite composition from a TC to a DC does not compromise device performance. On the contrary, it enhances the V_{OC} by an average of 10 mV and reduces the hysteresis of the PSCs, as evidenced by the current density-voltage (J-V) characteristics and the statistical analysis (Figure 5.12, Figure 5.13 and Table 5.2). This improvement yields a champion performance of 19.2% in the backward scan with a V_{OC} of 1.21 V, a J_{SC} of 20.0 mA cm^{-2}, and a FF of 79.4% of the DC PSCs. Statistical evaluation using *Welch's t test*[236] confirms that the observed improvement in V_{OC} is statistically significant (Table A.10) and cannot be attributed to a change in the bandgap (Figure A.15).

Optimizing the DC perovskite composition with the dual bimolecular passivation strategy (DC opt.) significantly enhances the V_{OC}, FF and J_{SC} compared to the DC PSCs as confirmed by *Welch's t test* (Table A.10). This optimization results in a remarkable improvement in device performance, with a champion PCE of 20.9% in the backward scan, featuring a V_{OC} of 1.24 V, a J_{SC} of 20.8 mA cm^{-2}, and a FF of 81.0% (Figure 5.12). Particularly

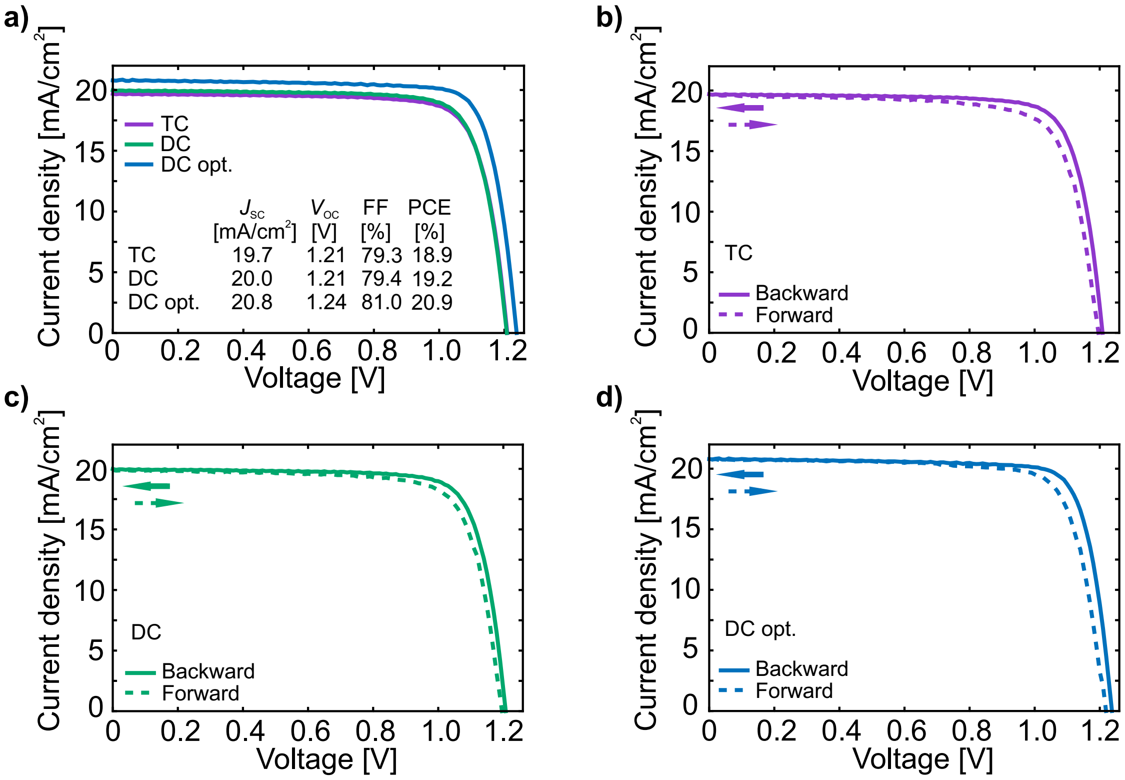

	J_{SC} [mA/cm^2]	V_{OC} [V]	FF [%]	PCE [%]
TC	19.7	1.21	79.3	18.9
DC	20.0	1.21	79.4	19.2
DC opt.	20.8	1.24	81.0	20.9

Figure 5.12: Current density *versus* voltage (J-V) characteristics of the best-performing perovskite solar cells (PSCs) for a) all parameters to facilitate comparison, and b) the triple-cation (TC), c) the double-cation (DC), and d) the optimized double-cation (DC opt.) in both scan directions (backward and forward). Adapted from reference[285] with permission from Wiley.

Table 5.2: Photovoltaic parameters (open-circuit voltage (V_{OC}), short-circuit current density (J_{SC}), fill factor (FF), power conversion efficiency (PCE) and hysteresis index (HI)) of the triple-cation (TC), the double-cation (DC) and the optimized double-cation (DC opt.) champion opaque perovskite solar cells (PSCs).

Perovskite name	Scan direction	V_{OC} [V]	J_{SC} [mA cm^{-2}]	FF [%]	PCE [%]	HI [%]
TC	backward	1.21	19.7	79.3	18.9	6.1
	forward	1.20	19.6	75.5	17.7	
DC	backward	1.21	20.0	79.4	19.2	4.5
	forward	1.20	19.9	76.8	18.3	
DC opt.	backward	1.24	20.8	81.0	20.9	5.2
	forward	1.22	20.7	78.3	19.8	

striking is the average enhancement in V_{OC} by 20 to 30 mV compared to the DC devices. This cannot be attributed to a shift in the bandgap (Figure A.9), but rather correlates with reduced non-radiative recombination losses, consistent with the reduced n_{id} in intensity-dependent PLQY measurements (Figure 5.11). Furthermore, the reduced standard deviation in the statistical data (Figure 5.13) suggests improved repeatability and process stability for the optimized DC PSCs.

While both the TC and DC perovskite composition exhibit comparable EQE spectra, the optimized DC PSCs demonstrate a substantial improvement over the entire spectral range (Figure 5.14a). Since the device architecture and the absorption spectra (Figure 5.14b) remain unchanged throughout all devices, the observed increase in EQE can be attributed to more efficient charge-carrier extraction. This leads to an enhancement in the integrated J_{SC} by around 1 mA cm^{-2} to 19.7 mA cm^{-2} for the optimized DC PSCs. The improved charge-carrier extraction is likely linked to the more vertical crystal orientation observed in GIWAXS measurements (Figure 5.9) and the presence of a 2D capping layer accumulating at the grain boundaries upon adding surface passivation, as revealed by AFM and SEM measurements (Figure 5.10). This is consistent with observations in vertically oriented and 2D/3D perovskite films.[353]

To assess the specific contributions of dual versus single bimolecular passivation, devices are fabricated with bimolecular passivation applied either exclusively in the bulk or exclusively at the surface of the perovskite layer (Figure A.16). When bimolecular passivation is exclusively used in the bulk (with LiF as surface passivation), the V_{OC} is reduced by approximately 30 mV compared to the DC PSCs, resulting in a lower overall PCE. Devices with

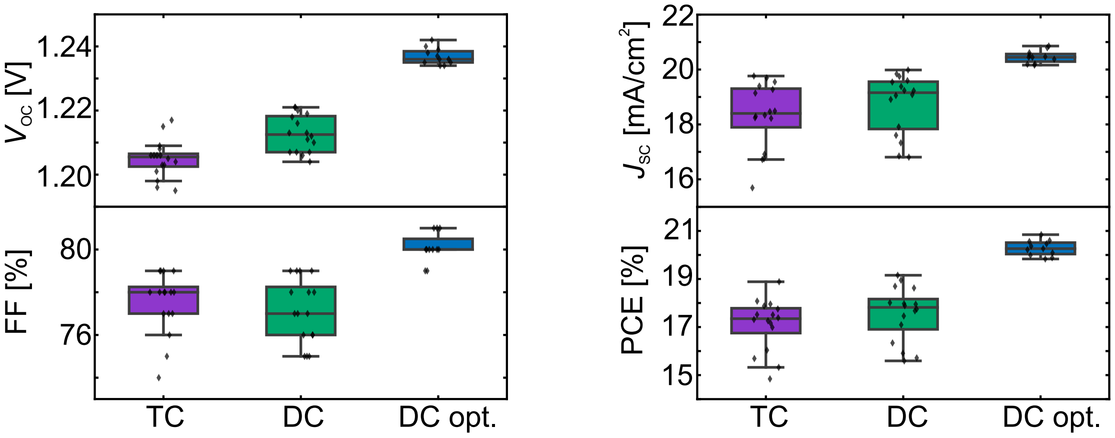

Figure 5.13: Statistical distribution (in total 43 devices) of the open-circuit voltage (V_{OC}), fill factor (FF), short-circuit current density (J_{SC}) and power conversion efficiency (PCE) for triple-cation (TC), double-cation (DC) and optimized double-cation (DC opt.) opaque perovskite solar cells (PSCs). Adapted from reference[285] with permission from Wiley.

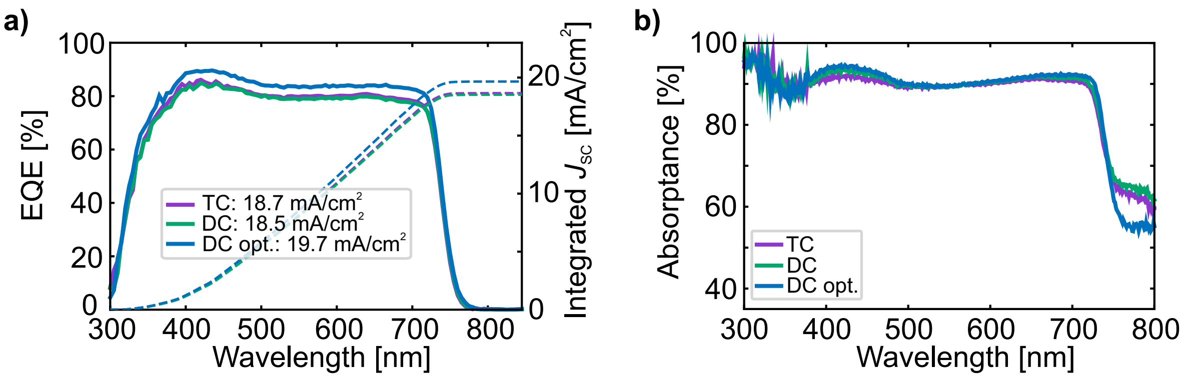

Figure 5.14: a) External quantum efficiency (EQE) spectra as well as the corresponding integrated short-circuit current density (J_{SC}) and b) absorptance spectra for triple-cation (TC), double-cation (DC) and optimized double-cation (DC opt.) opaque perovskite solar cells (PSCs). Adapted from reference[285] with permission from Wiley.

bimolecular passivation introduced exclusively at the surface (without bulk passivation) already achieve high PCEs, with notable improvements in V_{OC}, FF, and J_{SC}. Strikingly, however, the dual bimolecular passivation strategy yields the highest device performance, further enhancing the FF by approximately 4% relative to bimolecular surface passivation alone and increasing the J_{SC} by around 0.5 mA cm^{-2}. These improvements highlight the synergistic effect of combining bulk and surface passivation.

While monomolecular passivation is more commonly reported in the literature,[311,352,354–357] a comparative study by Liu *et al.*[112] demonstrates that bimolecular passivation offers superior performance for both bulk and surface passivation. A comprehensive comparison between monomolecular and the here presented bimolecular passivation is provided in Pappenberger *et al.*[285], showing that bimolecular passivation leads to enhanced FF and J_{SC}.

For bulk passivation, bimolecular agents have been incorporated *via* the organic cation solution in this study, which corresponds to the second step of the two-step deposition method. Given the flexibility of this method, where Pb-containing precursor materials and organic cations are deposited separately, bulk passivation can in principle be introduced in both deposition steps. However, experimental results (Figure A.17) indicate that efficiency improvements are only achieved when the bimolecular passivation is introduced in the organic cation solution.

The increased compositional complexity and different surface properties of TC perovskites often result in a less homogeneous formation of surface passivation layers compared to simpler DC systems, which makes the passivation effect less predictable.[358,359] However, even without further optimization, the dual bimolecular passivation strategy can be successfully applied to TC PSCs (Figure A.18), yielding a champion performance of 19.1% in the backward scan, along with improved V_{OC} by ≈ 30 mV and J_{SC}. This result underscores the versatility and effectiveness of the passivation strategy across different perovskite compositions.

Overall, the results highlight a significant improvement in all device parameters for the optimized DC PSCs using dual bimolecular passivation. Among the bulk and surface passivation strategies investigated in this thesis, dual bimolecular passivation proves to be the most effective one (Figure A.19). Notably, both V_{OC} and J_{SC} reach approximately 90% of the detailed balance (DB) limit. These results underscore the critical role of dual passivation at both the perovskite/C_{60} interface and the grain boundaries of the perovskite thin films in achieving high-performance PSCs.

While the achieved efficiency of 20.9% at a bandgap of 1.67 eV remains below state-of-the-art solution-based one-step processed PSCs – with efficiencies exceeding 22% for bandgaps above 1.65 eV[282] – the performance gap between both solution-based deposition methods is steadily narrowing. At the time this study was conducted, the 20.9% efficiency represented the highest value reported for solution-based two-step processed PSCs in the *p-i-n* architecture with a bandgap beyond 1.65 eV.[57,58,64]

5.3.4 Long-Term Operational Stability

To systematically investigate degradation mechanisms that can affect the operational stability of PSCs, three standardized stability tests are used: ISOS-D1 (dark storage, 25 °C, intermittent *J*-*V* measurements) to test dark storage stability, ISOS-D2 (dark storage, 85 °C, intermittent *J*-*V* measurements) to evaluate thermal stability, and ISOS-L1 (100 mW cm^{-2}, 25 °C, MPP tracking) to assess light-induced degradation.[226] All stability measurements are performed under N_2 atmosphere. For each parameter, multiple ST devices with the layer stack glass/ITO/NiO_x/2PACz/perovskite/surface passivation/C_{60}/SnO_x/IZO/Au are subjected to these test conditions to assess their long-term performance and degradation behavior. The corresponding mean values and standard deviations are provided. Both TC and DC devices use LiF as surface passivation, a material known to be susceptible to thermal degradation.[47,97,300,305] However, it should be noted that within the scope of the present analysis, this specific degradation mechanism cannot be isolated from other contributing pathways.

The effect of dark storage on stability is evaluated by exposing semitransparent PSCs under ISOS-D1 test conditions for 1000 h. The normalized PCE, FF, V_{OC} and J_{SC} derived from intermittent *J*-*V* measurements for TC, DC and optimized DC PSCs are shown in Figure 5.15. Notably, the optimized DC devices maintain stable performance throughout the testing period (retaining 98.2% of their initial PCE), while the TC and DC devices exhibit performance degradation (≈ 30% absolute loss for TC and ≈ 15% absolute loss for DC PSCs). Interestingly, both TC and DC devices show a pronounced decline within the first 200 h, followed by a plateau, indicating stabilization over the remaining 800 h. The TC devices reach T_{80} after 130 h, whereas the DC devices stabilize at the T_{80} threshold. As shown in Figure 5.15, the primary contributors to the PCE loss in TC and DC devices are reductions in FF and J_{SC}. While the V_{OC} remains stable for both DC and optimized DC devices, the TC devices experience a noticeable

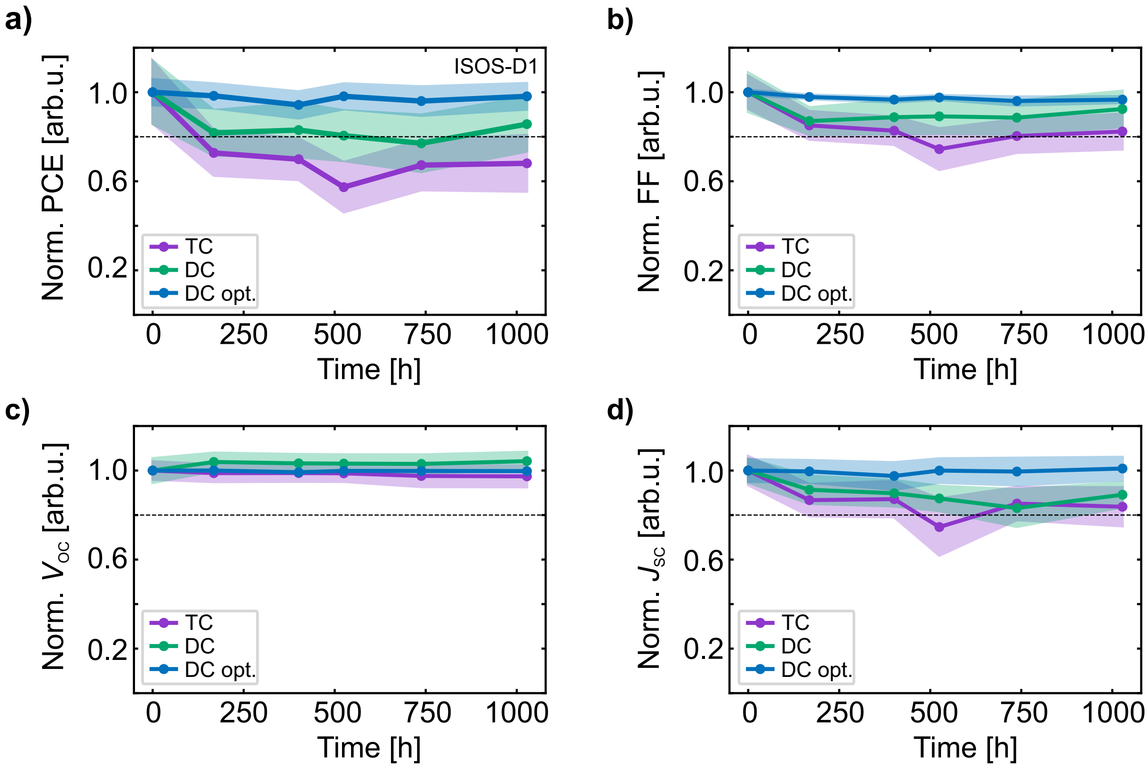

Figure 5.15: Normalized a) power conversion efficiency (PCE), b) fill factor (FF), c) open-circuit voltage (V_{OC}), and d) short-circuit current density (J_{SC}) from current density *versus* voltage (*J*-*V*) measurements of semitransparent (ST) triple-cation (TC), double-cation (DC) and optimized double-cation (DC opt.) perovskite solar cells (PSCs) under ISOS-D1 testing conditions (dark storage, 25 °C, intermittent *J*-*V*) for 1000 h. Mean values and standard deviations based on eight devices per parameter are provided. Adapted from reference[285] with permission from Wiley.

decline of ≈ 3%.

The impact of elevated temperatures on the stability of dark-stored PSCs is assessed by accelerated aging tests on semitransparent devices under ISOS-D2 test conditions for 1000 h. Figure 5.16 presents the normalized PCE, FF, V_{OC} and J_{SC} obtained from intermittent *J-V* measurements for TC, DC and optimized DC devices. In comparison to the measurements under ISOS-D1 test conditions, elevated temperatures significantly affect device stability. TC devices show the most pronounced performance degradation, reaching T_{80} after 250 h. In contrast, both DC and optimized DC devices exhibit similar degradation profiles, with a T_{80} time of 400 h. Analysis of the remaining device parameters clearly indicates that the reduction in FF is the dominant factor contributing to the overall decline in PCE. Specifically, the FF decreases by approximately 45% for TC devices and around 30% for both DC and optimized DC devices. Notably, the V_{OC} remains relatively stable for optimized DC devices, with only a minor reduction of ≈ 3%. More substantial losses are observed for the TC (≈ 6% absolute loss) and the DC (≈ 5% absolute loss) devices. These findings align with literature reports, which attribute such degradation under prolonged thermal stress (over a period of 500 h) to increased non-radiative recombination, occurring either within the perovskite layer or at the interfaces to the charge transport layers, leading to a reduction in both FF and V_{OC}.[360–362]

In the final step, the operational stability of the PSCs is evaluated not only under dark-storage conditions but also under continuous light exposure. To this end, semitransparent PSCs are subjected to ISOS-L1 test conditions for 300 h. Due to problems with the quality of the NiO_x layer, only 2PACz is used as the HTL for ISOS-L1 measurements. The implications of this change for long-term device stability have not been investigated in detail. The normalized PCE, J_{SC} and V_{OC} are presented in Figure 5.17. Interestingly, under ISOS-L1 test conditions, TC, DC and optimized DC devices exhibit similar behavior to that under ISOS-D1 test conditions. TC PSCs exhibit a rapid decline in performance within the first 5 h, followed by a more gradual degradation over the remaining 295 h. The

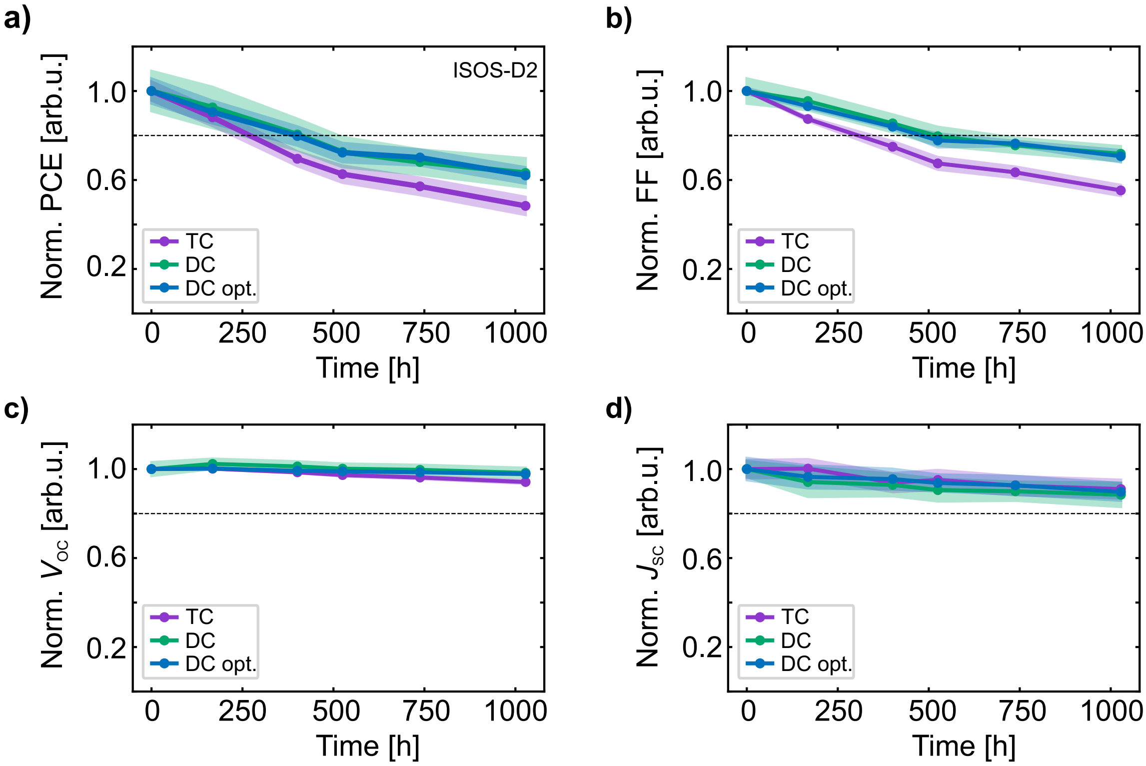

Figure 5.16: Normalized a) power conversion efficiency (PCE), b) fill factor (FF), c) open-circuit voltage (V_{OC}), and d) short-circuit current density (J_{SC}) from current density *versus* voltage (*J-V*) measurements of semitransparent (ST) triple-cation (TC), double-cation (DC) and optimized double-cation (DC opt.) perovskite solar cells (PSCs) under ISOS-D2 testing conditions (dark storage, 85 °C, intermittent *J-V*) for 1000 h. Mean values and standard deviations based on twelve devices per parameter are provided. Adapted from reference[285] with permission from Wiley.

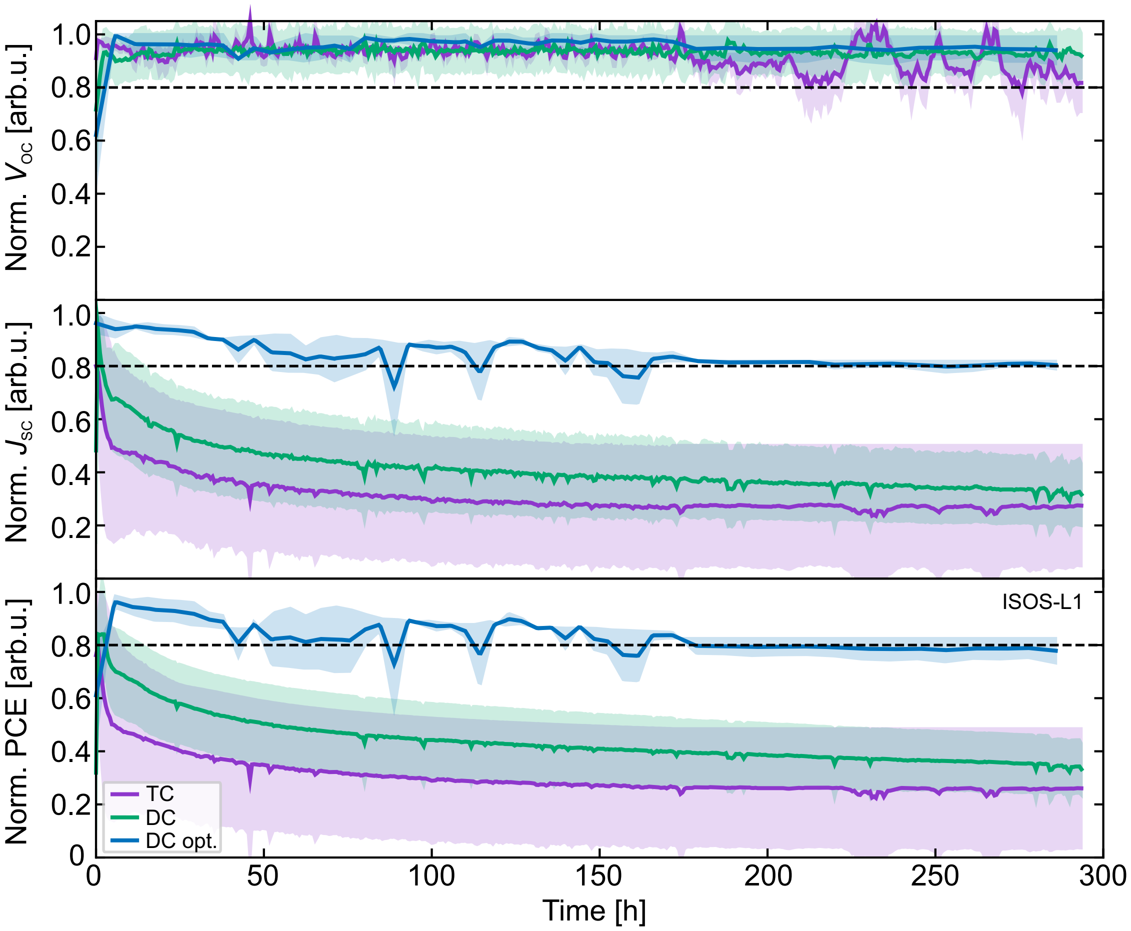

Figure 5.17: Normalized open-circuit voltage (V_{OC}), short-circuit current density (J_{SC}) and power conversion efficiency (PCE) at the maximum power point (MPP) tracking of semitransparent (ST) triple-cation (TC), double-cation (DC) and optimized double-cation (DC opt.) perovskite solar cells (PSCs) under ISOS-L1 test conditions (100 mW cm^{-2}, 25 °C, MPP tracking) for 300 h. Mean values and standard deviations based on 2-5 devices per parameter are provided. The data fluctuations originate from the measurement setup. Due to problems with the quality of the NiO_x layer, only 2PACz is used as the hole transport layer. Adapted from reference[285] with permission from Wiley.

DC devices show a similar trend but maintain a consistently higher performance level throughout the 300 h testing period. Optimized DC PSCs demonstrate the most stable device performance, showing an initial light-soaking effect within the first 5 h and reaching T_{80} after 180 h. As shown in Figure 5.17, analysis of the remaining device parameters reveals that the primary factor driving the reduction in PCE is the decrease in J_{SC}, while the V_{OC} remains largely unaffected across all devices.

The degradation mechanisms observed under various stress conditions highlight that transitioning from a triple-cation to a MA-free perovskite composition enhances the operational stability of PSCs. Additionally, although recent studies have reported accelerated degradation arising from diammonium salt surface treatments,[363–365] the dual bimolecular passivation strategy introduced here contributes to improved long-term operational stability. This improvement is likely associated with suppressed ion migration enabled by the 2D capping layer.[351,352] Nevertheless, further optimization is required, as the current results have yet to reach the benchmark set by state-of-the-art stability metrics – maintaining $> 90\%$ of their initial PCE after about 1200 h of continuous illumination.[366]

5.4 X-ray Photoelectron Spectroscopy Analysis of Surface Passivation Strategies

Post-treatment of the perovskite film aims to enhance the quality of the perovskite/C_{60} interface, reducing non-radiative recombination losses and thereby improving device performance and long-term operational stability.[106,297–299]
Effective post-treatments for perovskite films fabricated *via* the solution-based two-step deposition method remain largely unexplored, and post-treatment strategies developed for one-step processed perovskite films are often not directly transferable. Notably, in this work, both evaporated LiF and a bimolecular passivation strategy using a combination of $PDAI_2$ and BAI (solution-based) have demonstrated promising results in passivating the perovskite surface.

To gain a deeper understanding of the underlying mechanisms of both passivation strategies, X-ray photoelectron spectroscopy (XPS) measurements are used. XPS is a surface-sensitive technique that enables analysis of the chemical and electronic structure of the topmost layers. Measurements are performed on the following half-stacks, using the bulk-passivated DC perovskite (with 0.1 mg mL^{-1} $PDAI_2$+BAI in the organic cation solution, Section 5.3) as perovskite thin film:

- Ref: ITO/2PACz/perovskite, without surface passivation.
- LiF: ITO/2PACz/perovskite/LiF, 1 nm evaporated LiF as surface passivation.
- $PDAI_2$+BAI: ITO/2PACz/perovskite/$PDAI_2$+BAI, with 1.25 mg mL^{-1} $PDAI_2$ and BAI dissolved in IPA as surface passivation. This corresponds to the optimized DC perovskite composition.

Figure 5.18a displays the XPS survey spectra for all three configurations. The reference sample exhibits a spectrum consistent with previously reported data for untreated perovskites.[367] All expected elemental peaks are present, and the low intensity of the O 1s core-level signal indicates successful sample transfer without significant oxidation. Both LiF and $PDAI_2$+BAI surface passivation treatments result in an enhanced O 1s signal, suggesting an increased oxygen content at the surface. For the LiF-passivated sample, F 1s, F 2s and Li 1s core-level signals confirm the presence of LiF on the surface (Figure 5.18b and Figure 5.19a).

Analysis of the low binding energy region (LBER) reveals a distinct change in surface stoichiometry upon $PDAI_2$+BAI surface treatment (Figure 5.19a and Table 5.3). A pronounced increase in Br content, accompanied by a reduction in Cs content, indicates that the bimolecular passivation strategy modifies the chemical composition of the perovskite surface. In contrast, the LiF-passivated sample maintains a composition close to the reference, with only minor Br diffusion toward the surface. Taking a closer look at the valence band (VB) maximum provides

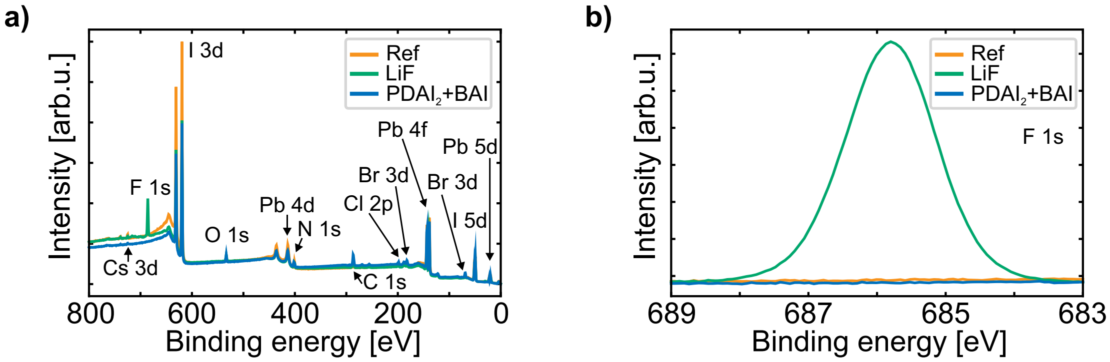

Figure 5.18: a) X-ray photoelectron spectroscopy (XPS) mono-Al-K_α survey spectra and b) F 1s core-level of perovskite thin films without surface passivation (Ref), with LiF (LiF) as surface passivation and with a combination of $PDAI_2$ and BAI ($PDAI_2$+BAI) as surface passivation. The bulk-passivated double-cation (DC) perovskite (with 0.1 mg mL^{-1} $PDAI_2$+BAI in the organic cation solution) is used as perovskite thin film.

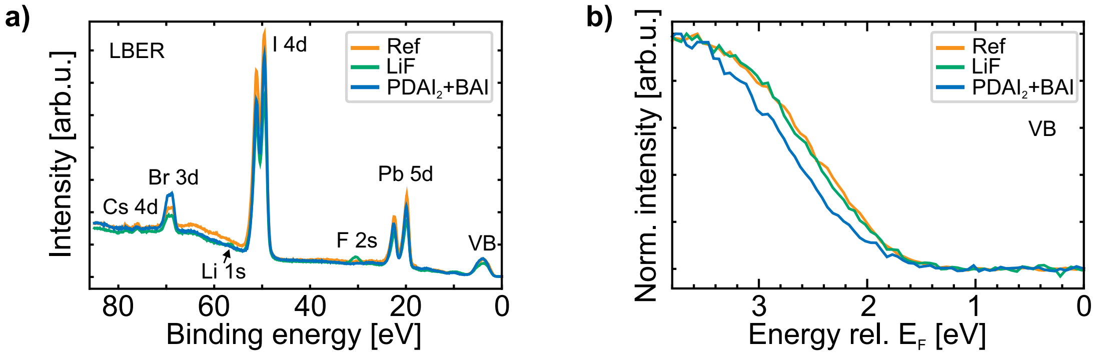

Figure 5.19: X-ray photoelectron spectroscopy (XPS) mono-Al-K_α spectra for a) low binding energy region (LBER) and b) valence band (VB) maximum of perovskite thin films without surface passivation (Ref), with LiF (LiF) as surface passivation and with a combination of $PDAI_2$ and BAI ($PDAI_2$+BAI) as surface passivation. The bulk-passivated double-cation (DC) perovskite (with 0.1 mg mL^{-1} $PDAI_2$+BAI in the organic cation solution) is used as perovskite thin film.

Table 5.3: Elemental composition in the low binding energy region (LBER), extracted from X-ray photoelectron spectroscopy (XPS) mono-Al-K_α measurements for perovskite thin films without surface passivation (Ref), with LiF (LiF) as surface passivation and with a combination of $PDAI_2$ and BAI ($PDAI_2$+BAI) as surface passivation. The estimated absolute error is $\approx 10\%$, while the error of the relative changes is much smaller ($< 2\%$). The bulk-passivated double-cation (DC) perovskite (with 0.1 mg mL^{-1} $PDAI_2$+BAI in the organic cation solution) is used as perovskite thin film.

Element	Ref [%]	LiF [%]	$PDAI_2$+BAI [%]
Pb	29	27	26
I	65	64	61
Br	6	8	13
Cs	1	1	0.3

further insights into the passivation effect (Figure 5.19b). The VB maximum of the LiF-passivated sample remains unchanged compared to the reference sample. However, the $PDAI_2$+BAI-passivated sample exhibits a significant shift of 150 meV (± 10 meV) away from the Fermi level (E_F). Since other elemental peaks (e.g., I 3d and Cs 3d, Figure 5.21) do not show a similar shift, the observed shift is unlikely to result from doping effects. Instead, it indicates a widening of the surface bandgap, attributed to changes in surface stoichiometry induced by the passivation treatment.

Analysis of the N 1s and C 1s core-level signals (Figure 5.20) shows spectral features characteristic of untreated perovskite thin films for the reference sample.[367] LiF-passivated samples exhibit a similar N 1s core-level signal, albeit slightly broadened, likely due to a modified chemical environment. The C 1s spectrum reveals an additional peak at $\approx$ 287 eV, attributed to C-C bonds, possibly originating from C_{60} fragments due to prior evaporation in the same evaporation chamber. For the $PDAI_2$+BAI-passivated sample, additional N and C signals at $\approx$ 403 eV and $\approx$ 287 eV, respectively, are observed, consistent with the presence of nitrogen and carbon in the passivation agents. Detailed analysis of the Pb $4f_{7/2}$ core-level signal (Figure 5.21a) reveals three distinct contributions:

- A main peak at $\approx$ 138.3 eV, corresponding to Pb in the perovskite environment.
- A smaller peak at $\approx$ 136.8 eV, attributed to metallic Pb (Pb^0), a typical non-radiative recombination channel.[368]
- A shoulder at $\approx$ 140.0 eV, indicating oxidized Pb.

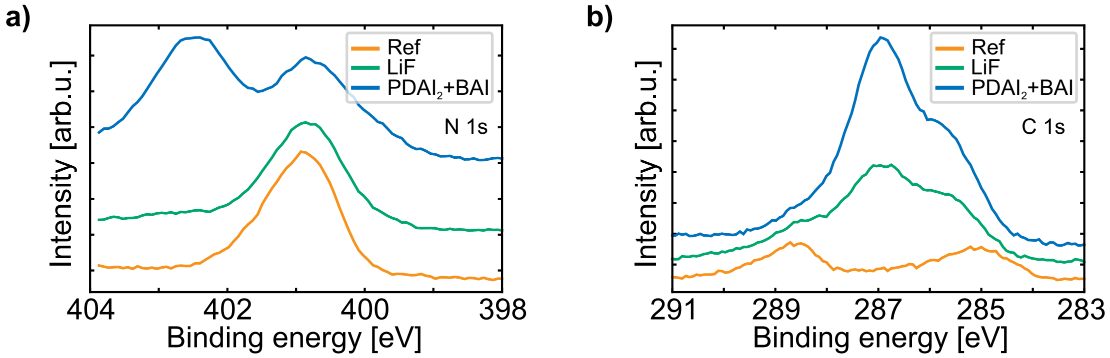

Figure 5.20: X-ray photoelectron spectroscopy (XPS) mono-Al-K$_\alpha$ spectra for a) N 1s core-level and b) C 1s core-level of perovskite thin films without surface passivation (Ref), with LiF (LiF) as surface passivation and with a combination of PDAI$_2$ and BAI (PDAI$_2$+BAI) as surface passivation. The bulk-passivated double-cation (DC) perovskite (with 0.1 mg mL^{-1} PDAI$_2$+BAI in the organic cation solution) is used as perovskite thin film.

The reference sample contains both Pb species – Pb^0 and oxidized Pb. The LiF-passivated sample shows a slight reduction in the Pb^0 content but an increased fraction of oxidized Pb compared to the reference sample. In contrast, PDAI$_2$+BAI surface treatment significantly reduces both Pb^0 and oxidized Pb, indicating effective passivation of defect states and suppression of non-radiative recombination. These observations are consistent with the reduced n_{id} from intensity-dependent PLQY measurements (Figure 5.11) and improvements in V_{OC} and FF (Figure 5.13) for the optimized DC perovskite. Additionally, the main Pb peak shifts by ≈ 0.1 eV, suggesting a subtle change in the chemical environment induced by PDAI$_2$+BAI surface treatment.

I 3d$_{5/2}$ and Cs 3d$_{5/2}$ core-level signals (Figure 5.21b/c) remain largely unaffected upon surface passivation, indicating stable chemical environments for these elements. Interestingly, a pronounced Cl signal is detected in the PDAI$_2$+BAI-passivated sample (Figure 5.21d), most likely originating from MACl. This contrasts with previous reports claiming that MACl completely evaporates during the final annealing step.[209] The absence of Cl in both the reference and LiF-passivated samples, combined with its exclusive presence in the PDAI$_2$+BAI-passivated sample, suggests that this passivation strategy promotes Cl incorporation into the perovskite surface. This aspect will be discussed in more detail in Section 6.3.

To shed light on the morphology of the surface passivation layer, a homogeneous layer is assumed. Using the Beer-Lambert law, an "effective" thickness d can be calculated using the attenuation of the XPS signal:

$$d = -\lambda \cdot \ln\left(\frac{I}{I_0}\right), \tag{5.1}$$

where λ is the inelastic mean free path of the photoelectrons, I_0 is the reference peak intensity and I is the attenuated peak intensity.

The LiF-passivated sample exhibits a similar "effective" thickness for all elemental peaks (Figure 5.22a), consistent with the formation of a homogeneous LiF layer. The estimated thickness of this layer is ≈ 1 nm, which aligns well with the nominal deposition from the evaporation system. A slightly negative value in the Br 3d core-level signal suggests Br diffusion toward the surface, corroborating the changes in surface stoichiometry observed in the low binding energy region (Table 5.3).

In contrast, the "homogeneous passivation layer" model does not adequately describe the PDAI$_2$+BAI-passivated sample (Figure 5.22a), as evidenced by the large spread in the "effective" thickness. Combined with the intensity ratio I(PDAI$_2$+BAI)/I(Ref) (Figure 5.22b), these results indicate a modified surface composition, including Br enrichment and reduced Cs content, pointing to a strong chemical interaction between the passivation agents and the perovskite surface. This is in line with the morphological features observed in SEM and AFM measurements (Figure 5.10).

Physical surface passivation such as evaporated LiF induces only minor changes in surface composition, with slight

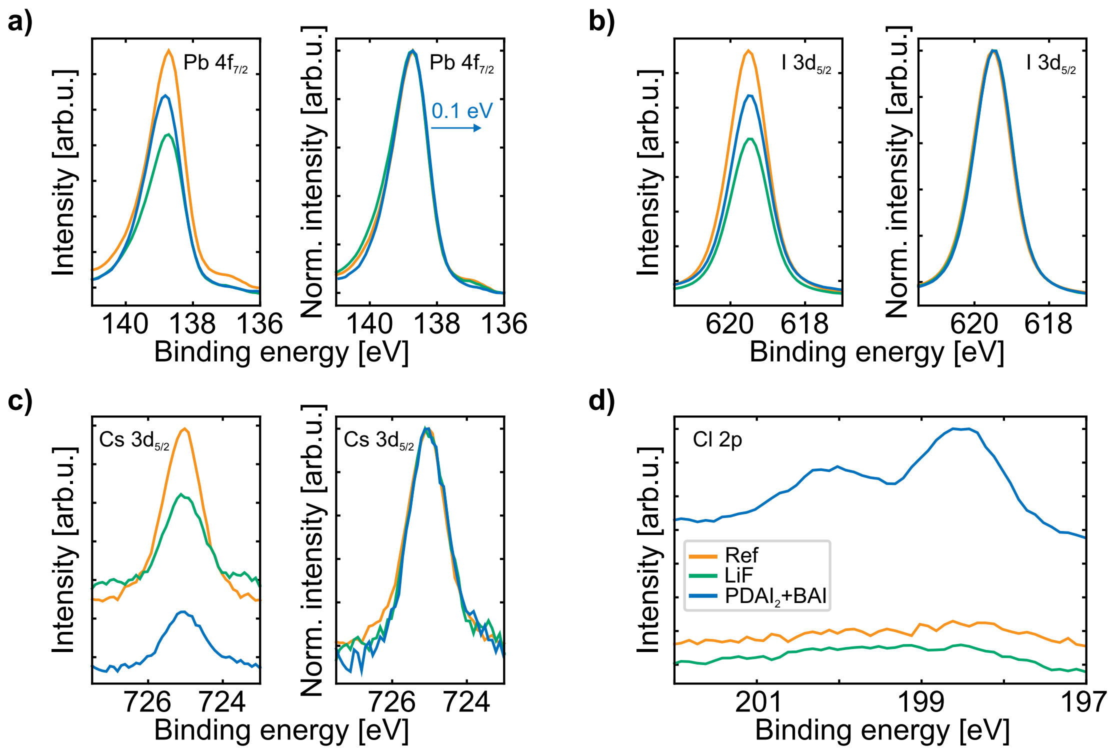

Figure 5.21: X-ray photoelectron spectroscopy (XPS) mono-Al-K$_\alpha$ spectra for a) Pb 4f$_{7/2}$ core-level, b) I 3d$_{5/2}$ core-level, c) Cs 3d$_{5/2}$ core-level and d) Cl 2p core-level of perovskite thin films without surface passivation (Ref), with LiF (LiF) as surface passivation and with a combination of PDAI$_2$ and BAI (PDAI$_2$+BAI) as surface passivation. a), b) and c) show both intensity and normalized intensity. In the normalized intensity representation in a), the PDAI$_2$+BAI spectrum is shifted by 0.1 eV. The bulk-passivated double-cation (DC) perovskite (with 0.1 mg mL^{-1} PDAI$_2$+BAI in the organic cation solution) is used as perovskite thin film.

Br diffusion toward the surface. In contrast, chemical surface passivation using a bimolecular passivation with PDAI$_2$ and BAI significantly modifies the surface stoichiometry, resulting in a widened surface bandgap as indicated by a 150 meV shift of the VB maximum away from E_F. This widening of the surface bandgap likely facilitates electron extraction to the ETL. Additionally, PDAI$_2$+BAI passivation effectively suppresses metallic Pb^0 and oxidized Pb

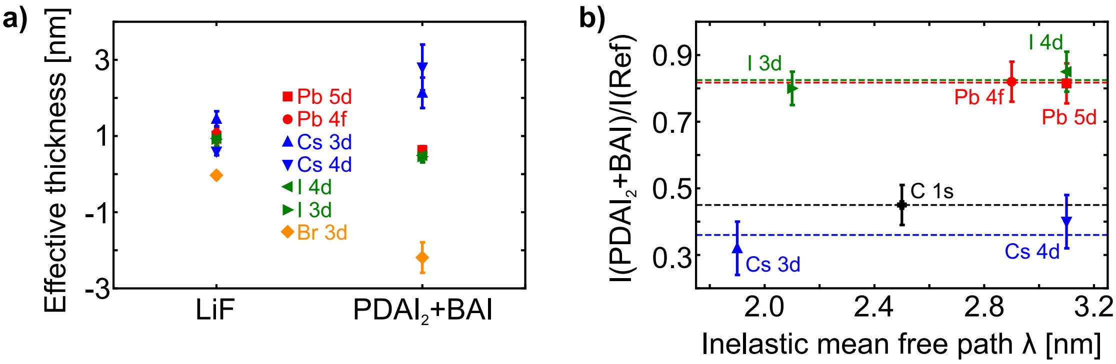

Figure 5.22: a) Effective thickness of the passivation layer calculated from the core-level signals. b) Intensity ratio of PDAI$_2$+BAI to Ref of different perovskite core-level lines as a function of the inelastic mean free path λ. Horizontal dashed lines indicate the average ratio for each element. The bulk-passivated double-cation (DC) perovskite (with 0.1 mg mL^{-1} PDAI$_2$+BAI in the organic cation solution) is used as perovskite thin film.

species, thereby reducing defect states and mitigating non-radiative recombination at the perovskite/C_{60} interface. Collectively, these effects contribute to the improved performance and stability of the optimized DC PSCs.

5.5 Two-Terminal Perovskite/Silicon Tandem Solar Cell Integration

Following the successful optimization of the perovskite layer with a suitable bandgap and an effective passivation strategy in SJ PSCs, the process is transferred to Si bottom cells for the fabrication of 2T perovskite/Si TSCs. The device architecture of the TSCs consists of the layer stack Si/ITO/NiO_x/2PACz/perovskite/$PDAI_2$+BAI/C_{60}/SnO_x/IZO/Ag/MgF_2 with an active area of 1.0 cm^2 (Figure 5.1b).

While the Si PV industry predominantly utilizes random pyramidal textures with a peak-to-valley distance of $\approx$ 5 µm for optimal light management,[76,369–371] such large textures pose compatibility challenges for solution-processed perovskite thin films, often resulting in poor surface coverage and device performance.[76,97,342,372,373] To overcome these limitations, vapor deposition or hybrid routes combining vapor deposition with solution-based processing are typically used to achieve conformal perovskite coverage on micron-sized pyramids.[87,88,374] As a compromise between light harvesting and solution-process compatibility, submicron pyramidal textures ($<$ 2 µm) have been proposed.[41,301,375,376] In the following, the optimized solution-based two-step processed perovskite films are tested on various Si bottom cell architectures, including planar, small-textured and large-textured substrates.

Implementing the optimized perovskite layer on planar Si bottom cells demonstrates high device performance, reaching an efficiency of 28% in the backward scan with a small hysteresis of 1.1% (Figure 5.23a). This is competitive with the previously reported efficiency of 27.64% for a 2T perovskite/Si TSC on a planar Si bottom cell fabricated *via* a fully solution-based two-step process.[57] The observed V_{OC} of 1.93 V aligns well with expectations based on the individual performance of the SJ PSC (1.24 V) and the Si bottom cell ($\approx$ 0.7 V), but remains below the radiative limit of 2.24 V.[104,105] However, analysis of the EQE spectra (Figure 5.23b) reveals a current mismatch of 0.9 mA cm^{-2} between both cells, indicating that the Si bottom cell limits the overall J_{SC} of the tandem device. It should be noted that the J_{SC} derived from the *J*-*V* characteristic exceeds the integrated J_{SC} of the Si bottom cell by $\approx$ 1 mA cm^{-2}, suggesting a minor overestimation of the device performance.

Although conventional fully solution-based processes typically have difficulty producing functional perovskite layers on large pyramidal textures, an initial test is performed on Si bottom cells with a pyramid height distribution of approximately 2-5 µm (referred to as large-textured). The *J*-*V* characteristic and EQE spectral response of the champion device are shown in Figure 5.24a/b. The best-performing 2T perovskite/Si tandem device achieves

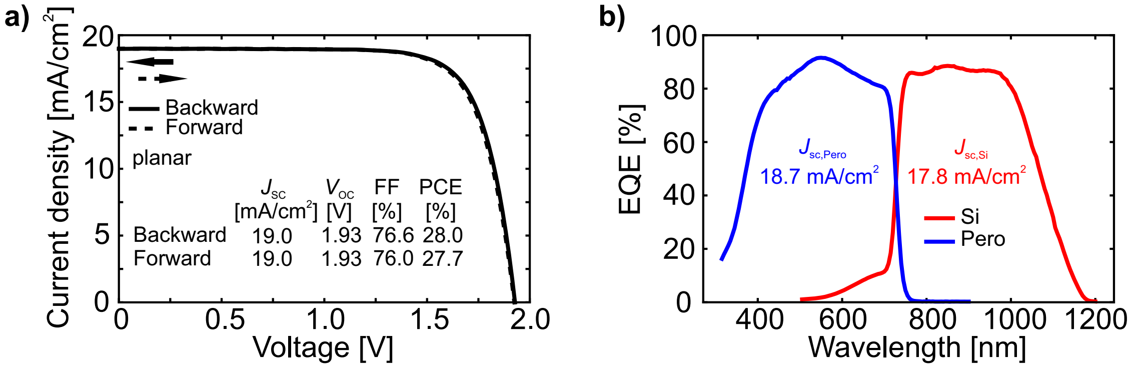

Figure 5.23: a) Current density *versus* voltage (*J*-*V*) characteristics and b) external quantum efficiency (EQE) of the champion planar two-terminal (2T) perovskite/silicon (Si) tandem solar cell (TSC, active area: 1.0 cm^2, planar) with a perovskite bandgap of $E_g = 1.67$ eV (DC opt. perovskite) and with 100 nm of MgF_2 as antireflective coating. The molarity of the perovskite precursor solution (1.5 M) as well as the bulk and surface passivation concentration are the same as for single-junction (SJ) perovskite solar cells (PSCs). Adapted from reference[285] with permission from Wiley.

a PCE of 24.1%, demonstrating that a fully solution-based two-step deposition method is capable of forming high-quality perovskite films on large pyramidal textures. Nevertheless, a PCE gap of approximately 4% persists between the planar and large-textured 2T perovskite/Si TSCs, primarily attributed to the low FF of 69.9%, clearly reflecting low R_{shunt} and high R_{series}. Furthermore, the *J*-*V* characteristic exhibits a pronounced hysteresis of 15%. The EQE spectra reveal a current mismatch of 1.5 mA cm^{-2} for both cells, indicating that the TSC is top-limited and further optimizations of the perovskite layer thickness, bandgap and antireflective coating are needed. The reduced J_{SC} of the perovskite top cell is likely due to the increased perovskite film thickness compared to the SJ device, as well as an unoptimized molarity of the organic cation solution, making efficient charge-carrier extraction challenging.[108,377–379] Cross-sectional SEM images confirm that the solution-based two-step processed perovskite film is actually able to cover textures up to 2 µm in height (Figure 5.24c). However, further analysis reveals that some

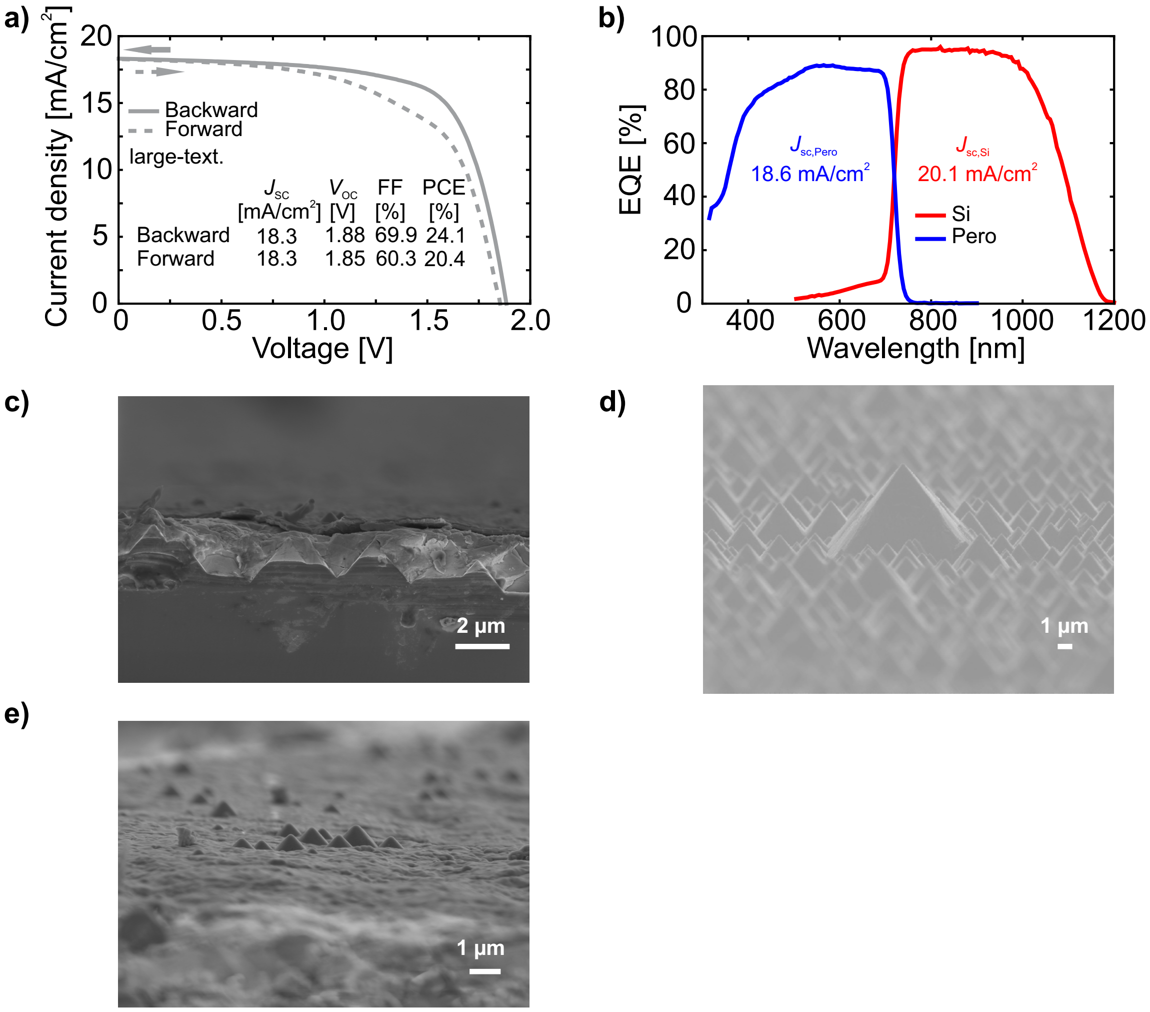

Figure 5.24: a) Current density *versus* voltage (*J*-*V*) characteristics and b) external quantum efficiency (EQE) of the champion large-textured two-terminal (2T) perovskite/silicon (Si) tandem solar cell (TSC, active area: 1.0 cm^2, pyramid height ≈ 2-5 µm) with a perovskite bandgap of $E_g = 1.67$ eV (DC opt. perovskite) and with 100 nm of MgF_2 as antireflective coating. The molarity of the perovskite precursor solution is adjusted to 1.9 M, with the concentration of the bulk passivation scaled accordingly. The surface passivation concentration is reduced to 0.3 mg mL^{-1} compared to single-junction (SJ) perovskite solar cells (PSCs). c) Cross-sectional scanning electron microscopy (SEM) image of the perovskite film on top of the textured Si bottom cell, d) top-view SEM image of the Si bottom cell with pyramidal outliers exceeding 5 µm in height and e) tilted top-view SEM image of the perovskite film on top of the textured Si bottom cell. Adapted from reference[285] with permission from Wiley.

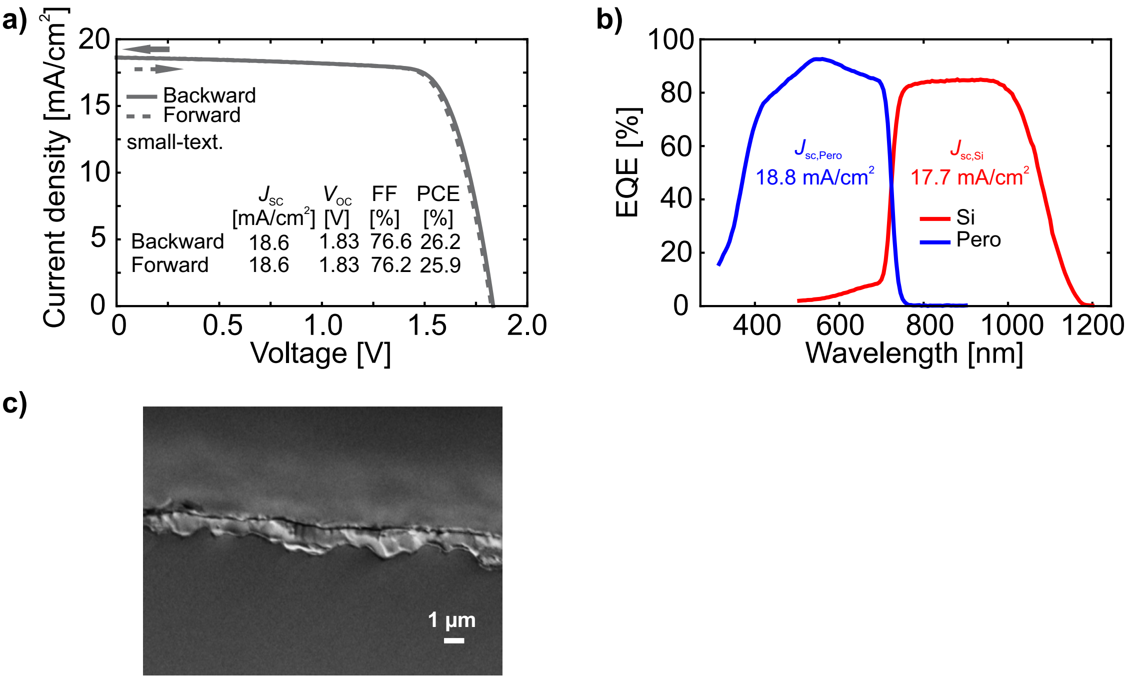

Figure 5.25: a) Current density *versus* voltage (*J*-*V*) characteristics, b) external quantum efficiency (EQE) and c) cross-sectional scanning electron microscopy (SEM) image of the champion small-textured two-terminal (2T) perovskite/silicon (Si) tandem solar cell (TSC, active area: 1.0 cm^2, pyramid height ≈ 0.5-1 µm) with a perovskite bandgap of $E_g = 1.67$ eV (DC opt. perovskite) and with 100 nm of MgF_2 as antireflective coating. The molarity of the perovskite precursor solution is adjusted to 1.7 M, with the concentration of the bulk passivation scaled accordingly. The surface passivation concentration is the same as for single-junction (SJ) perovskite solar cells (PSCs). Adapted from reference[285] with permission from Wiley.

of the Si bottom cells feature pyramidal outliers exceeding 5 µm in height (Figure 5.24d). While such outliers are not present on every Si bottom cell, their occurrence poses a challenge for complete perovskite coverage *via* solution processing. This explains the incomplete coverage observed in top-view SEM images, potentially increasing the risk of a shunted cell (Figure 5.24e). Nevertheless, the results demonstrate the feasibility of fabricating perovskite films even on large-textured Si bottom cells (2-5 µm) using the fully solution-based two-step method, while also highlighting the need for further process optimization to enhance device performance.

Reducing the pyramid height to below 2 µm (referred to as small-textured) results in a PCE of 26.2% in the backward scan, a V_{OC} of 1.83 V, a J_{SC} of 18.6 mA cm^{-2}, and a FF of 76.6% for the champion TSC (Figure 5.25a). While the efficiency remains below record values of 35%,[14] this represents one of the highest reported efficiencies for a 2T perovskite/Si TSC on a small-textured Si bottom cell fabricated *via* a fully solution-based two-step process. Compared to the large-textured tandem devices, the FF is significantly improved, and the *J*-*V* characteristic exhibits only a small hysteresis of 1.1%. However, similar to the large-textured TSCs, a low shunt resistance is observed, indicating non-optimal perovskite film quality. The EQE spectra reveal a current mismatch of 1.1 mA cm^{-2} (Figure 5.25b), with the TSC being bottom-limited. This bottom cell limitation is rather unusual for textured Si bottom cells, as the texture is designed to enhance optical light-incoupling through reduced reflection, which typically results in J_{SC} of > 19 mA cm^{-2}.[380] Consequently, further advancements in light management are essential for future efficiency improvements. In contrast to large-textured Si bottom cells, SEM images confirm complete perovskite coverage on submicron pyramidal textures (Figure 5.25c).

Considering the bandgap energy, interestingly, all perovskite thin films exhibit a shift in the bandgap toward higher energies (Figure 5.26a), despite using the optimized DC perovskite with a bandgap of 1.67 eV. This shift is likely attributed to altered crystallization behavior of the perovskite on top of the Si bottom cell, as well as an increased

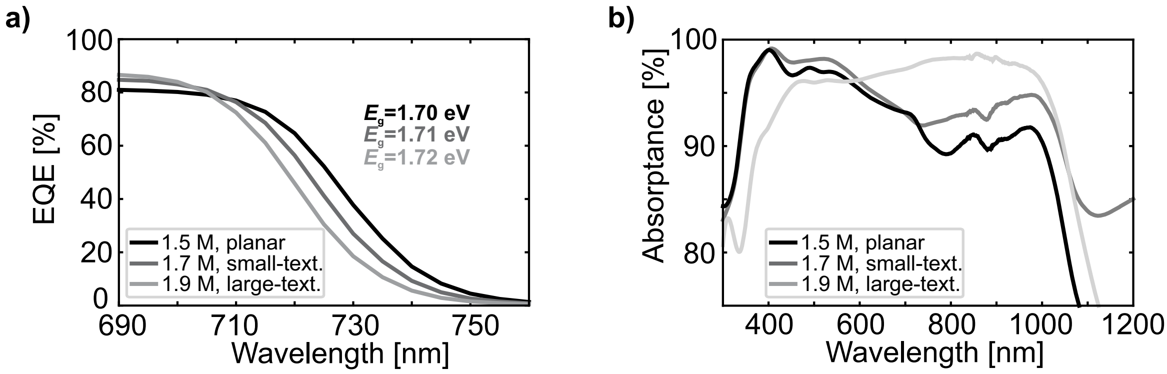

Figure 5.26: Optical bandgap (E_g) extracted from the inflection point of the external quantum efficiency (EQE) spectra, and b) absorptance spectra of planar (1.5 M perovskite solution concentration), small-textured (1.7 M perovskite solution concentration) and large-textured (1.9 M perovskite solution concentration) two-terminal (2T) perovskite/silicon (Si) tandem solar cells (TSCs). The absorptance spectra are smoothed using a Savitzky-Golay filter (window length = 51, polynomial order = 3) to reduce measurement noise and the artifact observed around 900 nm originates from the measurement setup. Adapted from reference[285] with permission from Wiley.

film thickness resulting from higher perovskite precursor solution molarity. The absorptance spectra of the three different 2T perovskite/Si tandem configurations (Figure 5.26b) highlight the critical role of light management in enhancing optical absorption, particularly in the long wavelength range of ≈ 700-1000 nm, and consequently, device performance. Notably, the large-textured Si bottom cells exhibit the highest absorptance, approaching nearly 100% in the near infrared region, underscoring their effectiveness in maximizing light harvesting. Although the achieved efficiencies remain below those of state-of-the-art 2T perovskite/Si TSCs – where efficiencies exceeding 33% have been demonstrated on micron-scale textured Si bottom cells (pyramid height $>$ 1 µm) using a hybrid two-step deposition method[89] – the results presented here represent the highest efficiencies obtained for 2T perovskite/Si TSCs processed *via* the fully solution-based two-step method at the time of this study. Moreover, this work constitutes the first systematic investigation of fully solution-based two-step processed perovskite thin films on different pyramidal texture heights in 2T perovskite/Si tandem configuration, highlighting the versatility of the developed deposition method. While this study serves as a proof of concept, further advancements – such as enhanced light management, precise bandgap engineering and layer thickness optimization – will be crucial to unlocking the full efficiency potential of these devices.

5.6 Summary

This chapter advances compositional engineering and surface passivation strategies to enhance device performance and long-term operational stability of wide-bandgap PSCs fabricated with a fully solution-based two-step deposition method – a fabrication method of increasing relevance for scalable, industrially relevant 2T perovskite/Si tandem integration. Building on the wide-bandgap perovskite thin film developed in Chapter 4, the incorporation of CsI in the bulk improves the perovskite film morphology and crystallinity, leading to enhanced charge-carrier extraction and increased J_{SC} at the device level – an important factor for current matching in 2T tandem configuration. However, Cs incorporation simultaneously introduces detrimental interfacial effects at the perovskite/C_{60} interface, as evidenced by a reduced V_{OC}. Applying a 1 nm LiF layer as surface passivation effectively compensates these interfacial losses and restores the V_{OC}, increasing the PCE from 15.9% for the Control devices to 18.5% for the devices with CsI and LiF.

To further address voltage deficits and improve long-term operational stability, a novel dual bimolecular passivation strategy using $PDAI_2$ and BAI for both bulk and surface passivation is introduced for a MA-free perovskite composition. By passivating bulk and surface defects, this strategy effectively reduces non-radiative recombination at both the perovskite/C_{60} interface and grain boundaries, resulting in an overall improvement in V_{OC}. Additionally, enhanced crystallinity and the formation of a 2D capping layer atop the 3D perovskite promote charge-carrier extraction, leading to an increase in J_{SC}. As a result, the device performance improves from 19.2% up to 20.9%, with a V_{OC} of 1.24 V, a J_{SC} of 20.8 mA cm^{-2}, and a FF exceeding 80%. Notably, both V_{OC} and J_{SC} reach approximately 90% of the DB limit for $E_g \approx 1.67$ eV. At the time this study was conducted, this represented the highest reported PCE for a MA-free *p-i-n* type PSC with a bandgap of 1.67 eV processed *via* a fully solution-based two-step method. As of that date, and to the best of my knowledge, only two additional studies had reported wide-bandgap ($E_g \geq 1.63$ eV) PSCs in the *p-i-n* architecture fabricated *via* a fully solution-based two-step method.[57,284] The most recent study – published after the results presented here – achieved nearly 22% PCE for a perovskite with $E_g \approx 1.68$ eV (Table A.7).[284]

The dual bimolecular passivation strategy significantly enhances operational stability, reaching T_{80} after 180 h of continuous illumination at 25 °C in N_2 atmosphere. Despite the stability improvements, it still lags behind current state-of-the-art stability metrics with $> 90\%$ of their initial PCE after about 1200 h of continuous illumination.[366]

XPS analysis provides a deeper mechanistic understanding of the investigated surface passivation strategies LiF and $PDAI_2$+BAI. LiF forms a homogeneous layer of 1 nm thickness, and, due to its physical passivation nature, induces only minor changes in surface chemistry of the perovskite thin film. In contrast, $PDAI_2$+BAI surface treatment chemically modifies the perovskite surface, widening the surface bandgap by 150 meV due to higher Br content. Furthermore, $PDAI_2$+BAI passivation effectively reduces the presence of metallic Pb^0 and oxidized Pb species, thereby lowering the defect density and suppressing non-radiative recombination – key factors contributing to the improved device performance and stability.

Finally, the optimized perovskite thin film with dual bimolecular passivation is integrated into 2T perovskite/Si tandem architectures using planar, small-textured (pyramid height ≈ 0.5-1 µm), and large-textured (pyramid height ≈ 2-5 µm) Si bottom cells. Efficiencies of 28.0% for planar, 26.2% for small-textured, and 24.1% for large-textured Si bottom cells are achieved, demonstrating the compatibility of the developed fully solution-based two-step deposition method with industrially relevant Si surface textures. Although these efficiencies remain below state-of-the-art 2T perovskite/Si TSCs – where efficiencies exceeding 33% have been demonstrated on micron-scale textured Si bottom cells (pyramid height > 1 µm) using a hybrid two-step deposition[89] – the results presented here represent the highest efficiencies reported for 2T perovskite/Si TSCs processed *via* the fully solution-based two-step method at the time of this study. Moreover, this work constitutes the first systematic investigation of fully solution-based two-step processed perovskite thin films on different pyramidal texture heights in 2T perovskite/Si tandem configuration, highlighting the versatility of the developed deposition method. Notably, a subsequent study[284] – published after the results presented here – achieved an efficiency of 31.12% for a 2T perovskite/Si TSC with a fully solution-based two-step processed perovskite thin film on submicron-textured Si bottom cells.

The impact of this study extends beyond the devices demonstrated in this chapter. The bimolecular surface passivation strategy developed here has already been successfully transferred to hybrid-processed PSCs and 2T perovskite/Si tandems in subsequent studies by Pesch *et al.*[69], and Petry and Pappenberger *et al.*[204], highlighting its robustness and broader applicability across fabrication platforms.

In conclusion, this chapter highlights the potential of compositional engineering and strategic defect management using advanced passivation techniques (research question **III**) to improve thin-film formation (research question **II**), device performance and long-term operational stability (research question **V**). Ultimately, the resulting perovskite thin film is successfully implemented in 2T perovskite/Si TSCs (research question **IV**), providing a foundation for the development of high-efficiency, stable, and industrially relevant 2T perovskite/Si TSCs using the fully solution-based two-step deposition method.

6 CsCl Seed Layer for Improved Stability and Fabrication Yield of Solution-Based Two-Step Processed Perovskite Thin Films

In industrial photovoltaic manufacturing, silicon solar cells typically feature micron-sized pyramidal textures to enhance light-incoupling and reduce reflection losses. For industrially relevant two-terminal perovskite/silicon tandem solar cells, uniform, conformal, and defect-free perovskite coverage on such pronounced surface textures is therefore essential to achieve efficient current matching and high device performance. However, conventional solution-based deposition methods have difficulty reliably covering such surface textures, leading to incomplete perovskite coverage, thickness variations, and reduced fabrication yield. To address this challenge, this chapter introduces a first step toward a hybrid deposition route, combining vapor deposition with the fully solution-based two-step deposition method developed in Chapter 5. Specifically, a 5 nm thick CsCl seed layer is vapor-deposited at the hole transport layer/perovskite interface to promote nucleation and controlled film formation in regions where solution processing alone proves insufficient. While CsCl is known to improve perovskite film formation, its poor solubility in common precursor solvents hinders direct incorporation into the solution process, making vapor deposition a practical and industry-compatible alternative. This chapter systematically examines the impact of the CsCl seed layer on the microstructure of both the inorganic scaffold and the perovskite thin film (research questions ***II & III****), with the overarching goal of enhancing film quality, device performance, and long-term operational stability (research question* ***V****). Finally, the CsCl-seeded perovskite thin film is integrated into a two-terminal perovskite/silicon tandem architecture to evaluate its compatibility with textured silicon bottom cells (research question* ***IV****). By assessing surface coverage and film morphology across different surface textures, this chapter investigates the role of the CsCl seed layer in improving process repeatability and fabrication yield – key requirements for low-cost, industrial manufacturing of tandem solar cells.*

Parts of this chapter review the research article "CsCl Seed Layer for Improved Stability and Fabrication Yield of Solution-Based Two-Step Processed Perovskite Thin Films" (manuscript in preparation) by *R. Pappenberger (R.P.)* as first author, together with *A. Diercks*, *R. Singh*, *A. Welle*, *T. Zhao*, *J. Petry*, and *U. W. Paetzold.*
R.P. contributed to this work by conceptualizing the study, leading experimental investigations, data curation, formal analysis, and visualization. The contributions of all authors involved in this study are listed in Table A.5 according to the CRediT system.

6.1 Motivation

Commercial Si bottom cells used in state-of-the-art PV modules typically feature micrometer-scale random pyramidal textures ($\approx$ 2-5 µm), which significantly enhance light-incoupling and trapping compared to their planar counterparts. Such surface texturing is essential for achieving a high J_{SC} and, consequently, maximizing device performance of 2T perovskite/Si TSCs.[41–46] However, conformal perovskite coverage over such pronounced textures remains a major challenge for conventional solution-based deposition methods. Incomplete film coverage can lead to severe shunting pathways and thickness inhomogeneities, drastically reducing both device performance and fabrication yield.[76,373] Vapor-deposition techniques provide conformal perovskite coverage on textured substrates, but they often suffer from limited device performance and poor process repeatability due to the volatile nature of organic components and the complexity of multi-source co-deposition.[374,381–385]

Among various perovskite fabrication techniques, the two-step deposition method – comprising the subsequent deposition of the inorganic precursor materials and the organic cations – has emerged as a promising route to process uniform and high-quality perovskite thin films. This method is highly versatile and compatible with large-area deposition techniques such as vapor deposition,[67] slot-die coating,[70] ink-jet printing[68], and hybrid deposition routes – combining vapor deposition with solution-based deposition.[76–81] Hybrid deposition routes in particular have demonstrated high perovskite film quality on textured Si bottom cells suitable for 2T tandem integration.[89] Yet, a key question remains unresolved: Can a fully solution-based deposition method – with its advantages in simplicity and cost-effectiveness – be adapted to reliably cover textured substrates without relying on fully vapor-deposited inorganic scaffolds?

One promising strategy to promote perovskite film crystallization involves the incorporation of alkali halides such as CsCl into the inorganic scaffold. While CsCl is known to enhance perovskite crystallinity,[386] its poor solubility in common precursor solvents (DMF/DMSO) hinders direct incorporation into solution-based precursors. As a practical alternative, CsCl can be vapor-deposited as an ultrathin seed layer at the HTL/perovskite interface. Previous studies have demonstrated that CsBr seed layers can mitigate residual PbI_2 at the HTL/perovskite interface and improve film formation in hybrid-processed perovskite films on textured Si bottom cells,[78] while CsCl seed layers in fully vapor-processed perovskite films have been shown to improve crystallization and bandgap control.[387] However, the influence of such a CsCl seed layer in fully solution-based wide-bandgap PSCs remains unexplored. Introducing a seed layer in this context represents a conceptual bridge between fully solution-based and hybrid two-step deposition methods, combining the simplicity of solution-based processing with the structural benefits of vapor deposition. This strategy aims to overcome one of the critical hurdles in the fabrication of industrially viable perovskite/Si TSCs: reliable perovskite coverage on micrometer-textured Si bottom cells combined with a high fabrication yield.

Section 6.2 introduces the CsCl seed layer strategy within the fully solution-based two-step method used in this chapter. Section 6.3 presents a systematic material characterization, examining the crystallinity and morphology of both inorganic scaffolds and perovskite films. To assess the influence of the CsCl seed layer at device level, PSCs are fabricated and the corresponding results are discussed in Section 6.4. Section 6.5 investigates the impact of the CsCl seed layer on long-term device stability, while Section 6.6 validates the process compatibility with the 2T perovskite/Si tandem configuration, focusing on textured Si bottom cells.

6.2 Fabrication Process

This chapter builds upon the wide-bandgap perovskite thin film developed in Chapter 5 with the nominal composition $Cs_{0.16}FA_{0.84}Pb(I_{0.79}Br_{0.21})_3$ (DC opt.). The solution-based two-step method used to fabricate the perovskite thin films in this chapter is schematically illustrated in Figure 6.1a. Devices without any further modification serve as reference (labeled as Ref), while devices with a vapor-deposited CsCl seed layer at the HTL/perovskite interface are labeled as CsCl. Applying the CsCl seed layer is straightforward, requiring only a single vapor-deposition step

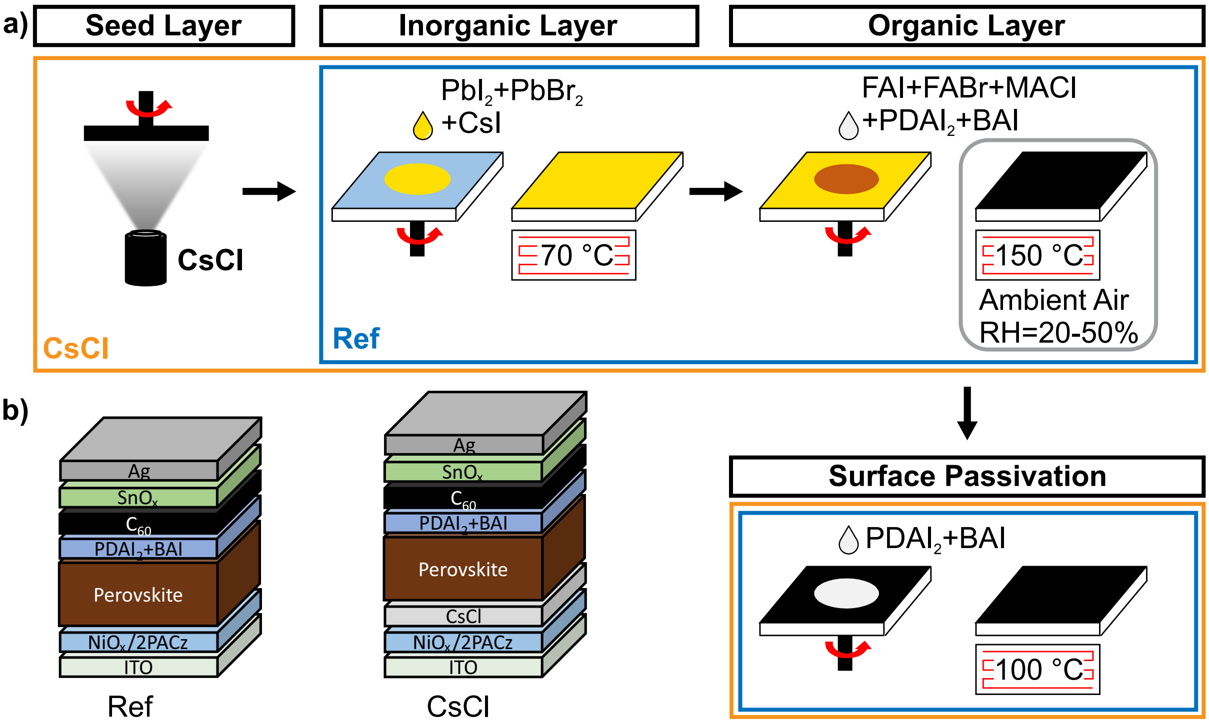

Figure 6.1: a) Schematic illustration of the solution-based two-step deposition method for fabricating the perovskite thin film discussed in this chapter. The reference (Ref) devices follow the established route from Chapter 5 (DC opt.), while CsCl devices include an additional CsCl vapor-deposition step prior to inorganic precursor deposition. Both configurations use the same organic cation solution and surface passivation based on the developed DC opt. recipe. The perovskite film is annealed under ambient conditions with a relative humidity (RH) of $\approx$ 20-50%. b) Schematic of the perovskite solar cell (PSC) architecture (*p*-*i*-*n*) used in this chapter.

without post-deposition annealing. The CsCl seed layer thickness is optimized to 5 nm (Figure A.20). Both Ref and CsCl devices use a combination of $PDAI_2$ and BAI for bulk and surface passivation, following the optimized recipe established in Chapter 5. The PSCs follow the layer stack ITO/NiO_x/2PACz/perovskite/$PDAI_2$+BAI/C_{60}/SnO_x/Ag (Figure 6.1b). SnO_x is used instead of BCP to better reflect the final device architecture of the TSCs.

6.3 Microstructure Analysis

To examine the influence of the CsCl seed layer on the surface morphology and microstructure of inorganic scaffolds and perovskite films, XRD, GIWAXS, SEM, and AFM measurements are performed on half-stacks with the architecture ITO/NiO_x/2PACz/inorganic or perovskite layer. Perovskite films with surface passivation are also included in the analysis; however, a more detailed discussion of the effects of surface passivation is provided in Chapter 5, Section 5.3.1.

XRD measurements (Figure 6.2a) confirm that both Ref and CsCl inorganic scaffolds exhibit characteristic PbI_2 diffraction peaks at $\approx 12.2°$ ((001) crystal plane) and at $\approx 25.0°$ ((002) crystal plane) with comparable intensity. For the inorganic scaffold with CsCl seed layer, no diffraction peak associated with CsCl is detected, indicating that the CsCl seed layer does not form a separate crystalline phase within the scaffold or is likely too thin to be detected by XRD. This suggests that CsCl acts primarily as an interfacial modifier rather than contributing to the crystalline structure of the inorganic scaffold. Perovskite films without surface passivation display characteristic diffraction peaks at $\approx 13.7°$, $\approx 19.6°$, $\approx 24.2°$ and $\approx 28.1°$, corresponding to the (100), (110), (111) and (200) crystal planes of the 3D perovskite, respectively. Both configurations – Ref and CsCl – retain a comparable amount of residual

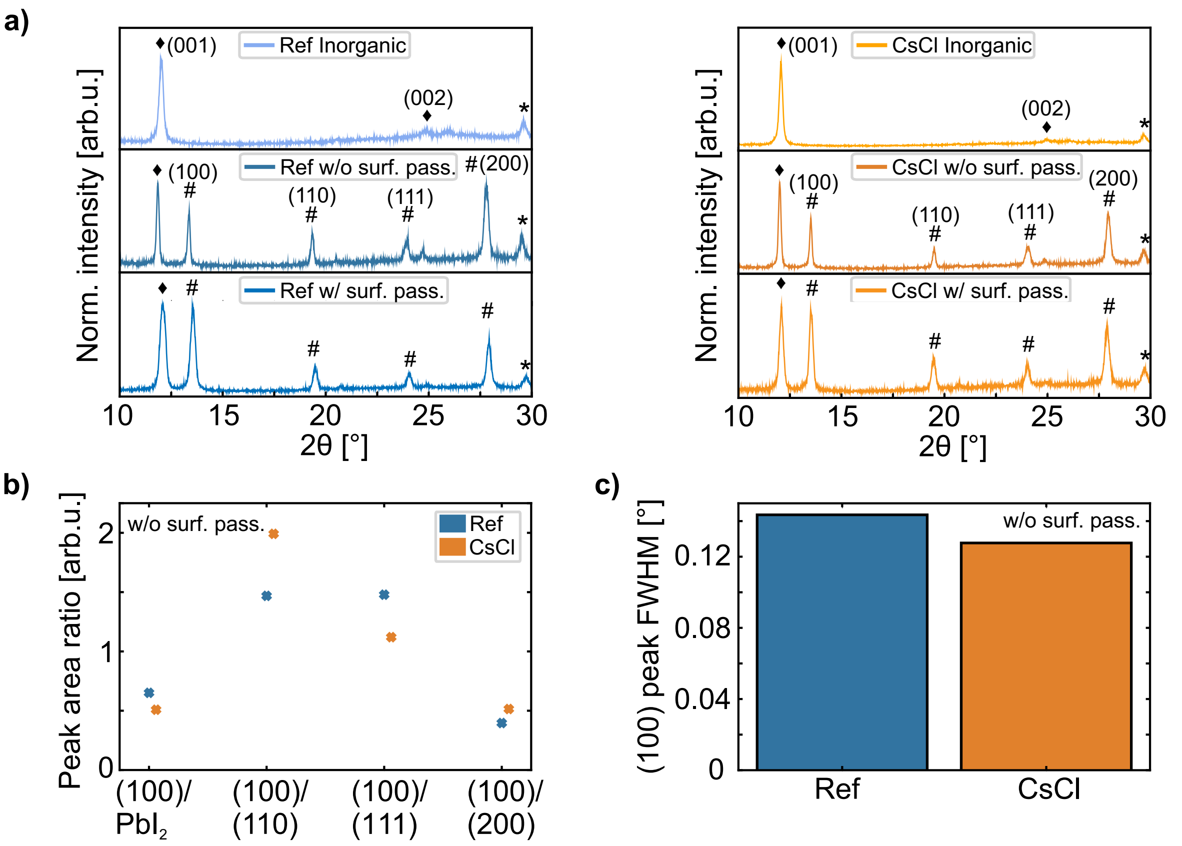

Figure 6.2: a) X-ray diffraction (XRD) patterns (♦ denotes the PbI$_2$ phase, # the perovskite phase and $*$ the indium tin oxide (ITO) phase) of the inorganic scaffolds and perovskite films without any further modification (Ref) and with 5 nm CsCl seed layer (CsCl) fabricated on glass/indium tin oxide (ITO)/NiO$_x$/2PACz. b) Peak area ratios, and c) full width at half maximum (FWHM) of the (100) perovskite peak of perovskite films without surface passivation.

PbI$_2$ in the perovskite film (Figure 6.2b), which is further reduced upon applying bimolecular surface passivation. CsCl perovskite films exhibit a more pronounced (111) crystal orientation (Figure 6.2b), a trend unaffected by the bimolecular surface passivation (Figure A.21a). A dominant (111) crystal orientation has previously been associated with enhanced stability,[388] a point that will be discussed in detail in Section 6.5.

Analysis of the FWHM of the (100) perovskite peak (Figure 6.2c) reveals a slightly narrower peak for CsCl perovskite films (0.13°) compared to Ref perovskite films (0.14°). This trend becomes more pronounced after applying surface passivation (Figure A.21b), where the FWHM increases to 0.27° for Ref but only to 0.21° for CsCl perovskite films. The consistently reduced FWHM indicates improved crystal quality and hints at a lower defect density in perovskite films with CsCl seed layer, an effect further enhanced by surface passivation.

GIWAXS measurements are conducted on both the inorganic scaffold and the perovskite film to complement the XRD analysis and provide deeper insights into the preferred crystal orientations (Figure A.22). For the inorganic scaffold (Figure 6.3a), the (001) PbI$_2$ crystal plane remains unaffected by the presence of a CsCl seed layer. Both Ref and CsCl inorganic scaffolds exhibit a selective out-of-plane orientation, corresponding to a horizontal layer growth of PbI$_2$ platelets. This growth mode represents the intrinsic growth mode of pure PbI$_2$ deposited *via* spin coating.[389] The corresponding perovskite films reveal a subtle difference in the preferred crystal orientation of the (100) perovskite phase (Figure 6.3b). For perovskite films without surface passivation, CsCl perovskite films exhibit a noticeably narrower scattering distribution at 60°, indicating a more uniform crystal orientation compared to Ref perovskite films. This suggests that the CsCl seed layer promotes controlled nucleation and reduces orientation disorder within the perovskite film. After applying surface passivation, the crystal orientation shifts slightly toward higher scattering angles – particularly pronounced in CsCl perovskite films – suggesting a

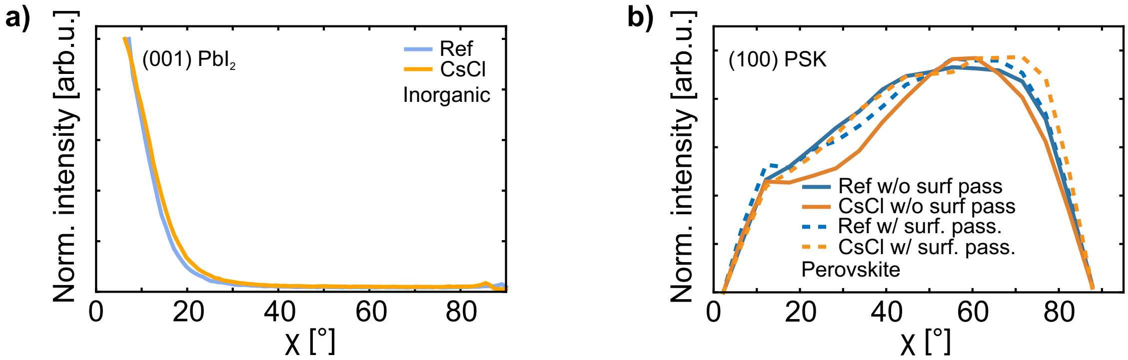

Figure 6.3: Pole figure of the a) (100) PbI_2 phase for inorganic scaffolds, and the b) (100) perovskite (PSK) phase for perovskite films (without and with surface passivation) without any further modification (Ref) and with 5 nm CsCl seed layer (CsCl) fabricated on glass/indium tin oxide (ITO)/NiO_x/2PACz.

preferential vertical orientation of the perovskite crystallites. Such vertical alignment, consistent with observations in Chapter 5, Section 5.3.1 has been associated with improved charge-carrier transport.

The surface morphology of the inorganic scaffolds and perovskite films is characterized by SEM and AFM measurements. Top-view SEM images (Figure 6.4) show that both inorganic scaffolds possess a porous structure with visible pinholes, which become less frequent upon introducing a CsCl seed layer. This observation is supported by AFM measurements (Figure 6.5), showing a slight reduction in RMS surface roughness from 34.6 nm (Ref) to 32.2 nm (CsCl). Cross-sectional SEM images (Figure A.23) confirm that the porosity extends throughout the entire inorganic scaffold. Such porosity can be advantageous as it facilitates infiltration of the organic precursor solution and promotes complete conversion to the perovskite phase. However, excessive pinholes may introduce defects and negatively impact device performance.

The corresponding perovskite films exhibit a similar surface morphology, but CsCl perovskite films show a modest increase in grain size – from 364 nm for Ref to 396 nm for CsCl perovskite films (Figure A.24). This trend is consistent with the slight decrease in the FWHM of the (100) perovskite diffraction peak (Figure 6.2c), suggesting improved crystallinity. Notably, cross-sectional SEM images (Figure A.23) show no discernible grain boundaries

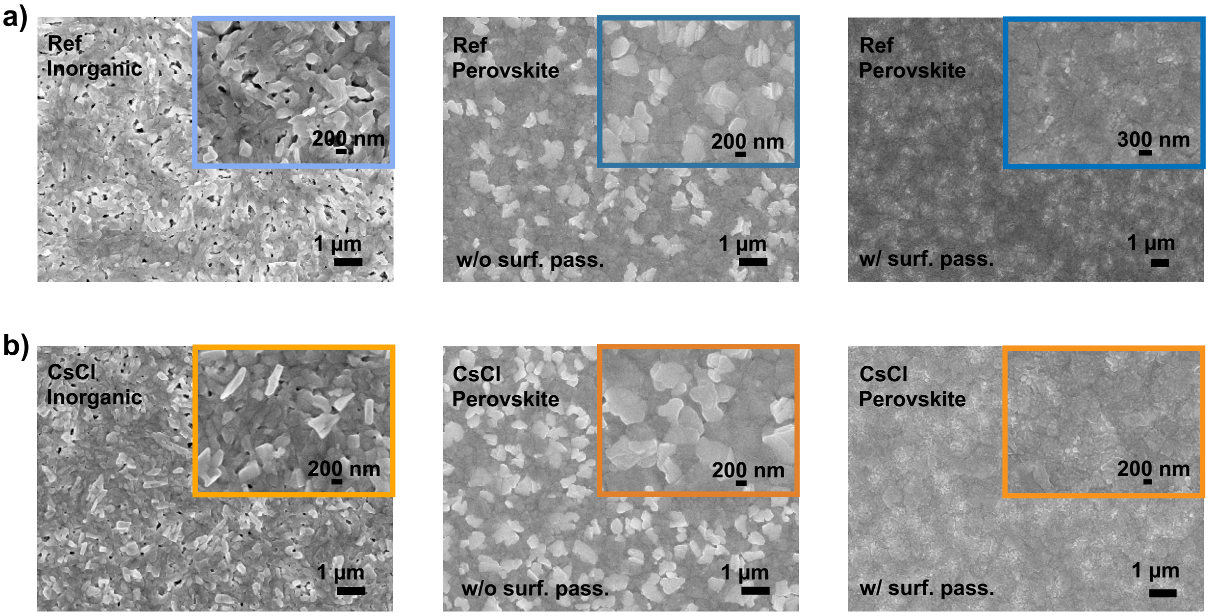

Figure 6.4: Top-view scanning electron microscopy (SEM) images of the inorganic scaffolds and the perovskite films (without and with surface passivation) a) without any further modification (Ref), and b) with 5 nm CsCl seed layer (CsCl) fabricated on glass/indium tin oxide (ITO)/NiO_x/2PACz.

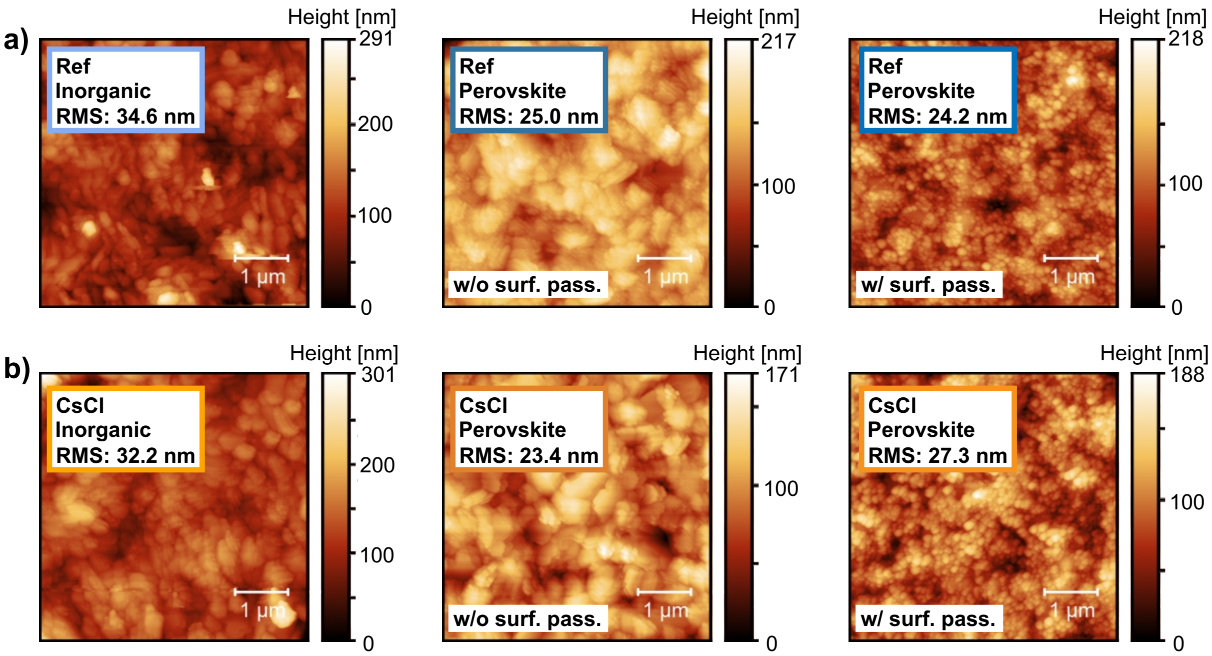

Figure 6.5: Atomic force microscopy (AFM) images of the inorganic scaffolds and the perovskite films (without and with surface passivation) a) without any further modification (Ref), and b) with 5 nm CsCl seed layer (CsCl) fabricated on glass/indium tin oxide (ITO)/NiO$_x$/2PACz. For each parameter, two to three measurements are taken, and the average root-mean-square (RMS) value is calculated.

throughout the perovskite layer, indicating excellent film uniformity and high-quality crystallization for both Ref and CsCl perovskite films. CsCl perovskite films maintain a slightly lower RMS surface roughness (23.4 nm compared to 25.0 nm for Ref). A reduction in surface roughness for both the inorganic scaffold and the perovskite film has also been reported by Li *et al.*[78] when using a CsBr seed layer. This decrease in roughness is attributed to perovskite lattice expansion induced by the seed layer. Owing to the bottom-up crystallization characteristic of two-step deposition, the presence of the seed layer directs the overlying perovskite to crystallize preferentially along the (100) orientation, as also evidenced by XRD measurements (Figure 6.2b). Such oriented vertical growth leads to a smoother surface, which likely enhances interfacial coupling with the ETL and contributes to improved

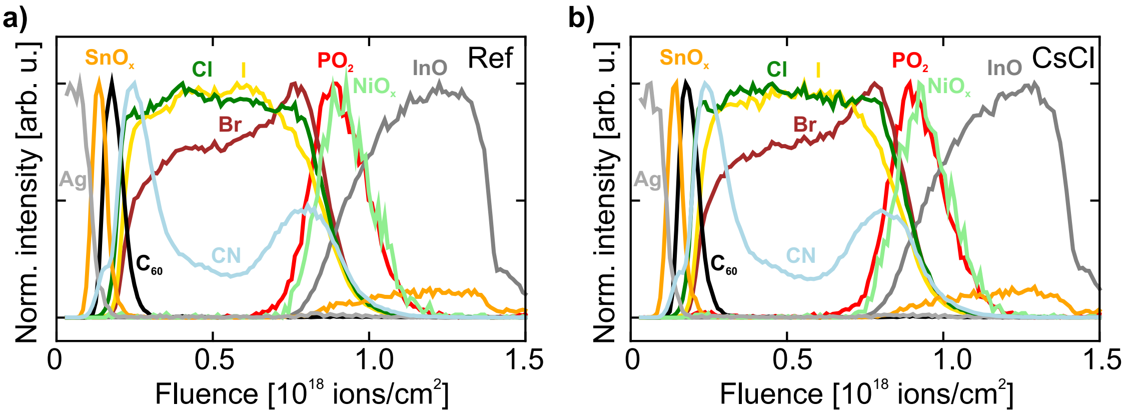

Figure 6.6: Normed time-of-flight secondary ion mass spectrometry (ToF-SIMS) measurements (negative polarity) of perovskite solar cells (PSCs) a) without any further modification (Ref), and b) with 5 nm CsCl seed layer (CsCl). The PSCs have the layer stack glass/ITO/NiO$_x$/2PACz/perovskite/PDAI$_2$+BAI/C$_{60}$/SnO$_x$/Ag. The following fragments are displayed: InO: $\mathrm{InO^-}$; NiO$_x$: $\mathrm{NiO^-}$; PO$_2$: $\mathrm{PO_2^-}$; I: $\mathrm{I^-}$; Cl: $\Sigma(^{37}\mathrm{Cl^-}, \mathrm{Cl^-})$; Br: $^{81}\mathrm{Br^-}$; CN: $\mathrm{CN_2^-}$; C$_{60}$: $\Sigma(\mathrm{C_3^-}, \mathrm{C_4^-}, \mathrm{C_6^-})$; SnO$_x$: $\Sigma(^{116}\mathrm{SnO^-}, ^{118}\mathrm{SnO^-}, \mathrm{SnO^-})$; Ag: $\Sigma(^{109}\mathrm{AgO^-}, \mathrm{AgO^-})$.

device performance.[78] However, after applying the surface passivation layer, the RMS surface roughness increases to 27.3 nm for CsCl perovskite films, whereas it decreases to 24.2 nm for Ref perovskite films. The origin of this effect is unclear and requires further investigation. Both the top-view SEM images (Figure 6.4) and the AFM images (Figure 6.5) show that the surface passivation layer exhibits the same lamellar structure previously observed in Chapter 5, Figure 5.10.

To probe the qualitative elemental distribution as a function of depth, ToF-SIMS depth profiling is conducted on both Ref and CsCl PSCs with the layer stack ITO/NiO_x/2PACz/(CsCl)/perovskite/$PDAI_2$+BAI/C_{60}/SnO_x/Ag. The characteristic negatively charged secondary ions of the relevant species in the final PSCs are displayed in Figure 6.6. Both PSCs – Ref and CsCl – exhibit an almost identical elemental distribution across the entire layer stack. Notably, Cl is detected in both perovskite films, indicating that Cl introduced *via* MACl not only acts as an additive during film formation but also becomes incorporated into the perovskite bulk. This incorporation is likely due to the bimolecular surface passivation with $PDAI_2$ and BAI, which prevents complete MACl evaporation during the final annealing step, as confirmed by XPS analysis in Chapter 5, Section 5.4. However, ToF-SIMS measurements cannot unambiguously confirm the presence of MA in the perovskite film, since CN fragments originate from both FA and MA. Regarding elemental distribution, both Cl and I are homogeneously distributed throughout the perovskite layer, whereas Br tends to accumulate at the HTL interface. Interestingly, organic CN fragments are enriched at both the HTL and ETL interfaces, suggesting preferential segregation of organic species at the perovskite/CTL interfaces.

Materials characterization indicates that the CsCl seed layer maintains the already high perovskite film quality while subtly modifying the microstructure in a potentially beneficial manner by enhancing grain growth, reducing pinhole density, and improving crystallinity.

6.4 Photovoltaic Performance

To assess the impact of the CsCl seed layer on device performance, PSCs are fabricated in *p-i-n* architecture with the layer stack ITO/NiO_x/2PACz/(CsCl)/perovskite/$PDAI_2$+BAI/C_{60}/SnO_x/Ag (Figure 6.1b).

Table 6.1: Photovoltaic parameters (open-circuit voltage (V_{OC}), short-circuit current density (J_{SC}), fill factor (FF), power conversion efficiency (PCE) and hysteresis index (HI)) of the champion opaque perovskite solar cells (PSCs) without any further modification (Ref), and with 5 nm CsCl seed layer (CsCl).

Perovskite name	Scan direction	V_{OC} [V]	J_{SC} [mA cm^{-2}]	FF [%]	PCE [%]	HI [%]
Ref	backward	1.21	19.5	77.8	18.3	7.7
	forward	1.20	19.4	72.5	16.9	
CsCl	backward	1.20	19.7	80.4	19.0	5.5
	forward	1.20	19.7	76.4	18.0	

PSCs with CsCl seed layer exhibit a significantly improved FF and reduced hysteresis in the *J-V* characteristics (Table 6.1 and Figure 6.7a/b/c) and the statistical analysis of the PV parameters (Figure 6.8). A similar FF enhancement has previously been reported by Li *et al.*[78] using a CsBr seed layer. The enhanced FF enables a champion performance of 19.0% in the backward scan with a V_{OC} of 1.20 V, a J_{SC} of 19.7 mA cm^{-2}, and a FF of 80.4%. Despite using the same perovskite composition as in Chapter 5, Section 5.3 (DC opt.) for both Ref and CsCl PSCs, a general decline in device parameters is observed, and the previously achieved champion performance could not be reproduced. The underlying cause remains unclear but may partly relate to the transition from BCP to SnO_x as ETL. Statistical analysis using *Welch's t test*[236] confirms that the FF – and consequently the PCE – improvement for the CsCl devices is statistically significant (Table A.11).

A modest increase in J_{SC} is observed for CsCl PSCs in the backward scan (Figure 6.8), although EQE measurements

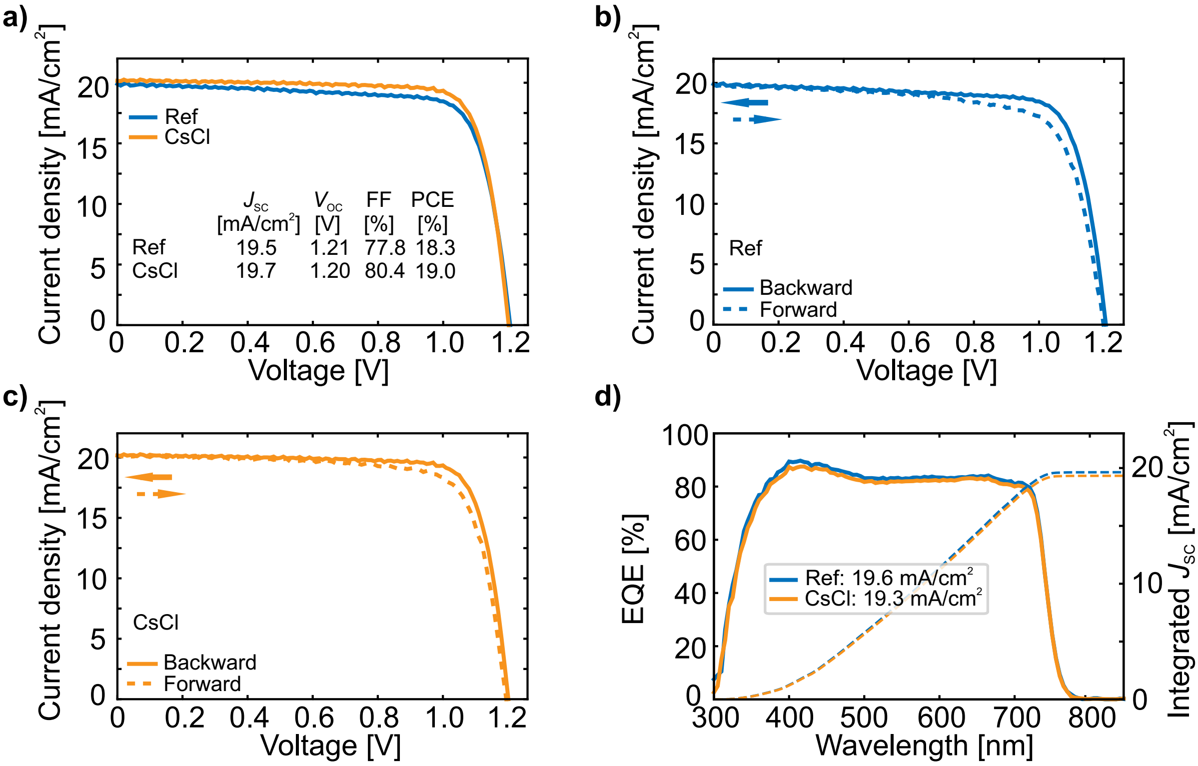

Figure 6.7: Current density *versus* voltage (*J*-*V*) characteristics of the best-performing perovskite solar cells (PSCs) a) for all parameters to facilitate comparison, and b) without any further modification (Ref), and c) with 5 nm CsCl seed layer (CsCl) in both scan directions (backward and forward). d) External quantum efficiency (EQE) spectra as well as the corresponding integrated short-circuit current density (J_{SC}).

do not support this trend (Figure 6.7d). The small Cl content introduced by the CsCl seed layer is insufficient to alter the perovskite bandgap (Figure A.25a), and the absorption spectra remain comparable (Figure A.25b), suggesting marginally improved charge-carrier extraction for CsCl PSCs. This improvement may be linked to the more vertical perovskite crystal orientation indicated by GIWAXS measurements (Figure 6.3b).

Despite improved charge-carrier extraction and enhanced FF, the V_{OC} decreases by ≈ 9 mV compared to Ref PSCs. PLQY measurements support this observation (Figure A.26), showing a reduced PLQY and $V_{OC\text{-imp}}$ for CsCl

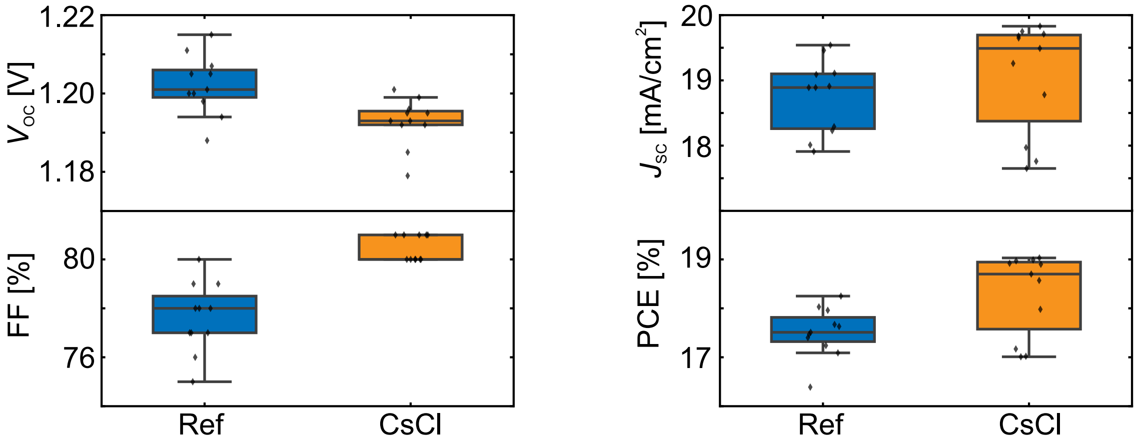

Figure 6.8: Statistical distribution (in total 22 devices) of the open-circuit voltage (V_{OC}), fill factor (FF), short-circuit current density (J_{SC}) and power conversion efficiency (PCE) for opaque perovskite solar cells (PSCs) without any further modification (Ref), and with 5 nm CsCl seed layer (CsCl).

perovskite films without C_{60} ETL. This reduction is accompanied by an increased n_{id} (1.20 for Ref and 1.29 for CsCl), indicating less favorable bulk properties. Interestingly, adding the C_{60} ETL increases the PLQY and $V_{OC\text{-imp}}$ values above the values for Ref perovskite films, suggesting improved interfacial quality at the perovskite/C_{60} interface. Together with the reduced hysteresis, this points to CsCl primarily enhancing interfacial properties. However, n_{id} further increases (1.20 for Ref and 1.35 for CsCl), highlighting persistent bulk-related non-radiative recombination losses. The influence of the CsCl seed layer on the interface energy-level alignment, as previously observed for CsBr seed layer by Li *et al.*[78], is unknown and requires further investigation.

Overall, the results highlight that introducing a 5 nm CsCl seed layer at the HTL/perovskite interface proves to be an effective strategy for *p-i-n* PSCs. The slightly beneficial influenced microstructural properties caused by the CsCl seed layer results in enhanced device performance, particularly a significantly improved FF. However, the observed reduction in V_{OC} requires further optimization.

6.5 Long-Term Operational Stability

In order to evaluate the impact of the CsCl seed layer on device stability, three standardized ISOS protocols are used to probe degradation under different stress conditions: dark storage (ISOS-D1: dark storage, 25°C, intermittent *J*-*V*), elevated temperatures (ISOS-D2: dark storage, 85°C, intermittent *J*-*V*), and continuous light exposure (ISOS-L1: 100 mW cm^{-2}, 25 °C, MPP tracking).[226] All stability measurements are performed under N_2 atmosphere. For each parameter, multiple semitransparent PSCs with the layer stack glass/ITO/NiO_x/2PACz/(CsCl)/perovskite/$PDAI_2$+BAI/C_{60}/ SnO_x/IZO/Au are subjected to these test conditions. The corresponding mean values and standard deviations

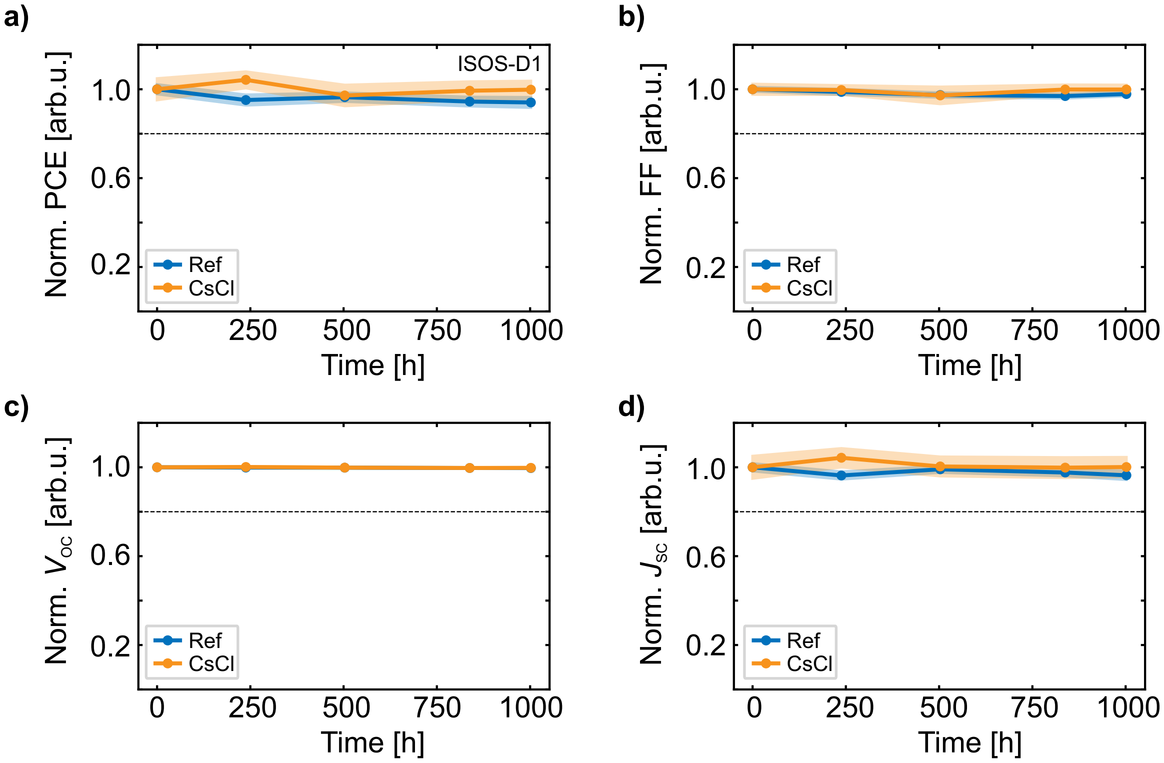

Figure 6.9: Normalized a) power conversion efficiency (PCE), b) fill factor (FF), c) open-circuit voltage (V_{OC}), and d) short-circuit current density (J_{SC}) from current density *versus* voltage (*J*-*V*) measurements of semitransparent (ST) perovskite solar cells (PSCs) without any further modification (Ref) and with 5 nm CsCl seed layer (CsCl) under ISOS-D1 testing conditions (dark storage, 25 °C, intermittent *J*-*V*) for 1000 h. Mean values and standard deviations based on twelve devices per parameter are provided.

are provided.

To examine the effect of dark storage on stability, semitransparent devices are stored under ISOS-D1 test conditions for 1000 h. Figure 6.9 shows the normalized PCE, FF, V_{OC} and J_{SC} from intermittent *J-V* measurements for Ref and CsCl PSCs. Both configurations – Ref and CsCl – exhibit stable performance over 1000 h. Ref devices retain 94.1% of their initial efficiency, while CsCl devices show virtually no degradation, maintaining 99.8% of their initial PCE. As illustrated in Figure 6.9, the minor efficiency loss in Ref devices is primarily attributed to a reduction in FF ($\approx 2\%$ absolute loss) and J_{SC} ($\approx 4\%$ absolute loss), whereas the V_{OC} remains stable in both configurations.

Compared to ISOS-D1 conditions, elevated temperatures – as already observed in Chapter 5, Section 5.3.4 – have a pronounced impact on device stability. Accelerated aging under ISOS-D2 test conditions (dark, 85 °C) for 1000 h reveals severe thermal degradation (Figure 6.10), in both device configurations – Ref and CsCl – reaching T_{80} within the first 100 h. After 1000 h, the Ref devices retain only 14.4% of their initial efficiency, while CsCl devices maintain 15.6% of their initial PCE. Analysis of the remaining PV parameters (Figure 6.10) shows that the primary contributors to the PCE loss are reductions in J_{SC} ($\approx 68\%$ absolute loss for Ref, $\approx 64\%$ absolute loss for CsCl) and FF ($\approx 50.5\%$ absolute loss for Ref, $\approx 52.8\%$ absolute loss for CsCl), while the V_{OC} declines by less than 10% in both configurations. Literature reports[360–362] attribute such degradation under prolonged high-temperature exposure (> 500 h) to increased non-radiative recombination within the perovskite layer or at the charge-transport interfaces, ultimately reducing FF and V_{OC}.

To evaluate the operational stability of the PSCs not only under dark storage conditions but also under light exposure, semitransparent PSCs are subjected to ISOS-L1 test conditions for 1000 h (Figure 6.11). CsCl devices exhibit superior device stability, retaining 83% of their initial efficiency after 1000 h, outperforming Ref devices. The Ref devices reach T_{80} after 670 h and stabilize near this value, maintaining 78% of their initial PCE after 1000 h. Both configurations show a light-soaking effect during the first 2 h. Interestingly, Ref devices exhibit markedly

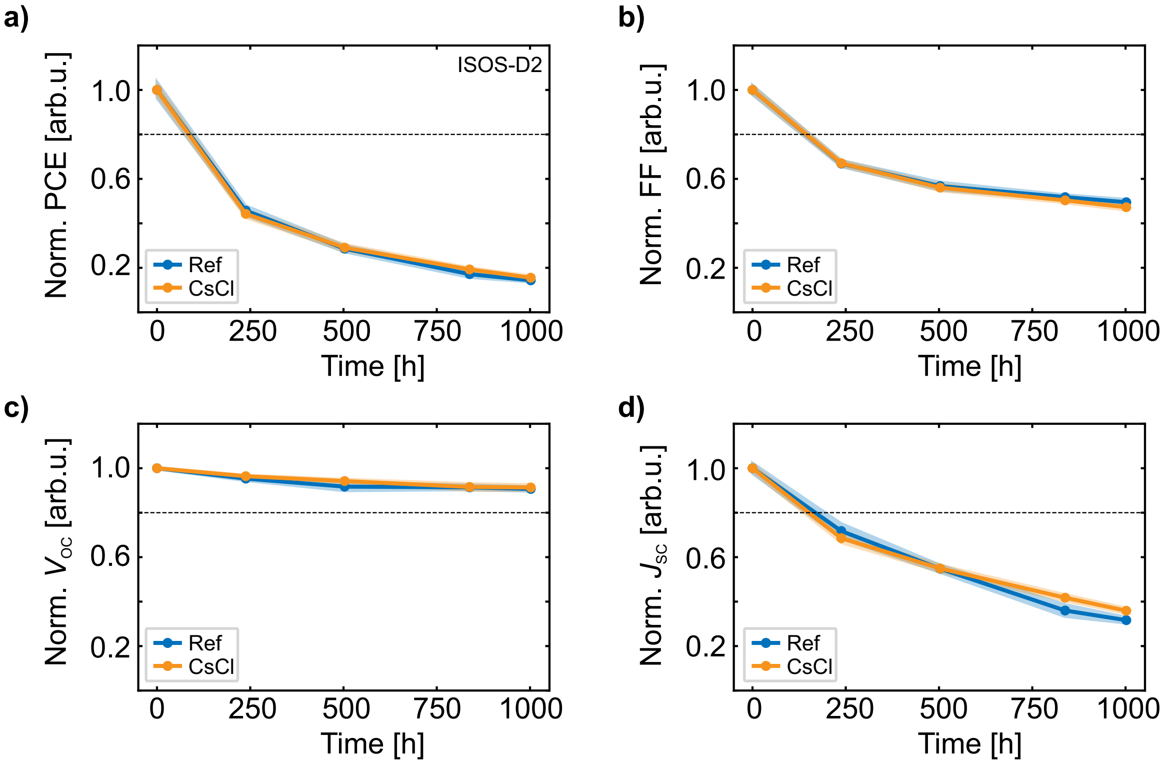

Figure 6.10: Normalized a) power conversion efficiency (PCE), b) fill factor (FF), c) open-circuit voltage (V_{OC}), and d) short-circuit current density (J_{SC}) from current density *versus* voltage (*J-V*) measurements of semitransparent (ST) perovskite solar cells (PSCs) without any further modification (Ref) and with 5 nm CsCl seed layer (CsCl) under ISOS-D2 testing conditions (dark storage, 85 °C, intermittent *J-V*) for 1000 h. Mean values and standard deviations based on twelve devices per parameter are provided.

improved long-term operational stability compared to previous ISOS-L1 measurements (Chapter 5, Section 5.3.4, Figure 5.17, DC opt.), suggesting that a bilayer of NiO_x and 2PACz as HTL provides superior stability compared to 2PACz alone. Analysis of individual PV parameters (Figure 6.11) indicates that efficiency loss is primarily driven by a reduction in J_{SC} ($\approx$ 17% absolute loss for Ref, $\approx$ 13% absolute loss for CsCl), while the V_{OC} remains comparatively stable ($\approx$ 9.2% absolute loss for Ref, $\approx$ 8.4% absolute loss for CsCl). Since J_{SC} and FF represent the dominant loss channels under all stress conditions, the performance decline is attributed primarily to interfacial and transport-related issues rather than to changes in the bandgap. Ion migration and contact degradation induced by thermal and light stress increase non-radiative recombination and series resistance, thereby limiting photocurrent and FF. Elevated temperature in ISOS-D2 and photo-induced effects in ISOS-L1 accelerate these processes, confirming that insufficient charge-carrier extraction and interface stability are the main failure modes under these aging conditions.[390]

The enhanced stability of CsCl PSCs may also be linked to the shift toward a more favorable (111) perovskite crystal orientation, as observed in XRD measurements (Figure 6.2).

In summary, the degradation analysis under different stress conditions demonstrates that introducing a CsCl seed layer at the HTL/perovskite interface enhances long-term operational stability, particularly under dark storage and

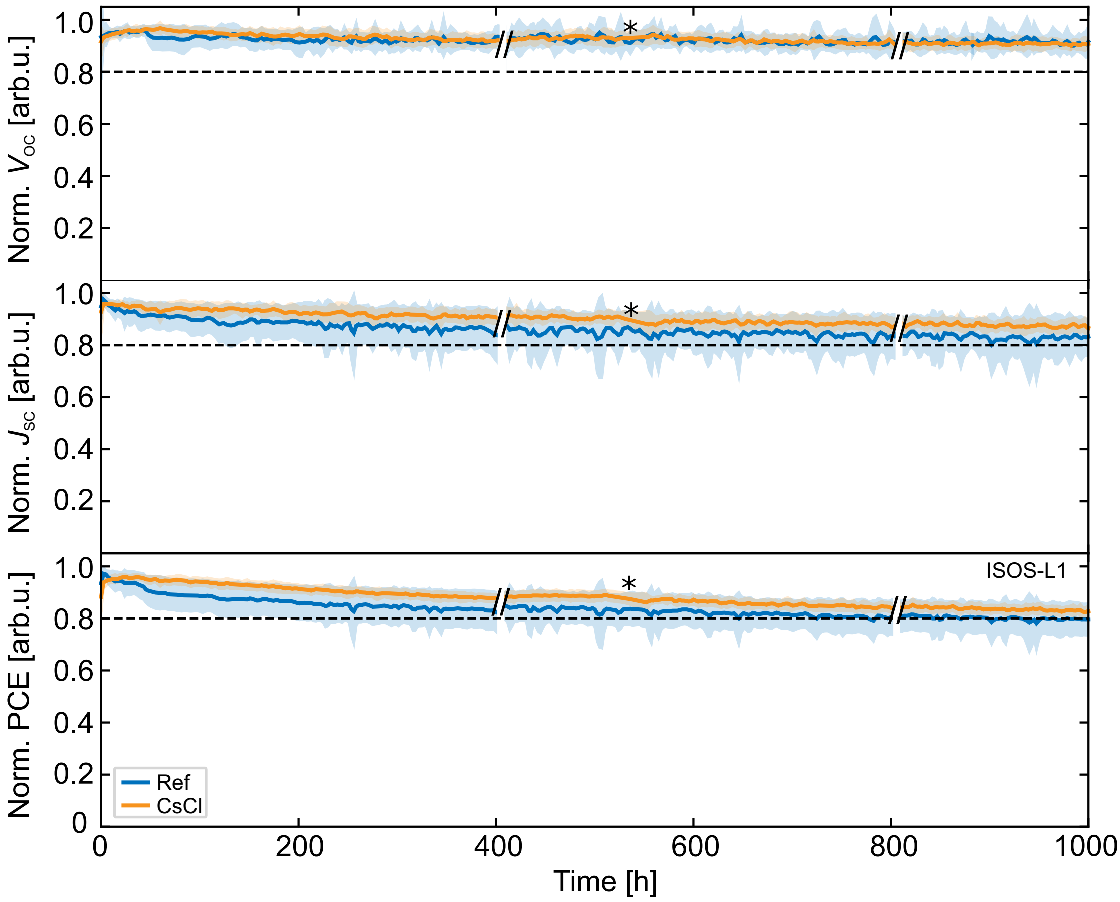

Figure 6.11: Normalized open-circuit voltage (V_{OC}), short-circuit current density (J_{SC}) and power conversion efficiency (PCE) at the maximum power point (MPP) tracking of semitransparent (ST) perovskite solar cells (PSCs) without any further modification (Ref) and with 5 nm CsCl seed layer (CsCl) under ISOS-L1 test conditions (100 mW cm^{-2}, 25 °C, MPP tracking) for 1000 h. Mean values and standard deviations based on 10-14 devices per parameter are provided. The data fluctuations originate from the measurement setup. // indicates brief periods when the solar simulator lamp was turned off, while $*$ marks a short interruption in the measurement. To account for these pauses, the measurement duration was extended, ensuring a total exposure time of 1000 h.

continuous light exposure. This trend is consistent with previous observations for CsCl and CsBr seed layers.[78,387] However, the pronounced performance loss at elevated temperatures, combined with the fact that the current devices have not yet reached state-of-the-art stability metrics – maintaining $> 90\%$ of their initial PCE after about 1200 h of continuous illumination[366] – underscores the need for further compositional and interface optimization.

6.6 Two-Terminal Perovskite/Silicon Tandem Solar Cell Integration

Building on the successful implementation of the CsCl seed layer in SJ PSCs, this strategy is extended to Si bottom cells for the fabrication of 2T perovskite/Si TSCs. The 2T perovskite/Si TSC architecture consists of the layer stack Si/ITO/NiO_x/2PACz/(CsCl)/perovskite/$PDAI_2$+BAI/C_{60}/SnO_x/IZO/Ag/MgF_2 with an active area of 1.0 cm^2 (similar to Figure 5.1b). As demonstrated in Chapter 5, Section 5.5, the fully solution-based two-step deposition method is compatible with planar, submicron, and micron-scale pyramidal Si surface textures, demonstrating the versatility of the process. However, large industrial textures ($\approx$ 2-5 µm) increase the risk of shunting, which can severely impact fabrication yield. The thin CsCl seed layer is a promising candidate to improve perovskite coverage across different Si textures, thereby enhancing process reliability. To examine the surface morphology and microstructure, SEM and GIWAXS measurements are performed on inorganic scaffolds and perovskite films deposited on small-textured (0.5-1 µm) and large-textured (2-5 µm) Si bottom cells.

First, inorganic scaffolds and perovskite films on small-textured Si bottom cells (0.5-1 µm) are analyzed. The cross-sectional SEM image of the inorganic scaffold with CsCl seed layer reveals a porous structure, fully covering the pyramidal texture (Figure 6.12a). Supplementary top-view SEM images for both Ref and CsCl inorganic scaffolds show surface morphologies comparable to those on glass substrates, with visible pinholes and no pronounced

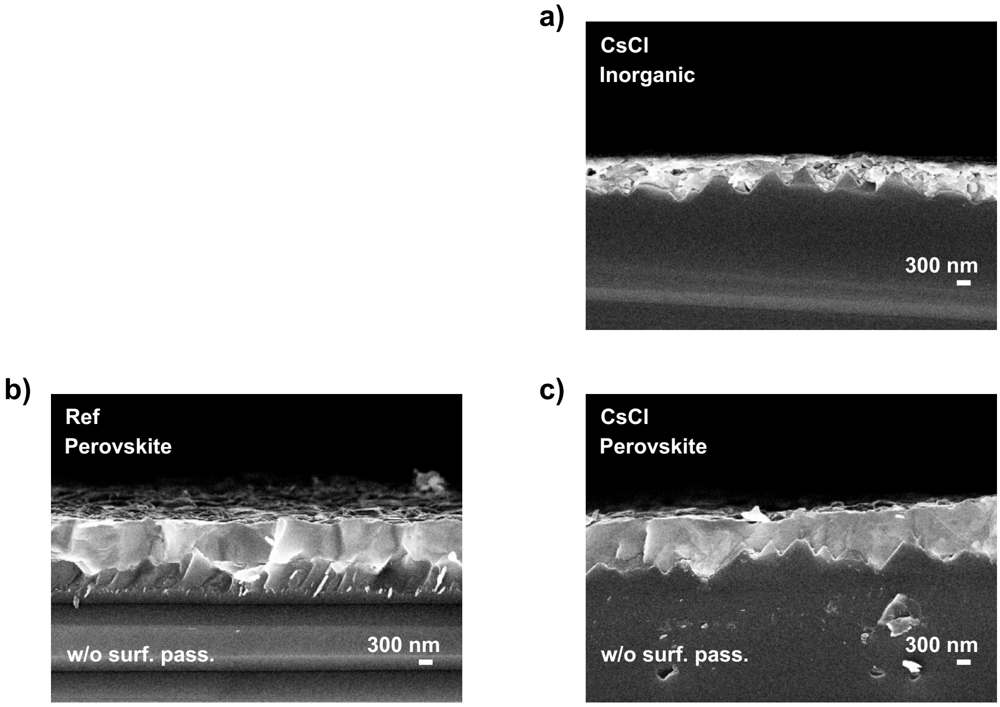

Figure 6.12: Cross-sectional scanning electron microscopy (SEM) images of a) inorganic scaffold with 5 nm CsCl seed layer (CsCl) and perovskite films b) without any further modification (Ref), and c) with 5 nm CsCl seed layer (CsCl) on small-textured silicon (Si) bottom cells (pyramid height $\approx$ 0.5-1 µm). The inorganic scaffold and perovskite films are prepared on Si/indium tin oxide (ITO)/NiO_x/2PACz. The perovskite films are without surface passivation. Unfortunately, it was not possible to focus on the Ref inorganic scaffold, which is why no image can be shown.

differences between both configurations (Figure A.27a/b). GIWAXS measurements (Figure A.28a/b) validate that the inorganic scaffold growth is not affected by the small-textured substrate. After conversion to the perovskite, both Ref and CsCl perovskite films form a homogeneous layer that fully covers the pyramidal texture (Figure 6.12b/c). Notably, no grain boundaries are observed throughout the perovskite layer in the imaged region, indicating uniform film formation and high-quality crystallization even on textured surfaces. Top-view SEM images (Figure A.27c/d) reveal enlarged grain sizes compared to those on glass substrates (Figure A.24), with a slight increase for CsCl perovskite films (442 nm vs. 417 nm for Ref, Figure A.29). GIWAXS analysis of the perovskite films (Figure A.28c/d) further shows a notable shift of the (100) perovskite phase from $\approx 60^\circ$ on glass substrates (Figure A.22b and Figure 6.3b) to a broader peak maximum between 10° and 40°, indicating a tendency toward a more horizontally oriented crystal growth on small-textured Si bottom cells. The surface texture does not need to be considered when determining the crystal orientation because the fully solution-based two-step processed perovskite film does not grow conformally on the pyramids.

When the texture height is increased to the industrial standard (large-textured, 2-5 µm), the inorganic scaffold is insufficient to fully cover the pyramids as shown by SEM images (Figure 6.13a/b, and Figure A.30a/b). For both Ref and CsCl inorganic scaffolds, several pyramid tips remain partially exposed. However, notably, the CsCl seed layer appears to promote a thin coating over the pyramidal tips, thus improving overall coverage compared to the Ref inorganic scaffold. Aside from coverage challenges, the scaffold morphology – porosity and pinholes – resembles that on glass substrates and small-textured Si bottom cells. Corresponding GIWAXS measurements (Figure A.31a/b) confirm that the overall inorganic scaffold structure remains largely unaffected by the substrate texture. After conversion to the perovskite, complete coverage of large-textured substrates remains challenging: Uncovered pyramids are still visible in cross-sectional (Figure 6.13c/d) and top-view (Figure A.30c/d) SEM images of Ref perovskite films, indicating that the texture height is too large for complete coverage *via* fully solution-based processing. However, the CsCl seed layer consistently improves film coverage, with fewer exposed pyramidal tips, suggesting its beneficial role in promoting perovskite film formation on large-textured substrates. Grain size

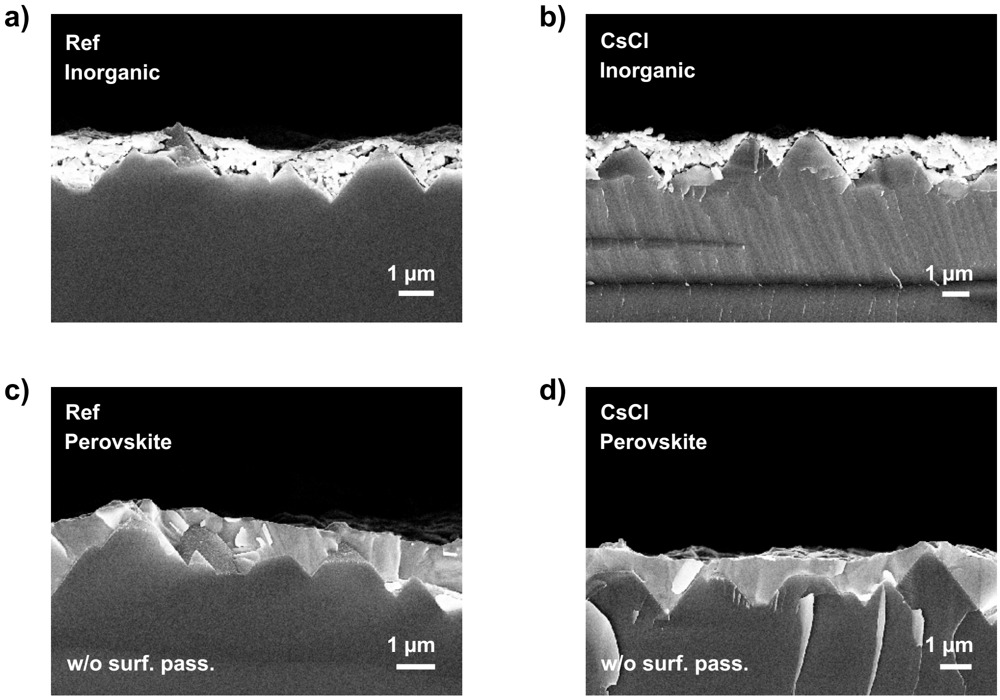

Figure 6.13: Cross-sectional scanning electron microscopy (SEM) images of inorganic scaffolds a) without any further modification (Ref), and b) with 5 nm CsCl seed layer (CsCl), and perovskite films c) without any further modification (Ref), and d) with 5 nm CsCl seed layer (CsCl) on large-textured silicon (Si) bottom cells (pyramid height ≈ 2-5 µm). The inorganic scaffolds and perovskite films are prepared on Si/indium tin oxide (ITO)/NiO_x/2PACz. The perovskite films are without surface passivation.

distributions for Ref (429 nm) and CsCl (426 nm) perovskite films remain comparable (Figure A.32). The GIWAXS results (Figure A.31c/d) show the same (100) perovskite phase re-orientation trend observed for perovskite films on small-textured Si bottom cells, indicating that the texture-induced shift in crystal orientation is independent of texture height.

Table 6.2: Statistical comparison of functional (not shunted) two-terminal (2T) perovskite/silicon (Si) tandem solar cells (TSCs) without any further modification (Ref), and with 5 nm CsCl seed layer (CsCl), evaluated over two fabrication batches, with six TSCs per Si bottom cell type (planar, small-textured or large-textured) and parameter (Ref or CsCl) in total (three TSCs per batch).

Si bottom cell type	Ref	CsCl
Planar	66%	83%
Small texture	16%	71%
Large texture	50%	100%

Finally, 2T perovskite/Si TSCs are successfully fabricated. A statistical comparison across two fabrication batches – six TSCs per bottom cell type and parameter in total (three TSCs per batch) – demonstrates a significant impact of the CsCl seed layer on the fabrication yield (Table 6.2). For planar Si bottom cells, the fabrication yield increases moderately from 66% (Ref) to 83% (CsCl). For textured Si bottom cells, the effect is more pronounced: The fabrication yield increases from 16% to 71% for small-textured Si bottom cells, and from 50% to 100% for large-textured Si bottom cells. These results demonstrate that introducing a CsCl seed layer at the HTL/perovskite interface substantially improves perovskite film formation on – for solution-processing – challenging textured surfaces, effectively reducing shunting issues and improving overall fabrication reliability.

6.7 Summary

This chapter demonstrates that introducing an ultrathin (5 nm) vapor-deposited CsCl seed layer at the HTL/perovskite interface prior to inorganic precursor deposition offers a simple yet highly effective strategy to improve device performance, long-term operational stability, and fabrication yield within a fully solution-based two-step process. By bridging vapor-assisted nucleation control with solution processing, this strategy addresses one of the key challenges in transferring high-performance perovskite thin films to industrially relevant textured Si bottom cells: the need for reliable and defect-free perovskite coverage.

Although the CsCl seed layer induces only subtle yet beneficial changes in perovskite microstructure – such as larger grain sizes, reduced pinhole density, and improved crystallinity – its impact on device metrics is substantial. SJ PSCs exhibit a marked improvement in FF, reduced hysteresis, and achieve a champion PCE of 19.0% for a 1.67 eV bandgap absorber. While this performance remains below the efficiencies of the champion devices presented in Chapter 5, likely due to the transition from BCP to SnO_x as ETL and precursor degradation effects, operational stability is markedly improved. Devices with CsCl seed layer retain 84% of their initial efficiency after 1000 h of continuous illumination at 25°C in N_2 atmosphere, outperforming PSCs without CsCl seed layer and highlighting the stabilizing influence of improved crystallization control. Nevertheless, state-of-the-art stability metrics – with devices retaining more than 90% of their initial PCE after about 1200 h of continuous illumination[366] – remain a benchmark, indicating that further optimization is required.

When transferred to 2T perovskite/Si TSCs, the CsCl seed layer strategy significantly improves the fabrication yield on submicron- and micron-textured Si bottom cells – without requiring adjustments in the established fully solution-based two-step deposition method. This compatibility with industrially relevant surface textures represents a decisive step toward industrial tandem manufacturing, where reliable perovskite coverage and high process repeatability are critical.

Beyond the specific material system investigated here, the results establish a broader design principle: ultrathin seed layers can positively influence nucleation and film formation, even within solution-processed wide-bandgap perovskite thin films. While further studies are needed to confirm transferability across other solution-based deposition methods (e.g., one-step deposition, slot-die coating, ink-jet printing), the results strongly suggest that CsCl seed layers offer a practical and scalable route to improve efficiency and long-term operational stability in PSC fabrication, while enabling integration into industrially textured 2T perovskite/Si TSCs.

While the present study focuses on CsCl seed layers, it remains an open question whether similar effects could be achieved using other cesium halides such as CsBr or CsI. Exploring these systems represents an important direction for future research, particularly given their potential influence on crystallization kinetics and halide distribution. Nonetheless, the findings presented here offer a first clear indication that ultrathin seed layers can positively impact perovskite film formation.

Beyond its beneficial role in tandem device fabrication, the CsCl seed layer strategy also suggests a potential application in emerging triple-junction PSC architectures. In such devices, several solution-processed layers are often mutually incompatible due to solvent-induced dissolution. A thin CsCl interlayer could serve as a protective buffer layer, mitigating solvent damage to underlying films and permitting processing steps that were previously incompatible. Although this concept appears highly promising, it remains unexplored and warrants dedicated future investigation.

In conclusion, this chapter highlights the potential of CsCl seed layers at the HTL/perovskite interface (research question **III**) to optimize thin-film formation (research question **II**), enhance device performance and long-term operational stability (research question **V**), and facilitate successful implementation of the perovskite thin film in industrially relevant 2T perovskite/Si tandem architectures (research question **IV**). Together, these results represent an important step toward high-efficiency, stable *p-i-n* PSCs and 2T perovskite/Si TSCs using the fully solution-based two-step method, advancing the development of industrially relevant tandem designs.

7 A Materials Perspective on Inorganic Deposition Routes for Hybrid Two-Step Processed Perovskite Thin Films

Advancing two-terminal perovskite/silicon tandem photovoltaics from laboratory-scale research toward high-throughput industrial manufacturing requires perovskite fabrication methods that combine excellent optoelectronic quality of wide-bandgap perovskite thin films with high process repeatability, compatibility with industrially textured silicon bottom cells, and large-area manufacturability. In practice, however, most existing perovskite fabrication methods have difficulty meeting these requirements. Fully solution-based methods often fail to cover micron-scale silicon surface textures, compromising device performance and fabrication yield, while conventional co-deposition – although capable of achieving conformal coverage – suffers from substantial process complexity, poor repeatability, and limited scalability for industrial implementation. To address these challenges, this chapter introduces a fully sequential hybrid two-step deposition route, combining the conformal coverage capability of vapor deposition with the simplicity and cost-effectiveness of solution-based processing. Building on both the fully solution-based two-step method and the CsCl seed layer strategy developed in previous chapters, the inorganic components – CsCl and PbI_2 *– are deposited sequentially in two separate vapor-deposition steps, followed by spin coating of the organic cation solution. This sequential vapor-deposition route of the inorganic precursors offers a simplified and industry-compatible alternative to conventional co-deposition, and provides improved process flexibility for integration into large-scale manufacturing. Comprehensive microstructural and elemental analyses of the resulting inorganic scaffolds and perovskite films elucidate how the inorganic precursor deposition route influences crystallization dynamics, film morphology, and halide distribution in the resulting wide-bandgap perovskite films (research question* ***II****). Beyond material characterization, device-level studies assess photovoltaic performance and process repeatability. Furthermore, the compatibility of the sequential deposition route with planar and textured silicon bottom cells is systematically evaluated to determine its suitability for industrially relevant two-terminal tandem integration (research question* ***IV****). Taken together, this chapter explores the potential of fully sequential hybrid deposition as a promising and scalable strategy for producing high-quality wide-bandgap perovskite thin films with improved process control and conformity on textured silicon surfaces, thereby bridging the gap between laboratory-scale processing and industrial manufacturing of two-terminal perovskite/silicon tandem solar cells.*

Parts of this chapter review the published research article "Benchmarking Inorganic Deposition Routes for Hybrid Two-Step Processed Perovskite Solar Cells: A Materials Perspective" in *Solar RRL* 10.4 (2026) by *J. Petry (J.P.)**, *R. Pappenberger (R.P.)**, *A. Welle*, *T. Zhao*, *A. Diercks*, *R. Pesch*, *M. Krause*, *P. Fassl*, and *U. W. Paetzold*.[204] *J.P.* and *R.P.* made equal contributions to this work and share first authorship. Some figures in this chapter were adapted from reference[204] with permission from Wiley.
R.P. contributed to this project by co-conceptualizing the study, leading experimental investigations, data curation, formal analysis, and visualization, as well as writing the original draft of the manuscript. The contributions of all authors involved in this study are listed in Table A.6 according to the CRediT system.

7.1 Motivation

For perovskite PV technologies to progress from laboratory research to industrial manufacturing, fabrication methods must be capable of large-area processing, ensure high perovskite film quality, and be compatible with the micron-scale surface textures (≈ 2-5 µm) of commercial Si bottom cells. Therefore, developing industry-compatible, scalable processes is essential for the successful commercialization of PSCs and perovskite/Si TSCs.[72,205,391,392]

Although the one-step spin-coating method currently achieves the highest efficiencies for SJ PSCs,[14] the method struggles to reliably cover micron-textured Si bottom cells, often resulting in incomplete surface coverage and shunting paths that drastically degrade device performance and fabrication yield.[76,373] As shown in the previous chapter, introducing a CsCl seed layer at the HTL/perovskite interface can improve solution-processed perovskite film coverage on textured substrates within the fully solution-based two-step method, mitigating some of these limitations without relying on full vapor deposition.

Vapor-deposition methods are inherently compatible with large-area processing and provide excellent conformity on pronounced surface textures,[71–75] yet several challenges remain in translating these methods to industrial-scale manufacturing. In particular, the deposition of volatile organic precursors leads to poor process repeatability and constrains achievable deposition rates, ultimately reducing fabrication throughput.[374,381–385,391]

The hybrid two-step deposition method has therefore emerged as a promising alternative. By combining vapor deposition of the inorganic precursors with a subsequent solution-based deposition of the organic cations, this method allows for enhanced compositional flexibility, facile introduction of additives, and the use of environmentally friendly solvents.[76–81] Hybrid two-step deposition of the perovskite thin film has been successfully demonstrated in both SJ PSCs[80,82–86] and 2T perovskite/Si TSCs, where efficiencies exceeding 31% have been reported on micron-scale textured Si bottom cells.[87–89] A key requirement for industrial scalability, however, is the choice of deposition method for the organic cation solution. Scalable deposition methods such as blade coating, slot-die coating, spray coating, or inkjet printing have already shown success in SJ PSCs,[68,69,393–396] and the first large-area 2T perovskite/Si tandem device fabricated *via* blade-coating achieved a promising PCE approaching 28%.[397]

Despite the progress in scalable coating techniques for the organic cation solution, a major challenge for industrial implementation of PSCs – and one that has thus far been widely overlooked – is the need for high-throughput fabrication of the vapor-deposited inorganic scaffold.[391] Wide-bandgap perovskite thin films with bandgaps exceeding 1.65 eV – required for optimal current matching in 2T perovskite/Si TSCs – need inorganic scaffold compositions beyond pure PbI_2 to achieve high perovskite film quality. Therefore, widening the bandgap necessitates the vapor deposition of additional inorganic precursors such as $PbBr_2$,[398] $PbCl_2$,[399] CsCl,[69,400] CsBr,[79,83,87,88,212,393,400–405] or CsI[206,398]. In conventional co-deposition of the inorganic precursors, all inorganic precursor materials are vapor-deposited simultaneously, demanding precise control over the relative sublimation rates. The process becomes extremely sensitive to fluctuations in precursor vapor fluxes and temperature drifts, which restricts process repeatability and constrains the maximum achievable deposition rates, posing a fundamental bottleneck for industrial-scale implementation.[391] To overcome these challenges, sequential deposition of the inorganic precursors has been proposed by Petry *et al.*[391] By allowing each material source to operate independently at its optimal deposition rate, the process becomes more robust, easier to control, and substantially more compatible with high-throughput manufacturing. Despite its potential, sequential deposition of the inorganic precursors has remained largely unexplored within hybrid two-step deposition methods, and a systematic comparison to the conventional co-deposition method is still missing. Addressing this knowledge gap is essential to evaluate whether a separation of the inorganic scaffold deposition into two distinct vapor-deposition steps can enhance process repeatability without compromising film quality and device performance. Understanding how the deposition route influences inorganic scaffold formation, organic cation uptake, and conversion into the final perovskite phase is therefore critical for designing industrially viable perovskite/Si tandem architectures.[406]

Motivated by these considerations, this chapter investigates a fully sequential vapor-deposited inorganic scaffold within the hybrid two-step deposition method. By vapor-depositing CsCl and PbI_2 sequentially, the method introduces a simplified and more flexible process aimed at improving throughput, reducing process complexity, and ensuring compatibility with textured Si bottom cells.

Section 7.2 introduces the hybrid two-step deposition method used in this chapter, including the co- and sequential deposition routes of the inorganic precursors. Section 7.3 provides a detailed analysis of the layer morphology of the inorganic scaffolds and the resulting perovskite films obtained from each deposition route. Section 7.4 investigates the crystal orientation, revealing how the deposition route governs the preferred growth direction of the PbI_2 platelets. Section 7.5 examines the elemental distribution in both the inorganic scaffold and the perovskite thin film to elucidate the impact of the deposition sequence on compositional uniformity and conversion behavior. Building on these material insights, Section 7.6 investigates the PV performance of wide-bandgap PSCs fabricated *via* both deposition routes and analyzes the associated impact of the deposition route on process repeatability. Finally, Section 7.7 assesses the inorganic growth behavior of co- and sequentially deposited inorganic scaffolds on different textured Si bottom cells, focusing on its potential for scalable, industrially relevant 2T perovskite/Si tandem fabrication.

7.2 Fabrication Process

The schematic illustrations for both co-deposition (labeled as Co) and sequential deposition (labeled as Seq) of the inorganic precursor materials PbI_2 and CsCl are illustrated in Figure 7.1a/b. CsCl is used in this study instead of other inorganic precursor materials such as CsBr, as it has been shown to promote crystallization and improve overall film quality[386] – consistent with the findings in Chapter 6. In the co-deposition route, both inorganic precursor materials are sublimated simultaneously, whereas in the sequential deposition route CsCl is deposited first, followed by a subsequent deposition of PbI_2. Conversion to the perovskite thin film is achieved by depositing the organic cation solution *via* spin coating, based on an established recipe introduced by Li *et al.*[78] and Er-raji *et al.*[80], followed by thermal annealing under ambient conditions (Figure 7.1c). The resulting half-stack devices comprise the layer

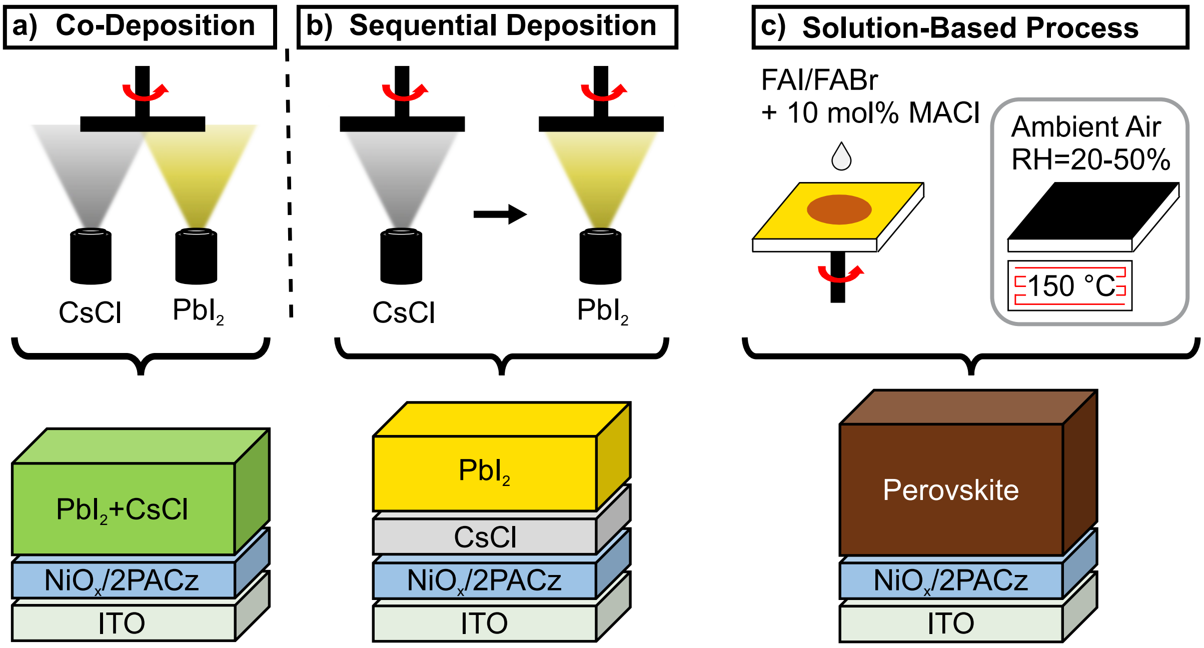

Figure 7.1: Schematic illustration of the two hybrid two-step deposition routes studied in this chapter. a) co- (Co) and b) sequential (Seq) deposition routes of the inorganic precursors CsCl and PbI_2, with the corresponding layer sequence depicted below each process. c) Schematic illustration of the perovskite thin film obtained after the deposition of the organic cation solution and subsequent thermal annealing under ambient conditions with a relative humidity (RH) of ≈ 20-50%. Adapted from reference[204] with permission from Wiley.

sequence glass/ITO/NiO_x/2PACz/perovskite. In this study, the perovskite thin film has the nominal composition $Cs_{0.18}FA_{0.82}Pb(I_{0.76}Br_{0.18}Cl_{0.06})_3$ with a target bandgap of 1.69-1.70 eV (Figure A.35b and Figure A.41b).

To ensure a consistent comparison between both deposition routes, the conversion of the inorganic scaffold into the perovskite thin film is optimized by adjusting the molarity of the organic cation solution. Specifically, FAI/FABr precursor solutions with a molarity between 0.65 M and 0.90 M, each containing 10 mol% MACl as an additive, are prepared for this purpose. As the optimal organic cation molarity varies between fabrication batches depending on the deposition route (as further discussed in Section 7.6), all material characterization presented in Section 7.3 to Section 7.5 is based on Batch A. Therefore, the respective optimal organic cation solution molarities from Batch A for the perovskite conversion – 0.65 M for co-deposition and 0.75 M for sequential deposition – are used to enable a representative and consistent comparison. Detailed PV performance metrics for Batch A are provided in Figure A.33 (Co PSCs) and Figure A.34 (Seq PSCs), with the corresponding champion PSCs displayed in Figure A.35. Both deposition routes yield *p-i-n* PSCs with a low hysteresis index (HI $< 5\%$), indicative of reliable device operation.

7.3 Layer Morphology and Microstructure

The influence of the deposition route on the morphology and microstructure of the inorganic scaffold, as well as on the corresponding perovskite film, is investigated using SEM and AFM measurements. These analyses are performed on half-stacks with the architecture ITO/NiO_x/2PACz/inorganic scaffold or perovskite layer.

Differences in the inorganic scaffolds depending on the deposition route are readily apparent upon visual inspection (Figure A.36). Co-deposition of the inorganic scaffold results in a comparatively smooth surface appearance, whereas sequential deposition leads to a distinctly rougher surface. These visual differences in inorganic scaffold morphology motivate a more detailed structural analysis using SEM and AFM, as presented in Figure 7.2.

SEM images confirm pronounced morphological differences in the inorganic scaffolds obtained by co- and sequential deposition. The co-deposited inorganic scaffold exhibits a dense, uniform morphology with a smooth surface and a layer thickness of approximately 330 nm, consistent with QCM measurements during deposition and surface

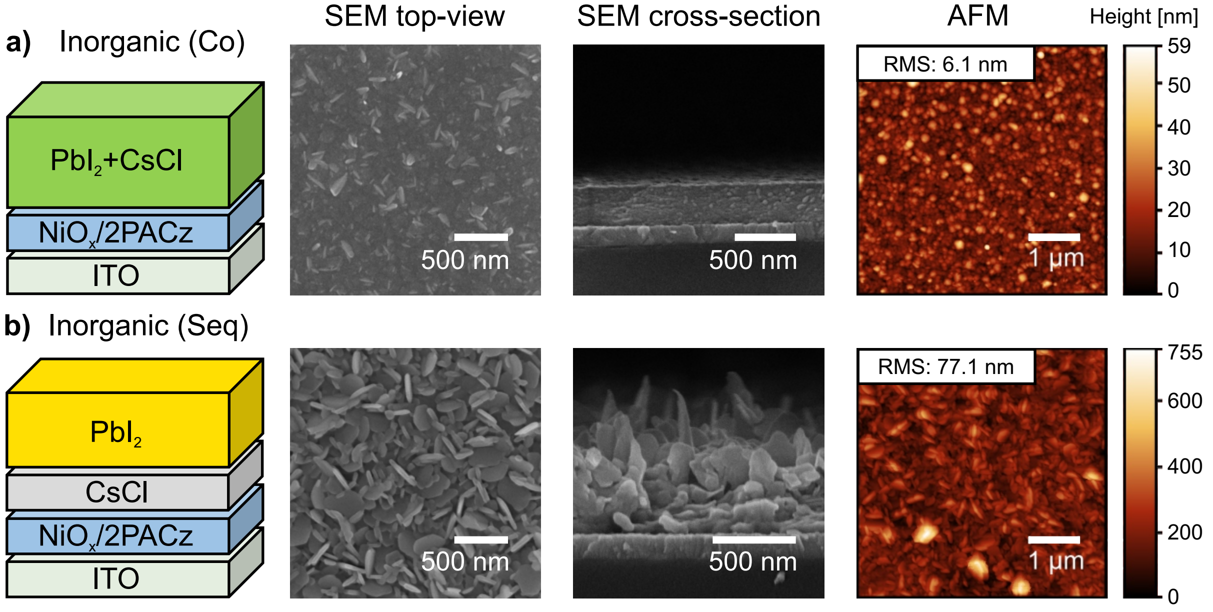

Figure 7.2: Scanning electron microscopy (SEM) images (top-view and cross-sectional) and atomic force microscopy (AFM) images of the inorganic scaffold deposited *via* a) co- (Co) and b) sequential (Seq) deposition on glass/indium tin oxide (ITO)/NiO_x/2PACz. Two to three measurements are taken for each parameter, and the average root-mean-square (RMS) value is calculated for AFM measurements. Adapted from reference[204] with permission from Wiley.

profilometry (Figure A.37a). Individual PbI_2 platelets are not discernible in the co-deposited inorganic scaffold. In contrast, the sequentially deposited inorganic scaffold displays a highly irregular surface structure, making precise thickness determination challenging. With surface profilometry (Figure A.37b), a higher average layer thickness of 409 ± 4 nm is measured. The sequential deposition of the precursor materials results in a microstructure of the inorganic scaffold characterized by vertically and slightly tilted PbI_2 platelets relative to the substrate surface, clearly visible in both top-view and cross-sectional SEM images.

AFM measurements further support these findings, highlighting a significant difference in surface roughness between both deposition routes. The co-deposited inorganic scaffold exhibits an order of magnitude lower root-mean-square (RMS) surface roughness of 6.1 ± 0.1 nm compared to 77.1 ± 0.4 nm for the sequentially deposited inorganic scaffold. The increased surface roughness indicates a higher porosity of the layer, which is known to facilitate the infiltration of the organic cation solution into the inorganic scaffold.[68,193] To assess this effect, the absorption behavior of a 50 pL droplet dispensed onto the inorganic scaffold surface is analyzed using confocal scanning microscopy (Figure A.38). On the co-deposited inorganic scaffold, dried droplets leave a distinct accumulation of crystalline organic salts at the center, suggesting limited droplet absorption. Conversely, the sequentially deposited inorganic scaffold shows far less organic salt residue, indicating improved droplet absorption.

Despite the pronounced differences in inorganic scaffold morphology, the resulting perovskite layers – fabricated by spin coating the respective optimal organic cation molarity – exhibit comparable thin-film morphologies for both deposition routes (Figure 7.3 and Figure A.36). Top-view and cross-sectional SEM images reveal a similar microstructure, which is consistent with AFM measurements showing RMS surface roughness values of 29.6 ± 0.7 nm for co-deposition and 26.8 ± 0.3 nm for sequential deposition. In contrast to the comparable surface morphology, surface profilometry (Figure A.37) indicates a substantially increased perovskite layer thickness for the sequential deposition route, increasing from 524 ± 4 nm (co-deposition) to 682 ± 5 nm (sequential deposition). The corresponding expansion coefficients ($\text{thickness}_{\text{perovskite}}/\text{thickness}_{\text{inorganic}}$) of 1.62 for co-deposition and 1.67 for sequential deposition further suggest a slightly increased incorporation of organic cations for sequentially deposited inorganic scaffolds. Additional insights from confocal scanning microscopy (Figure A.38) confirm that the perovskite films

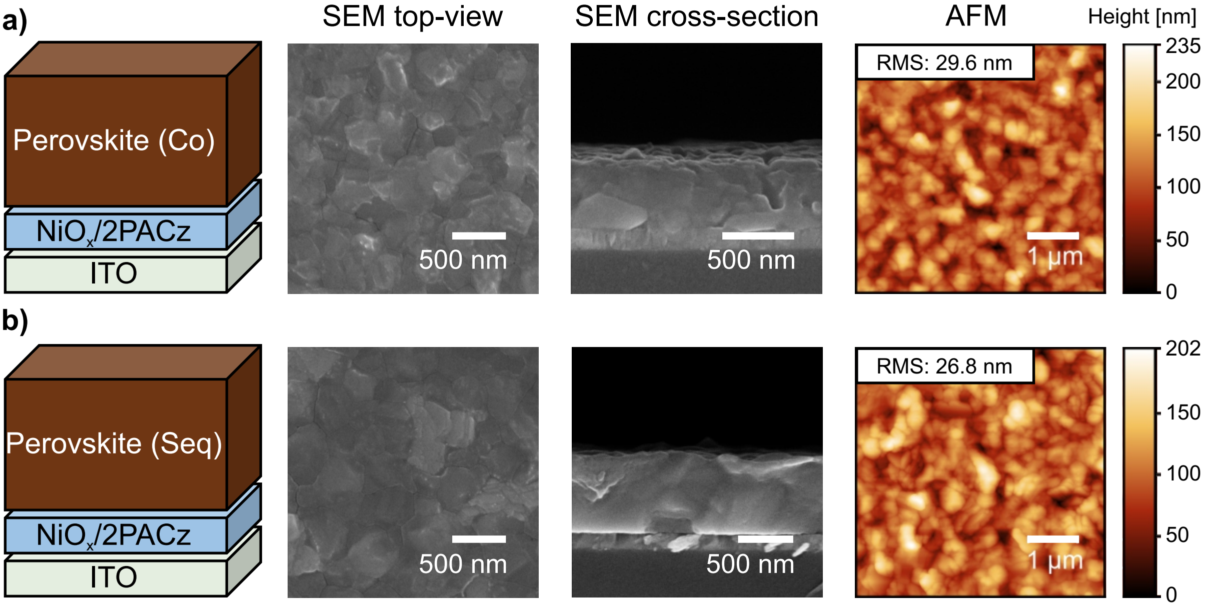

Figure 7.3: Scanning electron microscopy (SEM) images (top-view and cross-sectional) and atomic force microscopy (AFM) images of the perovskite films with a) co- (Co) and b) sequential (Seq) deposited inorganic scaffold on glass/indium tin oxide (ITO)/NiO_x/2PACz. Two to three measurements are taken for each parameter, and the average root-mean-square (RMS) value is calculated for AFM measurements. The optimal molarity from Batch A is used for the organic cation solution. Adapted from reference[204] with permission from Wiley.

formed on both scaffold types exhibit a comparable visual appearance.

Overall, while the choice of deposition route leads to substantial differences in the morphology and microstructure of the inorganic scaffold, the morphology of the perovskite layer remains largely unaffected by the deposition route.

7.4 Crystal Orientation

To quantify the influence of the deposition route on the preferred growth orientation and overall crystallinity in both the inorganic scaffold and the perovskite film, GIWAXS measurements are conducted (Figure 7.4).[407] Considering the inorganic scaffold, GIWAXS measurements reveal a distinct change in the preferred orientation of the (001) PbI_2 crystal plane depending on the deposition route (Figure 7.4a/b/c). Co-deposition results in a selective out-of-plane orientation, whereas sequential deposition favors in-plane alignment. Consequently, in co-deposition, the presence of CsCl promotes an exclusive horizontal alignment of the (a,b)-plane of PbI_2 relative to the substrate

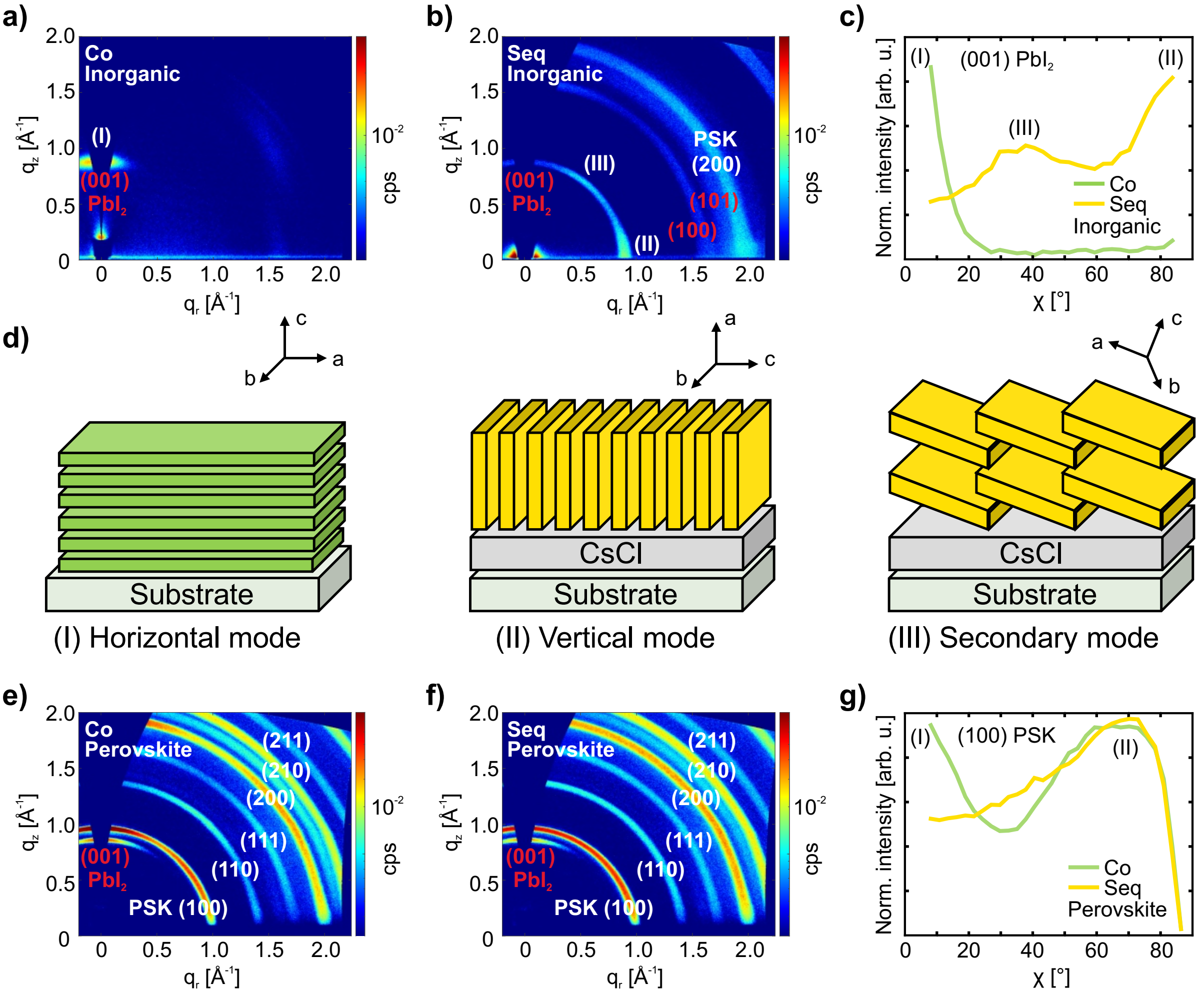

Figure 7.4: Grazing-incidence wide-angle X-ray scattering (GIWAXS) patterns of the inorganic scaffold deposited *via* a) co- (Co) and b) sequential (Seq) deposition, and of the perovskite films prepared *via* e) co- (Co) and f) sequential (Seq) deposition of the inorganic scaffold on glass/indium tin oxide (ITO)/NiO_x/2PACz. d) Schematic illustration depicting the orientation of the PbI_2 platelets in the inorganic scaffold for co-deposition (I) and sequential deposition (II)/(III). Distribution of crystallite orientation of the c) (001) PbI_2 phase in the inorganic scaffolds and g) (100) perovskite (PSK) phase in the perovskite films. For the perovskite films, the optimal molarity of the organic cation solution from Batch A is used. Adapted from reference[204] with permission from Wiley.

(horizontal mode (I), Figure 7.4d), similar to the preferred orientation observed by Meng *et al.* for spin-coated PbI_2[389], and for the fully solution-based two-step processed inorganic scaffolds discussed in Chapter 6, Figure 6.3a. In contrast, sequential deposition yields a preferred vertical growth, with the (a,b)-plane of PbI_2 perpendicular to the substrate (vertical mode (II), Figure 7.4d), which appears to be the intrinsic growth mode for pure PbI_2 in vapor-deposition processes.[67] This preference is likely thermodynamic in origin: Growth within the (a,b)-plane is stabilized by ionic bonding and therefore favored, whereas growth along the c-axis is governed by weaker van der Waals interactions.[408] Additionally, a secondary preferred PbI_2 orientation is observed for sequential deposition, where the (a,b)-plane is tilted about 40° relative to the substrate (secondary mode (III), Figure 7.4d). This is consistent with findings by Diercks *et al.*,[67] who compared the surface-dependent growth of pure PbI_2 on different HTL systems observing a similar secondary orientation at 40° for PTAA, NiO_x and TaTm. The surface-dependent mechanism responsible for this secondary mode may originate from the underlying CsCl layer; however, this hypothesis requires further investigation.

For the sequentially deposited inorganic scaffold (Figure 7.4b), the GIWAXS signal with scattering vector $q = 2.0\ \text{Å}^{-1}$ coincides with the (200) perovskite phase and is likewise detected in the corresponding XRD measurements at 27.6° (Figure A.39b), suggesting that interfacial reactions between CsCl and PbI_2 can initiate partial perovskite formation. It is hypothesized that the local concentrations of CsCl and PbI_2 in the co-deposited inorganic scaffold are insufficient to initiate comparable perovskite formation (Figure A.39a).

GIWAXS analysis of the corresponding perovskite films reveals a subtle difference in the preferred crystal orientation of the (100) perovskite phase (Figure 7.4e/f/g). Both perovskite films exhibit a discrete Bragg spot around 70°, indicating an intrinsic perovskite growth preference. A similar preferred orientation is also observed for the fully solution-based two-step process discussed in previous chapters (Chapter 5, Figure 5.9 and Chapter 6, Figure 6.3b), demonstrating its universal occurrence across different two-step deposition methods. Interestingly, a secondary small-angle Bragg peak appears exclusively for the co-deposition route (pole figure of the (100) perovskite plane in Figure 7.4g), which is attributed to a templating effect from the horizontally aligned PbI_2 platelets of the inorganic scaffold and a likely topotactic reaction that partially preserves the crystallographic orientation from the precursor phase.[409–411]

Complementary XRD measurements of the inorganic scaffolds confirm the strong crystal orientation dependence on deposition route (Figure A.39). Specifically, the (001) PbI_2 diffraction peak is more prominent for co-deposition, while the (003) PbI_2 peak is more pronounced for sequential deposition. In the resulting perovskite films, similar diffraction peaks with comparable peak area ratios are observed for both deposition routes (Figure A.39c). However, the (110) and (111) perovskite peaks are more pronounced relative to the (100) perovskite peak in perovskite films with sequentially deposited inorganic scaffold. A small amount of unreacted PbI_2 is detected for both deposition routes, consistent with the observations reported in previous chapters for fully solution-based two-step processed perovskite films. No diffraction peaks associated with Cs-containing phases are detected, indicating complete conversion of CsCl into the perovskite phase and the absence of secondary phases. Both deposition routes yield similar FWHM values of the (100) perovskite peak (Figure A.39d), suggesting that the resulting perovskite layers exhibit comparable crystal quality. A detailed analysis – which can be found in Petry and Pappenberger *et al.*[204] – reveals that both the peak ratio of the (100) perovskite peak to the (001) PbI_2 peak, as well as the FWHM of the (100) perovskite peak, correlate with the molarity of the organic cation solution, underscoring the importance of optimizing this parameter for best device performance.

These results suggest that the deposition route has a profound influence on the crystal growth orientation of PbI_2 platelets in the inorganic scaffold. The crystal orientation is partially retained during conversion to the perovskite phase, suggesting a templating effect imparted by the initial PbI_2 alignment.

7.5 Elemental Distribution

So far, material characterization indicates that the deposition route strongly affects the microstructure of the inorganic scaffold, while only marginally influencing the formation of the perovskite film. To probe the qualitative elemental distribution as a function of depth, a series of ToF-SIMS depth profiles are conducted on half-stacks with the architecture ITO/NiO_x/2PACz/inorganic scaffold or perovskite. First, characteristic positively charged secondary ions of the relevant species for the inorganic scaffolds (Figure 7.5a/b) and the perovskite films (Figure 7.5c/d) are analyzed. Ni fragments ($\Sigma(^{58}\mathrm{Ni}^+,^{60}\mathrm{Ni}^+)$), originating from the underlying NiO_x HTL, are detected for both deposition routes and serve as a positional reference.

Pronounced differences in elemental distribution are observed between co-deposited (Figure 7.5a) and sequentially deposited (Figure 7.5b) inorganic scaffolds. For the co-deposited inorganic scaffold, CsI (CsI^+) and CsCl ($\mathrm{Cs_3Cl_2^+}$) fragments accumulate at the top surface (ETL side) and are not homogeneously distributed throughout the inorganic scaffold. In contrast, sequential deposition of the inorganic scaffold leads to the expected layering: CsCl is located exclusively at the perovskite/HTL interface, whereas PbI_2-containing fragments ($\Sigma(^{206}\mathrm{PbI}^+,^{207}\mathrm{PbI}^+,^{208}\mathrm{PbI}^+)$) accumulate predominantly at the top surface (ETL side), consistent with the process order. An additional signal of CsI at the CsCl/PbI_2 interface indicates a spontaneous interdiffusion process of iodide into the CsCl layer. For co-deposition, PbI_2-containing species accumulate both at the top and bottom of the inorganic scaffold, possibly

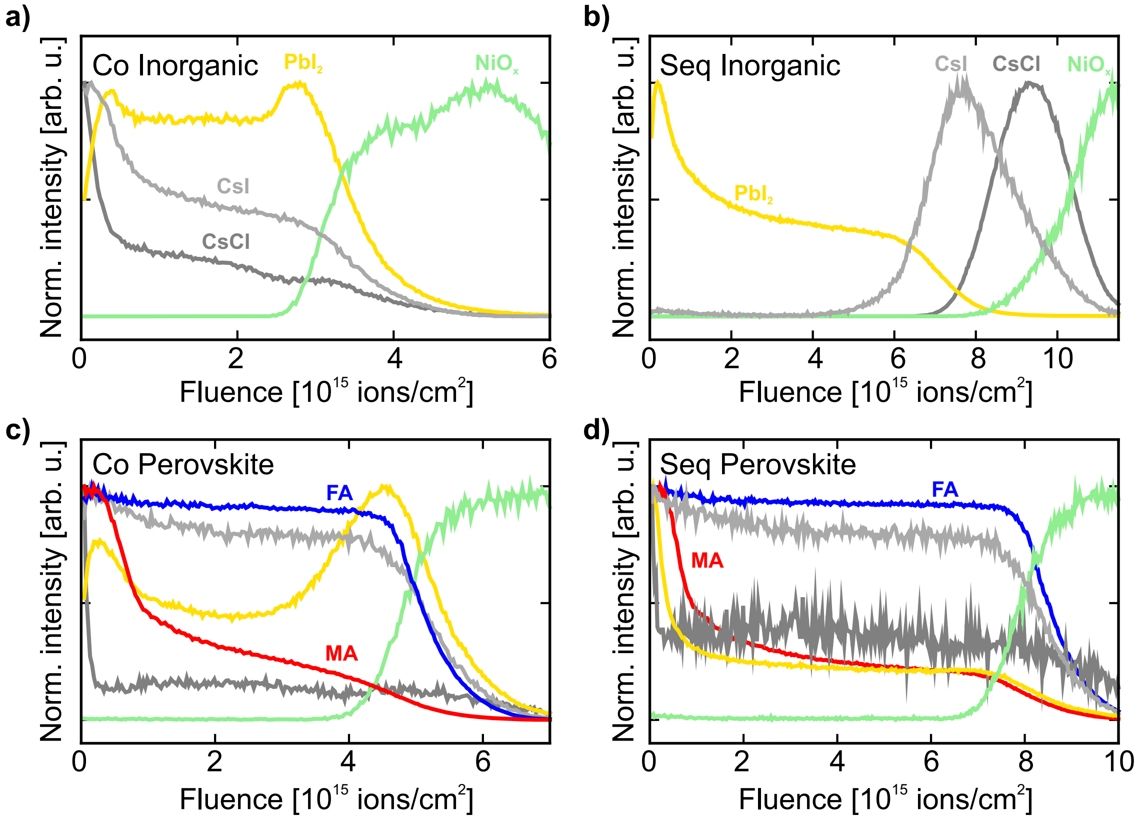

Figure 7.5: Normed time-of-flight secondary ion mass spectrometry (ToF-SIMS) measurements (positive polarity) of the inorganic scaffold deposited *via* a) co- (Co) and b) sequential (Seq) deposition, and of the perovskite films prepared *via* c) co- (Co) and d) sequential (Seq) deposition of the inorganic scaffold on glass/indium tin oxide (ITO)/NiO_x/2PACz. For the perovskite films, the optimal molarity of the organic cation solution from Batch A is used. The following fragments are displayed: NiO_x: $\Sigma(^{58}\mathrm{Ni}^+,^{60}\mathrm{Ni}^+)$; PbI_2: $\Sigma(^{206}\mathrm{PbI}^+,^{207}\mathrm{PbI}^+,^{208}\mathrm{PbI}^+)$; CsCl: $\mathrm{Cs_3Cl_2^+}$; CsI: CsI^+; formamidinium (FA): $\mathrm{CH_5N_2^+}$; methylammonium (MA): $\Sigma(\mathrm{CH_4^+},\mathrm{NH_4^+},\mathrm{CH_2N^+},\mathrm{CH_3N^+})$. Adapted from reference[204] with permission from Wiley.

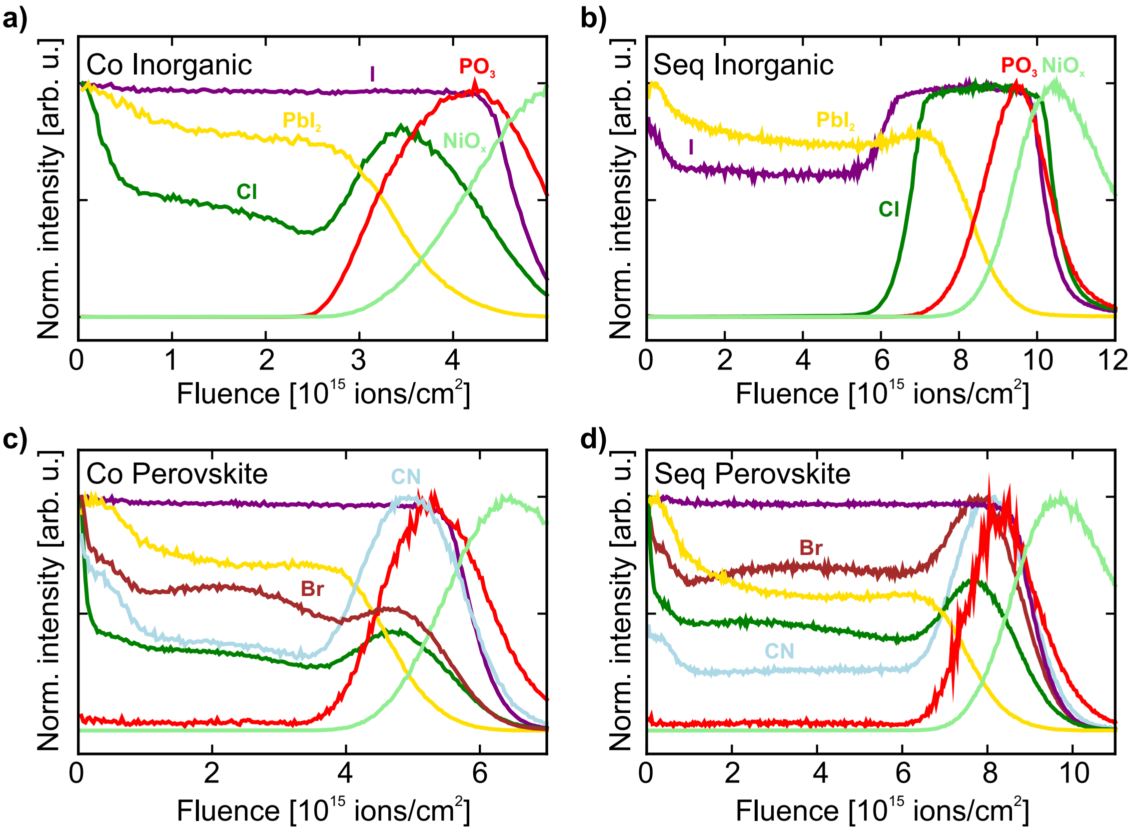

Figure 7.6: Normed time-of-flight secondary ion mass spectrometry (ToF-SIMS) measurements (negative polarity) of the inorganic scaffold deposited *via* a) co- (Co) and b) sequential (Seq) deposition, and of the perovskite films prepared *via* c) co- (Co) and d) sequential (Seq) deposition of the inorganic scaffold on glass/indium tin oxide (ITO)/NiO$_x$/2PACz. For the perovskite films, the optimal molarity of the organic cation solution from Batch A is used. The following fragments are displayed: NiO$_x$: $\mathrm{NiO_2^-}$; PO$_3$: $\Sigma(\mathrm{PO_3^-}, \mathrm{PO_2^-})$; PbI$_2$: $^{207}\mathrm{PbI_3^-}$; Cl: $\mathrm{Cl^-}$; I: $\mathrm{I^-}$; Br: $\mathrm{Br^-}$; CN: $\mathrm{CN^-}$. Adapted from reference[204] with permission from Wiley.

due to the relatively high PbI$_2$ deposition rate causing initial substrate coverage.

After conversion to the perovskite layer (Figure 7.5c/d), Cs ions appear uniformly distributed throughout the layer for both deposition routes, implying a high ionic diffusivity for Cs. The PbI$_2$ fragments retain largely the position set by the deposition of the inorganic scaffold. In perovskite layers with co-deposited inorganic scaffold (Figure 7.5c), PbI$_2$ fragments tend to accumulate near the perovskite/HTL interface, whereas for perovskite layers with sequentially deposited inorganic scaffold (Figure 7.5d) PbI$_2$ fragments are more concentrated at the top surface. Regardless of the deposition route, the organic fragment of FA ($\mathrm{CH_5N_2^+}$) is homogeneously distributed throughout the perovskite layer, whereas MA-related fragments ($\Sigma(\mathrm{CH_4^+}, \mathrm{NH_4^+}, \mathrm{CH_2N^+}, \mathrm{CH_3N^+})$) accumulate primarily at the top surface. This indicates that MACl not only acts as an additive but is also incorporated into the perovskite bulk, which is in contrast to previous reports.[412–414] However, the proportion of incorporated MACl has not been determined.

Complementary measurements of negatively charged secondary ions (Figure 7.6) reveal distinct halide distributions in the inorganic scaffold – especially for I ($\mathrm{I^-}$) and Cl ($\mathrm{Cl^-}$) ions. For the co-deposited inorganic scaffold, I ions are homogeneously distributed throughout the inorganic and the perovskite layer (Figure 7.6a/c). In contrast, sequential deposition leads to an accumulation of I ions at the HTL side, indicating substantial ion diffusion of I into the CsCl layer and interfacial formation of CsI – consistent with the $\mathrm{CsI^+}$ signal. Cl ions tend to accumulate at both interfaces for the co-deposited inorganic scaffold but only at the HTL side for the sequentially deposited inorganic scaffold, indicating reduced Cl ion diffusivity compared to I ions. In the perovskite films, the halide distribution is comparable for both deposition routes. Notably, I ions are homogeneously distributed throughout the layer, while

Cl and Br (Br^-) ions show modest accumulation at the center of the perovskite layer.

These findings highlight that the deposition route of the inorganic scaffold governs the elemental distribution and ion diffusion behavior within both the inorganic scaffold and the resulting perovskite thin film. Cs ions exhibit high ion diffusivity, becoming homogeneously distributed irrespective of their initial position in the inorganic scaffold. In contrast, Pb-containing fragments display lower ion diffusivity and largely retain their original spatial distribution. The presence of CsI fragments prior to thermal treatment implies a high reactivity with spontaneous reaction of the inorganic precursors. Among the halide species, a lower diffusion tendency is identified for Cl and Br ions compared to I ions.

7.6 Photovoltaic Performance

Following the material-level analysis of the inorganic scaffold as well as the perovskite film depending on the deposition route, PSCs are fabricated in *p-i-n* architecture with the layer stack ITO/NiO_x/2PACz/perovskite/$PDAI_2$+BAI/C_{60}/BCP/Ag.

To evaluate the process repeatability, six consecutive batches are fabricated with both co- and sequential deposition of the inorganic scaffold. For each batch, Figure 7.7a displays the median PCE, where symbol colors denote the molarity that yielded the highest PCE within that batch. Two key observations emerge: First, despite the fundamentally different inorganic process sequences, both deposition routes can achieve comparable device performance.

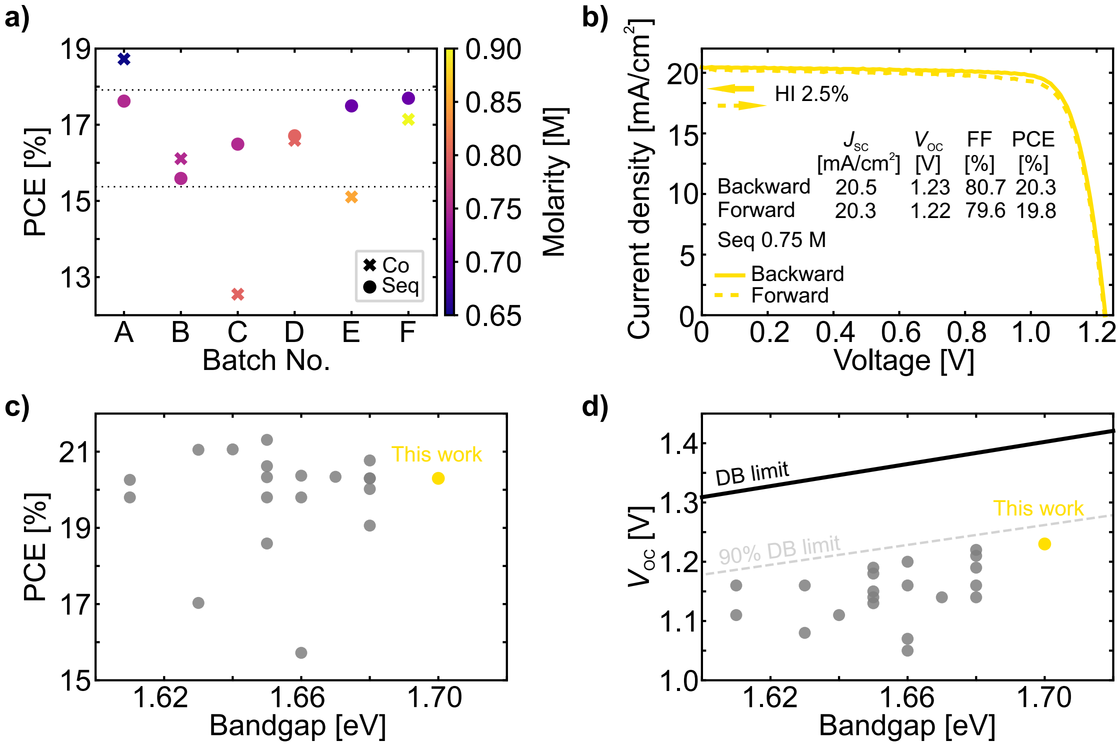

Figure 7.7: a) Comparison of process repeatability of perovskite solar cells (PSCs) with median power conversion efficiencies (PCEs) fabricated *via* co- (Co) and sequential (Seq) deposition of the inorganic scaffold. For each individual batch, Co and Seq PSCs are fabricated in parallel. Symbol colors correspond to the molarity of the organic cation solution resulting in the highest PCE. b) Champion PSC fabricated with sequentially deposited inorganic scaffold with an optimal organic cation molarity of 0.75 M. HI indicates the hysteresis index. c) PCE *versus* bandgap, and d) open-circuit voltage (V_{OC}) *versus* bandgap for wide-bandgap (> 1.60 eV) hybrid two-step processed PSCs in relation to the detailed balance (DB) limit. Adapted from reference[204] with permission from Wiley.

Second, co-deposition exhibits pronounced batch-to-batch variability, whereas sequential deposition yields more consistent performance across multiple batches. As a consequence, the optimum organic cation molarity as well as the device performance varies substantially for co-deposition (0.65-0.90 M, median PCE: 12.6%-18.7%), while a much narrower optimum (0.70-0.80 M, median PCE: 15.6%-17.7%) is retained for sequential deposition. A complete overview of the PCE trends for each batch is provided in Figure A.40. Final QCM film thicknesses are monitored for each batch (Table A.12), and only minor variations in the measured CsCl QCM thickness are observed for co-deposition (30 ± 1 nm), ruling out significant changes in the nominal inorganic scaffold composition.

While the elemental distribution analysis indicates local elemental variations, which can possibly influence band alignment and thus device performance,[415,416] the differences observed appear to have no discernible effect on the measured device metrics. However, dedicated follow-up studies are needed to conclusively validate this finding.

The champion device obtained from the sequential deposition route (Figure 7.7b) achieves a PCE of 20.3% in the backward scan with a V_{OC} of 1.23 V, a J_{SC} of 20.5 mA cm^{-2}, and a FF of 80.7%, with a bandgap of 1.70 eV (Figure A.41b). This device performance ranks among the highest reported PCEs for the hybrid two-step deposition route and features a remarkably high V_{OC}, approaching 90% of the DB limit for this bandgap (Figure 7.7c/d with all literature values given in Table A.13), positioning sequential deposition of the inorganic scaffold as a promising deposition route for the fabrication of highly efficient PSCs. MPP tracking confirms stable device performance over 4000 s (Figure A.41c). However, a more comprehensive stability study and further process optimizations are required, given that device stability likely depends strongly on the organic cation molarity, as indicated by the analysis of Petry and Pappenberger *et al.*[204] In particular, fractional deviations in precursor stoichiometry are found to influence device stability, supporting this hypothesis.[417]

Deposition rates of 1 Å s^{-1} for PbI_2 and 0.1 Å s^{-1} for CsCl are selected based on literature reports for co-deposition of the inorganic scaffold.[78,80] These rates are increased using both vertical scale-up (higher rate per source) and horizontal scale-out (multiple sources) strategies[391] and a detailed analysis can be found in Petry and Pappenberger *et al.*[204] Increasing the CsCl rate from 0.1 to 0.8 Å s^{-1} or the PbI_2 rate from 1 to 3 Å s^{-1} have no measurable effect on device performance. Further throughput enhancement is achieved by running two PbI_2 sources simultaneously at 3+3 Å s^{-1}, again without compromising device efficiency. Overall, these results demonstrate the compatibility of the sequential inorganic scaffold deposition route with high-throughput PSC fabrication.

Furthermore, the sequential deposition route is compatible with scalable deposition techniques, such as inkjet printing of the organic cation solution. Using sequential deposition of CsBr and PbI_2 for the inorganic scaffold, SJ PSCs with 19.8% efficiency are realized within the research group.[69] The scalability of the method is validated on a large-area substrate (6.4×6.4 cm^2), yielding a uniform thin film and high PCE homogeneity across the entire substrate. It should be noted that in the vapor-deposition system used in this thesis, film homogeneity is governed primarily by source emission characteristics and geometry rather than the deposition route itself.[418]

These results highlight an improved process repeatability for the sequential deposition route compared to the commonly used co-deposition route of the inorganic scaffold, both in terms of maximum achievable PCE and a more consistent optimal process window.

7.7 Two-Terminal Perovskite/Silicon Tandem Solar Cell Integration

Building on the systematic investigation and successful implementation of the sequential deposition route in SJ PSCs, this strategy is extended to Si bottom cells for fabricating 2T perovskite/Si TSCs.

To evaluate the robustness and applicability of the sequential deposition route on textured Si substrates – a critical aspect for industrially relevant Si bottom cells – initial compatibility studies are carried out and directly compared to the co-deposition route. The primary objective of these tests is to determine whether the substrate texturing influences the morphology and microstructure of the resulting inorganic scaffold, which in turn critically affects perovskite conversion quality and device performance. For this purpose, 550 nm thick inorganic scaffolds are co- or sequentially deposited on planar, small-textured (pyramid height ≈ 0.5-1 µm), and large-textured (pyramid height

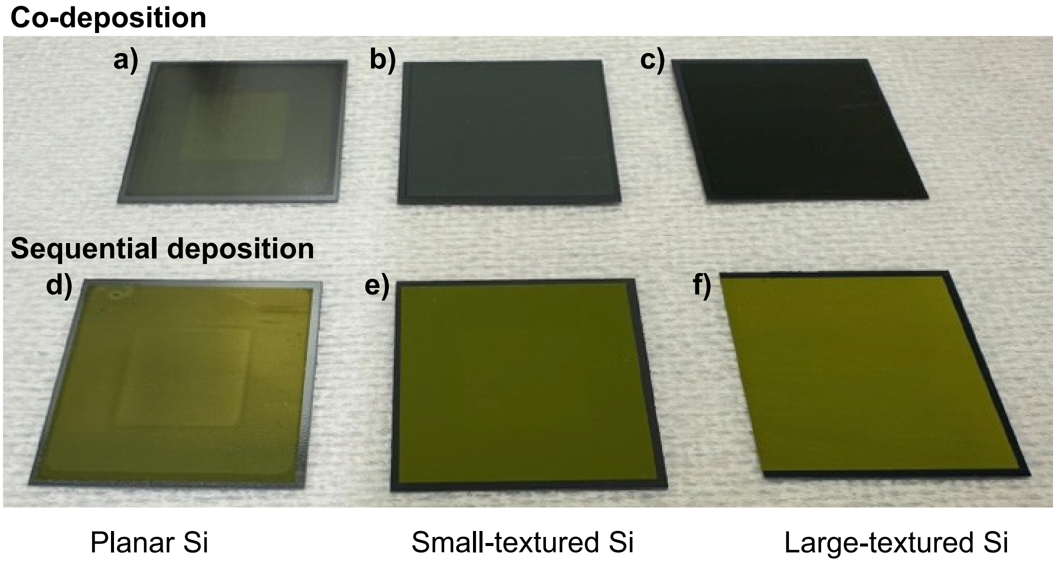

Figure 7.8: Optical photographs of the inorganic scaffold deposited *via* co- (Co) and sequential (Seq) deposition on a)/d) planar, b)/e) small-textured (pyramid height ≈ 0.5-1 µm) and c)/f) large-textured (pyramid height ≈ 2-5 µm) silicon (Si) bottom cells. The inorganic scaffolds and perovskite films are prepared on Si/indium tin oxide (ITO)/NiO_x/2PACz. Adapted from reference[204] with permission from Wiley.

≈ 2-5 µm) Si bottom cells resulting in half-stack devices with the layer sequence Si/ITO/NiO_x/2PACz/inorganic scaffold.

Already upon visual inspection (Figure 7.8), clear qualitative differences between both deposition routes become evident. For co-deposition, the inorganic scaffold remains largely translucent for all surface structures, allowing the underlying Si bottom cell to remain visible. In contrast, sequential deposition results in a distinctly more opaque and visibly yellow layer, indicative of a rougher and more textured surface morphology. This observation mirrors the trend previously observed for inorganic scaffolds deposited on glass substrates (Figure A.36).

SEM images (Figure 7.9) support these findings and further highlight the strong dependence of inorganic scaffold morphology on surface texture. Co-deposited inorganic scaffolds form compact and homogeneous layers on planar substrates, consistent with the morphology obtained on glass substrates (Figure 7.2a). On large-textured substrates, however, the inorganic scaffold transitions to pronounced columnar growth following the substrate topography, while small-textured substrates yield an irregular intermediate morphology. Conversely, the sequential deposition route produces an inorganic scaffold with a morphology largely independent of the underlying Si bottom cell texture. Across all substrate types – glass substrates (Figure 7.2b) as well as planar, small-textured and large-textured Si bottom cells – the resulting inorganic scaffold exhibits a highly irregular surface structure with vertically and slightly tilted PbI_2 platelets. These findings indicate that sequential deposition can effectively decouple inorganic scaffold formation from substrate texturing.

A first demonstration of a complete 2T perovskite/Si TSC using the sequentially deposited inorganic scaffold on small-textured Si bottom cells with the layer stack Si/ITO/NiO_x/2PACz/perovskite/$PDAI_2$+BAI/C_{60}/SnO_x/IZO/Ag/MgF_2 (1.0 cm^2 active area, similar to Figure 5.1b) results in a champion performance of 24.1% in the backward scan (Figure 7.10a). While promising, this result remains below the TSC performance previously achieved with the fully solution-based two-step deposition method presented in this thesis (26.2%, Figure 5.25a) as well as the 33.1% reported by Er-raji *et al.*[89] using a hybrid two-step deposition method on small-textured Si bottom cells. In addition, the device exhibits a considerable hysteresis of 27.8%. These results clearly indicate that optimization of both the inorganic scaffold thickness and the organic cation solution molarity is needed to unlock the full potential of the sequential deposition route for integration in 2T perovskite/Si TSCs. Nonetheless, the J_{SC} already reaches encouraging values of close to 20 mA cm^{-2}, consistent with the EQE measurement (Figure 7.10b), suggesting that optical and photogeneration properties are already well-aligned with expectations.

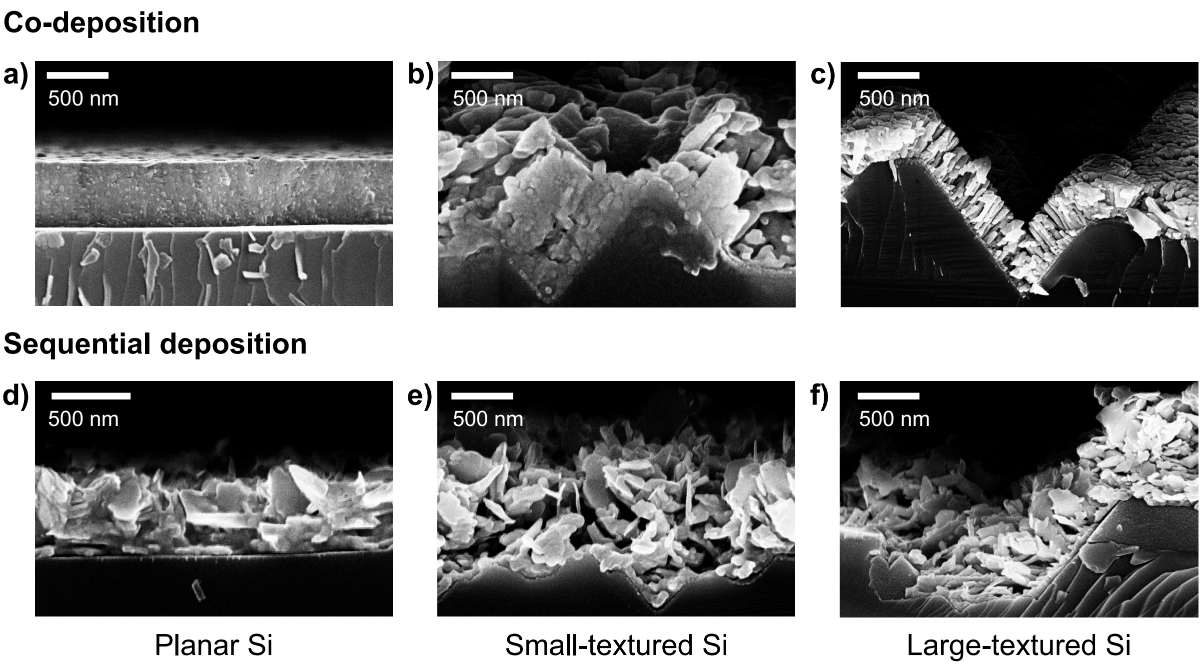

Figure 7.9: Cross-sectional scanning electron microscopy (SEM) images of the inorganic scaffold deposited *via* co- (Co) and sequential (Seq) deposition on a)/d) planar, b)/e) small-textured (pyramid height ≈ 0.5-1 µm) and c)/f) large-textured (pyramid height ≈ 2-5 µm) silicon (Si) bottom cells. The inorganic scaffolds and perovskite films are prepared on Si/indium tin oxide (ITO)/NiO_x/2PACz. Adapted from reference[204] with permission from Wiley.

Importantly, this study provided the basis for a subsequent work within the research group demonstrating that combining sequential deposition of the inorganic scaffold with a scalable deposition technique (inkjet printing) of the organic cation solution enables 2T perovskite/Si TSCs with efficiencies up to 27.4% on large-textured Si bottom cells.[69] This result highlights the strong compatibility of sequential deposition of the inorganic scaffold with textured Si substrates and underscores the significant promise of this route for industrially relevant tandem integration.

Overall, the initial compatibility study demonstrates that the sequential deposition route yields a texture-independent inorganic scaffold morphology, in contrast to the pronounced texture sensitivity observed for co-deposition. This

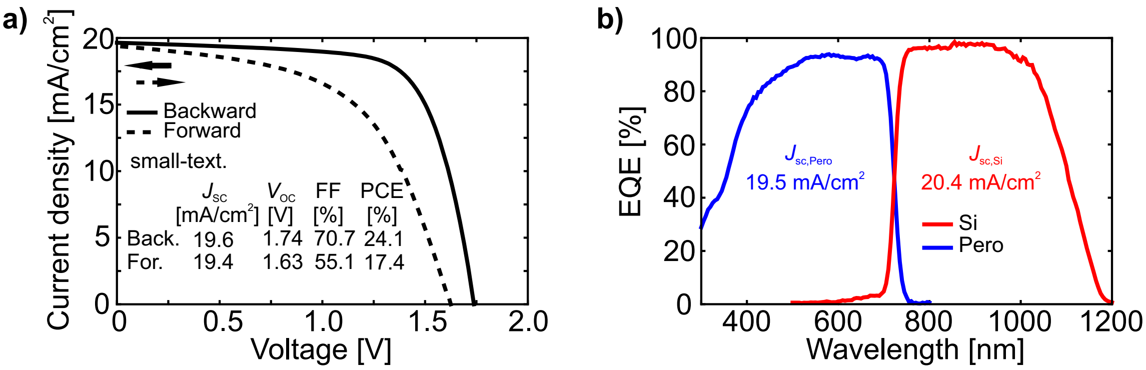

Figure 7.10: a) Current density *versus* voltage (*J*-*V*) characteristics, and b) external quantum efficiency (EQE) of the champion small-textured two-terminal (2T) perovskite/silicon (Si) tandem solar cell (TSC, active area: 1.0 cm^2, pyramid height ≈ 0.5-1 µm) with 125 nm of MgF_2 as antireflective coating. The inorganic precursors CsCl (50 nm) and PbI_2 are deposited sequentially. The molarity of the organic cation solution is 0.75 M. The surface passivation concentration is the same as for single-junction (SJ) perovskite solar cells (PSCs).

robustness positions sequential deposition as a highly promising strategy for reliable and scalable fabrication of 2T perovskite/Si TSCs.

7.8 Summary

This chapter introduces a fully sequential deposition route for fabricating the inorganic scaffold in wide-bandgap hybrid two-step processed PSCs. By sequential vapor-deposition of CsCl and PbI_2, the method provides a promising, industry-compatible alternative to the commonly used co-deposition route, which is known to suffer from significant process complexity and limited industrial scalability.

A systematic material-level characterization reveals a pronounced dependence of inorganic scaffold formation on the chosen deposition route, with significant differences in morphology, crystal orientation, and elemental distribution. Co-deposition yields a compact inorganic scaffold dominated by horizontally oriented PbI_2 platelets, whereas sequential deposition results in a highly porous inorganic scaffold with vertical and slightly tilted PbI_2 crystal orientation, reflected in an order-of-magnitude increase in surface roughness. Additionally, sequential deposition leads to a pronounced layered elemental profile.

Despite these pronounced differences in the inorganic scaffold, the resulting perovskite thin films exhibit similar morphologies and only minor variations in crystal orientation, indicating that the initial PbI_2 alignment acts primarily as a template during perovskite conversion rather than dictating overall film quality. Elemental analysis further reveals high ion diffusivity of Cs, I, and FA ions – resulting in homogeneous elemental distributions within the perovskite thin film – while Pb and Cl retain signatures of the initial inorganic scaffold structure.

Notably, both inorganic scaffold deposition routes result in comparable device efficiencies, demonstrating that the subtle differences in crystal orientation do not significantly impair device performance. Nevertheless, sequential deposition offers clear practical and industrial advantages. PSCs fabricated from sequentially deposited inorganic scaffolds achieve a champion performance of 20.3% ($E_g \approx 1.70$ eV), ranking among the highest reported efficiencies for wide-bandgap hybrid two-step processed PSCs to date. More critically from an industrial perspective, the sequential deposition route exhibits substantially enhanced process repeatability – a key requirement for reliable device fabrication and industrial manufacturing.

When implemented in a 2T perovskite/Si tandem architecture, co- and sequential deposition produce significantly different inorganic scaffold morphologies depending on the surface texture. Co-deposition forms a compact inorganic scaffold on planar substrates, an irregular morphology on submicron-scale textures and a pronounced columnar growth on micron-scale textures. In contrast, sequential deposition results in a texture-independent inorganic scaffold formation with reliable coverage on planar, submicron, and micron-scale textures, providing a practical advantage for processing on textured Si bottom cells.

In conclusion, this chapter systematically addresses thin-film formation (research question **II**) as a function of the deposition route for both SJ PSCs and 2T perovskite/Si TSCs (research question **IV**) within the hybrid two-step deposition method. The results demonstrate that the sequential deposition route combines high device performance with strong process robustness. By establishing a more controllable and industrially scalable alternative to co-deposition, this chapter positions sequential deposition of the inorganic scaffold as a viable strategy for high-throughput perovskite PV manufacturing.

8 Conclusion

8.1 Summary

Combining a wide-bandgap perovskite thin film ($E_g \approx 1.65$-$1.75\,\mathrm{eV}$) with Si in a 2T tandem configuration is one of the most promising approaches to surpass the theoretical efficiency limit of SJ PV technologies. For industrial relevance, however, perovskite deposition methods must be compatible with commercial Si bottom cells, which typically feature micrometer-scale pyramidal texturing. While such textured surfaces are essential for enhanced light-harvesting, they present a significant challenge for conventional solution-based perovskite fabrication methods, as deposition methods must be capable of forming dense, uniform, and defect-free perovskite thin films with thicknesses of several hundred nanometers on these textures. Moreover, the deposition method must be suitable for large-scale industrial manufacturing.

In response to these requirements, this work introduces solution-based two-step deposition routes – either fully solution-based or as a hybrid route combining vapor- and solution-based deposition – to enable high-quality wide-bandgap perovskite thin films on textured substrates. The overarching goal of this work is to develop a fundamental understanding of thin-film formation, interface quality, and process repeatability in solution-based two-step deposition processes, enabling their advancement toward industrial perovskite PV manufacturing.

In the following, the results and findings addressing the research questions outlined in Section 1.2 are summarized and discussed:

I: Bandgap engineering – How can the perovskite bandgap be tuned to a target of 1.68 eV for application in two-terminal perovskite/silicon tandem solar cells using a fully solution-based two-step deposition route?

Despite the advantages of fully solution-based two-step deposition for tandem integration, most studies have focused on narrow-bandgap perovskite thin films ($E_g < 1.60\,\mathrm{eV}$),[167,246,247] while the fabrication of wider bandgaps ($E_g > 1.65\,\mathrm{eV}$) – essential for 2T perovskite/Si tandem architecture – has remained comparatively underexplored. Prior to the start of this work, only a single report had demonstrated a PSC with a bandgap $\geq 1.63\,\mathrm{eV}$ in the *p-i-n* architecture fabricated *via* a fully solution-based two-step deposition route.[57]

To address this knowledge gap, this work presents the first systematic study of three bromide incorporation strategies within the fully solution-based two-step deposition method. Bromide is introduced either *via* 1. $PbBr_2$ in the inorganic deposition step, 2. FABr in the organic deposition step, or 3. a combined bromide incorporation in both deposition steps, i.e., *via* $PbBr_2$ in the first and FABr in the second deposition step. All three bromide incorporation strategies yield operational PSCs with bandgaps in the target range of 1.66-1.68 eV.

Among the three bromide incorporation strategies, combined bromide incorporation in both deposition steps proves most effective, i.e., showing the best device performance with a PCE of 15.9%, minimal hysteresis (< 5%) and a significantly enhanced V_{OC} of 1.19 V. A device study across a broader bandgap range of 1.59 to 1.70 eV further confirms that combined bromide incorporation consistently results in the highest V_{OC} compared to bromide incorporation in only one deposition step. This is likely due to more effective and homogeneous bromide incorporation, which facilitates conversion to the photoactive perovskite phase.

Overall, these results establish combined bromide incorporation in both deposition steps as the most effective strategy for achieving a target bandgap of 1.68 eV without compromising perovskite film quality in the fully solution-based two-step deposition method.

II: Thin-film formation – How do perovskite composition and deposition route influence the microstructure and optoelectronic properties of perovskite thin films fabricated *via* a fully solution-based or hybrid two-step deposition route?

Understanding and identifying parameters that influence thin-film formation is essential for optimizing the perovskite thin-film quality and, in turn, achieving the device performance and long-term operational stability required for the industrial application of perovskite PV.
For the fully solution-based two-step deposition method, compositional engineering has a pronounced influence on both microstructure and optoelectronic properties. Among the investigated bromide incorporation strategies, introducing bromide in both deposition steps yields the highest film quality, characterized by enhanced grain growth, reduced pinhole density, and improved crystallinity. In addition to these bulk improvements, combined bromide incorporation modestly improves the perovskite/C_{60} interface, reflected by a reduced ideality factor and corresponding suppression of non-radiative recombination.
Bulk incorporation of CsI enhances the conversion to the photoactive perovskite phase by reducing residual PbI_2, thereby improving morphology, crystallinity, and charge-carrier extraction, as reflected by an increased J_{SC} of $18.9\,mA\,cm^{-2}$ and a resulting PCE of 16.4%. However, despite these improvements in bulk properties, CsI introduces additional non-radiative recombination losses at the perovskite/C_{60} interface, reducing the V_{OC} to 1.14 V. These interfacial losses can be effectively mitigated by introducing a thin LiF surface passivation layer, which restores the V_{OC} to 1.20 V and increases the PCE to 18.5%.
Compositional versatility of the developed fully solution-based two-step deposition method is demonstrated by removing MA from the perovskite composition, transitioning from a TC perovskite to a DC perovskite. The DC perovskite films retain a morphology and optoelectronic properties similar to their TC counterpart, and in a direct comparison, device performance remains comparable (19.2% DC, 18.9% TC).
Introducing a 5 nm CsCl seed layer at the HTL/perovskite interface within the fully solution-based two-step deposition method preserves the already high intrinsic perovskite film quality while subtly enhancing microstructure through increased grain size, reduced pinhole density, and improved crystallinity.
In the hybrid two-step method, the choice of deposition route for the inorganic precursors significantly influences perovskite thin-film formation. Co-deposition of the inorganic precursors CsCl and PbI_2 produces a compact inorganic scaffold with horizontally oriented PbI_2 platelets. In contrast, sequential deposition (CsCl followed by PbI_2 deposition) results in a highly porous inorganic scaffold with vertically and slightly tilted PbI_2 orientation, accompanied by an order-of-magnitude increase in surface roughness and a more pronounced layered elemental profile. After conversion to the perovskite phase, both deposition routes yield perovskite films with similar morphologies and only minor differences in crystal orientation. Device implementation demonstrates comparable efficiencies for both deposition routes, while the sequential route offers superior process repeatability and achieves a champion performance of 20.3% for $E_g \approx 1.70\,eV$, ranking among the highest reported efficiencies for wide-bandgap hybrid two-step processed PSCs. This highlights the potential of sequential inorganic scaffold deposition as a viable and industry-compatible strategy for high-throughput perovskite PV manufacturing.

III: Additive and interface engineering – Which additive and interface engineering strategies can enhance perovskite film quality and thereby improve device performance and fabrication yield using a fully solution-based two-step deposition route?

Despite the improvements achieved through combined bromide incorporation, the final devices still exhibit a V_{OC} deficit of approximately 70 mV relative to $V_{OC\text{-imp}}$ and a J_{SC} below $18\,mA\,cm^{-2}$. For wide-bandgap perovskite top cells for 2T tandem integration, however, reaching a V_{OC} as close as possible to the DB limit (≈ 1.38 eV for $E_g \approx 1.68$ eV) and achieving a J_{SC} exceeding 20 mA cm^{-2} – required for current matching with the Si bottom cell – are essential for maximizing device performance.[38,39,104] These remaining shortcomings highlight the need for refined compositional engineering and targeted passivation strategies to further improve voltage output and charge-carrier extraction.

Additive and interface engineering play a central role in suppressing non-radiative recombination in both the perovskite bulk and at the perovskite/CTL interfaces. In this work, three complementary strategies prove particularly effective for fully solution-based two-step processed PSCs.

First, incorporating CsI in the perovskite bulk and applying a thin LiF surface passivation layer combine the improved bulk properties induced by CsI with the interfacial passivation provided by LiF at the perovskite/C_{60} interface. This compositional and interfacial engineering strategy increases the PCE from 15.9% to 18.5%, representing one of the highest efficiencies for a wide-bandgap PSC fabricated *via* a fully solution-based two-step method at the time the study was conducted.

Second, a dual bimolecular passivation strategy using $PDAI_2$ and BAI is implemented in the bulk of a MA-free (DC) perovskite thin film and introduced as surface passivation in place of LiF. This dual bimolecular passivation strategy effectively reduces residual PbI_2 at the perovskite/HTL interface and shifts the perovskite crystal orientation to a more vertical alignment, facilitating charge-carrier extraction. Furthermore, non-radiative recombination losses are significantly suppressed at grain boundaries and at the perovskite/C_{60} interface. XPS analysis reveals that the bimolecular surface passivation strategy modifies the surface stoichiometry, widening the surface bandgap by $\approx$ 150 meV due to bromide enrichment and thereby facilitating electron extraction to the ETL. The bimolecular surface passivation strategy reduces metallic Pb^0 and oxidized Pb species, lowering the density of defect states at the perovskite surface. As a result, the devices with dual bimolecular passivation achieve an efficiency of 20.9% with a V_{OC} of 1.24 V and a FF $> 80\%$. At the time of this study, this represented the highest reported efficiency for a MA-free *p-i-n* type PSC with a bandgap of 1.67 eV processed *via* a fully solution-based two-step method.

Third, introducing a 5 nm CsCl seed layer at the HTL/perovskite interface subtly improves perovskite crystal quality, resulting in an increased FF, reduced hysteresis, and a PCE of 19.0% at $E_g \approx 1.67$ eV. Most importantly, the CsCl seed layer significantly improves the fabrication yield of functional 2T perovskite/Si TSCs on textured Si bottom cells – without requiring adjustments in the perovskite fabrication process.

Collectively, these results demonstrate that carefully selected bulk additives, surface passivation layers, and seed-layer engineering provide powerful strategies for high-performance perovskite film fabrication within the fully solution-based two-step deposition route, thereby strengthening its potential for industrially relevant perovskite PV.

IV: Tandem integration – How does the surface texture of the silicon bottom cell influence the integration of perovskite thin films in two-terminal perovskite/silicon tandem solar cells fabricated *via* a fully solution-based or hybrid two-step deposition route?

For industrially relevant 2T perovskite/Si tandem devices, the perovskite thin film must reliably cover commercial Si bottom cells, which typically feature micrometer-sized pyramidal textures.

The optimized fully solution-based two-step processed wide-bandgap perovskite thin films developed in this work are successfully integrated on planar, small-textured (pyramid height $\approx$ 0.5-1 µm), and large-textured (pyramid height $\approx$ 2-5 µm) Si bottom cells. In these 2T tandem configurations, efficiencies of 28.0% for planar, 26.2% for small-textured, and 24.1% for large-textured Si bottom cells are achieved. While these efficiencies remain below state-of-the-art tandem devices, they represented the highest values obtained for 2T perovskite/Si tandems processed *via* a fully solution-based two-step method at the time of this study. Moreover, this work constitutes the first systematic investigation of fully solution-based two-step processed perovskite thin films on different pyramidal texture heights in 2T perovskite/Si tandem configuration, highlighting the compatibility of the developed deposition method even on large-textured substrates. Incorporating a thin CsCl seed layer at the HTL/perovskite interface improves the fabrication yield of functional 2T perovskite/Si TSCs on textured Si bottom cells – where uniform coverage is most challenging – without requiring changes to either the perovskite composition or the deposition parameters.

In the hybrid two-step deposition method, comparing co-deposition and sequential deposition of the inorganic precursors reveals pronounced differences in inorganic scaffold morphology across different substrate textures. Co-deposition forms a compact inorganic scaffold on planar substrates, an irregular morphology on submicron-scale textures, and a columnar growth on micron-scale textures. In contrast, sequential deposition results in a texture-independent inorganic scaffold growth, offering a promising strategy for scalable and reliable fabrication of 2T perovskite/Si tandems in an industrial context. First tandem devices based on the sequential deposition route achieve an efficiency of 24.1%, and subsequent work within the research group demonstrates that efficiencies up to 27.4% can be reached by combining sequential deposition of the inorganic scaffold with inkjet printing of the organic cation solution.[69]

V: Stability – How stable are the fully solution-based two-step processed perovskite solar cells under relevant operational and stress conditions?

Long-term operational stability is a key requirement for the commercialization of PSCs. Therefore, the operational stability of the fully solution-based two-step processed PSCs is evaluated under standardized ISOS stress conditions,[226] including dark storage (ISOS-D1, dark storage, 25 °C, intermittent *J-V* measurements), thermal stress (ISOS-D2, dark storage, 85 °C, intermittent *J-V* measurements), and light-induced degradation (ISOS-L1, 100 mW cm^{-2}, 25 °C, MPP tracking). Removing MA from the perovskite composition – transitioning from a TC to a DC perovskite composition – improved long-term operational stability. Under ISOS-D1 conditions, DC devices maintain performance near the T_{80} threshold over 1000 h, whereas TC devices reach T_{80} after 130 h. Dark storage under elevated temperatures (85 °C, ISOS-D2) results in a T_{80} of $\approx$ 400 h for DC devices compared to 250 h for TC devices. During continuous illumination (ISOS-L1) for 300 h, DC devices show a rapid initial efficiency loss within the first 5 h but retain a higher overall PCE than the TC counterpart.

Stability improvements correlate strongly with reduced non-radiative recombination from both bulk and interfacial defects. The optimized dual bimolecular passivation strategy (MA-free, DC opt.) further improves operational stability compared to the DC devices, reaching T_{80} after 670 h and maintaining 78% of the initial efficiency after 1000 h of continuous illumination (ISOS-L1). These devices show negligible degradation during dark storage but remain sensitive to thermal stress, exhibiting pronounced performance losses at 85 °C. Introducing a CsCl seed layer at the HTL/perovskite interface further enhances stability, with the seed-layer-treated devices retaining 84% of their initial efficiency after 1000 h under ISOS-L1 conditions, outperforming devices without CsCl seed layer.

Collectively, these results demonstrate that stability under relevant operating conditions is primarily limited by thermally activated degradation pathways, while dark and moderate-temperature light-soaking conditions are well tolerated. Combining MA-free compositions, interfacial passivation, and seed-layer engineering effectively suppresses non-radiative recombination in fully solution-based two-step processed PSCs, providing a clear route toward more stable wide-bandgap PSCs. Nevertheless, further optimization is required, as the current results have yet to reach the benchmark set by state-of-the-art stability metrics.[366]

In summary, the results presented in this work outline a coherent pathway from bandgap engineering (combined bromide incorporation) to microstructure control (compositional and inorganic scaffold engineering), and finally to defect and interface management (CsI/LiF, $PDAI_2$+BAI, CsCl seed layer) in solution-based two-step processed PSCs. Together, these advances enable successful 2T perovskite/Si tandem integration on a range of Si surface textures while simultaneously improving device stability and fabrication yield. The insights gained here provide actionable guidelines for further advancing wide-bandgap PSCs fabricated *via* solution-based two-step deposition methods and for developing industrially relevant 2T perovskite/Si TSCs.

8.2 Outlook

This work establishes solution-based two-step deposition routes as viable and versatile strategies for fabricating high-quality wide-bandgap perovskite thin films on industrially relevant textured Si bottom cells, demonstrating strong potential for high-performance 2T perovskite/Si TSCs. Building on these advances, the following outlook outlines the critical next steps required to further mature solution-based two-step deposition within the broader perovskite PV landscape. Particular emphasis is placed on three key pillars that define the path toward industrial deployment: scalability, efficiency, and long-term operational stability.

Extending the bandgap engineering strategy

While the present work establishes an effective bandgap engineering strategy within the solution-based two-step spin-coating process, broader investigations across different two-step deposition routes remain essential. These include fully solution-based methods such as inkjet printing, slot-die coating, and blade coating, as well as fully vapor-based deposition and hybrid two-step deposition routes that combine vapor deposition with solution-based deposition. Evaluating whether the advantages of combined bromide incorporation in both deposition steps translate to these scalable deposition methods is therefore a key next step, particularly in view of industrial manufacturing requirements, as differences in precursor deposition and conversion kinetics can significantly influence halide distribution, phase stability, and defect formation in wide-bandgap perovskite thin films.[196]

Beyond bromide incorporation, vapor deposition offers additional flexibility for bandgap engineering, since solubility constraints are circumvented. Consequently, future research should explore chloride incorporation as well as tailored combinations of $PbBr_2$/$PbCl_2$ and CsBr/CsCl precursors to expand the accessible compositional space. Such halide-mixing strategies may enable more precise control of the bandgap while mitigating halide phase segregation – one of the key challenges in the wide-bandgap perovskite regime.[254–256]

This thesis focuses on achieving a target bandgap of 1.68 eV, suitable for 2T perovskite/Si TSCs. Looking forward, adapting this strategy for other emerging perovskite PV technologies – such as all-perovskite TSCs, perovskite/CI(G)S TSCs, and triple-junction solar cells – will require extending the perovskite bandgap range above 1.8 eV.[18,33–36] However, several studies indicate that halide phase segregation, defect formation and voltage losses become increasingly problematic for perovskite bandgaps above 1.65 eV and it remains elusive if the current bandgap engineering strategy can be extended to these regimes. Addressing these challenges will likely require innovations in compositional engineering, passivation strategies, and interface energy-level alignment.[101,419]

Comparative studies across different two-step deposition methods will therefore be essential for establishing general design principles for reproducible bandgap engineering in wide-bandgap perovskite thin films and for enabling the transfer of optimized compositions to scalable fabrication techniques.

Mechanistic understanding of halide incorporation and redistribution

This work presents the first systematic investigation of bromide incorporation in fully solution-based two-step processed PSCs for bandgaps beyond 1.65 eV. The results demonstrate that both the sequence and the method of bromide incorporation have a pronounced impact on film quality and optoelectronic properties of the perovskite thin film. However, the underlying mechanistic origins of these effects are not yet fully understood. A deeper understanding of halide incorporation pathways is necessary for effective bandgap engineering and for repeatable fabrication of high-performance wide-bandgap perovskites, particularly in the context of scalable industrial manufacturing.[101,419]

To advance this understanding, future studies should elucidate the kinetics and mechanisms of halide incorporation and redistribution when bromide is introduced at different stages of the two-step deposition route. This requires correlating structural, electronic, and chemical information. Combining XRD with complementary techniques such as XPS, ultraviolet photoelectron spectroscopy (UPS), inverse photoemission spectroscopy (IPES) and ToF-SIMS has proven powerful for comprehensively studying thin-film formation, halide distribution, and interfacial reactions of wide-bandgap perovskite films.[367,420,421] Moreover, *in situ* and time-resolved analysis during precursor conversion, crystallization, and annealing would provide critical insight into phase evolution and bandgap development, thereby linking incorporation pathways to operational stability and device performance.[422]

Transition to industrial-scale processes

The device areas demonstrated in this work – 10.5 mm^2 for SJ PSCs and 1 cm^2 for 2T perovskite/Si TSCs – align with current laboratory standards for perovskite-based solar cells. However, a decisive next step toward commercialization is the upscaling of perovskite technology to industrially relevant module dimensions.[406] Spin coating, the primary deposition method used in this work, is the most widely adopted laboratory technique due to its simplicity, low cost, and ability to achieve record PCEs.[14] Yet this technique is not suitable for producing homogeneous films over large areas and therefore cannot meet the requirements of industrial manufacturing.[423]

A transition toward scalable deposition techniques – such as vapor deposition,[67,71] inkjet printing,[68,69,424] slot-die coating,[70,425] and blade coating[426,427] – is thus essential. The fully sequential inorganic scaffold deposition implemented in the hybrid two-step deposition route represents an initial step toward scalable, industrially relevant processing. Nevertheless, replacing spin coating remains indispensable. Demonstrating perovskite film uniformity and process repeatability of scalable deposition techniques across large areas and on textured substrates will be a key task on the path toward industrial perovskite PV manufacturing. Within the research group, initial progress toward this objective has already been achieved. Diercks *et al.*[67] introduced a two-step vapor-deposition method, Pesch *et al.*,[69] implemented inkjet printing of organic cations within the hybrid two-step method developed in this work, and Geistert *et al.*[70] adopted the fully solution-based two-step method developed in this work for slot-die coating.

Future work should focus on developing and validating scalable perovskite deposition routes that preserve the film quality, compositional flexibility, and versatility achieved in laboratory-scale two-step deposition methods.

Advancing 2T perovskite/Si tandem integration

The proof-of-concept tandem devices presented in this thesis validate the suitability of the developed solution-based two-step deposition routes for integration into 2T perovskite/Si architectures on both planar and textured Si substrates. However, fully unlocking the efficiency potential of 2T perovskite/Si tandems will require further progress, particularly in light management, interface quality, and precise bandgap engineering.[428–430] Furthermore, the separation of precursor deposition into two distinct steps necessitates adjusting the organic cation solution molarity relative to the inorganic scaffold.

Future tandem architectures can build on the development of advanced passivation concepts that extend beyond the dual bimolecular strategy explored in this thesis, thereby suppressing non-radiative recombination pathways and improving interfacial energetic alignment.[313] Further interface engineering will be essential – encompassing the identification of energetically better aligned HTL and ETL materials, and the optimization of layer thicknesses for the ETL, perovskite thin film, and TCO layer. Even minor adjustments to these layers can result in significant improvements in optical coupling, charge extraction, and ultimately device performance.[431]

Managing optical losses and ensuring effective light redistribution in textured 2T perovskite/Si tandem architectures remains a major challenge.[429] Advanced optical simulations, combined with experimental verification, will be crucial to refine layer thicknesses and maximize current matching between the subcells. Given the vast design space arising from numerous material combinations, compositional variations, and geometrical parameters, future progress is expected to be increasingly driven by data-guided optimization.[432]

Degradation pathways under realistic stress conditions

Long-term operational stability remains one of the key challenges for perovskite PV and is a decisive prerequisite for commercial viability.[123,308,406] Although this thesis evaluates the stability of fully solution-based two-step processed PSCs under ISOS-D1, ISOS-D2, and ISOS-L1 test conditions, more rigorous stress conditions are required to determine their suitability for real-world applications. These include continuous illumination at elevated temperatures, thermal and light cycling, electrical bias stress, and ultimately extended outdoor operation.[226]

Current research commonly targets T_{80} lifetimes of 1000-5000 h as an intermediate benchmark. While this marks important progress, it remains far from the 20-25 year operational lifetime required to compete with established Si PV technologies.[366,433,434]

The fully solution-based two-step processed wide-bandgap PSCs presented in this thesis exhibit stable performance under continuous illumination and dark storage, retaining $> 80\%$ of their initial efficiency after 1000 h. However, pronounced degradation occurs at elevated temperatures (85 °C), highlighting the need for further optimization. To effectively improve the thermal stability of solution-based two-step processed wide-bandgap PSCs, identifying the dominant degradation mechanism is essential. This processing route differs fundamentally from the conventional one-step spin-coating method due to different crystallization kinetics, ambient-atmosphere annealing, the role of PbI_2 residues at the perovskite/HTL interface, and halide kinetics. These process-dependent material characteristics may govern ion migration, interfacial reactions, phase instability, and defect evolution under stress conditions. Elucidating these mechanisms will enable the development of targeted stabilization strategies tailored to the two-step deposition method.

In addition, perovskite formation in hybrid two-step deposition routes differs from fully solution-based two-step fabrication processes.[206] The difference in inorganic precursor deposition and solvents used for the organic cation solution can lead to variations in intrinsic material properties that directly influence device stability. Consequently, comprehensive long-term operational stability studies of hybrid two-step processed PSCs are essential to evaluate their reliability and advance these fabrication methods toward commercial relevance.

Finally, stability assessments must be extended to 2T perovskite/Si tandem devices. Tandem-specific degradation pathways – such as current mismatch and optical-electrical coupling between the subcells – can profoundly impact long-term performance.[435]

The solution-based two-step deposition routes developed in this thesis provide a robust foundation for advancing both fully solution-based and hybrid two-step methods in future research, contributing to ongoing efforts toward scalable, high-performance, and industrially relevant PSCs and perovskite/Si TSCs.

Appendix

A.1 Resources and Tools

Unless otherwise stated, all experimental work was performed within the laboratory infrastructure of the Light Technology Institute (LTI) and the Institute of Microstructure Technology (IMT) at the Karlsruhe Institute of Technology (KIT). A detailed description of the experimental tools used for this work can be found in Chapter 3.

Various software tools were used to support data processing, visualization, and documentation throughout this thesis. All graphs and most of the data analysis were implemented using *Python*. Illustrative figures and sketches were created with *CorelDraw*. References were managed using *JabRef*. The thesis itself was written in *LaTeX*, using the online editor *Overleaf*.
AI-assisted technologies were utilized to support the writing process by checking spelling and suggesting grammatical improvements. These tools were exclusively used to enhance readability and language quality and did not contribute to the development of scientific content. All AI-generated suggestions were carefully reviewed and edited by the author, who takes full responsibility for the content of this work. The AI-based tools used include *M365 Copilot*, *ChatGPT (GPT-5)* and *DeepL*.

A.2 List of Materials

Table A.1: List of materials used in this thesis. The supplier names stand for Tokyo Chemical Industry Co. Ltd (TCI), Dyenamo, Alfa Aesar, Sigma-Aldrich, Greatcell Solar Materials (Greatcell), Luminescence Technology Corp. (Lumtec), VWR International (VWR) and ChemPur.

Name	Molecular formula	Purity [%]	CAS No.	Supplier
Lead(II) iodide	PbI_2	99.99	10101-63-0	TCI
Lead(II) bromide	$PbBr_2$	99.99	10031-22-8	TCI
Methylammonium iodide (MAI)	CH_6IN	99.99	14965-49-2	Dyenamo
Formamidinium iodide (FAI)	CH_6IN_2	99.99	879643-71-7	Greatcell
Methylammonium chloride (MACl)	CH_6ClN	99.99	593-51-1	Dyenamo
Formamidinium bromide (FABr)	CH_6BrN_2	99.99	146958-06-7	Dyenamo
n-Butylammonium iodide (BAI)	$C_4H_{12}IN$	>99	36945-08-1	Greatcell
Propane-1,3-diammonium iodide ($PDAI_2$)	$C_3H_{12}I_2N_2$	high	120675-53-8	Greatcell
Cesium iodide	CsI	99.99	7789-17-5	Alfa Aesar
Cesium iodide	CsI	>99	7789-17-5	TCI
Cesium chloride	CsCl	>99	7647-17-8	TCI
[2-(9H-carbazol-9-yl)ethyl]phosphonic acid (2PACz)	$C_{14}H_{14}NO_3P$	98	20999-38-6	TCI
Fullerene-C_{60}	C_{60}	99.5	99685-96-8	Sigma-Aldrich
Bathocuproine (BCP)	$C_{26}H_{20}N_2$	99.5	4733-39-5	Lumtec
Magnesium fluoride	MgF_2	99.9	7783-40-6	Sigma-Aldrich
Lithium fluoride	LiF	99.9	7789-24-4	ChemPur
N,N-dimethylformamide (DMF)	C_3H_7NO	99.8	68-12-2	Sigma-Aldrich
Dimethyl sulfoxide (DMSO)	C_2H_6OS	99.9	67-68-5	Sigma-Aldrich
Isopropanol (IPA)	C_3H_8O	99.5	67-63-0	Sigma-Aldrich
Ethanol (EtOH)	C_2H_6O	99.8	64-17-5	VWR
Silver	Ag	-	7440-22-4	-
Gold	Au	-	7440-57-5	-

A.3 Author Contributions According to CRediT System

When publishing within collaborative research projects, *CRediT (Contributor Roles Taxonomy)* is a taxonomy that allows for a high-level description of 14 roles played by contributors in the research process. It provides information about individual author contributions to the research project and reduces disagreements between collaboration partners.[436]

Table A.2: Overview of the categories used in this work to identify the contributions of different authors according to the contributor role taxonomy (CRediT) by Brand *et al.*[436]

Category	Definition
Conceptualization	Ideas; formulation or evolution of overarching research goals and aims
Methodology	Development or design of methodology; creation of models
Investigation	Conducting the research and investigation process, specifically performing the experiments, or data/evidence collection
Data Curation	Management activities to annotate (produce metadata), scrub data and maintain research data (including software code, where it is necessary for interpreting the data itself) for initial use and later reuse
Software	Programming, software development; designing computer programs; implementation of the computer code and supporting algorithms; testing of existing code components
Formal Analysis	Application of statistical, mathematical, computational, or other formal techniques to analyze or synthesize study data
Validation	Verification, whether as a part of the activity or separate, of the overall replication/reproducibility of results/experiments and other research outputs
Writing – Original Draft	Preparation, creation and/or presentation of the published work, specifically writing the initial draft (including substantive translation)
Writing – Review & Editing	Preparation, creation and/or presentation of the published work by those from the original research group, specifically critical review, commentary or revision - including pre- or post-publication stages
Visualization	Preparation, creation and/or presentation of the published work, specifically visualization/data presentation
Project Administration	Management and coordination responsibility for the research activity planning and execution
Funding Acquisition	Acquisition of the financial support for the project leading to this publication
Resources	Provision of study materials, reagents, materials, patients, laboratory samples, animals, instrumentation, computing resources, or other analysis tools
Supervision	Oversight and leadership responsibility for the research activity planning and execution, including mentorship external to the core team

A.3.1 Bandgap Engineering of Two-Step Processed Perovskite Top Cells for Perovskite-Based Tandem Photovoltaics

The research article "Bandgap Engineering of Two-Step Processed Perovskite Top Cells for Perovskite-Based Tandem Photovoltaics" was published in *Advanced Functional Materials* by *R. Pappenberger (R.P.)* as first author, together with *A. Diercks (A.D.)*, *J. Petry (J.P.)*, *S. Moghadamzadeh (S.M.)*, *P. Fassl (P.F.)*, and *U. W. Paetzold (U.W.P.)*.[239]

Table A.3: Author CRediT – Bandgap Engineering of Two-Step Processed Perovskite Top Cells for Perovskite-Based Tandem Photovoltaics

Category	Authors	Details
Conceptualization	***R.P.*** & *U.W.P.*	-
Methodology	*S.M.*	Tandem integration
Investigation	***R.P.***, *A.D.*, *P.F.*	Conducting of experiments by *R.P.*, SEM by *A.D.*, PLQY by *P.F.*
Data Curation	***R.P.***, *A.D.*, *P.F.*	Data preparation led by *R.P.*, supported by *A.D.* and *P.F.*
Software	-	-
Formal Analysis	***R.P.***, *A.D.*, *P.F.*	Data evaluation and interpretation led by *R.P.*, supported by *A.D.* and *P.F.*
Validation	-	-
Writing – Original Draft	***R.P.***	-
Writing – Review & Editing	***R.P.***, *A.D.*, *J.P.*, *P.F.* & *U.W.P.*	-
Visualization	***R.P.***	-
Project Administration	***R.P.*** & *U.W.P.*	-
Funding Acquisition	*U.W.P.*	-
Resources	*U.W.P.*	-
Supervision	*U.W.P.*	-

A.3.2 Versatile Two-Step Process for Perovskite-Based Tandem Photovoltaics

The research article "Versatile Two-Step Process for Perovskite-Based Tandem Photovoltaics" was published in *Solar RRL* by *R. Pappenberger (R.P.)* as first author, together with *R. Singh (R.S.)*, *A. Diercks (A.D.)*, *T. Zhao (T.Z.)*, *R. Pesch (Ra.P.)*, *J. Petry (J.P.)*, *D. Baumann (D.B.)*, *X. Liu (X.L.)*, and *U. W. Paetzold (U.W.P.)*.[285]

Table A.4: Author CRediT – Versatile Two-Step Process for Perovskite-Based Tandem Photovoltaics

Category	Authors	Details
Conceptualization	***R.P.*** & *U.W.P.*	-
Methodology	*X.L.*	Surface passivation introduced by *X.L.*
Investigation	***R.P.***, *R.S.*, *A.D.*, *T.Z.* & *Ra.P.*	Conducting of experiments by *R.P.*, long-term operational stability by *R.S.*, SEM for SJ by *A.D.*, GIWAXS by *T.Z.*, SEM for tandems by *Ra.P.*
Data Curation	***R.P.***, *R.S.*, *A.D.*, *T.Z.* & *Ra.P.*	Data preparation led by *R.P.*, supported by *R.S.*, *A.D.*, *T.Z.* and *Ra.P.*
Software	-	-
Formal Analysis	***R.P.***, *R.S.* & *T.Z.*	Data evaluation and interpretation led by *R.P.*, supported by *R.S.* and *T.Z.*
Validation	-	-
Writing – Original Draft	***R.P.***	-
Writing – Review & Editing	***R.P.***, *R.S.*, *A.D.*, *T.Z.*, *J.P.* & *U.W.P.*	-
Visualization	***R.P.*** & *D.B.*	Led by *R.P.*, supported by *D.B.*
Project Administration	***R.P.***	-
Funding Acquisition	*U.W.P.*	-
Resources	*U.W.P.*	-
Supervision	*U.W.P.*	-

A.3.3 CsCl Seed Layer for Improved Stability and Fabrication Yield of Solution-Based Two-Step Processed Perovskite Thin Films

The research article "CsCl Seed Layer for Improved Stability and Fabrication Yield of Solution-Based Two-Step Processed Perovskite Thin Films" by *R. Pappenberger (R.P.)* as first author, together with *A. Diercks (A.D.)*, *R. Singh (R.S.)*, *A. Welle (A.W.)*, *T. Zhao (T.Z.)*, *J. Petry (J.P.)*, and *U. W. Paetzold (U.W.P.)* is currently in preparation.

Table A.5: Author CRediT – CsCl Seed Layer for Improved Stability and Fabrication Yield of Solution-Based Two-Step Processed Perovskite Thin Films

Category	Authors	Details
Conceptualization	***R.P.***, *A.D.*, *J.P.* & *U.W.P.*	-
Methodology	-	-
Investigation	***R.P.***, *A.D.*, *R.S.*, *A.W.* & *T.Z.*	Conducting of experiments by *R.P.*, SEM by *A.D.*, long-term operational stability by *R.S.*, ToF-SIMS by *A.W.*, GIWAXS by *T.Z.*
Data Curation	***R.P.***, *A.D.*, *R.S.*, *A.W.* & *T.Z.*	Data preparation led by *R.P.*, supported by *A.D.*, *R.S.*, *A.W.* and *T.Z.*
Software	-	-
Formal Analysis	***R.P.***, *A.D.*, *A.W.* & *T.Z.*	Data evaluation and interpretation led by *R.P.*, supported by *A.D.*, *A.W.* and *T.Z.*
Validation	-	-
Writing – Original Draft	***R.P.***	-
Writing – Review & Editing	-	-
Visualization	***R.P.***	-
Project Administration	***R.P.***	-
Funding Acquisition	*U.W.P.*	-
Resources	*U.W.P.*	-
Supervision	*U.W.P.*	-

A.3.4 Benchmarking Inorganic Deposition Routes for Hybrid Two-Step Processed Perovskite Solar Cells: A Materials Perspective

The research article "Benchmarking Inorganic Deposition Routes for Hybrid Two-Step Processed Perovskite Solar Cells: A Materials Perspective" was published in *Solar RRL* by *J. Petry (J.P.)**, *R. Pappenberger (R.P.)**, *A. Welle (A.W.)*, *T. Zhao (T.Z.)*, *A. Diercks (A.D.)*, *R. Pesch (Ra.P.)*, *M. Krause (M.K.)*, *P. Fassl (P.F.)*, and *U. W. Paetzold (U.W.P.)*. *J.P.* and *R.P.* made equal contributions to this work and share first authorship.

Table A.6: Author CRediT – Benchmarking Inorganic Deposition Routes for Hybrid Two-Step Processed Perovskite Solar Cells: A Materials Perspective

Category	Authors	Details
Conceptualization	***R.P.***, *J.P.*, *P.F.* & *U.W.P.*	-
Methodology	-	-
Investigation	***R.P.***, *J.P.*, *A.W.*, *T.Z.*, *A.D.*, *Ra.P.* & *M.K.*	Conducting of experiments by *R.P.* & *J.P.*, ToF-SIMS by *A.W.*, GIWAXS by *T.Z.*, SEM by *A.D.*, picoliter droplet deposition by *Ra.P.*, inorganic deposition rate variation by *M.K.*
Data Curation	***R.P.***, *J.P.*, *A.W.*, *T.Z.*, *A.D.* & *Ra.P.*	Data preparation led by *R.P.* and *J.P.*, supported by *A.W.*, *T.Z.*, *A.D.* and *Ra.P.*
Software	-	-
Formal Analysis	***R.P.***, *J.P.*, *A.W.* & *T.Z.*	Data evaluation and interpretation led by *R.P.* and *J.P.*, supported by *A.W.* and *T.Z.*
Validation	-	-
Writing – Original Draft	***R.P.*** & *J.P.*	-
Writing – Review & Editing	***R.P.***, *J.P.*, *A.W.*, *T.Z.*, *A.D.*, *Ra.P.*, *M.K.*, *P.F.* & *U.W.P.*	-
Visualization	***R.P.*** & *J.P.*	-
Project Administration	***R.P.*** & *J.P.*	-
Funding Acquisition	*P.F.* & *U.W.P.*	-
Resources	*U.W.P.*	-
Supervision	*P.F.* & *U.W.P.*	-

A.4 Bandgap Engineering of Solution-Based Two-Step Processed Perovskite Thin Films

Table A.7: Literature overview for wide-bandgap ($E_g \geq 1.63\,\mathrm{eV}$) perovskite solar cells (PSCs) in the *p-i-n* architecture fabricated *via* a fully solution-based two-step deposition route.

Author	Year	Bandgap [eV]	PCE [%]	V_{OC} [V]	FF [%]	J_{SC} [mA cm^{-2}]	Reference
Chen *et al.*	2022	1.63	21.02	1.2	80.4	21.82	[57]
Luo *et al.*	2025	1.68	23.49	1.291	83.2	21.87	[284]

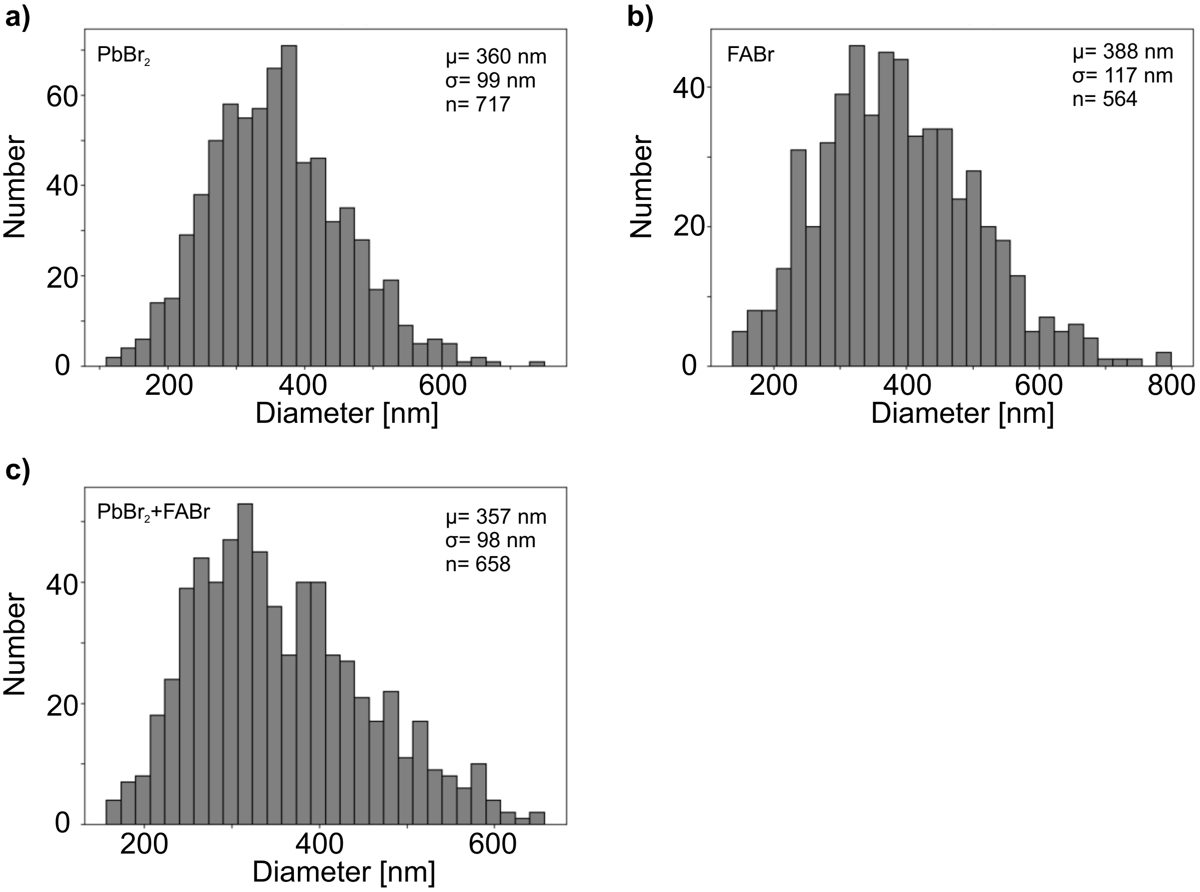

Figure A.1: Grain size analysis of scanning electron microscopy (SEM) images of perovskite films with bromide incorporated *via* a) $PbBr_2$, b) FABr or c) $PbBr_2$+FABr. The grain sizes were determined using a data evaluation program based on StarDist.

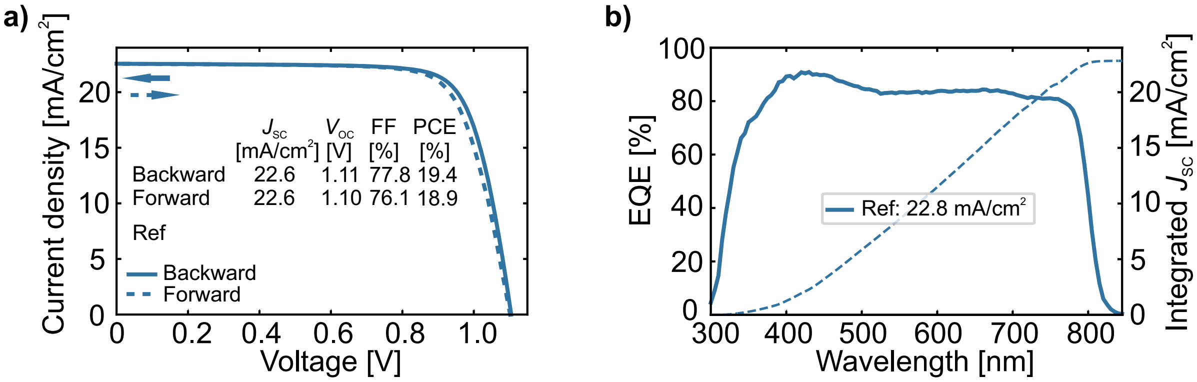

Figure A.2: a) Current density *versus* voltage (J-V) characteristics and b) external quantum efficiency (EQE) as well as the corresponding integrated short-circuit current density (J_{SC}) of the best performing narrow-bandgap perovskite solar cells (PSCs) (Ref, $E_g = 1.55\,eV$). Adapted from reference[239] with permission from Wiley.

Table A.8: *Welch's t test* results for the backward power conversion efficiency (PCE), open-circuit voltage (V_{OC}), short-circuit current density (J_{SC}) and fill factor (FF) of the opaque perovskite solar cells (PSCs) with incorporated bromide ($E_g \approx 1.68\,eV$) *via* $PbBr_2$, FABr or a combination of $PbBr_2$ and FABr ($PbBr_2$+FABr). The calculation was performed using a *t test* calculator.[437]

Parameter	Samples	P-value	Interpretation of difference
	$PbBr_2$ and FABr	0.0023	very statistically significant
PCE	$PbBr_2$ and $PbBr_2$+FABr	< 0.0001	extremely statistically significant
	FABr and $PbBr_2$+FABr	0.1001	not statistically significant
	$PbBr_2$ and FABr	0.5132	not statistically significant
V_{OC}	$PbBr_2$ and $PbBr_2$+FABr	0.1204	not statistically significant
	FABr and $PbBr_2$+FABr	0.0031	very statistically significant
	$PbBr_2$ and FABr	0.1001	not statistically significant
J_{SC}	$PbBr_2$ and $PbBr_2$+FABr	0.1847	not statistically significant
	FABr and $PbBr_2$+FABr	0.7044	not statistically significant
	$PbBr_2$ and FABr	0.0099	very statistically significant
FF	$PbBr_2$ and $PbBr_2$+FABr	0.0002	extremely statistically significant
	FABr and $PbBr_2$+FABr	0.0528	not quite statistically significant

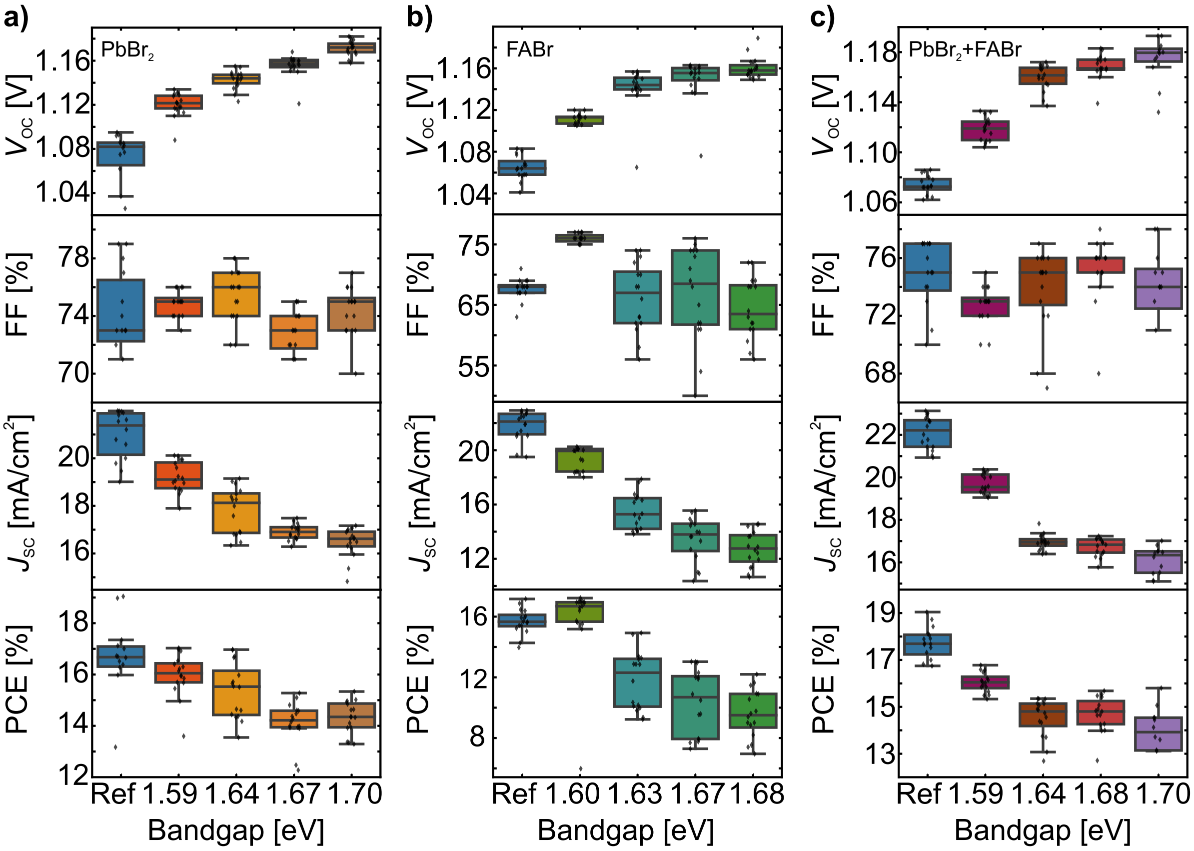

Figure A.3: Statistical distribution of the open-circuit voltage (V_{OC}), fill factor (FF), short-circuit current density (J_{SC}) and power conversion efficiency (PCE) of perovskite solar cells (PSCs) with increased bandgap ($E_g \approx$ 1.59-1.70 eV). PSCs without any modification are labeled as Ref (E_g = 1.55 eV). The bromide is incorporated *via* a) PbBr$_2$, b) FABr and c) PbBr$_2$+FABr. Adapted from reference[239] with permission from Wiley.

A.5 Perovskite Thin-Film Optimization for Enhanced Efficiency and Stability toward Tandem Integration

A.5.1 Optimization with CsI and LiF

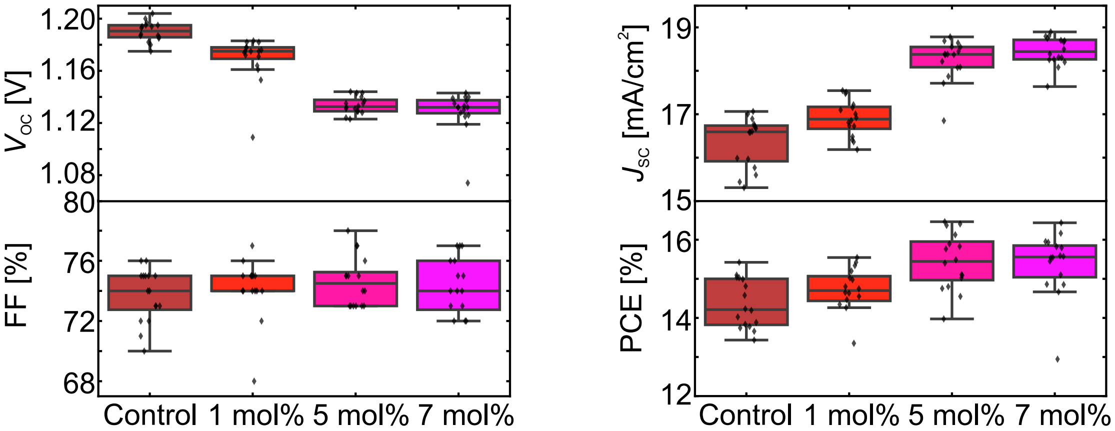

Figure A.4: Statistical distribution (in total 64 devices) of the open-circuit voltage (V_{OC}), fill factor (FF), short-circuit current density (J_{SC}) and power conversion efficiency (PCE) for opaque perovskite solar cells (PSCs) without any further modification (Control) and with different amounts of additional CsI (1-7 mol%). No surface passivation is applied.

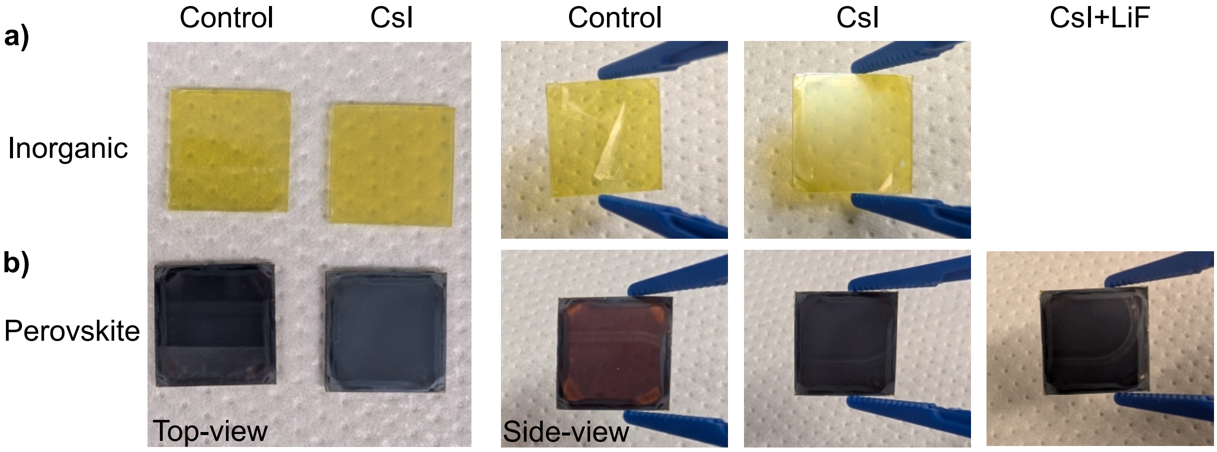

Figure A.5: Optical photographs of a) the inorganic scaffolds and b) the corresponding perovskite films without any further modification (Control), with additional CsI and with additional CsI and LiF (CsI+LiF) fabricated on glass/indium tin oxide (ITO)/NiO_x/2PACz.

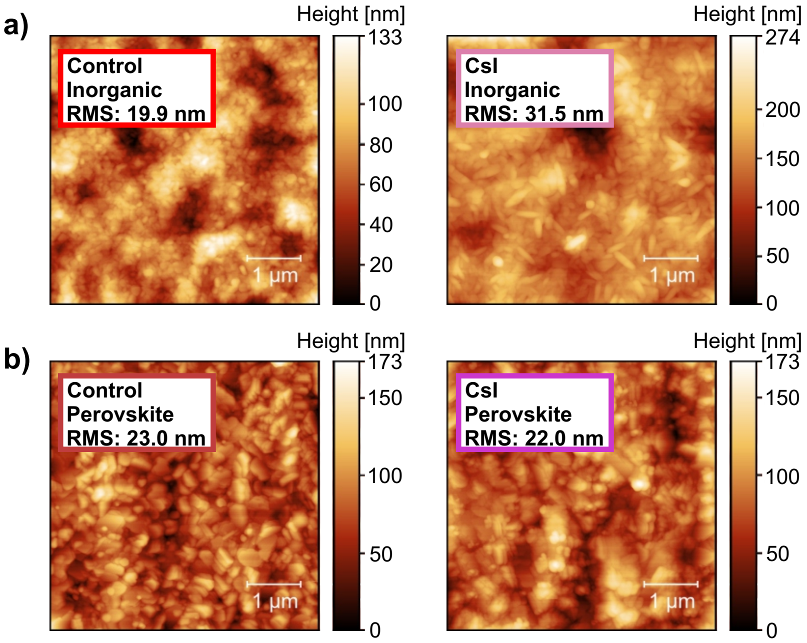

Figure A.6: Atomic force microscopy (AFM) images of a) the inorganic scaffolds and b) the corresponding perovskite films without any further modification (Control) and with additional CsI fabricated on glass/indium tin oxide (ITO)/NiO_x/2PACz. For each parameter, two to three measurements are taken, and the average root-mean-square (RMS) value is calculated.

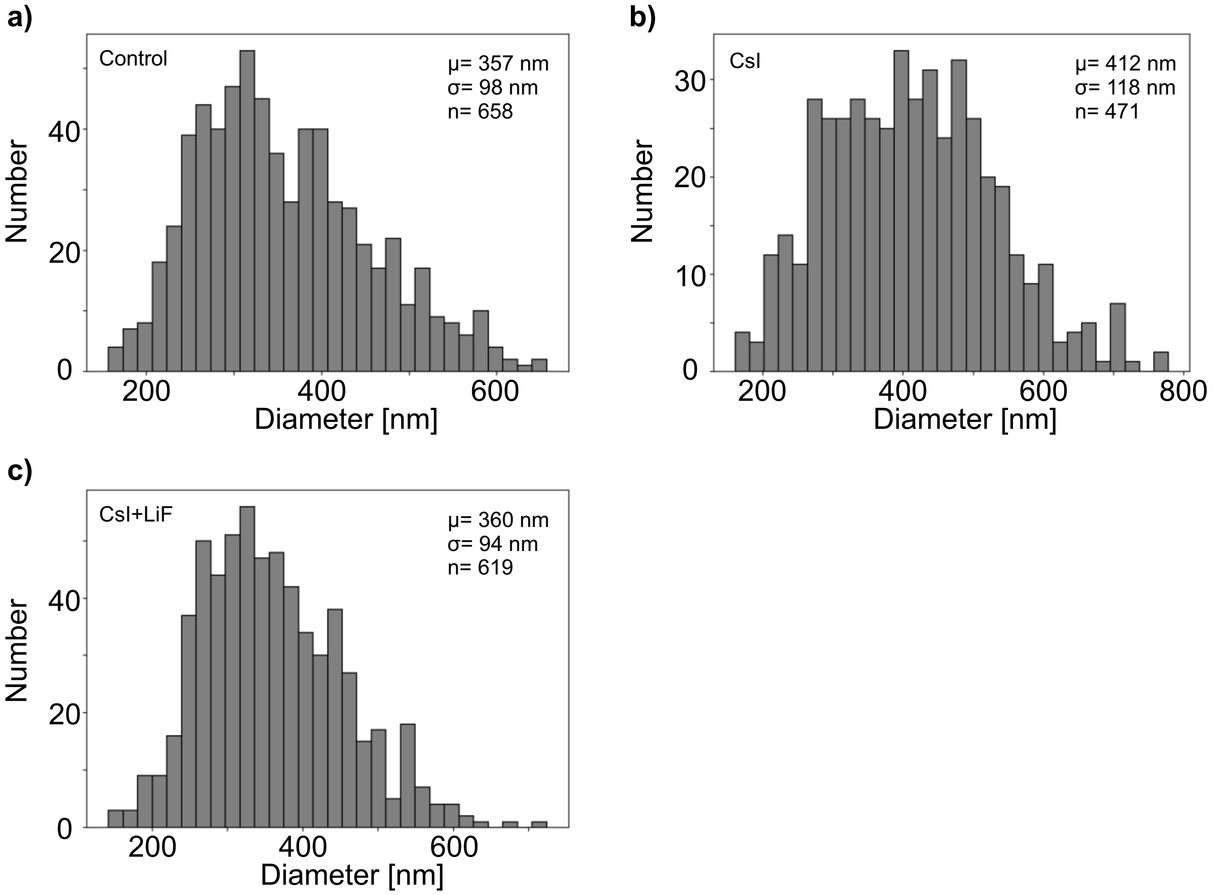

Figure A.7: Grain size analysis of scanning electron microscopy (SEM) images of perovskite films a) without any further modification (Control), b) with additional CsI and c) with additional CsI and LiF. The grain sizes were determined using a data evaluation program based on StarDist.

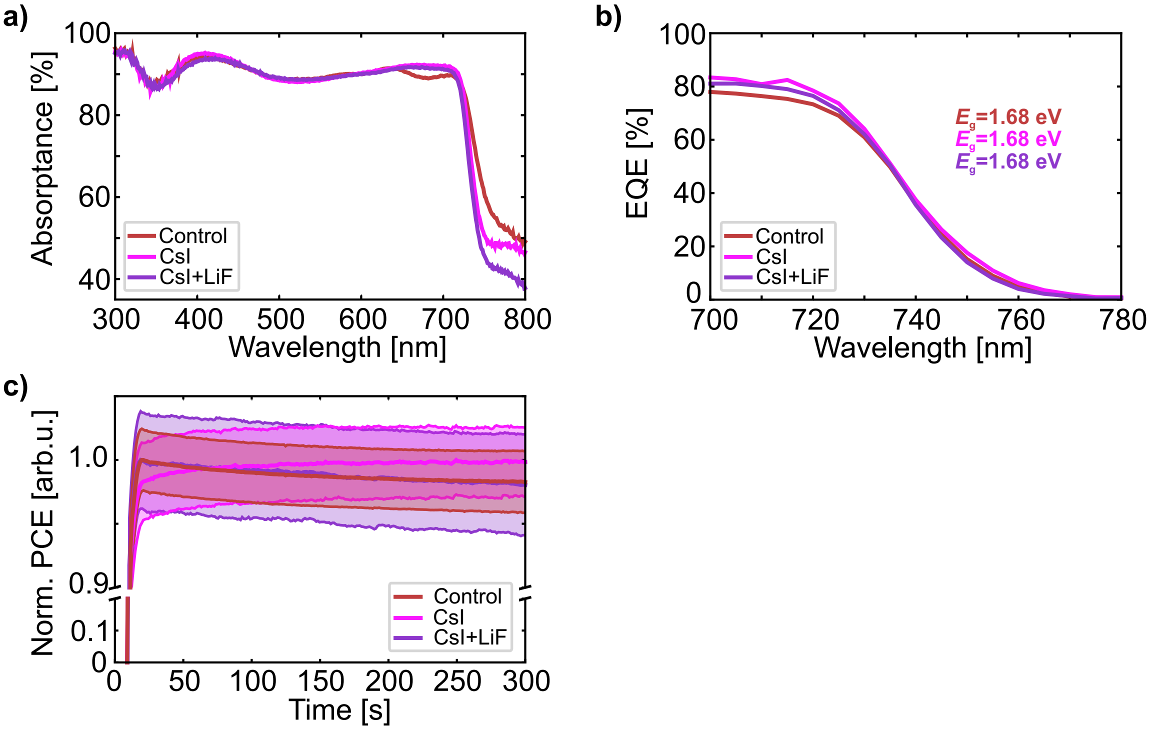

Figure A.8: a) Absorptance spectra, b) optical bandgap (E_g) extracted from the inflection point of the external quantum efficiency (EQE) spectra and c) mean value of the maximum power point (MPP) tracking of four selected cells (2 best-performing cells, 2 medium performing cells) for opaque perovskite solar cells (PSCs) without any further modification (Control), with additional CsI (CsI) and with additional CsI and LiF (CsI+LiF). Adapted from reference[239] with permission from Wiley.

Table A.9: *Welch's t test* results for the backward power conversion efficiency (PCE), open-circuit voltage (V_{OC}), short-circuit current density (J_{SC}) and fill factor (FF) of the wide-bandgap ($E_g \approx 1.68$ eV, bromide incorporation *via* $PbBr_2$+FABr) opaque perovskite solar cells (PSCs) without modification (Control) and with added CsI and a combination of CsI and LiF (CsI+LiF). The calculation was performed using a *t test* calculator.[437]

Parameter	Samples	P-value	Interpretation of difference
PCE	Control and CsI	0.0001	extremely statistically significant
	Control and CsI+LiF	<0.0001	extremely statistically significant
	CsI and CsI+LiF	0.0006	extremely statistically significant
V_{OC}	Control and CsI	<0.0001	extremely statistically significant
	Control and CsI+LiF	0.0059	very statistically significant
	CsI and CsI+LiF	<0.0001	extremely statistically significant
J_{SC}	Control and CsI	<0.0001	extremely statistically significant
	Control and CsI+LiF	<0.0001	extremely statistically significant
	CsI and CsI+LiF	0.0432	statistically significant
FF	Control and CsI	0.7098	not statistically significant
	Control and CsI+LiF	0.1977	not statistically significant
	CsI and CsI+LiF	0.1437	not statistically significant

A.5.2 Dual Bimolecular Passivation Strategy

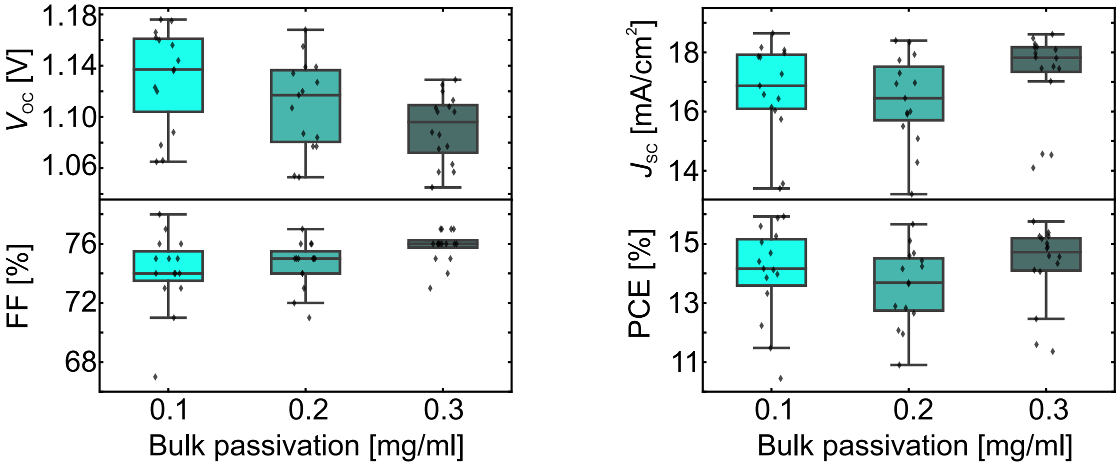

Figure A.9: Statistical distribution (in total 46 devices) of the open-circuit voltage (V_{OC}), fill factor (FF), short-circuit current density (J_{SC}) and power conversion efficiency (PCE) for opaque double-cation (DC) perovskite solar cells (PSCs) with varying concentration (0.1-0.3 mg mL^{-1}) of PDAI$_2$+BAI dissolved in isopropanol (IPA) for bulk passivation. All devices have 1 nm LiF for surface passivation. Adapted from reference[285] with permission from Wiley.

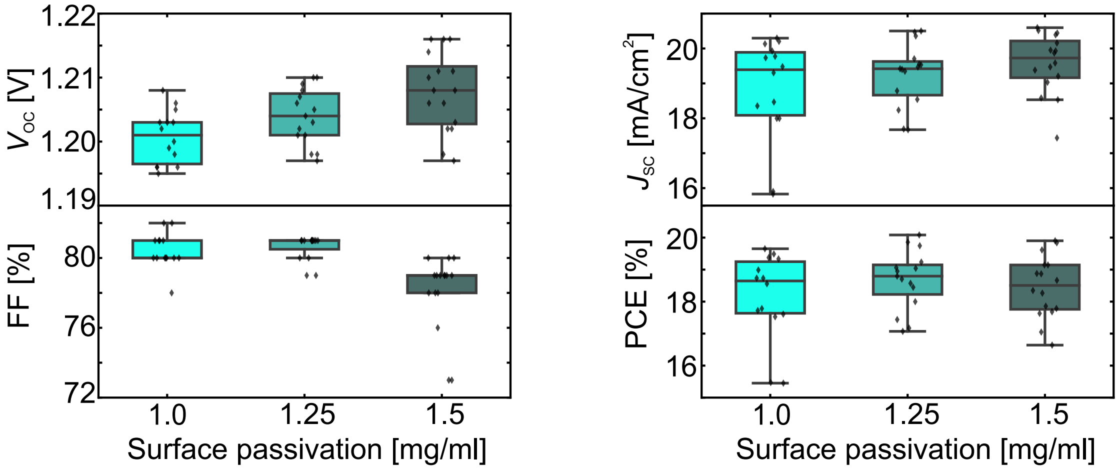

Figure A.10: Statistical distribution (in total 45 devices) of the open-circuit voltage (V_{OC}), fill factor (FF), short-circuit current density (J_{SC}) and power conversion efficiency (PCE) for opaque double-cation (DC) perovskite solar cells (PSCs) with varying concentration (1.0-1.25 mg mL^{-1}) of PDAI$_2$+BAI dissolved in isopropanol (IPA) for surface passivation. All devices have 0.1 mg mL^{-1} PDAI$_2$+BAI dissolved in IPA for bulk passivation. Adapted from reference[285] with permission from Wiley.

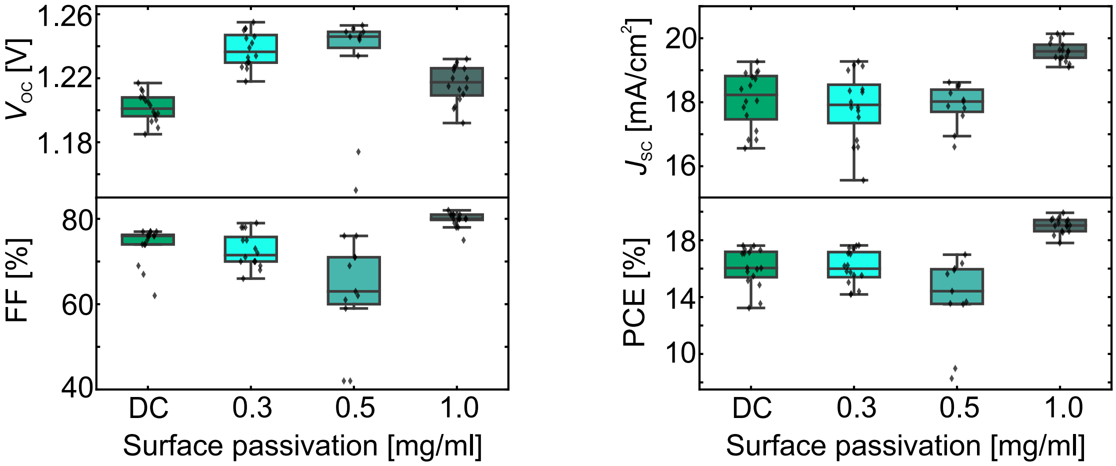

Figure A.11: Statistical distribution (in total 59 devices) of the open-circuit voltage (V_{OC}), fill factor (FF), short-circuit current density (J_{SC}) and power conversion efficiency (PCE) for opaque double-cation (DC) perovskite solar cells (PSCs) with varying concentration (0.3-1.0 mg mL^{-1}) of $PDAI_2$+BAI dissolved in isopropanol (IPA) for surface passivation. The DC devices have 1 nm LiF for surface passivation. All devices are without bulk passivation. Adapted from reference[285] with permission from Wiley.

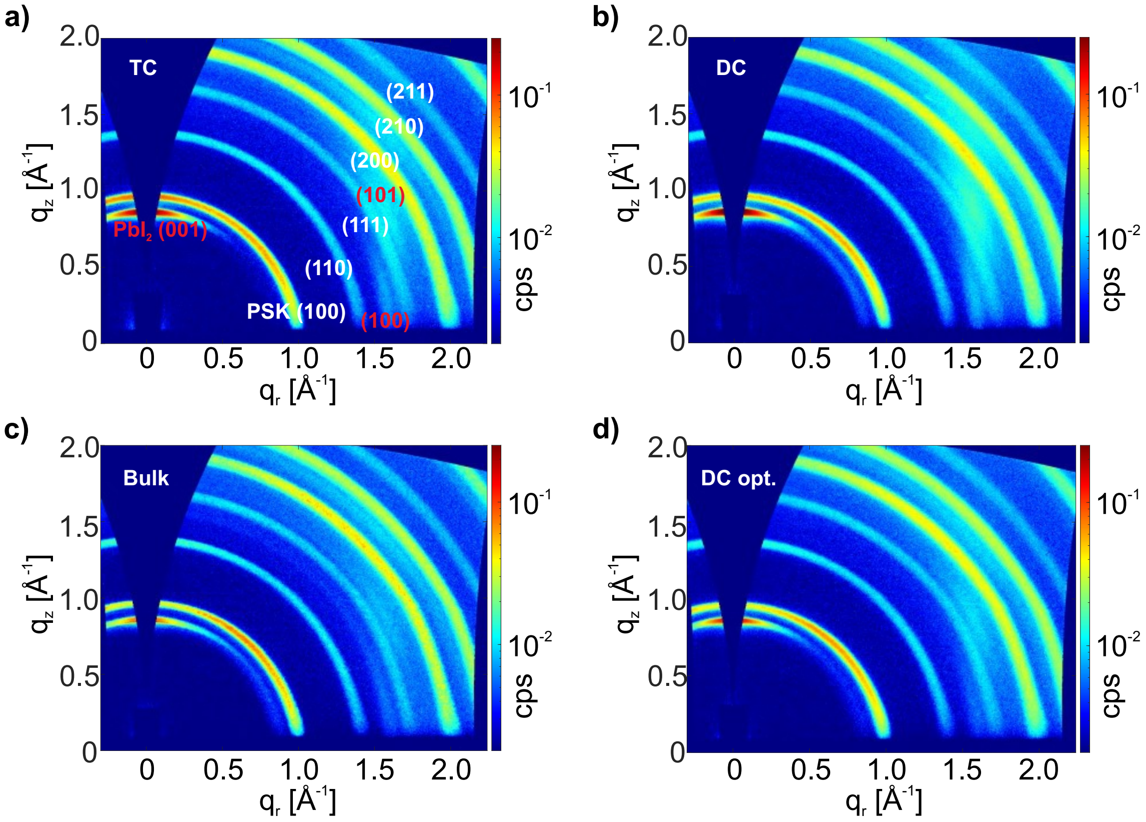

Figure A.12: Grazing-incidence wide-angle scattering (GIWAXS) patterns of a) triple-cation (TC), b) double-cation (DC), c) bulk-passivated double-cation (Bulk with 0.1 mg mL^{-1} $PDAI_2$+BAI dissolved in IPA) and d) optimized double-cation (DC opt.) perovskite films with denoted PbI_2 and perovskite (PSK) phases. TC, DC and Bulk perovskite films have 1 nm LiF as surface passivation. Measurements are performed on half-stacks with the architecture ITO/NiO_x/2PACz/perovskite. Adapted from reference[285] with permission from Wiley.

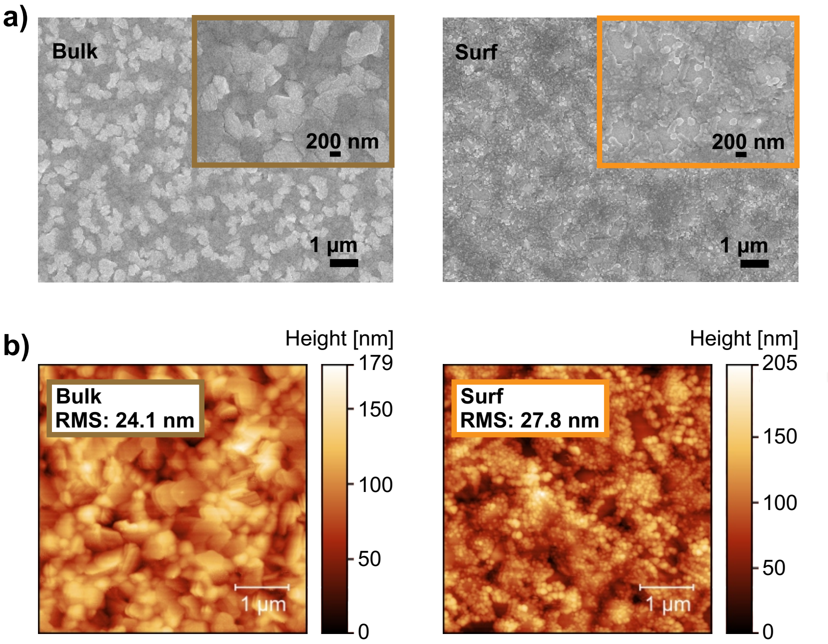

Figure A.13: a) Top-view scanning electron microscopy (SEM) images and b) atomic force microscopy (AFM) images of bulk-passivated (Bulk, with 0.1 mg mL^{-1} PDAI$_2$+BAI dissolved in IPA) and surface-passivated (Surf, with 1.25 mg mL^{-1} PDAI$_2$+BAI dissolved in IPA) perovskite films fabricated on glass/indium tin oxide (ITO)/NiO$_x$/2PACz. Bulk perovskite films have 1 nm LiF as surface passivation. Two to three measurements are taken for each parameter, and the average root-mean-square (RMS) value is calculated for AFM measurements. Adapted from reference[285] with permission from Wiley.

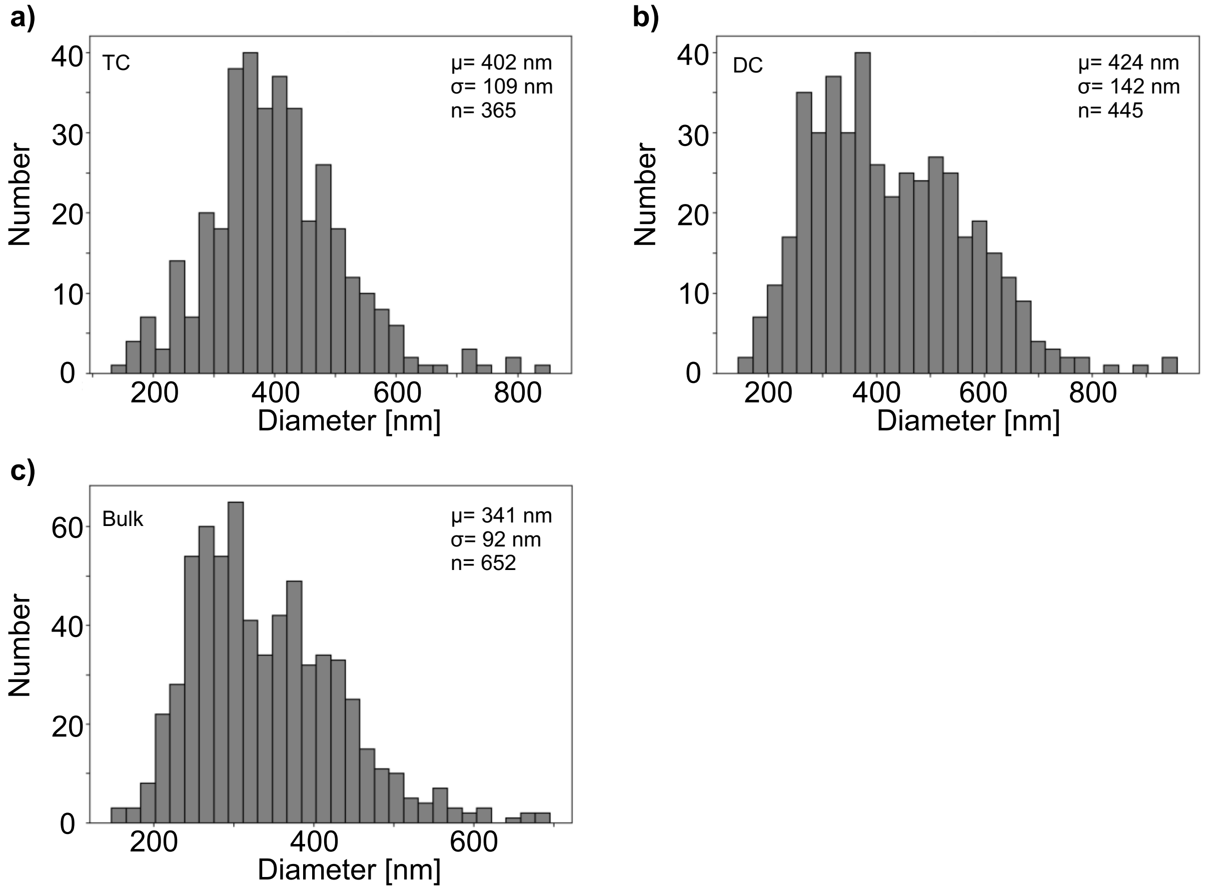

Figure A.14: Grain size analysis of scanning electron microscopy (SEM) images of a) triple-cation (TC), double-cation (DC) and bulk-passivated double-cation (Bulk with 0.1 mg mL^{-1} PDAI$_2$+BAI dissolved in IPA) perovskite films. The grain sizes were determined using a data evaluation program based on StarDist.

Table A.10: *Welch's t test* results for the backward power conversion efficiency (PCE), open-circuit voltage (V_{OC}), short-circuit current density (J_{SC}) and fill factor (FF) of triple-cation (TC), double-cation (DC) and optimized double-cation (DC opt.) opaque perovskite solar cells (PSCs). The calculation was performed using a *t test* calculator.[437]

Parameter	Samples	P-value	Interpretation of difference
PCE	TC and DC	0.2611	not statistically significant
	TC and DC opt.	< 0.0001	extremely statistically significant
	DC and DC opt.	< 0.0001	extremely statistically significant
V_{OC}	TC and DC	0.0006	extremely statistically significant
	TC and DC opt.	< 0.0001	extremely statistically significant
	DC and DC opt.	< 0.0001	extremely statistically significant
J_{SC}	TC and DC	0.2803	not statistically significant
	TC and DC opt.	< 0.0001	extremely statistically significant
	DC and DC opt.	< 0.0001	extremely statistically significant
FF	TC and DC	0.4794	not statistically significant
	TC and DC opt.	< 0.0001	extremely statistically significant
	DC and DC opt.	< 0.0001	extremely statistically significant

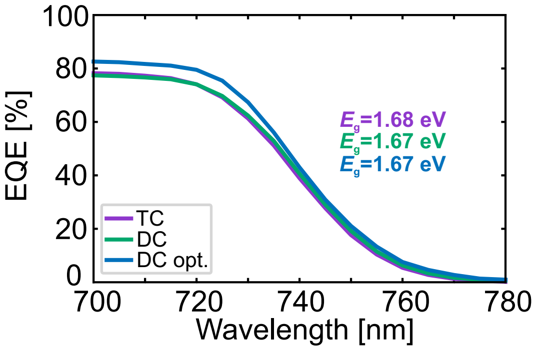

Figure A.15: Optical bandgap (E_{g}) extracted from the inflection point of the external quantum efficiency (EQE) spectra of triple-cation (TC), double-cation (DC), and optimized double-cation (DC opt.) perovskite solar cells (PSCs). Adapted from reference[285] with permission from Wiley.

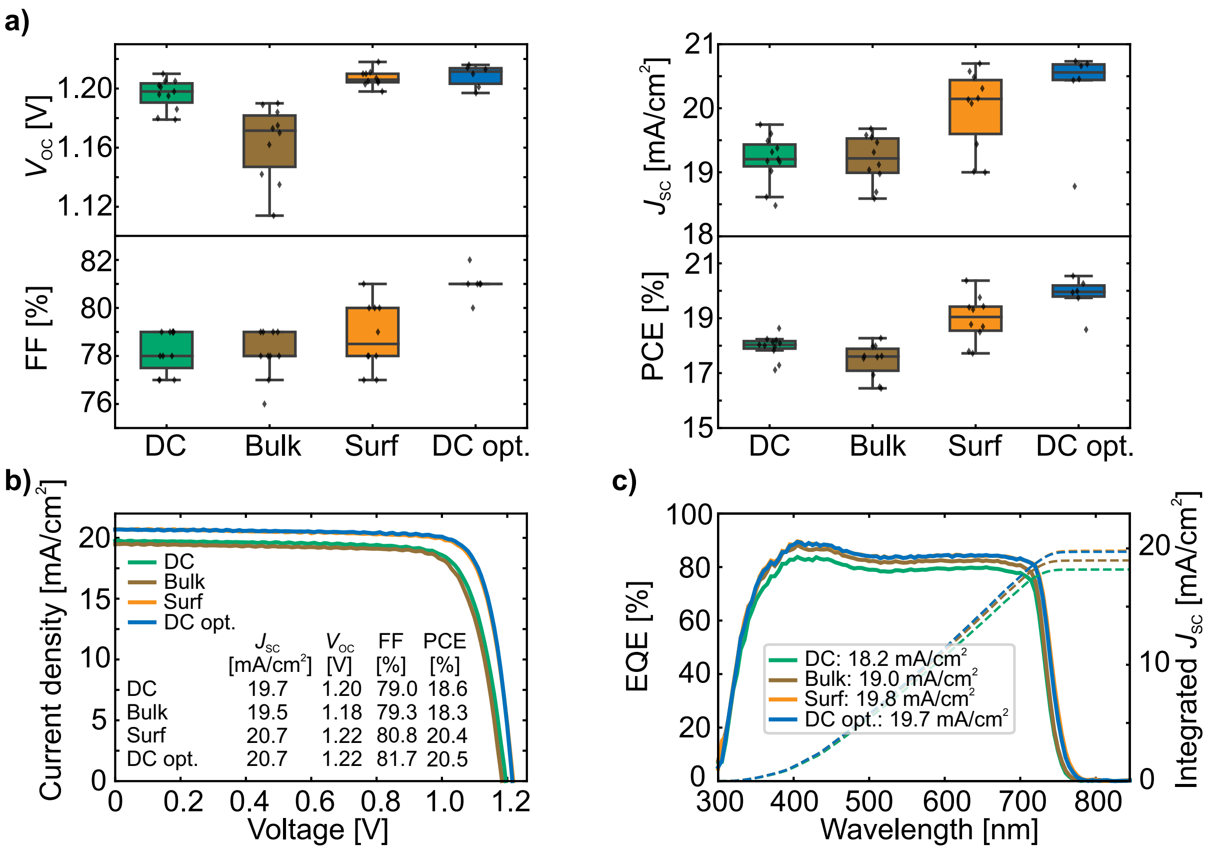

	J_{SC} [mA/cm^2]	V_{OC} [V]	FF [%]	PCE [%]
DC	19.7	1.20	79.0	18.6
Bulk	19.5	1.18	79.3	18.3
Surf	20.7	1.22	80.8	20.4
DC opt.	20.7	1.22	81.7	20.5

Figure A.16: a) Statistical distribution (in total 37 devices) of the open-circuit voltage (V_{OC}), fill factor (FF), short-circuit current density (J_{SC}) and power conversion efficiency (PCE), b) current density *versus* voltage (J-V) characteristics, and c) external quantum efficiency (EQE) as well as the corresponding integrated J_{SC} for double-cation (DC), bulk-passivated double-cation (Bulk with 0.1 mg mL^{-1} PDAI$_2$+BAI dissolved in IPA), surface-passivated (Surf, with 1.25 mg mL^{-1} PDAI$_2$+BAI dissolved in IPA) and optimized double-cation (DC opt., with both bulk and surface passivation) opaque perovskite solar cells (PSCs). The DC and Bulk devices have 1 nm LiF for surface passivation. Adapted from reference[285] with permission from Wiley.

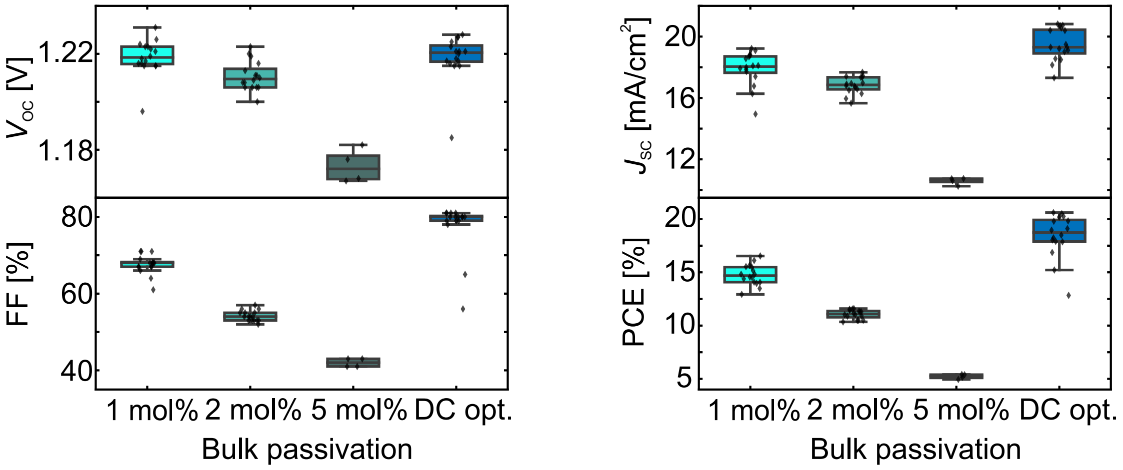

Figure A.17: Statistical distribution (in total 52 devices) of the open-circuit voltage (V_{OC}), fill factor (FF), short-circuit current density (J_{SC}) and power conversion efficiency (PCE) for double-cation (DC) perovskite solar cells (PSCs) with varying concentration (1-5 mol%) of PDAI$_2$+BAI dissolved in dimethyl sulfoxide (DMSO) for bulk passivation added in the inorganic solution and, for comparison, opaque PSCs with 0.1 mg mL^{-1} PDAI$_2$+BAI dissolved in isopropanol (IPA) for bulk passivation added in the organic solution (DC opt.). All devices have 1.25 mg mL^{-1} PDAI$_2$+BAI dissolved in IPA for surface passivation. Adapted from reference[285] with permission from Wiley.

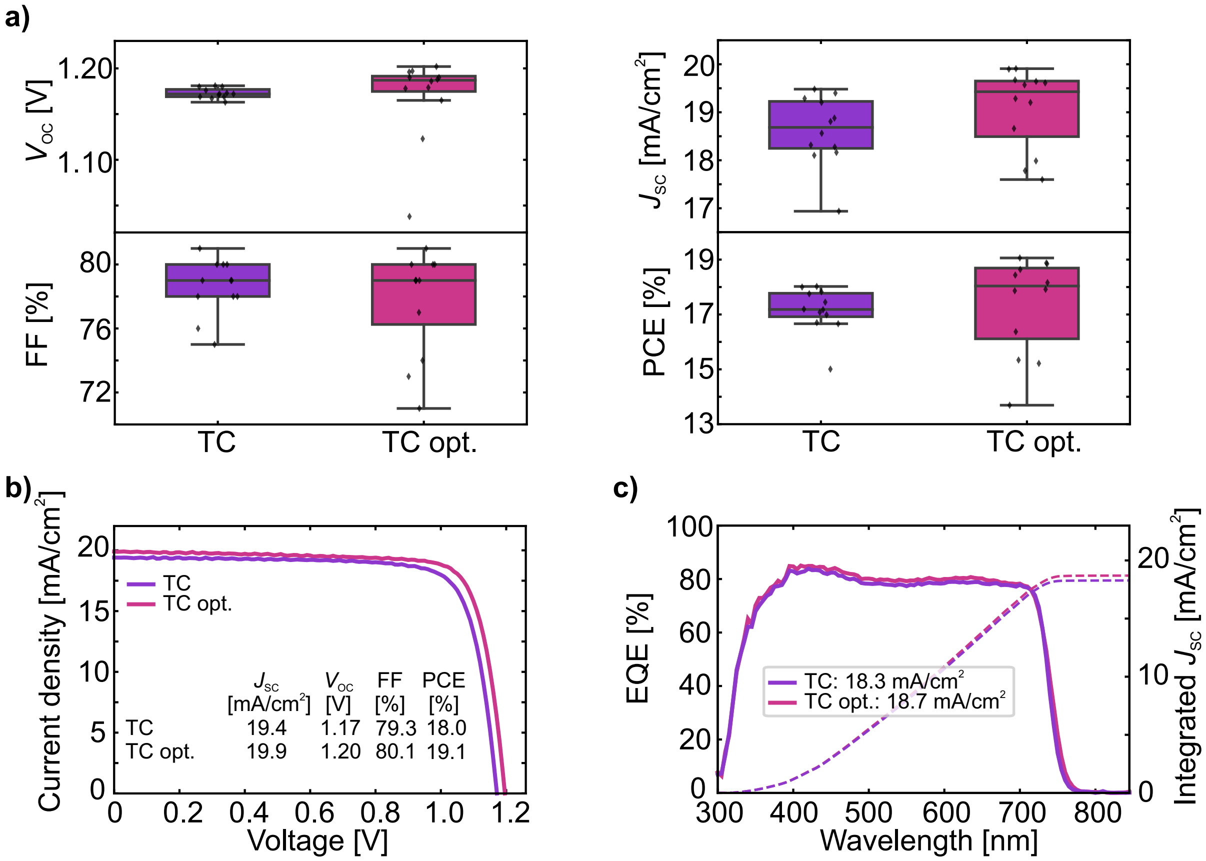

Figure A.18: a) Statistical distribution (in total 24 devices) of the open-circuit voltage (V_{OC}), fill factor (FF), short-circuit current density (J_{SC}) and power conversion efficiency (PCE), b) current density *versus* voltage (J-V) characteristics, and c) external quantum efficiency (EQE) as well as the corresponding integrated J_{SC} for triple-cation (TC) and optimized triple-cation (TC opt.) opaque perovskite solar cells (PSCs). For TC opt., the same concentrations for bulk and surface passivation are used as for DC opt. (0.1 mg mL^{-1} PDAI$_2$+BAI dissolved in IPA for bulk passivation, 1.25 mg mL^{-1} PDAI$_2$+BAI dissolved in IPA for surface passivation). Due to problems with the quality of the NiO$_x$ layer, only 2PACz is used here as the hole transport layer (HTL). Adapted from reference[285] with permission from Wiley.

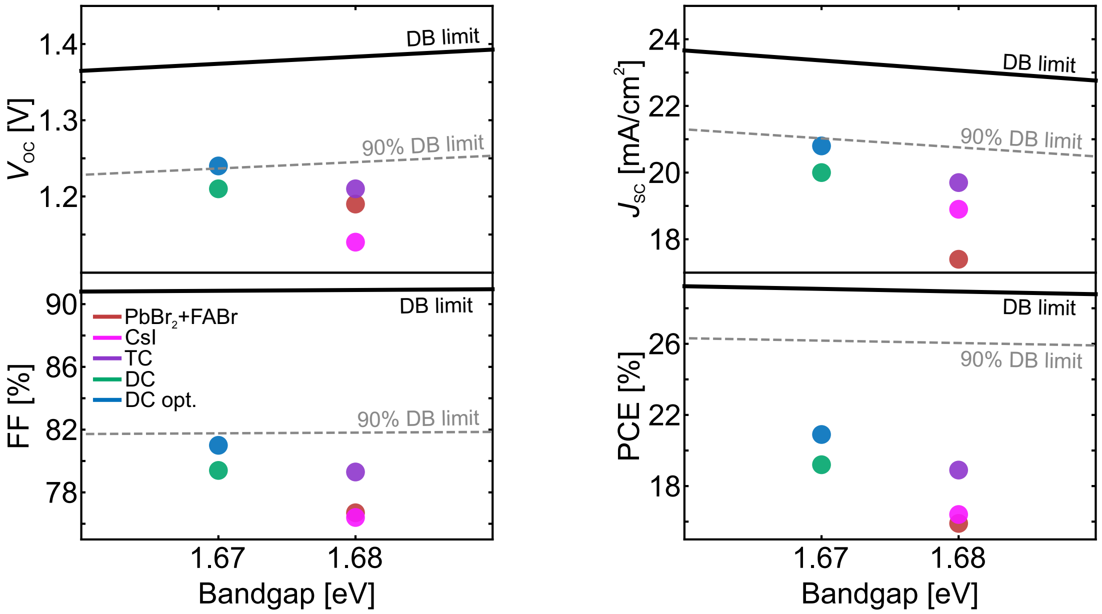

Figure A.19: Open-circuit voltage (V_{OC}), fill factor (FF), short-circuit current density (J_{SC}) and power conversion efficiency (PCE) *versus* bandgap for PbBr$_2$+FABr, CsI, triple-cation (TC), double-cation (DC) and optimized double-cation (DC opt.) opaque perovskite solar cells (PSCs) in relation to the detailed balance (DB) limit.

A.6 CsCl Seed Layer for Improved Stability and Fabrication Yield of Solution-Based Two-Step Processed Perovskite Thin Films

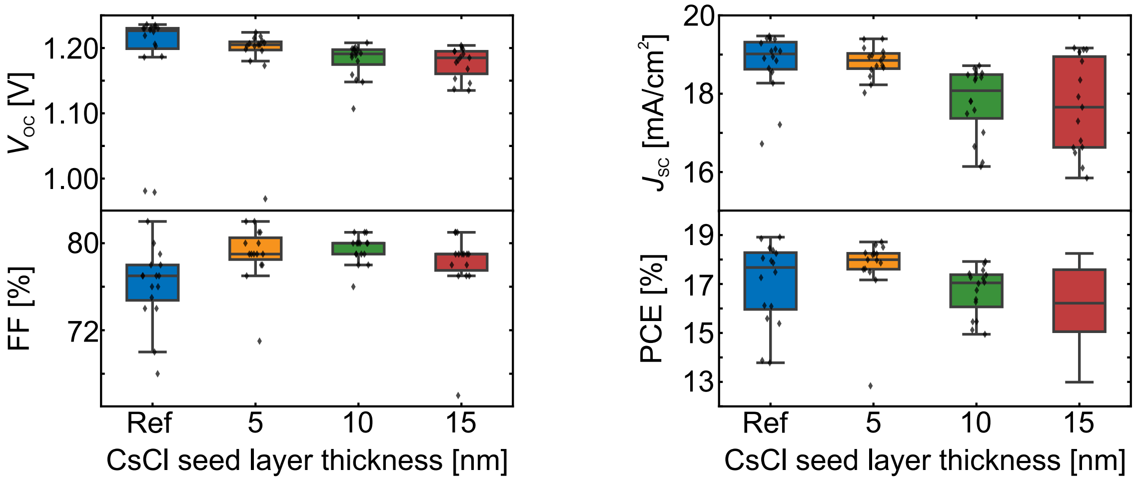

Figure A.20: Statistical distribution (in total 64 devices) of the open-circuit voltage (V_{OC}), fill factor (FF), short-circuit current density (J_{SC}) and power conversion efficiency (PCE) for opaque perovskite solar cells (PSCs) without any further modification (Ref) and with different thicknesses of the CsCl seed layer (5-15 nm). All perovskite films have a combination of $PDAI_2$+BAI for surface passivation. Here, 5 nm bathocuproine (BCP) is used instead of tin oxide (SnO_x).

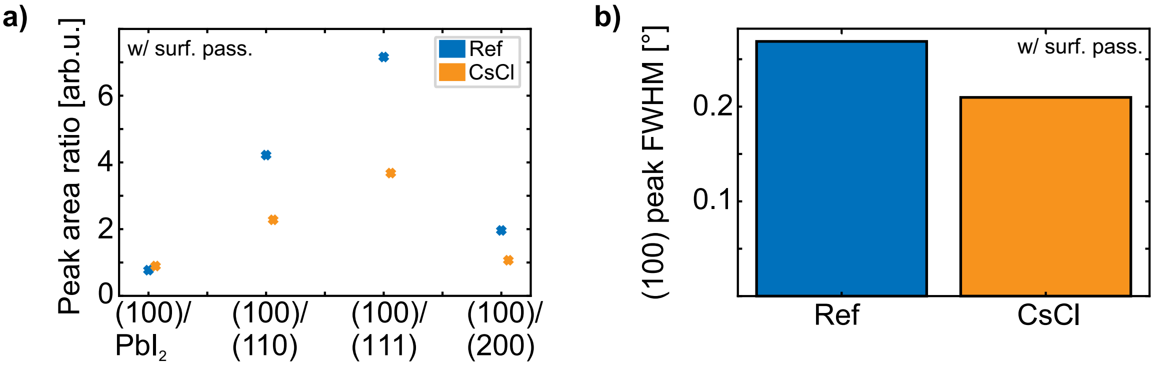

Figure A.21: a) Peak area ratios, and b) full width at half maximum (FWHM) of the (100) perovskite peak of perovskite films without any further modification (Ref) and with 5 nm CsCl seed layer (CsCl) fabricated on glass/indium tin oxide (ITO)/NiO_x/2PACz. All perovskite films have a combination of $PDAI_2$+BAI for surface passivation.

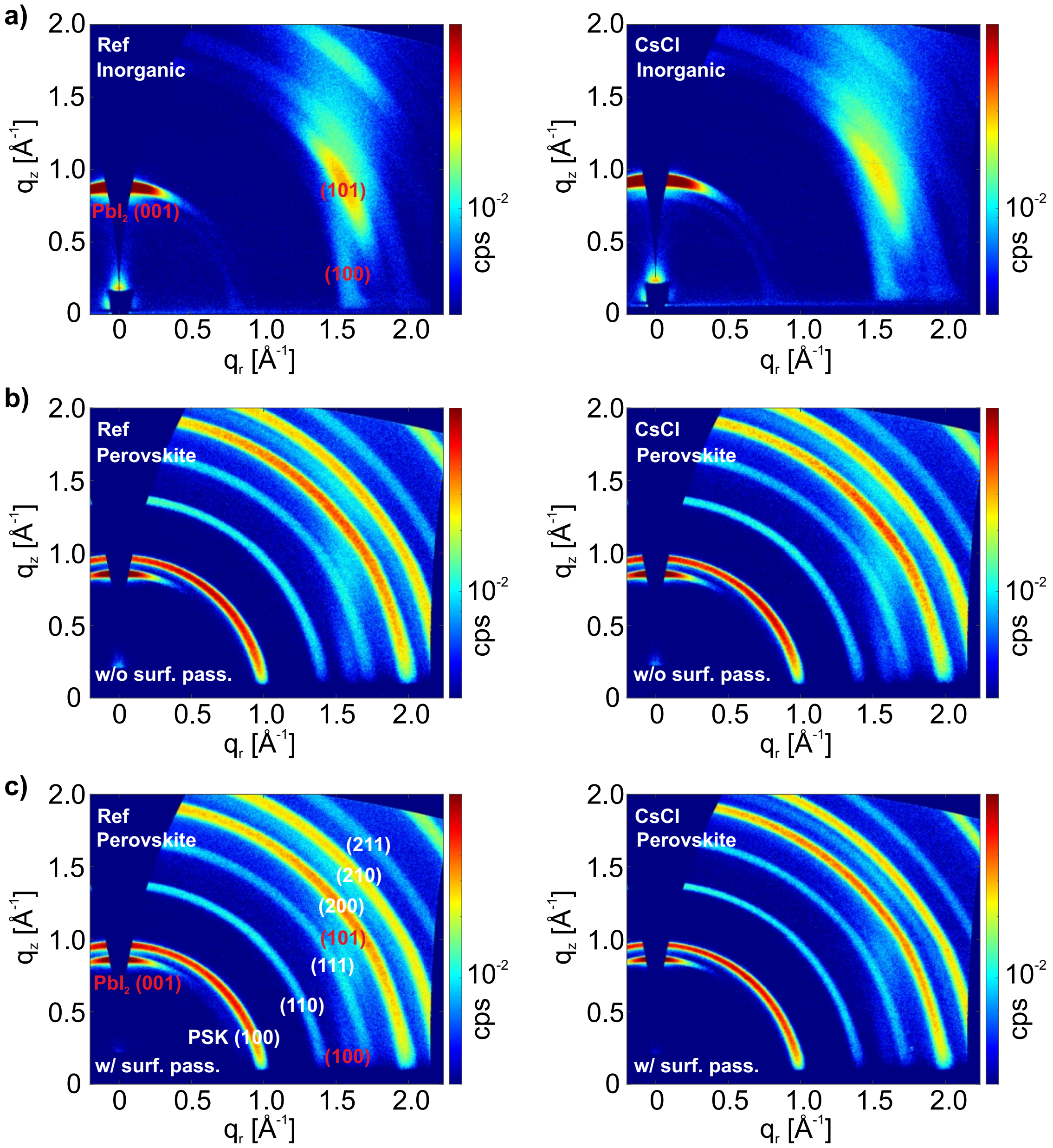

Figure A.22: Grazing-incidence wide-angle scattering (GIWAXS) patterns with denoted PbI_2 and perovskite (PSK) phases of a) inorganic scaffolds, b) perovskite films without surface passivation, and c) perovskite films with surface passivation without any further modification (Ref) and with 5 nm CsCl seed layer (CsCl) fabricated on glass/indium tin oxide (ITO)/NiO_x/2PACz.

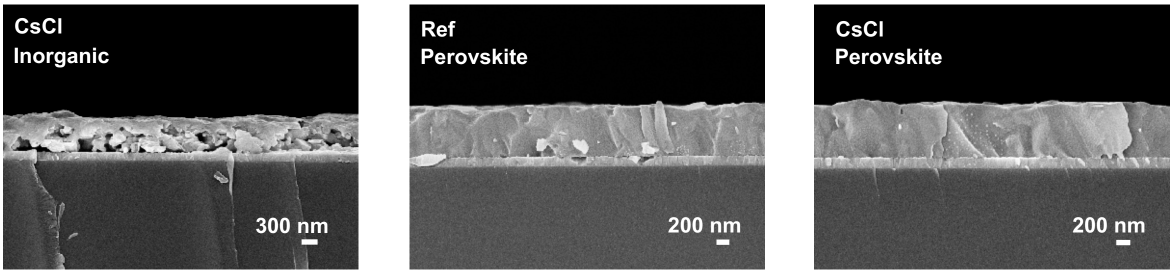

Figure A.23: Cross-sectional scanning electron microscopy (SEM) images of inorganic scaffold and perovskite films without any further modification (Ref) and with 5 nm CsCl seed layer (CsCl) fabricated on glass/indium tin oxide (ITO)/NiO_x/2PACz. The perovskite films are without surface passivation. Unfortunately, it was not possible to focus on the Ref inorganic scaffold, which is why no image can be shown.

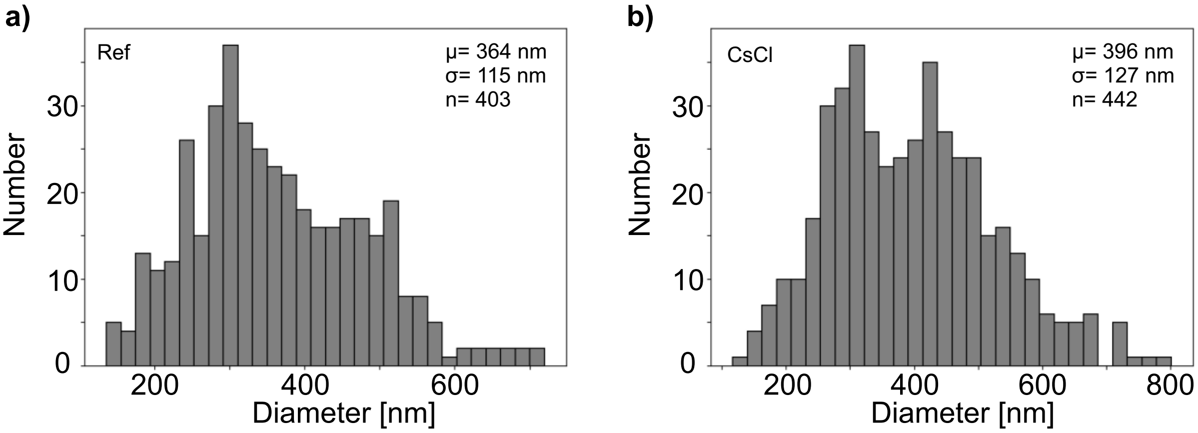

Figure A.24: Grain size analysis of scanning electron microscopy (SEM) images of perovskite films a) without any further modification (Ref), and b) with 5 nm CsCl seed layer (CsCl). The perovskite films are without surface passivation. The grain sizes were determined using a data evaluation program based on StarDist.

Table A.11: *Welch's t test* results for the backward power conversion efficiency (PCE), open-circuit voltage (V_{OC}), short-circuit current density (J_{SC}) and fill factor (FF) of the opaque perovskite solar cells (PSCs) without any further modification (Ref) and with 5 nm CsCl seed layer (CsCl). The calculation was performed using a *t test* calculator.[437]

Parameter	Samples	P-value	Interpretation of difference
PCE	Ref and CsCl	0.0178	statistically significant
V_{OC}	Ref and CsCl	0.0046	very statistically significant
J_{SC}	Ref and CsCl	0.3610	not statistically significant
FF	Ref and CsCl	<0.0001	extremely statistically significant

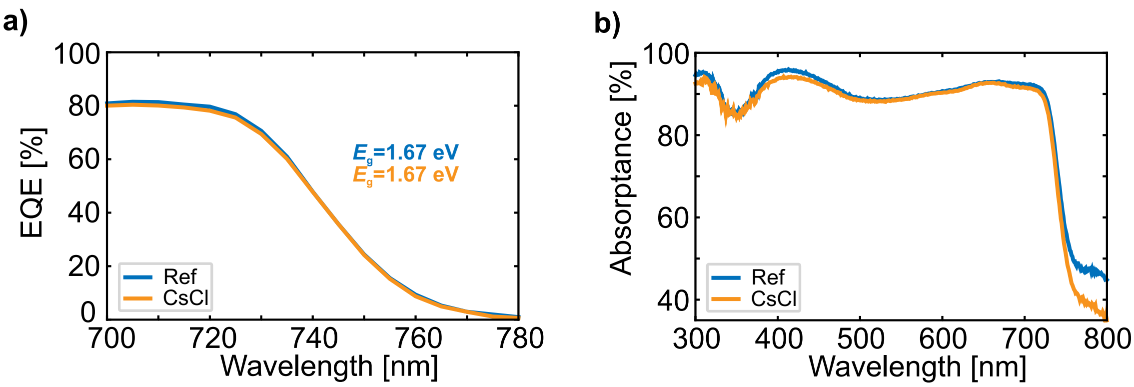

Figure A.25: a) Optical bandgap (E_g) extracted from the inflection point of the external quantum efficiency (EQE) spectra, and b) absorptance spectra for opaque perovskite solar cells (PSCs) without any further modification (Ref) and with 5 nm CsCl seed layer (CsCl).

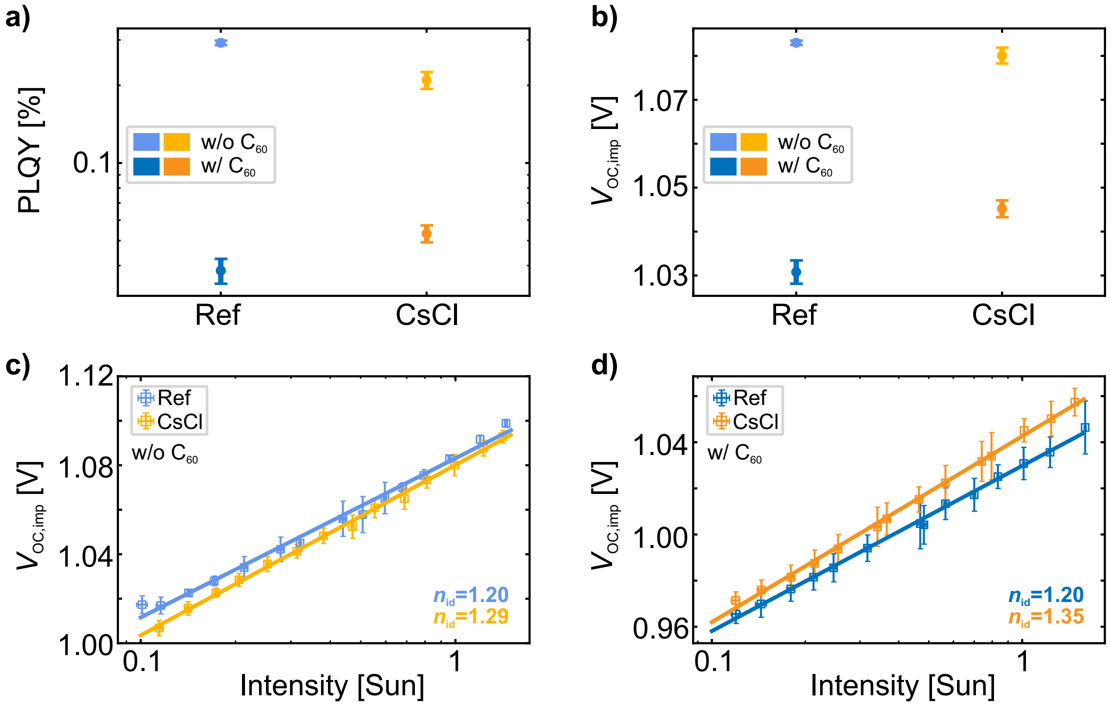

Figure A.26: a) Photoluminescence quantum yield (PLQY), b) the obtained implied V_{OC} ($V_{OC\text{-imp}}$), and the ideality factor (n_{id}) extracted from a fit to the $V_{OC\text{-imp}}$ (derived from intensity-dependent PLQY measurements) measured a) without and b) with C_{60} electron transport layer (ETL) of perovskite films without any further modification (Ref) and with 5 nm CsCl seed layer (CsCl) fabricated on glass/indium tin oxide (ITO)/NiO_x/2PACz. All perovskite films have $PDAI_2$+BAI as surface passivation. PLQY is measured from the hole transport layer (HTL) side. For each parameter, several perovskite films are measured, and the corresponding mean and standard deviation are plotted.

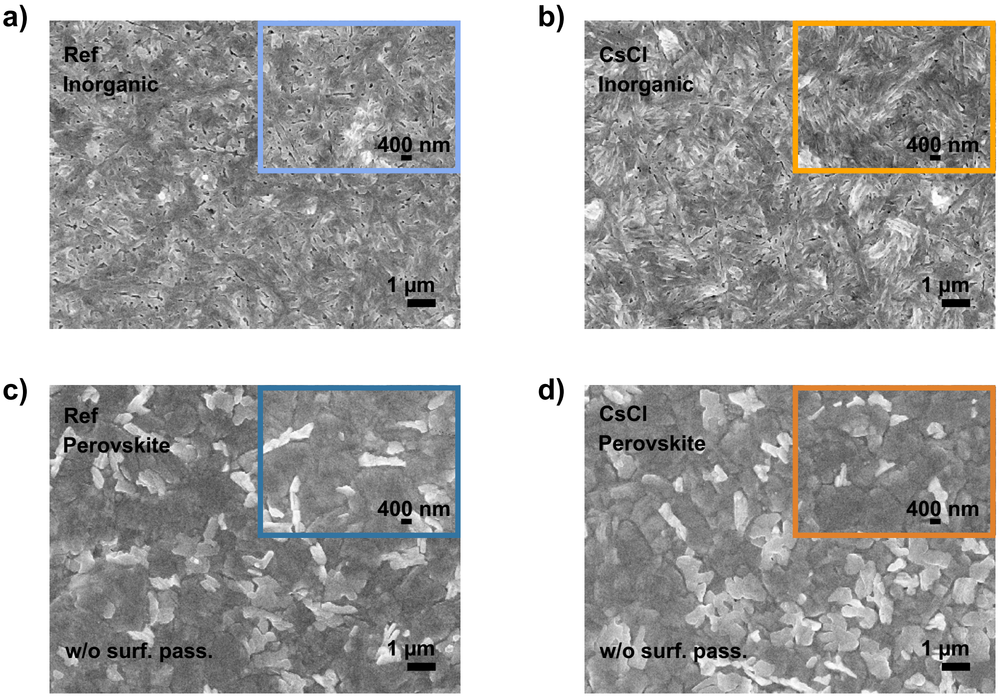

Figure A.27: Top-view scanning electron microscopy (SEM) images of inorganic scaffolds a) without any further modification (Ref), and b) with 5 nm CsCl seed layer (CsCl), and perovskite films c) without any further modification (Ref), and d) with 5 nm CsCl seed layer (CsCl) on small-textured silicon (Si) bottom cells (pyramid height ≈ 0.5-1 µm). The inorganic scaffold and perovskite films are prepared on Si/indium tin oxide (ITO)/NiO$_x$/2PACz. The perovskite films are without surface passivation.

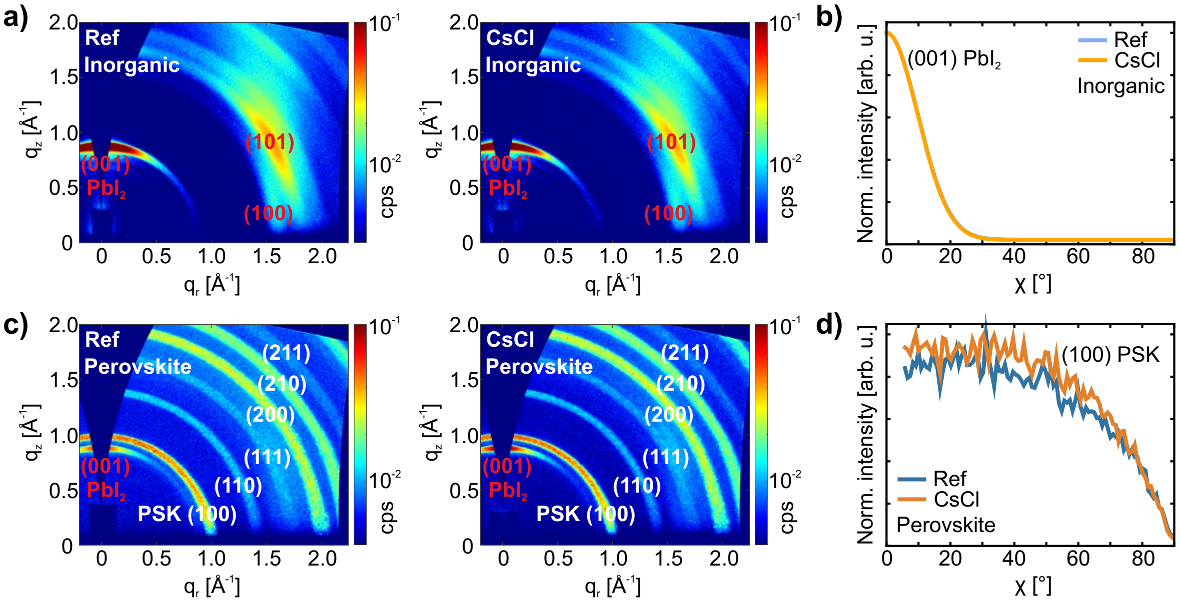

Figure A.28: Grazing-incidence wide-angle scattering (GIWAXS) patterns of a) inorganic scaffolds, and c) perovskite films, and the corresponding pole figures of the b) (100) PbI$_2$ phase for inorganic scaffolds, and the d) (100) perovskite (PSK) phase for perovskite films without any further modification (Ref) and with 5 nm CsCl seed layer (CsCl) on small-textured silicon (Si) bottom cells (pyramid height ≈ 0.5-1 µm). The inorganic scaffolds and perovskite films are prepared on Si/indium tin oxide (ITO)/NiO$_x$/2PACz. The perovskite films are without surface passivation.

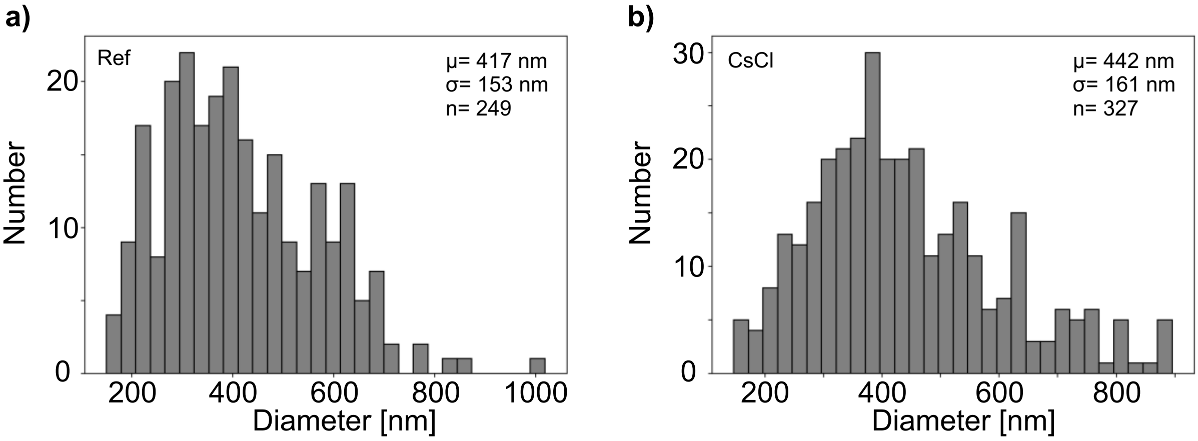

Figure A.29: Grain size analysis of scanning electron microscopy (SEM) images of perovskite films on small-textured silicon (Si) bottom cells (pyramid height ≈ 0.5-1 µm) a) without any further modification (Ref), and b) with 5 nm CsCl seed layer (CsCl). The perovskite films are without surface passivation. The grain sizes were determined using a data evaluation program based on StarDist.

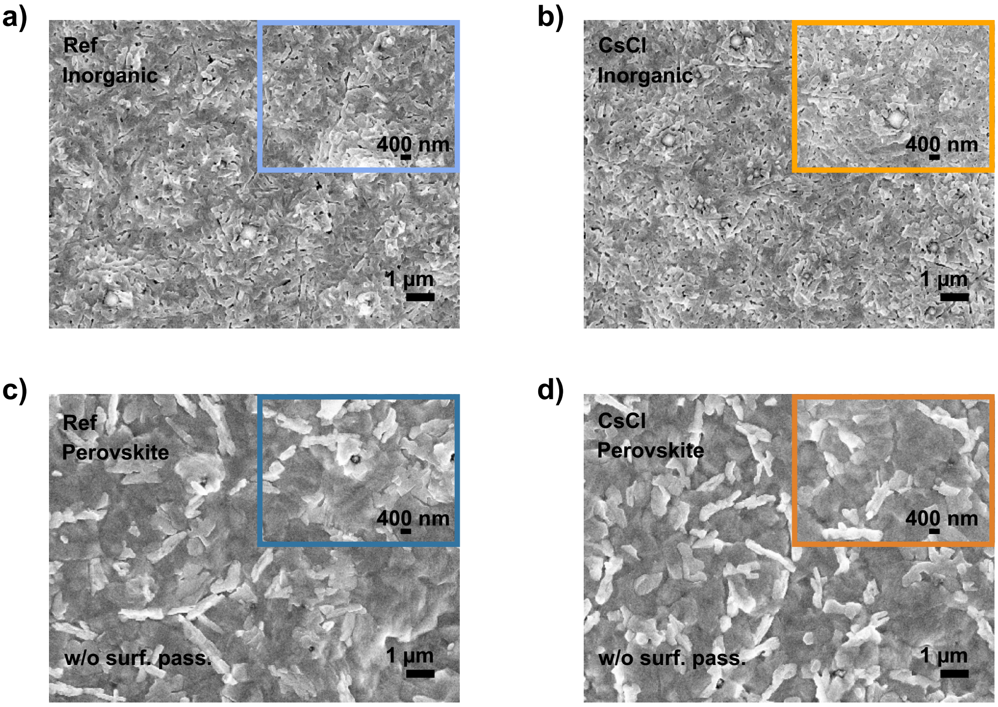

Figure A.30: Top-view scanning electron microscopy (SEM) images of inorganic scaffolds a) without any further modification (Ref), and b) with 5 nm CsCl seed layer (CsCl), and perovskite films c) without any further modification (Ref), and d) with 5 nm CsCl seed layer (CsCl) on large-textured silicon (Si) bottom cells (pyramid height ≈ 2-5 µm). The inorganic scaffolds and perovskite films are prepared on Si/indium tin oxide (ITO)/NiO_x/2PACz. The perovskite films are without surface passivation.

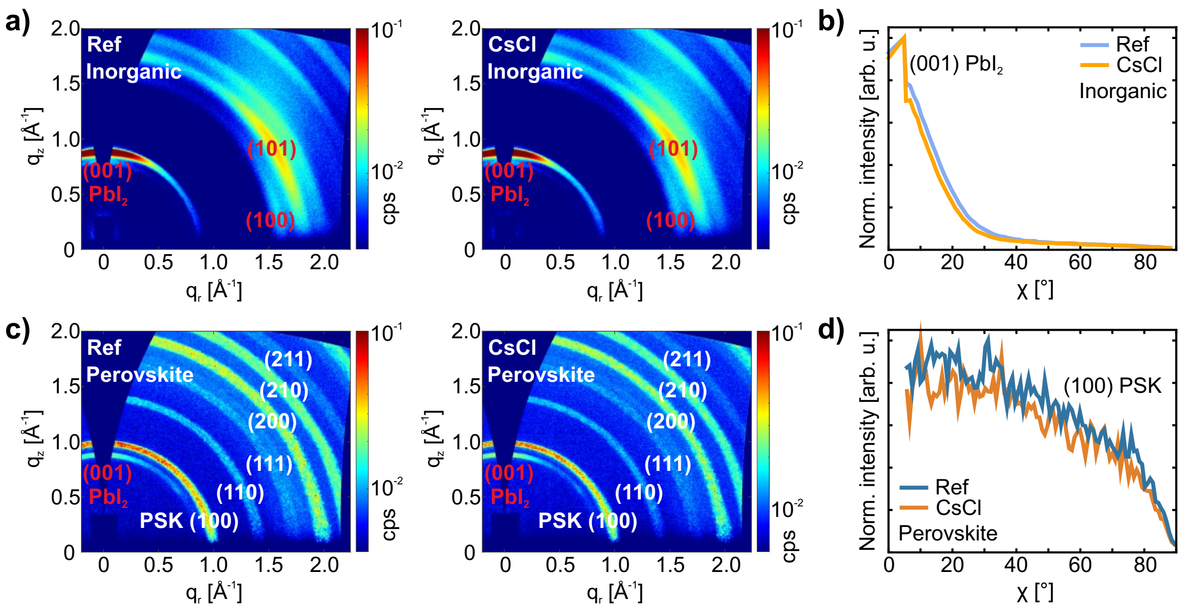

Figure A.31: Grazing-incidence wide-angle scattering (GIWAXS) patterns of a) inorganic scaffolds, and c) perovskite films, and the corresponding pole figures of the b) (100) PbI_2 phase for inorganic scaffolds, and the d) (100) perovskite (PSK) phase for perovskite films without any further modification (Ref) and with 5 nm CsCl seed layer (CsCl) on large-textured silicon (Si) bottom cells (pyramid height ≈ 2-5 µm). The inorganic scaffolds and perovskite films are prepared on Si/indium tin oxide (ITO)/NiO_x/2PACz. The perovskite films are without surface passivation.

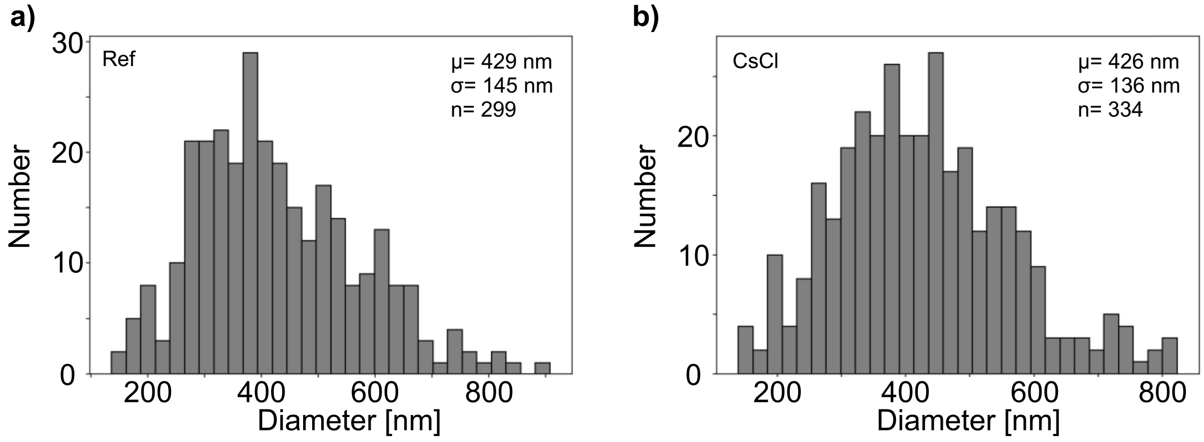

Figure A.32: Grain size analysis of scanning electron microscopy (SEM) images of perovskite films on large-textured silicon (Si) bottom cells (pyramid height ≈ 2-5 µm) a) without any further modification (Ref), and b) with 5 nm CsCl seed layer (CsCl). The perovskite films are without surface passivation. The grain sizes were determined using a data evaluation program based on StarDist.

A.7 A Materials Perspective on Inorganic Deposition Routes for Hybrid Two-Step Processed Perovskite Thin Films

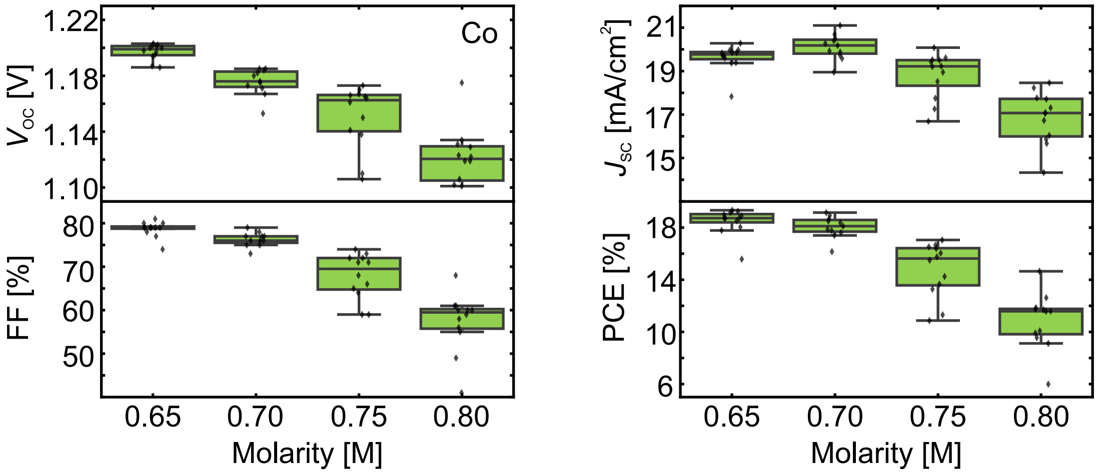

Figure A.33: Statistical distribution (in total 47 devices) of the open-circuit voltage (V_{OC}), fill factor (FF), short-circuit current density (J_{SC}) and power conversion efficiency (PCE) for opaque perovskite solar cells (PSCs) for different molarities of the organic cation solution for co-deposition (Co) of the inorganic scaffold from Batch A. Adapted from reference[204] with permission from Wiley.

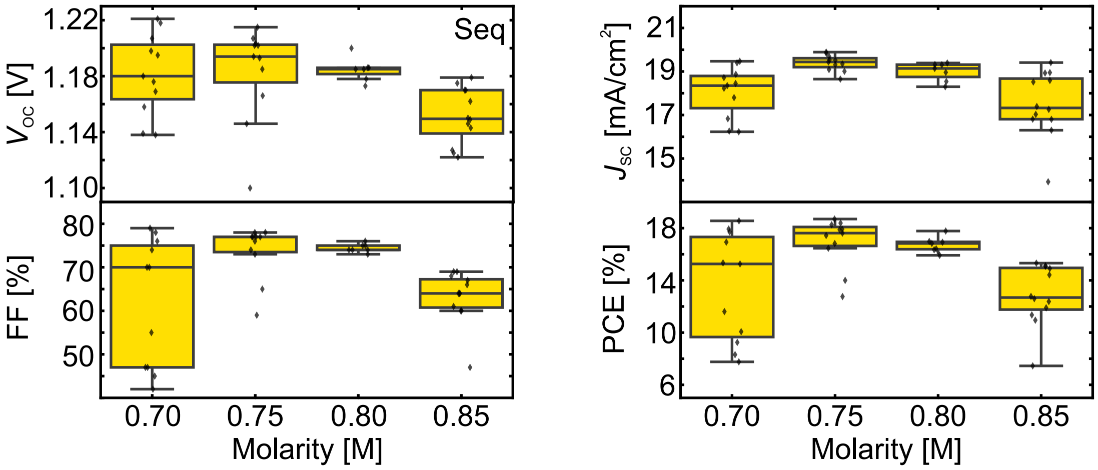

Figure A.34: Statistical distribution (in total 41 devices) of the open-circuit voltage (V_{OC}), fill factor (FF), short-circuit current density (J_{SC}) and power conversion efficiency (PCE) for opaque perovskite solar cells (PSCs) for different molarities of the organic cation solution for sequential deposition (Seq) of the inorganic scaffold from Batch A. Adapted from reference[204] with permission from Wiley.

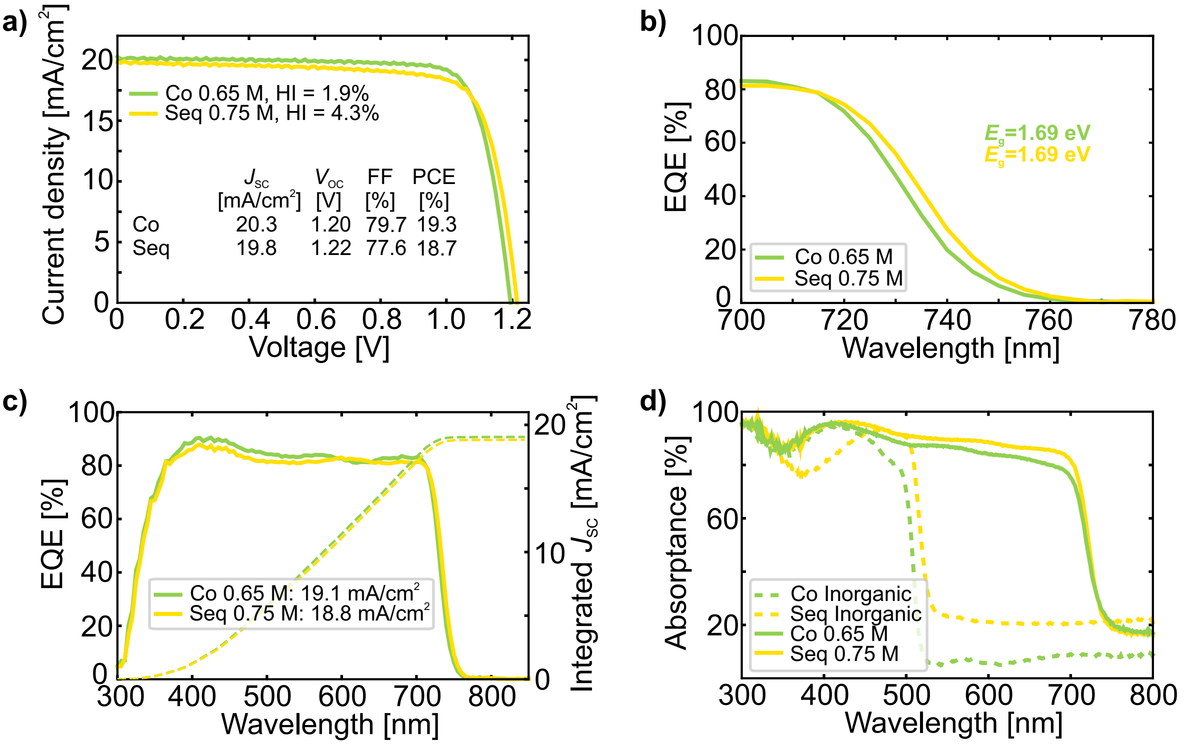

Figure A.35: a) Current density *versus* voltage (J-V) characteristics with HI indicating the hysteresis index, b) optical bandgap (E_g) extracted from the inflection point of the external quantum efficiency (EQE) spectra, and c) EQE spectra as well as the corresponding integrated short-circuit current density (J_{SC}) of the champion opaque perovskite solar cells (PSCs) from Batch A with co- (Co) and sequential (Seq) deposition of the inorganic scaffold. d) Absorptance spectra of the inorganic scaffolds as well as the perovskite films with optimal molarity of the organic cation solution from Batch A fabricated *via* co- (Co) and sequential (Seq) deposition of the inorganic scaffold. Adapted from reference[204] with permission from Wiley.

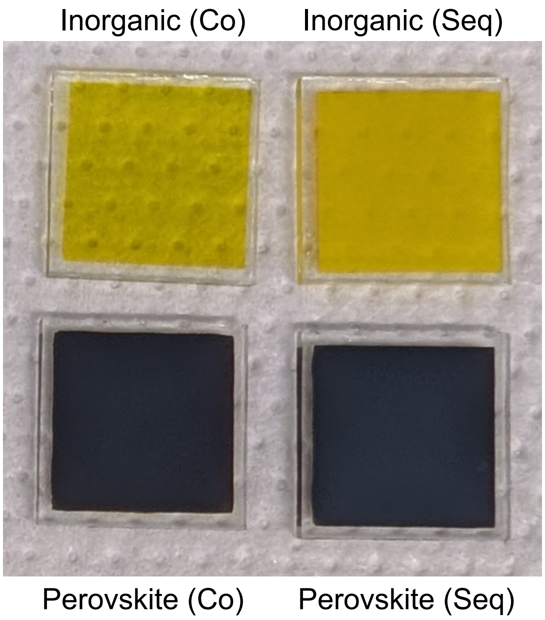

Figure A.36: Optical photographs of the inorganic scaffolds and the corresponding perovskite films deposited *via* co- (Co) and sequential (Seq) deposition of the inorganic scaffold on glass/indium tin oxide (ITO)/NiO_x/2PACz. For the perovskite films, the optimal molarity of the organic cation solution from Batch A is used. Adapted from reference[204] with permission from Wiley.

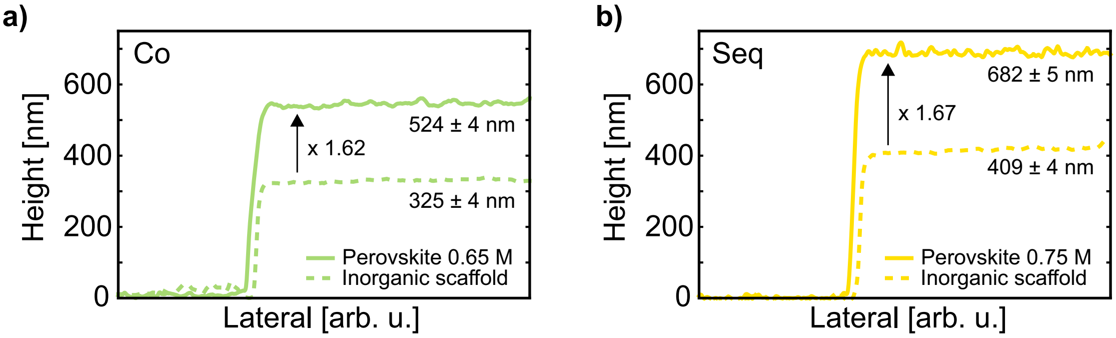

Figure A.37: Surface profilometry of a) the inorganic scaffold and b) the perovskite film with optimal molarity of the organic cation solution from Batch A for co- (Co) and sequential (Seq) deposition of the inorganic scaffold. The expansion coefficients ($\text{thickness}_{\text{perovskite}}/\text{thickness}_{\text{inorganic}}$) of Co and Seq are 1.62 and 1.67, respectively, indicating a slightly increased organic cation uptake in case of sequentially deposited inorganic scaffolds. Measurements are performed on half-stacks with the architecture indium tin oxide (ITO)/NiO_x/2PACz/inorganic scaffold or perovskite. Adapted from reference[204] with permission from Wiley.

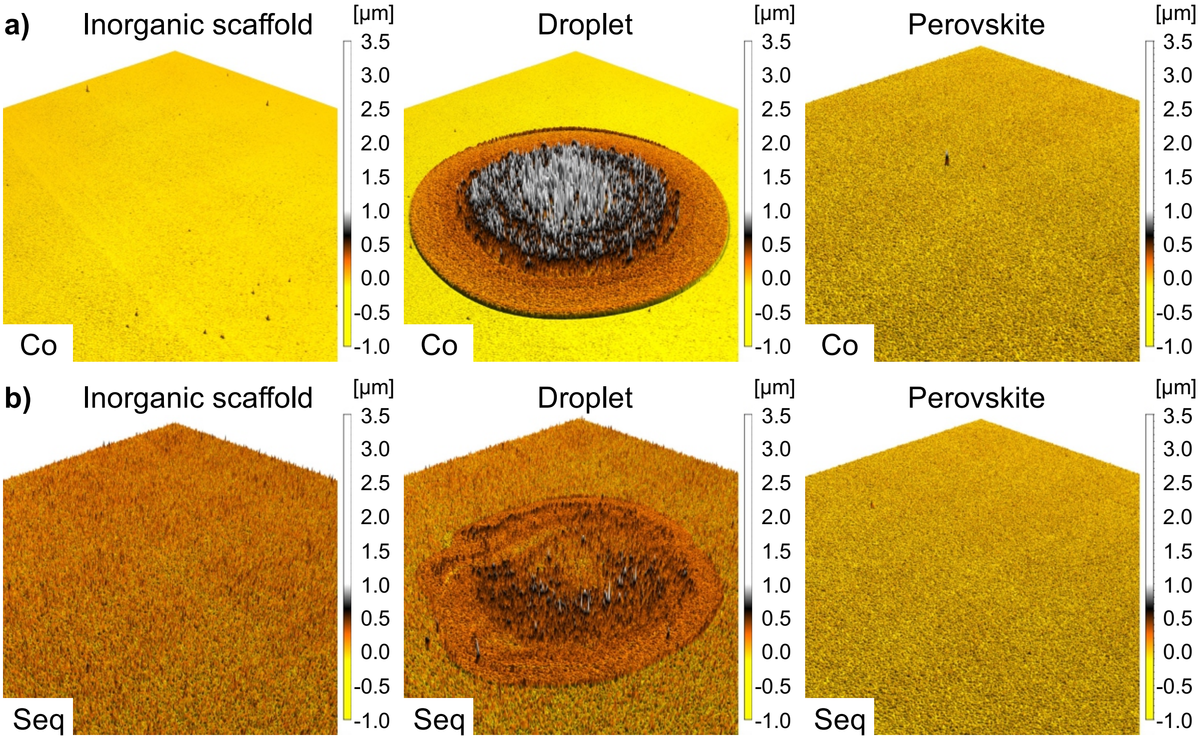

Figure A.38: Surface structure analysis *via* confocal scanning microscopy for a) co- (Co) and b) sequential (Seq) deposition of the inorganic scaffold on glass/indium tin oxide (ITO)/NiO_x/2PACz. For better visibility, a 10-fold height magnification is chosen for all images. For films with a deposited droplet, the interaction between a single $\approx$ 50 pL droplet and the inorganic scaffold is examined. For the perovskite films, the optimal molarity of the organic cation solution from Batch A is used. Adapted from reference[204] with permission from Wiley.

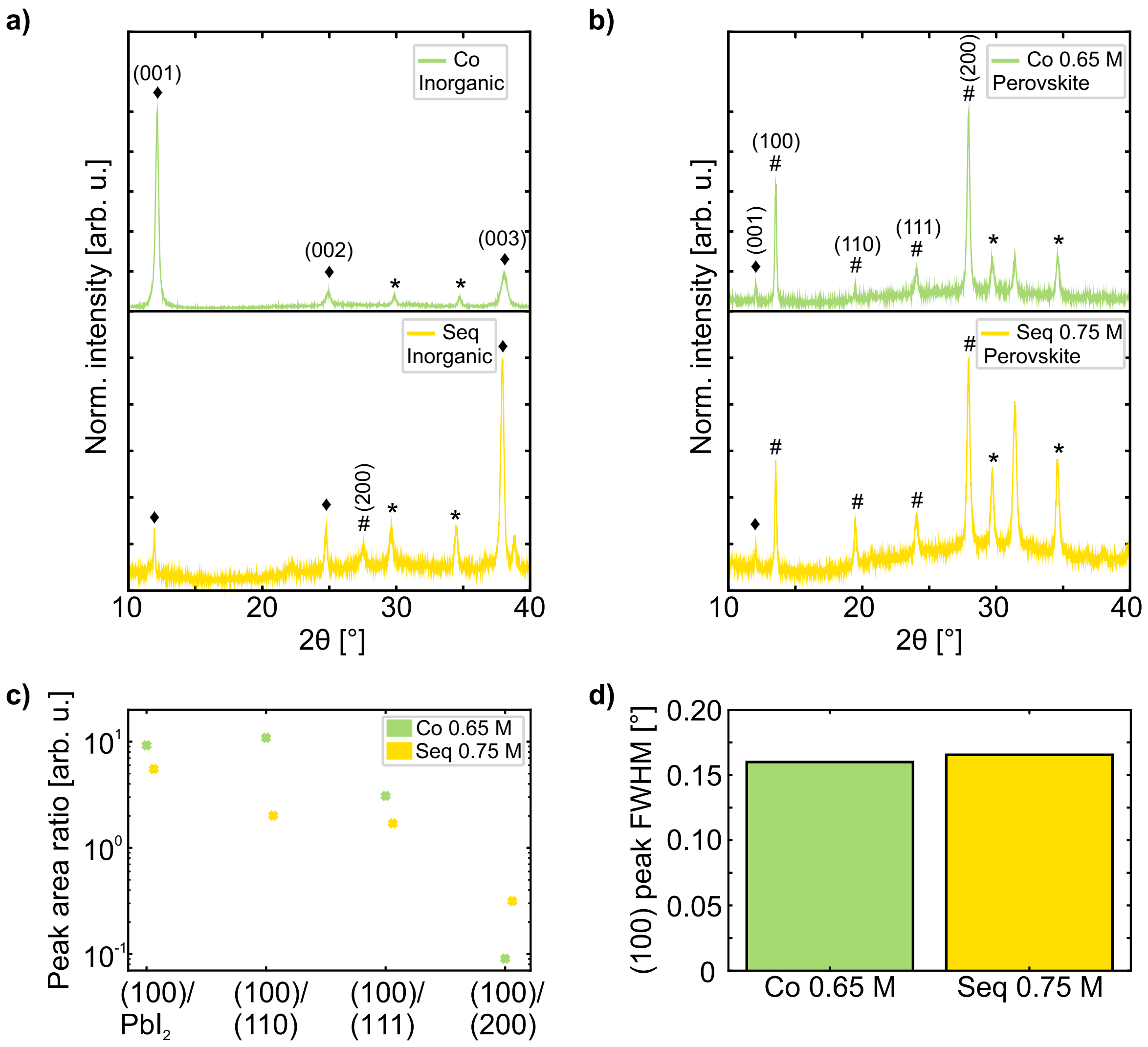

Figure A.39: X-ray diffraction (XRD) patterns (♦ denotes the PbI_2 phase, # the perovskite phase and ∗ the indium tin oxide (ITO) phase) for a) the inorganic scaffold and b) the perovskite film with optimal molarity of the organic cation solution from Batch A for co- (Co) and sequential (Seq) deposition of the inorganic scaffold. c) Peak area ratios, and d) full width at half maximum (FWHM) of the (100) perovskite peak of the perovskite films. Measurements are performed on half-stacks with the architecture indium tin oxide (ITO)/NiO_x/2PACz/inorganic scaffold or perovskite. Adapted from reference[204] with permission from Wiley.

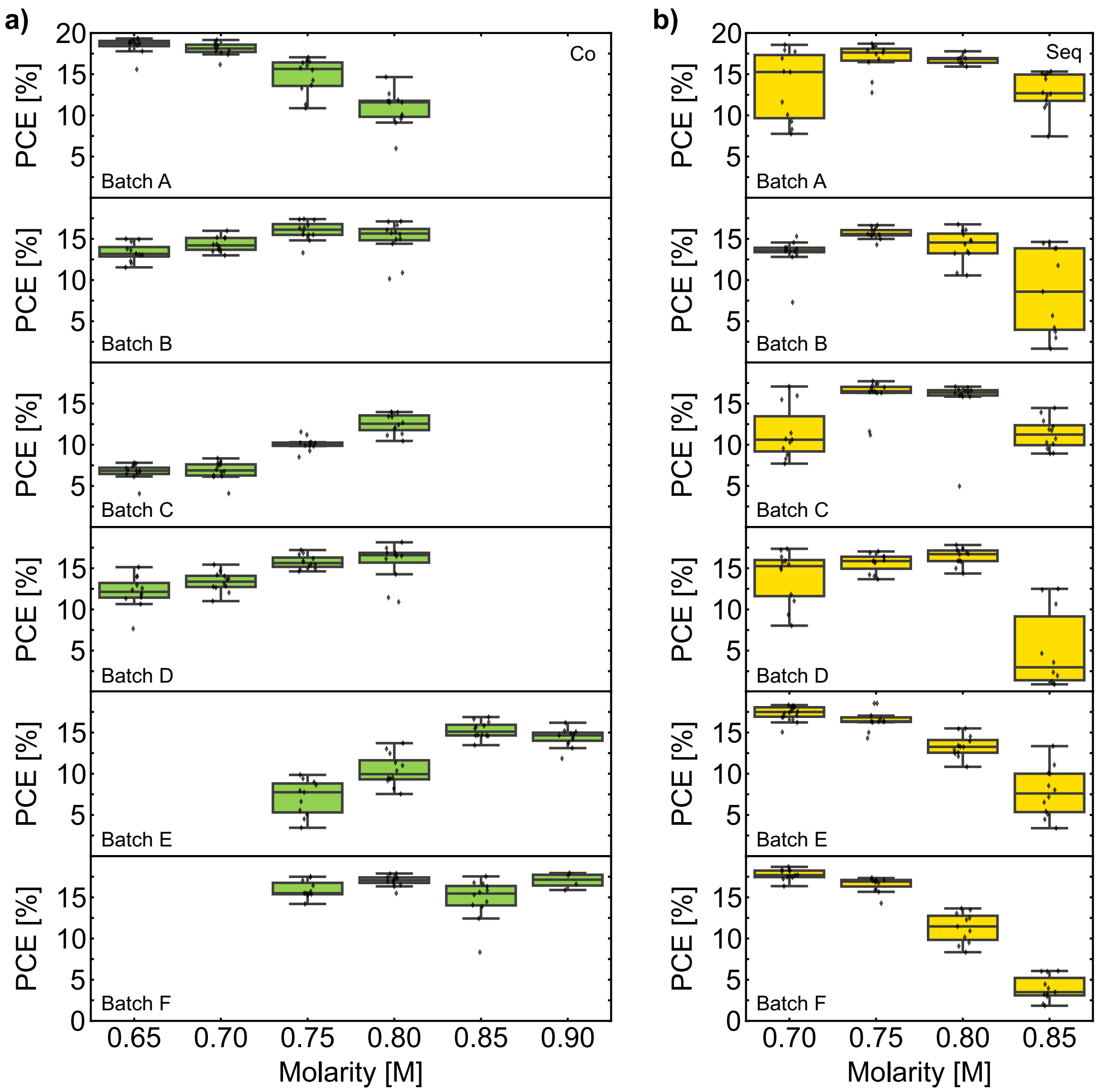

Figure A.40: Comparison of process repeatability of perovskite solar cells (PSCs) fabricated with a) co- (Co) and b) sequential (Seq) deposition of the inorganic scaffold. For each individual batch, Co and Seq PSCs are fabricated in parallel. Each batch comprises twelve pixels per organic cation molarity – for Co and Seq respectively. The rotation speed for the organic cation solution is increased from 4000 rpm in Batch A to 5500 rpm for Batch B–F to compensate for changed organic cation uptake after maintenance of the PEROvap system. Adapted from reference[204] with permission from Wiley.

Table A.12: Final quartz crystal microbalance (QCM) thicknesses of CsCl and PbI_2 for co- (Co) and sequential (Seq) deposition of the inorganic scaffold over multiple batches.

Batch No.	Seq Thickness [nm]		Co Thickness [nm]	
	PbI_2	CsCl	PbI_2	CsCl
A	300	30	300	not measured
B	300	30	300	29.7
C	300	30	300	30.2
D	300	30	300	29.7
E	300	30	300	29.7
F	300	30	300	30.1

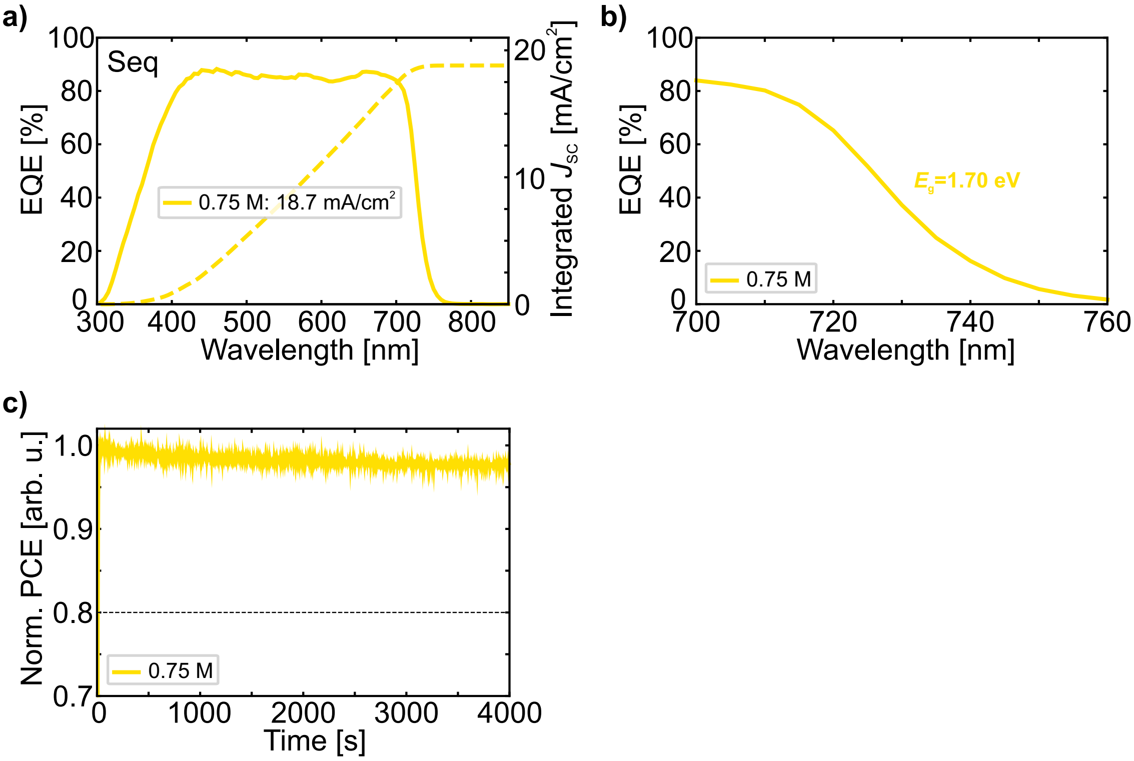

Figure A.41: a) External quantum efficiency (EQE) spectrum as well as the corresponding integrated short-circuit current density (J_{SC}), b) optical bandgap (E_g) extracted from the inflection point of the EQE spectrum, and c) maximum power point (MPP) tracking for the champion perovskite solar cell (PSC) fabricated with sequential (Seq) deposition of the inorganic scaffold and an organic cation molarity of 0.75 M. Adapted from reference[204] with permission from Wiley.

Table A.13: Literature overview for wide-bandgap ($E_g > 1.60\,\text{eV}$) perovskite solar cells (PSCs) in the *p*-*i*-*n* architecture fabricated *via* a hybrid two-step deposition route.

Author	Year	Bandgap [eV]	PCE [%]	V_{OC} [V]	FF [%]	J_{SC} [mA cm^{-2}]	Reference
This work	2026	1.70	20.30	1.23	80.7	20.5	[204]
Pesch *et al.*	2025	1.66	19.80	1.20	79.2	20.8	[69]
Chen *et al.*	2024	1.65	20.33	1.19	81.2	21.09	[404]
Li *et al.*	2024	1.61	19.80	1.11	83.6	21.31	[400]
Liu *et al.*	2024	1.66	20.37	1.16	83.3	21.09	[88]
Yang *et al.*	2024	1.65	18.59	1.18	76.5	20.61	[306]
Zheng *et al.*	2024	1.68	20.77	1.22	81.5	20.98	[393]
Said *et al.*	2024	1.68	19.06	1.16	81.1	20.3	[405]
Xiong *et al.*	2023	1.68	20.02	1.14	81.2	21.64	[401]
Afshord *et al.*	2023	1.64	21.06	1.11	79.5	23.9	[83]
Afshord *et al.*	2023	1.67	20.34	1.14	80.9	22.06	[83]
Yang *et al.*	2023	1.63	21.05	1.16	78.97	22.98	[402]
Er-raji *et al.*	2023	1.66	15.72	1.07	78.4	18.78	[80]
Luo *et al.*	2023	1.68	20.30	1.19	81.6	20.9	[79]
Luo *et al.*	2023	1.68	20.30	1.21	80.8	20.9	[399]
Sun *et al.*	2023	1.65	20.62	1.13	80.2	22.77	[403]
Zhang *et al.*	2023	1.61	20.26	1.16	79.96	21.84	[287]
Er-raji *et al.*	2023	1.66	14.30	1.05	75.7	18	[84]
Mao *et al.*	2022	1.65	21.31	1.14	80.6	23.19	[212]
Li *et al.*	2021	1.63	17.03	1.08	80.3	19.59	[78]
Soltanpoor *et al.*	2020	1.65	19.80	1.15	82.8	20.8	[438]

List of Figures

List of Tables

Bibliography

[1] IEA. *World Energy Outlook 2025*. Accessed January 2026. Paris: International Energy Agency (IEA), 2025. URL: `https://www.iea.org/reports/world-energy-outlook-2025`.

[2] J. Hansen et al. “Earth’s Energy Imbalance: Confirmation and Implications”. In: *Science* 308.5727 (2005), pp. 1431–1435. DOI: `10.1126/science.1110252`.

[3] N. M. Haegel et al. “Terawatt-scale photovoltaics: Transform global energy”. In: *Science* 364.6443 (2019), pp. 836–838. DOI: `10.1126/science.aaw1845`.

[4] L. Wagner et al. “Actions for sustainably scalable multi-terawatt photovoltaics”. In: *Nature Reviews Clean Technology* (2026). DOI: `10.1038/s44359-025-00129-y`.

[5] IEA. *Nuclear Power and Secure Energy Transitions*. Accessed January 2026. Paris: International Energy Agency (IEA), 2022. URL: `https://www.iea.org/reports/nuclear-power-and-secure-energy-transitions`.

[6] T. Appenzeller. *2025 Breakthrough of the year*. Accessed January 2026. URL: `https://www.science.org/content/article/breakthrough-2025`.

[7] F. M. Guangul et al. “Solar Energy as Renewable Energy Source: SWOT Analysis”. In: *2019 4th MEC International Conference on Big Data and Smart City (ICBDSC)*. IEEE, 2019, pp. 1–5. DOI: `10.1109/icbdsc.2019.8645580`.

[8] S. Philipps et al. *Photovoltaics Report*. Fraunhofer ISE. Accessed January 2026. 2025. URL: `https://www.ise.fraunhofer.de/en/publications/studies/photovoltaics-report.html`.

[9] C. Becker et al. “Tandemsolarzellen mit Perowskiten - Die neuen Stars der Photovoltaik,” in: *FVEE Themenheft* (2019), pp. 42–46.

[10] Ember Energy Research CIC (Ember). *Data Sets*. Accessed January 2026. URL: `https://ember-energy.org/`.

[11] C. Kost. *Study: Levelized Cost of Electricity - Renewable Energy Technologies*. Fraunhofer ISE. Accessed January 2026. 2024. URL: `https://www.ise.fraunhofer.de/en/publications/studies/cost-of-electricity.html`.

[12] A. Richter et al. “Reassessment of the Limiting Efficiency for Crystalline Silicon Solar Cells”. In: *IEEE Journal of Photovoltaics* 3.4 (2013), pp. 1184–1191. DOI: `10.1109/jphotov.2013.2270351`.

[13] T. Niewelt et al. “Reassessment of the intrinsic bulk recombination in crystalline silicon”. In: *Solar Energy Materials and Solar Cells* 235 (2022), p. 111467. DOI: `10.1016/j.solmat.2021.111467`.

[14] National Laboratory of the Rockies (NLR). *NLR Best Research-Cell Efficiency Chart*. Accessed March 2026. URL: `https://www.nlr.gov/pv/cell-efficiency.html`.

[15] Z. Chen et al. “A Study of the Performance of Submerged Arc Furnace Smelting of Industrial Silicon”. In: *Silicon* 10.3 (2017), pp. 1121–1127. DOI: `10.1007/s12633-017-9584-3`.

[16] W. Shockley et al. “Detailed Balance Limit of Efficiency of p-n Junction Solar Cells”. In: *Journal of Applied Physics* 32.3 (1961), pp. 510–519. DOI: `10.1063/1.1736034`.

[17] C. U. Kim et al. “Strategy for large-scale monolithic Perovskite/Silicon tandem solar cell: A review of recent progress”. In: *EcoMat* 3.2 (2021). DOI: `10.1002/eom2.12084`.

[18] H. Shen et al. “Monolithic Perovskite/Si Tandem Solar Cells: Pathways to Over 30% Efficiency”. In: *Advanced Energy Materials* 10.13 (2019), p. 1902840. DOI: `10.1002/aenm.201902840`.

[19] A. D. Vos. “Detailed balance limit of the efficiency of tandem solar cells”. In: *Journal of Physics D: Applied Physics* 13.5 (1980), pp. 839–846. DOI: `10.1088/0022-3727/13/5/018`.

[20] M. Heydarian et al. “Recent progress in monolithic two-terminal perovskite-based triple-junction solar cells”. In: *Energy & Environmental Science* 17.5 (2024), pp. 1781–1818. DOI: `10.1039/d3ee02822d`.

[21] M. He et al. “Top Cells for Silicon-Based Tandem Photovoltaics”. In: *Advanced Materials* 37.40 (2025). DOI: `10.1002/adma.202411858`.

[22] I. O. Abdulsalami et al. “Dye-sensitized solar cells: a systematic review of progress, challenges, and future perspectives”. In: *Discover Chemistry* 3.1 (2026). DOI: `10.1007/s44371-026-00548-1`.

[23] T. Ameri et al. “Organic tandem solar cells: A review”. In: *Energy & Environmental Science* 2.4 (2009), p. 347. DOI: `10.1039/b817952b`.

[24] T. Ameri et al. “Highly efficient organic tandem solar cells: a follow up review”. In: *Energy & Environmental Science* 6.8 (2013), p. 2390. DOI: `10.1039/c3ee40388b`.

[25] M. Giannouli. “Current Status of Emerging PV Technologies: A Comparative Study of Dye-Sensitized, Organic, and Perovskite Solar Cells”. In: *International Journal of Photoenergy* 2021 (2021). Ed. by K. Sudhakar, pp. 1–19. DOI: `10.1155/2021/6692858`.

[26] A. Kojima et al. “Organometal Halide Perovskites as Visible-Light Sensitizers for Photovoltaic Cells”. In: *Journal of the American Chemical Society* 131.17 (2009), pp. 6050–6051. DOI: `10.1021/ja809598r`.

[27] S. D. Stranks et al. “Electron-Hole Diffusion Lengths Exceeding 1 Micrometer in an Organometal Trihalide Perovskite Absorber”. In: *Science* 342.6156 (2013), pp. 341–344. DOI: `10.1126/science.1243982`.

[28] S. De Wolf et al. “Organometallic Halide Perovskites: Sharp Optical Absorption Edge and Its Relation to Photovoltaic Performance”. In: *The Journal of Physical Chemistry Letters* 5.6 (2014), pp. 1035–1039. DOI: `10.1021/jz500279b`.

[29] M. R. Filip et al. “Steric engineering of metal-halide perovskites with tunable optical band gaps”. In: *Nature Communications* 5.1 (2014). DOI: `10.1038/ncomms6757`.

[30] E. L. Unger et al. “Roadmap and roadblocks for the band gap tunability of metal halide perovskites”. In: *Journal of Materials Chemistry A* 5.23 (2017), pp. 11401–11409. DOI: `10.1039/c7ta00404d`.

[31] T. Ye et al. “Flexible Perovskite Solar Cells: Low Temperature Processing, Material Design, and Pathways to Scalable Green Photovoltaics”. In: *Carbon Neutralization* 4.5 (2025). DOI: `10.1002/cnl2.70047`.

[32] S. Olthof. “Perowskite im Rampenlicht”. In: *Physik Journal* 23.7 (July 2024), pp. 25–30.

[33] J. Tong et al. “Wide-Bandgap Metal Halide Perovskites for Tandem Solar Cells”. In: *ACS Energy Letters* 6.1 (2020), pp. 232–248. DOI: `10.1021/acsenergylett.0c02105`.

[34] S. Gharibzadeh et al. “2D/3D Heterostructure for Semitransparent Perovskite Solar Cells with Engineered Bandgap Enables Efficiencies Exceeding 25% in Four-Terminal Tandems with Silicon and CIGS”. In: *Advanced Functional Materials* 30.19 (2020), p. 1909919. DOI: `10.1002/adfm.201909919`.

[35] M. A. Ruiz-Preciado et al. “Monolithic Two-Terminal Perovskite/CIS Tandem Solar Cells with Efficiency Approaching 25%”. In: *ACS Energy Letters* 7.7 (2022), pp. 2273–2281. DOI: `10.1021/acsenergylett.2c00707`.

[36] J. Wen et al. “Present status of and future opportunities for all-perovskite tandem photovoltaics”. In: *Nature Energy* 10.6 (2025), pp. 681–696. DOI: `10.1038/s41560-025-01782-0`.

[37] L. Schmidt-Mende et al. “Roadmap on organic-inorganic hybrid perovskite semiconductors and devices”. In: *APL Materials* 9.10 (2021). DOI: `10.1063/5.0047616`.

[38] T. G. Allen et al. “A Practical Efficiency Target for Perovskite/Silicon Tandem Solar Cells”. In: *ACS Energy Letters* 10.1 (2024), pp. 238–245. DOI: `10.1021/acsenergylett.4c02152`.

[39] M. H. Futscher et al. “Efficiency Limit of Perovskite/Si Tandem Solar Cells”. In: *ACS Energy Letters* 1.4 (2016), pp. 863–868. DOI: `10.1021/acsenergylett.6b00405`.

[40] T. E. Scheul et al. “Wavelength and angle resolved reflectance measurements of pyramidal textures for crystalline silicon photovoltaics”. In: *Progress in Photovoltaics: Research and Applications* 28.12 (2020), pp. 1248–1257. DOI: `10.1002/pip.3319`.

[41] F. E. Subhan et al. “Optical optimization of double-side-textured monolithic perovskite-silicon tandem solar cells for improved light management”. In: *RSC Advances* 10.45 (2020), pp. 26631–26638. DOI: `10.1039/d0ra04634e`.

[42] M. De Bastiani et al. “Efficient bifacial monolithic perovskite/silicon tandem solar cells via bandgap engineering”. In: *Nature Energy* 6.2 (2021), pp. 167–175. DOI: `10.1038/s41560-020-00756-8`.

[43] F. Gota et al. “Energy yield modelling of textured perovskite/silicon tandem photovoltaics with thick perovskite top cells”. In: *Optics Express* 30.9 (2022), p. 14172. DOI: `10.1364/oe.447069`.

[44] W. Qarony et al. “Influence of Perovskite Interface Morphology on the Photon Management in Perovskite/Silicon Tandem Solar Cells”. In: *ACS Applied Materials & Interfaces* 12.13 (2020), pp. 15080–15086. DOI: `10.1021/acsami.9b21985`.

[45] A. S. Subbiah et al. “High-Performance Perovskite Single-Junction and Textured Perovskite/Silicon Tandem Solar Cells via Slot-Die-Coating”. In: *ACS Energy Letters* 5.9 (2020), pp. 3034–3040. DOI: `10.1021/acsenergylett.0c01297`.

[46] F. H. Isikgor et al. “Concurrent cationic and anionic perovskite defect passivation enables 27.4% perovskite/silicon tandems with suppression of halide segregation”. In: *Joule* 5.6 (2021), pp. 1566–1586. DOI: `10.1016/j.joule.2021.05.013`.

[47] A. Al-Ashouri et al. “Monolithic perovskite/silicon tandem solar cell with > 29% efficiency by enhanced hole extraction”. In: *Science* 370.6522 (2020), pp. 1300–1309. DOI: `10.1126/science.abd4016`.

[48] J. Xu et al. “Triple-halide wide-band gap perovskites with suppressed phase segregation for efficient tandems”. In: *Science* 367.6482 (2020), pp. 1097–1104. DOI: `10.1126/science.aaz5074`.

[49] W. Xu et al. “Suppressing Defects-Induced Nonradiative Recombination for Efficient Perovskite Solar Cells through Green Antisolvent Engineering”. In: *Advanced Materials* 32.38 (2020). DOI: `10.1002/adma.202003965`.

[50] J. Liu et al. “28.2%-efficient, outdoor-stable perovskite/silicon tandem solar cell”. In: *Joule* 5.12 (2021), pp. 3169–3186. DOI: `10.1016/j.joule.2021.11.003`.

[51] M. De Bastiani et al. “Mechanical Reliability of Fullerene/Tin Oxide Interfaces in Monolithic Perovskite/Silicon Tandem Cells”. In: *ACS Energy Letters* 7.2 (2022), pp. 827–833. DOI: `10.1021/acsenergylett.1c02148`.

[52] F. Huang et al. “From scalable solution fabrication of perovskite films towards commercialization of solar cells”. In: *Energy & Environmental Science* 12.2 (2019), pp. 518–549. DOI: `10.1039/c8ee03025a`.

[53] M. Jung et al. “Perovskite precursor solution chemistry: from fundamentals to photovoltaic applications”. In: *Chemical Society Reviews* 48.7 (2019), pp. 2011–2038. DOI: `10.1039/c8cs00656c`.

[54] Y. Dong et al. “Trivalent-Neodymium Additive Modulated $MAPbBr_3$ Perovskite Nucleation and Growth: Ultrawide Processing Window for One-Step Fabrication of Efficient Light-Emitting Perovskites”. In: *Advanced Electronic Materials* 6.3 (2020). DOI: `10.1002/aelm.201901162`.

[55] V. Cimrová et al. “Formamidinium Lead Iodide Perovskite Thin Films Formed by Two-Step Sequential Method: Solvent–Morphology Relationship”. In: *Materials* 16.3 (2023), p. 1049. DOI: `10.3390/ma16031049`.

[56] S. Laalioui. *Perovskite-Based Solar Cells: From Fundamentals to Tandem Devices*. Walter de Gruyter GmbH Berlin/Boston, 2022.

[57] B. Chen et al. “A Two-Step Solution-Processed Wide-Bandgap Perovskite for Monolithic Silicon-Based Tandem Solar Cells with $>27\%$ Efficiency”. In: *ACS Energy Letters* 7.8 (2022), pp. 2771–2780. DOI: `10.1021/acsenergylett.2c01488`.

[58] Q. Li et al. “Halogen Engineering for Operationally Stable Perovskite Solar Cells via Sequential Deposition”. In: *Advanced Energy Materials* 9.46 (2019), p. 1902239. DOI: `10.1002/aenm.201902239`.

[59] K. Liang et al. “Synthesis and Characterization of Organic-Inorganic Perovskite Thin Films Prepared Using a Versatile Two-Step Dipping Technique”. In: *Chemistry of Materials* 10.1 (1998), pp. 403–411. DOI: `10.1021/cm970568f`.

[60] D. Bi et al. “Using a two-step deposition technique to prepare perovskite ($CH_3NH_3PbI_3$) for thin film solar cells based on ZrO_2 and TiO_2 mesostructures”. In: *RSC Advances* 3.41 (2013), p. 18762. DOI: `10.1039/c3ra43228a`.

[61] J. Burschka et al. “Sequential deposition as a route to high-performance perovskite-sensitized solar cells”. In: *Nature* 499.7458 (2013), pp. 316–319. DOI: `10.1038/nature12340`.

[62] M. Hu et al. “Stabilized Wide Bandgap $MAPbBr_xI_{3-x}$ Perovskite by Enhanced Grain Size and Improved Crystallinity”. In: *Advanced Science* 3.6 (2015). DOI: `10.1002/advs.201500301`.

[63] T. Zhang et al. “Controllable Sequential Deposition of Planar $CH_3NH_3PbI_3$ Perovskite Films via Adjustable Volume Expansion”. In: *Nano Letters* 15.6 (2015), pp. 3959–3963. DOI: `10.1021/acs.nanolett.5b00843`.

[64] X. Liu et al. “Highly efficient wide-band-gap perovskite solar cells fabricated by sequential deposition method”. In: *Nano Energy* 86 (2021), p. 106114. DOI: `10.1016/j.nanoen.2021.106114`.

[65] S. Ternes et al. “Process Parameter Specification and Control in Solution Processing of Hybrid Perovskite Photovoltaics: From Domain-Specific Jargon to Evidence-Based, Unambiguous Description of Experimental Workflows”. In: *Advanced Energy Materials* 15.47 (2025). DOI: `10.1002/aenm.202503187`.

[66] Y. Han et al. “Review of Two-Step Method for Lead Halide Perovskite Solar Cells”. In: *Solar RRL* (2022), p. 2101007. DOI: `10.1002/solr.202101007`.

[67] A. Diercks et al. “Sequential Evaporation of Inverted $FAPbI_3$ Perovskite Solar Cells – Impact of Substrate on Crystallization and Film Formation”. In: *ACS Energy Letters* 10.3 (2025), pp. 1165–1173. DOI: `10.1021/acsenergylett.4c03315`.

[68] R. Pesch et al. “Hybrid Two-Step Inkjet-Printed Perovskite Solar Cells”. In: *Solar RRL* 8.13 (2024). DOI: `10.1002/solr.202400165`.

[69] R. Pesch et al. “Efficient Perovskite/Silicon Tandem Solar Cells Using Hybrid Two-Step Inkjet Printing with Edge Isolation Precision”. In: *Small Science* (2025). DOI: `10.1002/smsc.202500362`.

[70] K. Geistert et al. “Spatially Regulated Gas Flow Control for Batch-Drying of Large Area Slot-Die-Coated Perovskite Thin Films”. In: *Advanced Energy Materials* (2025). DOI: `10.1002/aenm.202500923`.

[71] T. Abzieher et al. “Vapor phase deposition of perovskite photovoltaics: short track to commercialization?” In: *Energy & Environmental Science* 17.5 (2024), pp. 1645–1663. DOI: `10.1039/d3ee03273f`.

[72] Y. Vaynzof. “The Future of Perovskite Photovoltaics–Thermal Evaporation or Solution Processing?” In: *Advanced Energy Materials* 10.48 (2020). DOI: `10.1002/aenm.202003073`.

[73] L. Gil-Escrig et al. “Vacuum Deposited Triple-Cation Mixed-Halide Perovskite Solar Cells”. In: *Advanced Energy Materials* 8.14 (2018). DOI: `10.1002/aenm.201703506`.

[74] T. Abzieher et al. “Efficient All-Evaporated pin-Perovskite Solar Cells: A Promising Approach Toward Industrial Large-Scale Fabrication”. In: *IEEE Journal of Photovoltaics* 9.5 (2019), pp. 1249–1257. DOI: `10.1109/jphotov.2019.2920727`.

[75] C. Momblona et al. “Efficient methylammonium lead iodide perovskite solar cells with active layers from 300 to 900 nm”. In: *APL Materials* 2.8 (2014). DOI: `10.1063/1.4890056`.

[76] F. Sahli et al. “Fully textured monolithic perovskite/silicon tandem solar cells with 25.2% power conversion efficiency”. In: *Nature Materials* 17.9 (2018), pp. 820–826. DOI: `10.1038/s41563-018-0115-4`.

[77] P. S. C. Schulze et al. “Perovskite hybrid evaporation/spin coating method: From band gap tuning to thin film deposition on textures”. In: *Thin Solid Films* 704 (2020), p. 137970. DOI: `10.1016/j.tsf.2020.137970`.

[78] Y. Li et al. “Wide Bandgap Interface Layer Induced Stabilized Perovskite/Silicon Tandem Solar Cells with Stability over Ten Thousand Hours”. In: *Advanced Energy Materials* 11.48 (2021), p. 2102046. DOI: `10.1002/aenm.202102046`.

[79] X. Luo et al. “Efficient Perovskite/Silicon Tandem Solar Cells on Industrially Compatible Textured Silicon”. In: *Advanced Materials* 35.9 (2023), p. 2207883. DOI: `10.1002/adma.202207883`.

[80] O. Er-raji et al. “Insights into Perovskite Film Formation Using the Hybrid Evaporation/Spin-Coating Route: An In Situ XRD Study”. In: *ACS Applied Energy Materials* 6.11 (2023), pp. 6183–6193. DOI: `10.1021/acsaem.3c00698`.

[81] O. Er-raji et al. “Tailoring perovskite crystallization and interfacial passivation in efficient, fully textured perovskite silicon tandem solar cells”. In: *Joule* 8.10 (2024), pp. 2811–2833. DOI: `10.1016/j.joule.2024.06.018`.

[82] O. Er-raji et al. “Loss Analysis of Fully-Textured Perovskite Silicon Tandem Solar Cells: Characterization Methods and Simulation toward the Practical Efficiency Potential”. In: *Solar RRL* 7.24 (2023), p. 2300659. DOI: `10.1002/solr.202300659`.

[83] A. Z. Afshord et al. “Efficient and Stable Inverted Wide-Bandgap Perovskite Solar Cells and Modules Enabled by Hybrid Evaporation-Solution Method”. In: *Advanced Functional Materials* 33.31 (2023). DOI: `10.1002/adfm.202301695`.

[84] O. Er-raji et al. “Toward efficient and industrially compatible fully textured perovskite silicon tandem solar cells: Controlled process parameters for reliable perovskite formation”. In: *Progress in Photovoltaics: Research and Applications* 33.1 (2023), pp. 86–99. DOI: `https://doi.org/10.1002/pip.3770`.

[85] Q. Xu et al. “Diffusible Capping Layer Enabled Homogeneous Crystallization and Component Distribution of Hybrid Sequential Deposited Perovskite”. In: *Advanced Materials* 36.5 (2023). DOI: `10.1002/adma.202308692`.

[86] A. Ullah et al. “Improved Crystallinity and Efficiency in Perovskite Solar Cells through Layered Hybrid Deposition”. In: *ACS Energy Letters* 10.1 (2024), pp. 30–33. DOI: `10.1021/acsenergylett.4c02797`.

[87] X. Y. Chin et al. “Interface passivation for 31.25%-efficient perovskite/silicon tandem solar cells”. In: *Science* 381.6653 (2023), pp. 59–63. DOI: `10.1126/science.adg0091`.

[88] Z. Liu et al. “Strained heterojunction enables high-performance, fully textured perovskite/silicon tandem solar cells”. In: *Joule* 8.10 (2024), pp. 2834–2850. DOI: `10.1016/j.joule.2024.06.015`.

[89] O. Er-raji et al. “Electron accumulation across the perovskite layer enhances tandem solar cells with textured silicon”. In: *Science* 390.6772 (2025). DOI: `10.1126/science.adx1745`.

[90] A. Shah et al. “Photovoltaic Technology: The Case for Thin-Film Solar Cells”. In: *Science* 285.5428 (1999), pp. 692–698. DOI: `10.1126/science.285.5428.692`.

[91] L. A. Iturralde Carrera et al. “Efficiency and Sustainability in Solar Photovoltaic Systems: A Review of Key Factors and Innovative Technologies”. In: *Eng* 6.3 (2025), p. 50. DOI: `10.3390/eng6030050`.

[92] Y. Galagan. “Perovskite solar cells from lab to fab: the main challenges to access the market”. In: *Oxford Open Materials Science* 1.1 (2020). DOI: `10.1093/oxfmat/itaa007`.

[93] X. Tian et al. “Perspectives for sustainability analysis of scalable perovskite photovoltaics”. In: *Energy & Environmental Science* 18.1 (2025), pp. 194–213. DOI: `10.1039/d4ee03956d`.

[94] C. Chen et al. “Achieving a high open-circuit voltage in inverted wide-bandgap perovskite solar cells with a graded perovskite homojunction”. In: *Nano Energy* 61 (2019), pp. 141–147. DOI: `10.1016/j.nanoen.2019.04.069`.

[95] A. Rajagopal et al. “Overcoming the Photovoltage Plateau in Large Bandgap Perovskite Photovoltaics”. In: *Nano Letters* 18.6 (2018), pp. 3985–3993. DOI: `10.1021/acs.nanolett.8b01480`.

[96] M. Jaysankar et al. “Minimizing Voltage Loss in Wide-Bandgap Perovskites for Tandem Solar Cells”. In: *ACS Energy Letters* 4.1 (2018), pp. 259–264. DOI: `10.1021/acsenergylett.8b02179`.

[97] S. Gharibzadeh et al. “Two birds with one stone: dual grain-boundary and interface passivation enables > 22% efficient inverted methylammonium-free perovskite solar cells”. In: *Energy & Environmental Science* 14.11 (2021), pp. 5875–5893. DOI: `10.1039/d1ee01508g`.

[98] Z. Liu et al. “Open-Circuit Voltages Exceeding 1.26 V in Planar Methylammonium Lead Iodide Perovskite Solar Cells”. In: *ACS Energy Letters* 4.1 (2018), pp. 110–117. DOI: `10.1021/acsenergylett.8b01906`.

[99] J. Yang et al. “Work function engineering to enhance open-circuit voltage in planar perovskite solar cells by g-C3N4 nanosheets”. In: *Nano Research* (2021). DOI: `10.1007/s12274-021-3408-x`.

[100] F. Peña-Camargo et al. “Halide Segregation versus Interfacial Recombination in Bromide-Rich Wide-Gap Perovskite Solar Cells”. In: *ACS Energy Letters* 5.8 (2020), pp. 2728–2736. DOI: `10.1021/acsenergylett.0c01104`.

[101] Z. Cui et al. “Issues of phase segregation in wide-bandgap perovskites”. In: *Materials Chemistry Frontiers* 7.10 (2023), pp. 1896–1911. DOI: `10.1039/d2qm01341j`.

[102] M. Stolterfoht et al. “The impact of energy alignment and interfacial recombination on the internal and external open-circuit voltage of perovskite solar cells”. In: *Energy & Environmental Science* 12.9 (2019), pp. 2778–2788. DOI: `10.1039/c9ee02020a`.

[103] J. Warby et al. “Understanding Performance Limiting Interfacial Recombination in *pin* Perovskite Solar Cells”. In: *Advanced Energy Materials* 12.12 (2022), p. 2103567. DOI: `10.1002/aenm.202103567`.

[104] S. Rühle. “Tabulated values of the Shockley-Queisser limit for single junction solar cells”. In: *Solar Energy* 130 (2016), pp. 139–147. DOI: `10.1016/j.solener.2016.02.015`.

[105] A. Zekry et al. “Chapter 1 - Solar Cells and Arrays: Principles, Analysis, and Design”. In: *Advances in Renewable Energies and Power Technologies*. Elsevier, 2018, pp. 3–56.

[106] L. Fu et al. “Defect passivation strategies in perovskites for an enhanced photovoltaic performance”. In: *Energy & Environmental Science* 13.11 (2020), pp. 4017–4056. DOI: `10.1039/d0ee01767a`.

[107] X. Zheng et al. “Managing grains and interfaces via ligand anchoring enables 22.3%-efficiency inverted perovskite solar cells”. In: *Nature Energy* 5.2 (2020), pp. 131–140. DOI: `10.1038/s41560-019-0538-4`.

[108] B. Chen et al. “Enhanced optical path and electron diffusion length enable high-efficiency perovskite tandems”. In: *Nature Communications* 11.1 (2020). DOI: `10.1038/s41467-020-15077-3`.

[109] E.-B. Kim et al. “A review on two-dimensional (2D) and 2D-3D multidimensional perovskite solar cells: Perovskites structures, stability, and photovoltaic performances”. In: *Journal of Photochemistry and Photobiology C: Photochemistry Reviews* 48 (2021), p. 100405. DOI: `10.1016/j.jphotochemrev.2021.100405`.

[110] R. Azmi et al. “Damp heat-stable perovskite solar cells with tailored-dimensionality 2D/3D heterojunctions”. In: *Science* 376.6588 (2022), pp. 73–77. DOI: `10.1126/science.abm5784`.

[111] S. Gharibzadeh et al. “Record Open-Circuit Voltage Wide-Bandgap Perovskite Solar Cells Utilizing 2D/3D Perovskite Heterostructure”. In: *Advanced Energy Materials* 9.21 (2019), p. 1803699. DOI: `10.1002/aenm.201803699`.

[112] C. Liu et al. “Bimolecularly passivated interface enables efficient and stable inverted perovskite solar cells”. In: *Science* 382.6672 (2023), pp. 810–815. DOI: `10.1126/science.adk1633`.

[113] G. Rose. “Ueber einige neue Mineralien des Urals”. In: *Journal für Praktische Chemie* 19.1 (1840), pp. 459–468. DOI: `10.1002/prac.18400190179`.

[114] H. Tang et al. “A Short Progress Report on High-Efficiency Perovskite Solar Cells”. In: *Nanoscale Research Letters* 12.1 (2017). DOI: `10.1186/s11671-017-2187-5`.

[115] H. L. Wells. “On the Caesium- and the Potassium-Lead Halides”. In: *American Journalof Science* 45.266 (1893), p. 121.

[116] D. Weber. “$CH_3NH_3SnBr_xI_{3-x}$ (x = 0-3), ein Sn(II)-System mit kubischer Perowskitstruktur”. In: *Zeitschrift für Naturforschung B* 33.8 (1978), pp. 862–865. DOI: `10.1515/znb-1978-0809`.

[117] H. S. Jung et al. “Perovskite Solar Cells: From Materials to Devices”. In: *Small* 11.1 (2014), pp. 10–25. DOI: `10.1002/smll.201402767`.

[118] N. Li et al. “Mixed Cation $FA_xPEA_{1-x}PbI_3$ with Enhanced Phase and Ambient Stability toward High-Performance Perovskite Solar Cells”. In: *Advanced Energy Materials* 7.1 (2016), p. 1601307. DOI: `10.1002/aenm.201601307`.

[119] A. K. Jena et al. “Halide Perovskite Photovoltaics: Background, Status, and Future Prospects”. In: *Chemical Reviews* 119.5 (2019), pp. 3036–3103. DOI: `10.1021/acs.chemrev.8b00539`.

[120] W.-J. Yin et al. “Unique Properties of Halide Perovskites as Possible Origins of the Superior Solar Cell Performance”. In: *Advanced Materials* 26.27 (2014), pp. 4653–4658. DOI: `10.1002/adma.201306281`.

[121] V. M. Goldschmidt. “Krystallbau und chemische Zusammensetzung”. In: *Berichte der deutschen chemischen Gesellschaft (A and B Series)* 60.5 (1927), pp. 1263–1296. DOI: `10.1002/cber.19270600550`.

[122] P. S. Whitfield et al. “Structures, Phase Transitions and Tricritical Behavior of the Hybrid Perovskite Methyl Ammonium Lead Iodide”. In: *Scientific Reports* 6.1 (2016). DOI: `10.1038/srep35685`.

[123] J.-P. Correa-Baena et al. “Promises and challenges of perovskite solar cells”. In: *Science* 358.6364 (2017), pp. 739–744. DOI: `10.1126/science.aam6323`.

[124] Y. Chen et al. “2D Ruddlesden-Popper Perovskites for Optoelectronics”. In: *Advanced Materials* 30.2 (2017). DOI: `10.1002/adma.201703487`.

[125] J. Hu et al. “Two-Dimensional Organic–Inorganic Hybrid Perovskites: A New Platform for Optoelectronic Application”. In: *Advanced Materials* 30.48 (2018). DOI: `10.1002/adma.201802041`.

[126] S. Ahmad et al. “Dion-Jacobson Phase 2D Layered Perovskites for Solar Cells with Ultrahigh Stability”. In: *Joule* 3.3 (2019), pp. 794–806. DOI: `10.1016/j.joule.2018.11.026`.

[127] K. A. Bush et al. “Compositional Engineering for Efficient Wide Band Gap Perovskites with Improved Stability to Photoinduced Phase Segregation”. In: *ACS Energy Letters* 3.2 (2018), pp. 428–435. DOI: `10.1021/acsenergylett.7b01255`.

[128] M. A. Green et al. “The emergence of perovskite solar cells”. In: *Nature Photonics* 8.7 (2014), pp. 506–514. DOI: `10.1038/nphoton.2014.134`.

[129] P. Kowalczewski et al. “Towards the efficiency limits of silicon solar cells: How thin is too thin?” In: *Solar Energy Materials and Solar Cells* 143 (2015), pp. 260–268. DOI: `10.1016/j.solmat.2015.06.054`.

[130] K. Galkowski et al. “Determination of the exciton binding energy and effective masses for methylammonium and formamidinium lead tri-halide perovskite semiconductors”. In: *Energy & Environmental Science* 9.3 (2016), pp. 962–970. DOI: `10.1039/c5ee03435c`.

[131] D. Marongiu et al. “The role of excitons in 3D and 2D lead halide perovskites”. In: *Journal of Materials Chemistry C* 7.39 (2019), pp. 12006–12018. DOI: `10.1039/c9tc04292j`.

[132] Y. Chen et al. “Extended carrier lifetimes and diffusion in hybrid perovskites revealed by Hall effect and photoconductivity measurements”. In: *Nature Communications* 7.1 (2016). DOI: `10.1038/ncomms12253`.

[133] A. Miyata et al. “Direct measurement of the exciton binding energy and effective masses for charge carriers in organic-inorganic tri-halide perovskites”. In: *Nature Physics* 11.7 (2015), pp. 582–587. DOI: `10.1038/nphys3357`.

[134] C. Wehrenfennig et al. “High Charge Carrier Mobilities and Lifetimes in Organolead Trihalide Perovskites”. In: *Advanced Materials* 26.10 (2013), pp. 1584–1589. DOI: `10.1002/adma.201305172`.

[135] S. Tao et al. “Absolute energy level positions in tin- and lead-based halide perovskites”. In: *Nature Communications* 10.1 (2019). DOI: `10.1038/s41467-019-10468-7`.

[136] R. Prasanna et al. “Band Gap Tuning via Lattice Contraction and Octahedral Tilting in Perovskite Materials for Photovoltaics”. In: *Journal of the American Chemical Society* 139.32 (2017), pp. 11117–11124. DOI: `10.1021/jacs.7b04981`.

[137] K. Mertens. *Photovoltaik: Lehrbuch zu Grundlagen, Technologie und Praxis*. 6th ed. Carl Hanser Verlag München, 2022.

[138] S. M. Sze et al. *Physics of Semiconductor Devices*. Wiley, 2006. DOI: `10.1002/0470068329`.

[139] P. Y. Yu et al. *Fundamentals of Semiconductors*. Springer Berlin Heidelberg, 2005. DOI: `10.1007/b137661`.

[140] C. Deibel et al. “Polymer-fullerene bulk heterojunction solar cells”. In: *Reports on Progress in Physics* 73.9 (2010), p. 096401. DOI: `10.1088/0034-4885/73/9/096401`.

[141] S. D. Stranks et al. “Metal-halide perovskites for photovoltaic and light-emitting devices”. In: *Nature Nanotechnology* 10.5 (2015), pp. 391–402. DOI: `10.1038/nnano.2015.90`.

[142] S. Tao. “Taming defects in halide perovskites: insights from atomistic simulations”. In: *Proceedings of the International Conference on Perovskite Thin Film Photovoltaics and Perovskite Photonics and Optoelectronics*. NIPHO22. Fundació Scito, 2021. DOI: `10.29363/nanoge.nipho.2022.009`.

[143] H. Wagner et al. “Defect mapping of GaAs with low dislocation density”. In: *Defect Recognition and Image Processing in Semiconductors 1997*. Routledge, 2017, pp. 165–168.

[144] D. Skorka et al. “Firing and gettering dependence of effective defect density in material exhibiting LeTID”. In: *AIP Conference Proceedings*. Vol. 1999. 2018, p. 130015. DOI: `10.1063/1.5049334`.

[145] S. Yamamoto et al. “A Low Defect Density SiN_x/(100)Si Interface Made by Hybrid-Excitation CVD”. In: *Defect Control in Semiconductors*. Elsevier, 1990, pp. 1157–1161. DOI: `10.1016/C2009-0-09913-9`.

[146] J. Dacuña et al. “Modeling space-charge-limited currents in organic semiconductors: Extracting trap density and mobility”. In: *Physical Review B* 84.19 (2011), p. 195209. DOI: `10.1103/physrevb.84.195209`.

[147] W.-J. Yin et al. “Unusual defect physics in $CH_3NH_3PbI_3$ perovskite solar cell absorber”. In: *Applied Physics Letters* 104.6 (2014). DOI: `10.1063/1.4864778`.

[148] J. Kim et al. “The Role of Intrinsic Defects in Methylammonium Lead Iodide Perovskite”. In: *The Journal of Physical Chemistry Letters* 5.8 (2014), pp. 1312–1317. DOI: `10.1021/jz500370k`.

[149] R. E. Brandt et al. “Searching for “Defect-Tolerant” Photovoltaic Materials: Combined Theoretical and Experimental Screening”. In: *Chemistry of Materials* 29.11 (2017), pp. 4667–4674. DOI: `10.1021/acs.chemmater.6b05496`.

[150] S. Sánchez et al. “Structure, composition, and stability of metal halide perovskites”. In: *Metal Halide Perovskites for Generation Manipulation and Detection of Light*. Ed. by J. P. Martinez-Pastor; P. P. Boix; G. Xing. SPIE, 2023. DOI: `10.1117/3.100002`.

[151] S. Krishnamoorthy et al., eds. *Advances in Fabrication and Investigation of Nanomaterials for Industrial Applications*. Springer International Publishing, 2024. DOI: `10.1007/978-3-031-42700-8`.

[152] W. Zhang, ed. *Metal Halide Perovskite Crystals: Growth Techniques, Properties and Emerging Applications*. Crystals, 2019. DOI: `10.3390/books978-3-03897-559-5`.

[153] L. Cheng et al. "Tailoring Interlayer Spacers for Efficient and Stable Formamidinium-Based Low-Dimensional Perovskite Solar Cells". In: *Advanced Materials* 34.4 (2021). DOI: `10.1002/adma.202106380`.

[154] P. Huang et al. "Toward Phase Stability: Dion-Jacobson Layered Perovskite for Solar Cells". In: *ACS Energy Letters* 4.12 (2019), pp. 2960–2974. DOI: `10.1021/acsenergylett.9b02063`.

[155] Z. Xu et al. "First-Principles Study of Enhanced Out-of-Plane Transport Properties and Stability in Dion-Jacobson Two-Dimensional Perovskite Semiconductors for High-Performance Solar Cell Applications". In: *The Journal of Physical Chemistry Letters* 10.13 (2019), pp. 3670–3675. DOI: `10.1021/acs.jpclett.9b01360`.

[156] H. Yu et al. "Thermal and Humidity Stability of Mixed Spacer Cations 2D Perovskite Solar Cells". In: *Advanced Science* 8.12 (2021). DOI: `10.1002/advs.202004510`.

[157] Y. Zheng et al. "Oriented and Uniform Distribution of Dion-Jacobson Phase Perovskites Controlled by Quantum Well Barrier Thickness". In: *Solar RRL* 3.9 (2019). DOI: `10.1002/solr.201900090`.

[158] G. Liu et al. "Introduction of Hydrophobic Ammonium Salts with Halogen Functional Groups for High-Efficiency and Stable 2D/3D Perovskite Solar Cells". In: *Advanced Functional Materials* 29.47 (2019). DOI: `10.1002/adfm.201807565`.

[159] I. C. Smith et al. "A Layered Hybrid Perovskite Solar-Cell Absorber with Enhanced Moisture Stability". In: *Angewandte Chemie International Edition* 53.42 (2014), pp. 11232–11235. DOI: `10.1002/anie.201406466`.

[160] L. N. Quan et al. "Ligand-Stabilized Reduced-Dimensionality Perovskites". In: *Journal of the American Chemical Society* 138.8 (2016), pp. 2649–2655. DOI: `10.1021/jacs.5b11740`.

[161] P. Gao et al. "Dimensionality engineering of hybrid halide perovskite light absorbers". In: *Nature Communications* 9.1 (2018). DOI: `10.1038/s41467-018-07382-9`.

[162] M. A. Mahmud et al. "Origin of Efficiency and Stability Enhancement in High-Performing Mixed Dimensional 2D-3D Perovskite Solar Cells: A Review". In: *Advanced Functional Materials* 32.3 (2021). DOI: `10.1002/adfm.202009164`.

[163] L. Etgar. "The merit of perovskite's dimensionality; can this replace the 3D halide perovskite?" In: *Energy & Environmental Science* 11.2 (2018), pp. 234–242. DOI: `10.1039/c7ee03397d`.

[164] C. Chen et al. "Arylammonium-Assisted Reduction of the Open-Circuit Voltage Deficit in Wide-Bandgap Perovskite Solar Cells: The Role of Suppressed Ion Migration". In: *ACS Energy Letters* 5.8 (2020), pp. 2560–2568. DOI: `10.1021/acsenergylett.0c01350`.

[165] Z. Huang et al. "Suppressed Ion Migration in Reduced-Dimensional Perovskites Improves Operating Stability". In: *ACS Energy Letters* 4.7 (2019), pp. 1521–1527. DOI: `10.1021/acsenergylett.9b00892`.

[166] D. Meggiolaro et al. "Formation of Surface Defects Dominates Ion Migration in Lead-Halide Perovskites". In: *ACS Energy Letters* 4.3 (2019), pp. 779–785. DOI: `10.1021/acsenergylett.9b00247`.

[167] Q. Jiang et al. "Surface passivation of perovskite film for efficient solar cells". In: *Nature Photonics* 13.7 (2019), pp. 460–466. DOI: `10.1038/s41566-019-0398-2`.

[168] Y. Lin et al. "Enhanced Thermal Stability in Perovskite Solar Cells by Assembling 2D/3D Stacking Structures". In: *The Journal of Physical Chemistry Letters* 9.3 (2018), pp. 654–658. DOI: `10.1021/acs.jpclett.7b02679`.

[169] H. Tsai et al. “High-efficiency two-dimensional Ruddlesden-Popper perovskite solar cells”. In: *Nature* 536.7616 (2016), pp. 312–316. DOI: `10.1038/nature18306`.

[170] P. Würfel et al. *Physics of Solar Cells: From Basic Principles to Advanced Concepts*. 3rd ed. Wiley-VCH, 2016.

[171] V. Wesselak et al. *Photovoltaik – Wie Sonne zu Strom wird*. 2nd ed. Springer Berlin Heidelberg, 2016. DOI: `10.1007/978-3-662-48906-2`.

[172] U. Würfel et al. “Charge Carrier Separation in Solar Cells”. In: *IEEE Journal of Photovoltaics* 5.1 (2015), pp. 461–469. DOI: `10.1109/jphotov.2014.2363550`.

[173] P. Caprioglio et al. “On the Relation between the Open-Circuit Voltage and Quasi-Fermi Level Splitting in Efficient Perovskite Solar Cells”. In: *Advanced Energy Materials* 9.33 (2019). DOI: `10.1002/aenm.201901631`.

[174] T. Kirchartz. “Generalized detailed balance theory of solar cells”. PhD thesis. RWTH Aachen, 2009. URL: `https://publications.rwth-aachen.de/record/50686`.

[175] U. Rau et al. “Charge Carrier Collection and Contact Selectivity in Solar Cells”. In: *Advanced Materials Interfaces* 6.20 (2019). DOI: `10.1002/admi.201900252`.

[176] A. Smets et al. *Solar Energy: The physics and engineering of photovoltaic conversion, technologies and systems*. UIT Cambridge Limited, 2016.

[177] X. Xu et al. “Porous and Intercrossed PbI_2–CsI Nanorod Scaffold for Inverted Planar FA–Cs Mixed-Cation Perovskite Solar Cells”. In: *ACS Applied Materials & Interfaces* 11.6 (2019), pp. 6126–6135. DOI: `10.1021/acsami.8b20933`.

[178] Q. Jiang et al. “Rapid advances enabling high-performance inverted perovskite solar cells”. In: *Nature Reviews Materials* 9.6 (2024), pp. 399–419. DOI: `10.1038/s41578-024-00678-x`.

[179] C. A. Nelson et al. “Exceeding the Shockley-Queisser limit in solar energy conversion”. In: *Energy & Environmental Science* 6.12 (2013), p. 3508. DOI: `10.1039/c3ee42098a`.

[180] L. M. Herz. “Charge-Carrier Dynamics in Organic-Inorganic Metal Halide Perovskites”. In: *Annual Review of Physical Chemistry* 67.1 (2016), pp. 65–89. DOI: `10.1146/annurev-physchem-040215-112222`.

[181] G. E. Eperon et al. “Metal halide perovskite tandem and multiple-junction photovoltaics”. In: *Nature Reviews Chemistry* 1.12 (2017). DOI: `10.1038/s41570-017-0095`.

[182] K. Alberi et al. “A roadmap for tandem photovoltaics”. In: *Joule* 8.3 (2024), pp. 658–692. DOI: `10.1016/j.joule.2024.01.017`.

[183] S. E. Sofia et al. “Metal Grid Contact Design for Four-Terminal Tandem Solar Cells”. In: *IEEE Journal of Photovoltaics* 7.3 (2017), pp. 934–940. DOI: `10.1109/jphotov.2017.2686651`.

[184] Y. Yao et al. “Phase-Stable Wide-Bandgap Perovskites for Four-Terminal Perovskite/Silicon Tandem Solar Cells with Over 30% Efficiency”. In: *Small* 18.38 (2022). DOI: `10.1002/smll.202203319`.

[185] J. E. Bishop et al. “Development of Spray-Coated Perovskite Solar Cells”. In: *ACS Applied Materials & Interfaces* 12.43 (2020), pp. 48237–48245. DOI: `10.1021/acsami.0c14540`.

[186] L. E. Scriven. “Physics and Applications of DIP Coating and Spin Coating”. In: *MRS Proceedings* 121 (1988). DOI: `10.1557/proc-121-717`.

[187] Y. Mouhamad et al. “Dynamics of polymer film formation during spin coating”. In: *Journal of Applied Physics* 116.12 (2014), p. 123513. DOI: `10.1063/1.4896674`.

[188] A. G. Emslie et al. “Flow of a Viscous Liquid on a Rotating Disk”. In: *Journal of Applied Physics* 29.5 (1958), pp. 858–862. DOI: `10.1063/1.1723300`.

[189] D. Meyerhofer. “Characteristics of resist films produced by spinning”. In: *Journal of Applied Physics* 49.7 (1978), pp. 3993–3997. DOI: `10.1063/1.325357`.

[190] N. J. Jeon et al. “Solvent engineering for high-performance inorganic–organic hybrid perovskite solar cells”. In: *Nature Materials* 13.9 (2014), pp. 897–903. DOI: `10.1038/nmat4014`.

[191] H. Taherianfard et al. “Effective Management of Nucleation and Crystallization Processes in Perovskite Formation via Facile Control of Antisolvent Temperature”. In: *ACS Applied Energy Materials* 3.2 (2020), pp. 1506–1514. DOI: `10.1021/acsaem.9b01916`.

[192] H. Li et al. “High-Efficiency and Stable Perovskite Solar Cells Prepared Using Chlorobenzene/Acetonitrile Antisolvent”. In: *ACS Appl. Mater. Interfaces* 11.38 (2019), pp. 34989–34996. DOI: `10.1021/acsami.9b12323`.

[193] A. Saadawy et al. “Temperature-Dependent Crystallization in Two-Step Perovskite Deposition Revealed by In Situ GIWAXS and Machine Learning-Guided Analysis”. In: *Advanced Functional Materials* (2026). DOI: `10.1002/adfm.202527797`.

[194] J.-W. Lee et al. “Two-step deposition method for high-efficiency perovskite solar cells”. In: *MRS Bulletin* 40.8 (2015), pp. 654–659. DOI: `10.1557/mrs.2015.166`.

[195] Q. Jiang et al. “Planar-Structure Perovskite Solar Cells with Efficiency beyond 21%”. In: *Advanced Materials* 29.46 (2017), p. 1703852. DOI: `10.1002/adma.201703852`.

[196] Z. Wu et al. “Scalable Two-Step Production of High-Efficiency Perovskite Solar Cells and Modules”. In: *Solar RRL* 7.1 (2022). DOI: `10.1002/solr.202200571`.

[197] D. M. Mattox. “Introduction”. In: *Handbook of Physical Vapor Deposition (PVD) Processing*. Elsevier, 2010, pp. 1–24. DOI: `10.1016/b978-0-8155-2037-5.00001-0`.

[198] L. Sun et al. “Chemical vapour deposition”. In: *Nature Reviews Methods Primers* 1.1 (2021). DOI: `10.1038/s43586-020-00005-y`.

[199] F. Lévy. “Film Growth and Epitaxy: Methods”. In: *Reference Module in Materials Science and Materials Engineering*. Elsevier, 2016, pp. 210–222. DOI: `10.1016/b978-0-12-803581-8.01012-2`.

[200] J. T. Gudmundsson et al. “Foundations of physical vapor deposition with plasma assistance”. In: *Plasma Sources Science and Technology* 31.8 (2022), p. 083001. DOI: `10.1088/1361-6595/ac7f53`.

[201] V. Cremers et al. “Conformality in atomic layer deposition: Current status overview of analysis and modelling”. In: *Applied Physics Reviews* 6.2 (2019). DOI: `10.1063/1.5060967`.

[202] D. Barrit et al. “Hybrid perovskite solar cells: In situ investigation of solution-processed PbI_2 reveals metastable precursors and a pathway to producing porous thin films”. In: *Journal of Materials Research* 32.10 (2017), pp. 1899–1907. DOI: `10.1557/jmr.2017.117`.

[203] J. Ma et al. “Crystallization kinetics modulation and defect suppression of all-inorganic $CsPbX_3$ perovskite films”. In: *Energy & Environmental Science* 15.2 (2022), pp. 413–438. DOI: `10.1039/d1ee03192a`.

[204] J. Petry et al. “Benchmarking Inorganic Deposition Routes for Hybrid Two-Step Processed Perovskite Solar Cells: A Materials Perspective”. In: *Solar RRL* 10.4 (2026). DOI: `10.1002/solr.202500698`.

[205] F. U. Kosasih et al. “Thermal evaporation and hybrid deposition of perovskite solar cells and mini-modules”. In: *Joule* 6.12 (2022), pp. 2692–2734. DOI: `10.1016/j.joule.2022.11.004`.

[206] O. Er-raji et al. “Insights into Perovskite Film Formation Using the Hybrid Evaporation/Spin-Coating Route: An In Situ XRD Study”. In: *ACS Applied Energy Materials* 6.11 (2023), pp. 6183–6193. DOI: `10.1021/acsaem.3c00698`.

[207] J. Bing et al. “A Review on Halide Perovskite Film Formation by Sequential Solution Processing for Solar Cell Applications”. In: *Energy Technology* 8.4 (2019). DOI: `10.1002/ente.201901114`.

[208] E. Gutierrez-Partida et al. “Large-Grain Double Cation Perovskites with 18 μs Lifetime and High Luminescence Yield for Efficient Inverted Perovskite Solar Cells”. In: *ACS Energy Letters* 6.3 (2021), pp. 1045–1054. DOI: `10.1021/acsenergylett.0c02642`.

[209] M. Kim et al. “Methylammonium Chloride Induces Intermediate Phase Stabilization for Efficient Perovskite Solar Cells”. In: *Joule* 3.9 (2019), pp. 2179–2192. DOI: `10.1016/j.joule.2019.06.014`.

[210] J. A. Schwenzer. “Thermische Stabilität von Metall-Halogenid-Perowskit-Solarzellen”. de. PhD thesis. Karlsruher Institut für Technologie (KIT), 2020. DOI: `10.5445/IR/1000122117`.

[211] A. Al-Ashouri et al. “Conformal monolayer contacts with lossless interfaces for perovskite single junction and monolithic tandem solar cells”. In: *Energy & Environmental Science* 12.11 (2019), pp. 3356–3369. DOI: `10.1039/c9ee02268f`.

[212] L. Mao et al. “Fully Textured, Production-Line Compatible Monolithic Perovskite/Silicon Tandem Solar Cells Approaching 29% Efficiency”. In: *Advanced Materials* 34.40 (2022), p. 2206193. DOI: `10.1002/adma.202206193`.

[213] Fluxim AG. *Characterization Techniques For Organic and Perovskite Solar Cells*. Accessed October 2025. URL: `https://www.fluxim.com/measurement-techniques-perovskite-solar-cells`.

[214] R. Patru et al. “Tetragonal-Cubic Phase Transition and Low-Field Dielectric Properties of $CH_3NH_3PbI_3$ Crystals”. In: *Materials* 14.15 (2021), p. 4215. DOI: `10.3390/ma14154215`.

[215] W. H. Miller. *A Treatise on Crystallography*. Cambridge: J. & J. J. Deighton, 1839.

[216] N. C. S. Vieira et al. “Indium tin oxide synthesized by a low cost route as SEGFET pH sensor”. In: *Materials Research* 16.5 (2013), pp. 1156–1160. DOI: `10.1590/s1516-14392013005000101`.

[217] Z. Dong et al. “Intermediate phase evolution for stable and oriented evaporated wide-bandgap perovskite solar cells”. In: *Nature Materials* (2025). DOI: `10.1038/s41563-025-02375-8`.

[218] P. Scherrer. “Bestimmung der Größe und der inneren Struktur von Kolloidteilchen mittels Röntgenstrahlen”. In: *Nachrichten von der Gesellschaft der Wissenschaften zu Göttingen, Mathematisch-Physikalische Klasse* 1918 (1918), pp. 98–100. URL: `http://eudml.org/doc/59018`.

[219] J. C. Fischer et al. “GIWAXS Characterization of Metal-Organic Framework Thin Films and Heterostructures: Quantifying Structure and Orientation”. In: *Advanced Materials Interfaces* 10.11 (2023). DOI: `10.1002/admi.202202259`.

[220] Z. Jiang. “GIXSGUI: a MATLAB toolbox for grazing-incidence X-ray scattering data visualization and reduction, and indexing of buried three-dimensional periodic nanostructured films”. In: *Journal of Applied Crystallography* 48.3 (2015), pp. 917–926. DOI: `10.1107/s1600576715004434`.

[221] A. Dolgonos et al. “Direct optical band gap measurement in polycrystalline semiconductors: A critical look at the Tauc method”. In: *Journal of Solid State Chemistry* 240 (2016), pp. 43–48. DOI: `10.1016/j.jssc.2016.05.010`.

[222] L. Krückemeier et al. “How to Report Record Open-Circuit Voltages in Lead-Halide Perovskite Solar Cells”. In: *Adv. Energy Mater.* 10, (2020), p. 1902573. DOI: `10.1002/aenm.201902573`.

[223] IEC. *Photovoltaic devices - Part 3: Measurement principles for terrestrial photovoltaic (PV) solar devices with reference spectral irradiance data*. 4th ed. IEC 60904-3, 2019.

[224] National Laboratory of the Rockies (NLR). *Reference Air Mass 1.5 Spectra*. Accessed March 2026. URL: `https://www.nlr.gov/grid/solar-resource/spectra-am1.5.html`.

[225] H. J. Snaith et al. “Anomalous Hysteresis in Perovskite Solar Cells”. In: *The Journal of Physical Chemistry Letters* 5.9 (2014), pp. 1511–1515. DOI: `10.1021/jz500113x`.

[226] M. V. Khenkin et al. “Consensus statement for stability assessment and reporting for perovskite photovoltaics based on ISOS procedures”. In: *Nature Energy* 5.1 (2020), pp. 35–49. DOI: `10.1038/s41560-019-0529-5`.

[227] H.-f. Meng et al. “Research on integrated system for solar simulator performance calibration according to IEC 60904-9”. In: *2011 International Conference on Optical Instruments and Technology: Optoelectronic Measurement Technology and Systems*. SPIE, 2011. DOI: `10.1117/12.916693`.

[228] C. H. Seaman. “Calibration of solar cells by the reference cell method – The spectral mismatch problem”. In: *Solar Energy* 29.4 (1982), pp. 291–298. DOI: `10.1016/0038-092x(82)90244-4`.

[229] J. Hohl-Eibinger et al. “Uncertainty of the spectral mismatch correction factor in STC measurements on photovoltaic devices”. In: *Progress in Photovoltaics: Research and Applications* 19.5 (2011), pp. 573–579. DOI: `10.1002/pip.1059`.

[230] T. Kirchartz et al. “What Makes a Good Solar Cell?” In: *Advanced Energy Materials* 8.28 (2018). DOI: `10.1002/aenm.201703385`.

[231] U. Rau et al. “Efficiency Potential of Photovoltaic Materials and Devices Unveiled by Detailed-Balance Analysis”. In: *Physical Review Applied* 7.4 (2017), p. 044016. DOI: `10.1103/physrevapplied.7.044016`.

[232] M. Stolterfoht et al. “How To Quantify the Efficiency Potential of Neat Perovskite Films: Perovskite Semiconductors with an Implied Efficiency Exceeding 28%”. In: *Advanced Materials* 32.17 (2020), p. 2000080. DOI: `10.1002/adma.202000080`.

[233] L. Krückemeier et al. “How to Report Record Open-Circuit Voltages in Lead-Halide Perovskite Solar Cells”. In: *Advanced Energy Materials* 10.1 (2019), p. 1902573. DOI: `10.1002/aenm.201902573`.

[234] P. Fassl et al. “Revealing the internal luminescence quantum efficiency of perovskite films via accurate quantification of photon recycling”. In: *Matter* 4.4 (2021), pp. 1391–1412. DOI: `10.1016/j.matt.2021.01.019`.

[235] M. Workman et al. “Ideality Factor Based Computational Analysis of Perovskite Solar Cells”. In: *2021 IEEE Conference on Technologies for Sustainability (SusTech)*. IEEE, 2021. DOI: `10.1109/sustech51236.2021.9467471`.

[236] B. L. Welch. “THE GENERALIZATION OF ‘STUDENT’S’ PROBLEM WHEN SEVERAL DIFFERENT POPULATION VARLANCES ARE INVOLVED”. In: *Biometrika* 34.1-2 (1947), pp. 28–35. DOI: `10.1093/biomet/34.1-2.28`.

[237] G. D. Ruxton. “The unequal variance t-test is an underused alternative to Student’s t-test and the Mann–Whitney U test”. In: *Behavioral Ecology* 17.4 (2006), pp. 688–690. DOI: `10.1093/beheco/ark016`.

[238] B. Derrick et al. “Why Welch’s test is Type I error robust”. In: *The Quantitative Methods for Psychology* 12.1 (2016), pp. 30–38. DOI: `10.20982/tqmp.12.1.p030`.

[239] R. Pappenberger et al. “Bandgap Engineering of Two-Step Processed Perovskite Top Cells for Perovskite-Based Tandem Photovoltaics”. In: *Advanced Functional Materials* 34.9 (2023). DOI: `10.1002/adfm.202311424`.

[240] Z. Wang et al. “Perovskite – a Perfect Top Cell for Tandem Devices to Break the S–Q Limit”. In: *Advanced Science* 6.7 (2019), p. 1801704. DOI: `10.1002/advs.201801704`.

[241] E. Aydin et al. “Interplay between temperature and bandgap energies on the outdoor performance of perovskite/silicon tandem solar cells”. In: *Nature Energy* 5.11 (2020), pp. 851–859. DOI: `10.1038/s41560-020-00687-4`.

[242] M. Jošt et al. “Textured interfaces in monolithic perovskite/silicon tandem solar cells: advanced light management for improved efficiency and energy yield”. In: *Energy & Environmental Science* 11.12 (2018), pp. 3511–3523. DOI: `10.1039/c8ee02469c`.

[243] S. Mariotti et al. “Interface engineering for high-performance, triple-halide perovskite-silicon tandem solar cells”. In: *Science* 381.6653 (2023), pp. 63–69. DOI: `10.1126/science.adf5872`.

[244] P. Zhao et al. “Antisolvent with an Ultrawide Processing Window for the One-Step Fabrication of Efficient and Large-Area Perovskite Solar Cells”. In: *Advanced Materials* 30.49 (2018). DOI: `10.1002/adma.201802763`.

[245] C.-C. Zhang et al. “Perovskite Films with Reduced Interfacial Strains via a Molecular-Level Flexible Interlayer for Photovoltaic Application”. In: *Advanced Materials* 32.38 (2020). DOI: `10.1002/adma.202001479`.

[246] W. Hui et al. “Stabilizing black-phase formamidinium perovskite formation at room temperature and high humidity”. In: *Science* 371.6536 (2021), pp. 1359–1364. DOI: `10.1126/science.abf7652`.

[247] P. Ahlawat et al. “A combined molecular dynamics and experimental study of two-step process enabling low-temperature formation of phase-pure α-$FAPbI_3$”. In: *Science Advances* 7.17 (2021). DOI: `10.1126/sciadv.abe3326`.

[248] J. H. Noh et al. “Chemical Management for Colorful, Efficient, and Stable Inorganic–Organic Hybrid Nanostructured Solar Cells”. In: *Nano Letters* 13.4 (2013), pp. 1764–1769. DOI: `10.1021/nl400349b`.

[249] T. Jesper Jacobsson et al. “Exploration of the compositional space for mixed lead halogen perovskites for high efficiency solar cells”. In: *Energy & Environmental Science* 9.5 (2016), pp. 1706–1724. DOI: `10.1039/c6ee00030d`.

[250] B. R. Sutherland et al. “Perovskite photonic sources”. In: *Nature Photonics* 10.5 (2016), pp. 295–302. DOI: `10.1038/nphoton.2016.62`.

[251] K. M. Yeom et al. “Recent Progress in Metal Halide Perovskite-Based Tandem Solar Cells”. In: *Advanced Materials* 32.51 (2020). DOI: `10.1002/adma.202002228`.

[252] E. T. Hoke et al. “Reversible photo-induced trap formation in mixed-halide hybrid perovskites for photovoltaics”. In: *Chemical Science* 6.1 (2015), pp. 613–617. DOI: `10.1039/c4sc03141e`.

[253] S. Liu et al. “Triple-junction solar cells with cyanate in ultrawide bandgap perovskites”. In: *Nature* (2024). DOI: `10.1038/s41586-024-07226-1`.

[254] A. J. Knight et al. “Halide Segregation in Mixed-Halide Perovskites: Influence of A-Site Cations”. In: *ACS Energy Letters* 6.2 (2021), pp. 799–808. DOI: `10.1021/acsenergylett.0c02475`.

[255] Z. Zhang et al. “Suppression of phase segregation in wide-bandgap perovskites with thiocyanate ions for perovskite/organic tandems with 25.06% efficiency”. In: *Nature Energy* 9.5 (2024), pp. 592–601. DOI: `10.1038/s41560-024-01491-0`.

[256] Y. Guo et al. “Unveiling the impact of photoinduced halide segregation on performance degradation in wide-bandgap perovskite solar cells”. In: *Energy & Environmental Science* 18.5 (2025), pp. 2308–2317. DOI: `10.1039/d4ee05604c`.

[257] W. Wang et al. “Effective Control of the Growth and Photoluminescence Properties of $CsPbBr_3$/Cs_4PbBr_6 Nanocomposites by Solvent Engineering”. In: *ACS Omega* 4.22 (Nov. 2019), pp. 19641–19646. DOI: `10.1021/acsomega.9b02248`.

[258] X. Cao et al. “Achieving one-step solution deposition of high quality $CsPbBr_3$ films for efficient solar cells through halide ion exchange”. In: *Journal of Alloys and Compounds* 919 (2022), p. 165722. DOI: `10.1016/j.jallcom.2022.165722`.

[259] G. Mahmoudi et al. “Inorganic–organic hybrid materials based on $PbBr_2$ and pyridine–hydrazone blocks – structural and theoretical study”. In: *RSC Advances* 6.65 (2016), pp. 60385–60393. DOI: `10.1039/c6ra13462a`.

[260] A. Jana et al. “Solvent-free, mechanochemical syntheses of bulk trihalide perovskites and their nanoparticles”. In: *Chemical Communications* 53.21 (2017), pp. 3046–3049. DOI: `10.1039/c7cc00666g`.

[261] G. Zeng et al. “Hexamethylphosphoramide-Assisted Structure and Morphology Regulation of a PbI_2 Film for Air-Processed Efficient Perovskite Solar Cells via a Two-Step Deposition Method”. In: *ACS Sustainable Chemistry & Engineering* (2023). DOI: `10.1021/acssuschemeng.2c07526`.

[262] H.-Y. Wang et al. “Adverse Effects of Excess Residual PbI_2 on Photovoltaic Performance, Charge Separation, and Trap-State Properties in Mesoporous Structured Perovskite Solar Cells”. In: *Chemistry - A European Journal* 23.16 (2017), pp. 3986–3992. DOI: `10.1002/chem.201605668`.

[263] S.-Y. Kim et al. “Perspective: Understanding of ripening growth model for minimum residual PbI_2 and its limitation in the planar perovskite solar cells”. In: *APL Materials* 4.10 (2016). DOI: `10.1063/1.4963841`.

[264] M. Sun et al. “Tailoring a dynamic crystalline process during the conversion of lead-halide perovskite layer to achieve high performance solar cells”. In: *Journal of Materials Chemistry A* 6.48 (2018), pp. 24793–24804. DOI: `10.1039/c8ta07462c`.

[265] J. Mo et al. “Enhanced efficiency of planar perovskite solar cells via a two-step deposition using DMF as an additive to optimize the crystal growth behavior”. In: *Journal of Materials Chemistry A* 5.25 (2017), pp. 13032–13038. DOI: `10.1039/c7ta01517h`.

[266] J. Wu et al. “DMF as an Additive in a Two-Step Spin-Coating Method for 20% Conversion Efficiency in Perovskite Solar Cells”. In: *ACS Applied Materials & Interfaces* 9.32 (2017), pp. 26937–26947. DOI: `10.1021/acsami.7b08504`.

[267] W. Zhou et al. “Light-Independent Ionic Transport in Inorganic Perovskite and Ultrastable Cs-Based Perovskite Solar Cells”. In: *The Journal of Physical Chemistry Letters* 8.17 (2017), pp. 4122–4128. DOI: `10.1021/acs.jpclett.7b01851`.

[268] D. W. deQuilettes et al. “Photo-induced halide redistribution in organic–inorganic perovskite films”. In: *Nature Communications* 7.1 (2016). DOI: `10.1038/ncomms11683`.

[269] C. Eames et al. “Ionic transport in hybrid lead iodide perovskite solar cells”. In: *Nature Communications* 6.1 (2015). DOI: `10.1038/ncomms8497`.

[270] N. Li et al. “Microscopic Degradation in Formamidinium-Cesium Lead Iodide Perovskite Solar Cells under Operational Stressors”. In: *Joule* 4.8 (2020), pp. 1743–1758. DOI: `10.1016/j.joule.2020.06.005`.

[271] M. Yavari et al. “A synergistic Cs_2CO_3 ETL treatment to incorporate Cs cation into perovskite solar cells *via* two-step scalable fabrication”. In: *Journal of Materials Chemistry C* 9.12 (2021), pp. 4367–4377. DOI: `10.1039/d0tc05877g`.

[272] W. Yang et al. “Unlocking Voltage Potentials of Mixed-Halide Perovskite Solar Cells via Phase Segregation Suppression”. In: *Advanced Functional Materials* 32.12 (2021), p. 2110698. DOI: `10.1002/adfm.202110698`.

[273] S. Zhang et al. “Defect/Interface Recombination Limited Quasi-Fermi Level Splitting and Open-Circuit Voltage in Mono- and Triple-Cation Perovskite Solar Cells”. In: *ACS Applied Materials & Interfaces* 12.33 (2020), pp. 37647–37656. DOI: `10.1021/acsami.0c02960`.

[274] J. Barbé et al. “Localized effect of PbI_2 excess in perovskite solar cells probed by high-resolution chemical-optoelectronic mapping”. In: *Journal of Materials Chemistry A* 6.45 (2018), pp. 23010–23018. DOI: `10.1039/c8ta09536a`.

[275] Y. Shi et al. “(3-Aminopropyl)trimethoxysilane Surface Passivation Improves Perovskite Solar Cell Performance by Reducing Surface Recombination Velocity”. In: *ACS Energy Letters* 7.11 (2022), pp. 4081–4088. DOI: `10.1021/acsenergylett.2c01766`.

[276] C. M. Wolff et al. “Orders of Recombination in Complete Perovskite Solar Cells – Linking Time-Resolved and Steady-State Measurements”. In: *Advanced Energy Materials* 11.45 (2021), p. 2101823. DOI: `10.1002/aenm.202101823`.

[277] N. E. Courtier. “Interpreting Ideality Factors for Planar Perovskite Solar Cells: Ectypal Diode Theory for Steady-State Operation”. In: *Physical Review Applied* 14.2 (2020), p. 024031. DOI: `10.1103/physrevapplied.14.024031`.

[278] M. A. Green et al. “Pushing to the Limit: Radiative Efficiencies of Recent Mainstream and Emerging Solar Cells”. In: *ACS Energy Letters* 4.7 (2019), pp. 1639–1644. DOI: `10.1021/acsenergylett.9b01128`.

[279] P. Caprioglio et al. “On the Origin of the Ideality Factor in Perovskite Solar Cells”. In: *Advanced Energy Materials* 10.27 (2020). DOI: `10.1002/aenm.202000502`.

[280] Y. Zhao et al. “Effects of ion migration and improvement strategies for the operational stability of perovskite solar cells”. In: *Physical Chemistry Chemical Physics* 23.1 (2021), pp. 94–106. DOI: `10.1039/d0cp04418k`.

[281] D.-H. Kang et al. “On the Current-Voltage Hysteresis in Perovskite Solar Cells: Dependence on Perovskite Composition and Methods to Remove Hysteresis”. In: *Advanced Materials* 31.34 (2019). DOI: `10.1002/adma.201805214`.

[282] Z. Song et al. “Inverted Wide-Bandgap 2D/3D Perovskite Solar Cells with > 22% Efficiency and Low Voltage Loss”. In: *Nano Letters* 23.14 (2023), pp. 6705–6712. DOI: `10.1021/acs.nanolett.3c01962`.

[283] Q. Cui et al. “Developing a Two-Step Sequential Deposition Approach for Wide-Bandgap Perovskite Thin Films and Efficient Tandem Solar Cells”. In: *EU PVSEC 2025*. 2025.

[284] S. Luo et al. “Boron-halide interactions for crystallization regulation of a 1.68 eV wide-bandgap perovskite prepared via a two-step method”. In: *Energy & Environmental Science* 18.24 (2025), pp. 10364–10379. DOI: `10.1039/d5ee03984c`.

[285] R. Pappenberger et al. “Versatile Two-Step Process for Perovskite-Based Tandem Photovoltaics”. In: *Solar RRL* 9.13 (2025). DOI: `10.1002/solr.202500193`.

[286] G. Yang et al. “Defect engineering in wide-bandgap perovskites for efficient perovskite-silicon tandem solar cells”. In: *Nature Photonics* 16.8 (2022), pp. 588–594. DOI: `10.1038/s41566-022-01033-8`.

[287] S. Zhang et al. “Minimizing buried interfacial defects for efficient inverted perovskite solar cells”. In: *Science* 380.6643 (2023), pp. 404–409. DOI: `10.1126/science.adg3755`.

[288] D. Menzel et al. “Field Effect Passivation in Perovskite Solar Cells by a LiF Interlayer”. In: *Advanced Energy Materials* 12.30 (2022), p. 2201109. DOI: `10.1002/aenm.202201109`.

[289] Y. Shao et al. “Grain boundary dominated ion migration in polycrystalline organic-inorganic halide perovskite films”. In: *Energy & Environmental Science* 9.5 (2016), pp. 1752–1759. DOI: `10.1039/c6ee00413j`.

[290] J. S. Yun et al. “Critical Role of Grain Boundaries for Ion Migration in Formamidinium and Methylammonium Lead Halide Perovskite Solar Cells”. In: *Advanced Energy Materials* 6.13 (2016). DOI: `10.1002/aenm.201600330`.

[291] L. Liu et al. “Grain-Boundary Patches by In Situ Conversion to Enhance Perovskite Solar Cells Stability”. In: *Advanced Materials* 30.29 (2018). DOI: `10.1002/adma.201800544`.

[292] C. Ran et al. “Defects in metal triiodide perovskite materials towards high-performance solar cells: origin, impact, characterization, and engineering”. In: *Chemical Society Reviews* 47.12 (2018), pp. 4581–4610. DOI: `10.1039/c7cs00868f`.

[293] S. G. Motti et al. “Controlling competing photochemical reactions stabilizes perovskite solar cells”. In: *Nature Photonics* 13.8 (2019), pp. 532–539. DOI: `10.1038/s41566-019-0435-1`.

[294] N. Phung et al. “The Role of Grain Boundaries on Ionic Defect Migration in Metal Halide Perovskites”. In: *Advanced Energy Materials* 10.20 (2020). DOI: `10.1002/aenm.201903735`.

[295] L. McGovern et al. “Grain Size Influences Activation Energy and Migration Pathways in $MAPbBr_3$ Perovskite Solar Cells”. In: *The Journal of Physical Chemistry Letters* 12.9 (2021), pp. 2423–2428. DOI: `10.1021/acs.jpclett.1c00205`.

[296] Z. Fang et al. “Defects in perovskite crystals”. In: *Journal of Semiconductors* 44.8 (2023), p. 080201. DOI: `10.1088/1674-4926/44/8/080201`.

[297] S. Akin et al. “New Strategies for Defect Passivation in High-Efficiency Perovskite Solar Cells”. In: *Advanced Energy Materials* 10.13 (2019). DOI: `10.1002/aenm.201903090`.

[298] E. Aydin et al. “Defect and Contact Passivation for Perovskite Solar Cells”. In: *Advanced Materials* 31.25 (2019). DOI: `10.1002/adma.201900428`.

[299] F. Gao et al. “Recent Progresses on Defect Passivation toward Efficient Perovskite Solar Cells”. In: *Advanced Energy Materials* 10.13 (2019). DOI: `10.1002/aenm.201902650`.

[300] J. Dagar et al. “Compositional and Interfacial Engineering Yield High-Performance and Stable p-i-n Perovskite Solar Cells and Mini-Modules”. In: *ACS Applied Materials & Interfaces* 13.11 (2021), pp. 13022–13033. DOI: `10.1021/acsami.0c17893`.

[301] Y. Hou et al. “Efficient tandem solar cells with solution-processed perovskite on textured crystalline silicon”. In: *Science* 367.6482 (2020), pp. 1135–1140. DOI: `10.1126/science.aaz3691`.

[302] E. Aydin et al. “Enhanced optoelectronic coupling for perovskite/silicon tandem solar cells”. In: *Nature* 623.7988 (2023), pp. 732–738. DOI: `10.1038/s41586-023-06667-4`.

[303] P. Tockhorn et al. “Nano-optical designs for high-efficiency monolithic perovskite-silicon tandem solar cells”. In: *Nature Nanotechnology* 17.11 (2022), pp. 1214–1221. DOI: `10.1038/s41565-022-01228-8`.

[304] S.-G. Choi et al. “LiF in Inverted Perovskite Solar Cells: Dipole or Doping?” In: *ACS Energy Letters* (2024), pp. 5360–5363. DOI: `10.1021/acsenergylett.4c02000`.

[305] B. Li et al. “Improving the stability of inverted perovskite solar cells towards commercialization”. In: *Communications Materials* 3.1 (2022). DOI: `10.1038/s43246-022-00291-x`.

[306] C. Yang et al. “Achievements, challenges, and future prospects for industrialization of perovskite solar cells”. In: *Light: Science & Applications* 13.1 (2024). DOI: `10.1038/s41377-024-01461-x`.

[307] M. K. Rao et al. “Review on persistent challenges of perovskite solar cells‘ stability”. In: *Solar Energy* 218 (2021), pp. 469–491. DOI: `10.1016/j.solener.2021.03.005`.

[308] D. Wang et al. “Stability of perovskite solar cells”. In: *Solar Energy Materials and Solar Cells* 147 (2016), pp. 255–275. DOI: `10.1016/j.solmat.2015.12.025`.

[309] S. Hu et al. “Optimized carrier extraction at interfaces for 23.6% efficient tin-lead perovskite solar cells”. In: *Energy & Environmental Science* 15.5 (2022), pp. 2096–2107. DOI: `10.1039/d2ee00288d`.

[310] C. Quarti et al. “Influence of Surface Termination on the Energy Level Alignment at the $CH_3NH_3PbI_3$ Perovskite/C_{60} Interface”. In: *Chemistry of Materials* 29.3 (2017), pp. 958–968. DOI: `10.1021/acs.chemmater.6b03259`.

[311] H. Chen et al. “Regulating surface potential maximizes voltage in all-perovskite tandems”. In: *Nature* 613.7945 (2022), pp. 676–681. DOI: `10.1038/s41586-022-05541-z`.

[312] Y.-W. Jang et al. “Intact 2D/3D halide junction perovskite solar cells via solid-phase in-plane growth”. In: *Nature Energy* 6.1 (2021), pp. 63–71. DOI: `10.1038/s41560-020-00749-7`.

[313] Z. Zhang et al. “Rationalization of passivation strategies toward high-performance perovskite solar cells”. In: *Chemical Society Reviews* 52.1 (2023), pp. 163–195. DOI: `10.1039/d2cs00217e`.

[314] X. Xu et al. “The Role of Diammonium Cation on the Structural and Optoelectronic Properties in 3D Cesium-Formamidinium Mixed-Cation Perovskite Solar Cells”. In: *Solar RRL* 3.8 (2019). DOI: `10.1002/solr.201900140`.

[315] S. Akin et al. “Organic Ammonium Halide Modulators as Effective Strategy for Enhanced Perovskite Photovoltaic Performance”. In: *Advanced Science* 8.10 (2021). DOI: `10.1002/advs.202004593`.

[316] T. Duong et al. “High Efficiency Perovskite-Silicon Tandem Solar Cells: Effect of Surface Coating versus Bulk Incorporation of 2D Perovskite”. In: *Advanced Energy Materials* 10.9 (2020). DOI: `10.1002/aenm.201903553`.

[317] D. S. Lee et al. “Passivation of Grain Boundaries by Phenethylammonium in Formamidinium-Methylammonium Lead Halide Perovskite Solar Cells”. In: *ACS Energy Letters* 3.3 (2018), pp. 647–654. DOI: `10.1021/acsenergylett.8b00121`.

[318] J.-W. Lee et al. “2D perovskite stabilized phase-pure formamidinium perovskite solar cells”. In: *Nature Communications* 9.1 (2018). DOI: `10.1038/s41467-018-05454-4`.

[319] M. Jung et al. “Structural features and their functions in surfactant-armoured methylammonium lead iodide perovskites for highly efficient and stable solar cells”. In: *Energy & Environmental Science* 11.8 (2018), pp. 2188–2197. DOI: `10.1039/c8ee00995c`.

[320] Z. Wang et al. “Efficient ambient-air-stable solar cells with 2D-3D heterostructured butylammonium-caesium-formamidinium lead halide perovskites”. In: *Nature Energy* 2.9 (2017). DOI: `10.1038/nenergy.2017.135`.

[321] D. H. Kim et al. “Bimolecular Additives Improve Wide-Band-Gap Perovskites for Efficient Tandem Solar Cells with CIGS”. In: *Joule* 3.7 (2019), pp. 1734–1745. DOI: `10.1016/j.joule.2019.04.012`.

[322] C. Fei et al. “Self-assembled propylammonium cations at grain boundaries and the film surface to improve the efficiency and stability of perovskite solar cells”. In: *Journal of Materials Chemistry A* 7.41 (2019), pp. 23739–23746. DOI: `10.1039/c9ta01755k`.

[323] X. Li et al. “Negative Pressure Engineering with Large Cage Cations in 2D Halide Perovskites Causes Lattice Softening”. In: *Journal of the American Chemical Society* 142.26 (2020), pp. 11486–11496. DOI: `10.1021/jacs.0c03860`.

[324] F. Bella et al. “Caesium for Perovskite Solar Cells: An Overview”. In: *Chemistry – A European Journal* 24.47 (2018), pp. 12183–12205. DOI: `10.1002/chem.201801096`.

[325] J.-W. Lee et al. “Rethinking the A cation in halide perovskites”. In: *Science* 375.6583 (2022). DOI: `10.1126/science.abj1186`.

[326] Y. Zheng et al. “Dual-Interface Modification for Inverted Methylammonium-Free Perovskite Solar Cells of 25.35% Efficiency with Balanced Crystallization”. In: *Advanced Energy Materials* 14.20 (2024). DOI: `10.1002/aenm.202304486`.

[327] B. Conings et al. “Intrinsic Thermal Instability of Methylammonium Lead Trihalide Perovskite”. In: *Advanced Energy Materials* 5.15 (2015). DOI: `10.1002/aenm.201500477`.

[328] E. J. Juarez-Perez et al. “Thermal degradation of $CH_3NH_3PbI_3$ perovskite into NH_3 and CH_3I gases observed by coupled thermogravimetry mass spectrometry analysis”. In: *Energy & Environmental Science* 9.11 (2016), pp. 3406–3410. DOI: `10.1039/c6ee02016j`.

[329] G. E. Eperon et al. “Formamidinium lead trihalide: a broadly tunable perovskite for efficient planar heterojunction solar cells”. In: *Energy & Environmental Science* 7.3 (2014), p. 982. DOI: `10.1039/c3ee43822h`.

[330] D. P. McMeekin et al. “A mixed-cation lead mixed-halide perovskite absorber for tandem solar cells”. In: *Science* 351.6269 (2016), pp. 151–155. DOI: `10.1126/science.aad5845`.

[331] S. Sidhik et al. “Deterministic fabrication of 3D/2D perovskite bilayer stacks for durable and efficient solar cells”. In: *Science* 377.6613 (2022), pp. 1425–1430. DOI: `10.1126/science.abq7652`.

[332] A. R. b. Mohd Yusoff et al. “Passivation and process engineering approaches of halide perovskite films for high efficiency and stability perovskite solar cells”. In: *Energy & Environmental Science* 14.5 (2021), pp. 2906–2953. DOI: `10.1039/d1ee00062d`.

[333] G. Niu et al. “Controlled orientation of perovskite films through mixed cations toward high performance perovskite solar cells”. In: *Nano Energy* 27 (2016), pp. 87–94. DOI: `10.1016/j.nanoen.2016.06.053`.

[334] R. Szostak et al. “Revealing the Perovskite Film Formation Using the Gas Quenching Method by In Situ GIWAXS: Morphology, Properties, and Device Performance”. In: *Advanced Functional Materials* 31.4 (2020). DOI: `10.1002/adfm.202007473`.

[335] C. Wang et al. “Low-Temperature Processed, Efficient, and Highly Reproducible Cesium-Doped Triple Cation Perovskite Planar Heterojunction Solar Cells”. In: *Solar RRL* 2.2 (2018), p. 1700209. DOI: `10.1002/solr.201700209`.

[336] G. Zhou et al. “Application of Cesium on the Restriction of Precursor Crystallization for Highly Reproducible Perovskite Solar Cells Exceeding 20% Efficiency”. In: *ACS Applied Materials & Interfaces* 10.11 (2018), pp. 9503–9513. DOI: `10.1021/acsami.8b01054`.

[337] M.Saliba et al. “Cesium-containing triple cation perovskite solar cells: improved stability, reproducibility and high efficiency”. In: *Energy & Environmental Science* 9.6 (2016), pp. 1989–1997. DOI: `10.1039/c5ee03874j`.

[338] N. Cheng et al. “Simultaneous Incorporation of CsI in the Two-step Deposition Process Boosts the Power Conversion Efficiency and Stability of Perovskite Solar Cells”. In: *ChemPhysChem* 25.3 (2023). DOI: `10.1002/cphc.202300599`.

[339] M. A. Green et al. “Solar Cell Efficiency Tables (Version 66)”. In: *Progress in Photovoltaics: Research and Applications* 33.7 (2025), pp. 795–810. DOI: `10.1002/pip.3919`.

[340] N. Zhou et al. “CsI Pre-Intercalation in the Inorganic Framework for Efficient and Stable $FA_{1\text{-}x}Cs_xPb_3(Cl)$ Perovskite Solar Cells”. In: *Small* 13.23 (2017), p. 1700484. DOI: `10.1002/smll.201700484`.

[341] T. Liu et al. “Cesium Halides-Assisted Crystal Growth of Perovskite Films for Efficient Planar Heterojunction Solar Cells”. In: *Chemistry of Materials* 30.15 (2018), pp. 5264–5271. DOI: `10.1021/acs.chemmater.8b02002`.

[342] A. Farag et al. “Efficient Light Harvesting in Thick Perovskite Solar Cells Processed on Industry-Applicable Random Pyramidal Textures”. In: *ACS Applied Energy Materials* 5.6 (2022), pp. 6700–6708. DOI: `10.1021/acsaem.1c04028`.

[343] M. A. Mahmud et al. “Double-Sided Surface Passivation of 3D Perovskite Film for High-Efficiency Mixed-Dimensional Perovskite Solar Cells”. In: *Advanced Functional Materials* 30.7 (2019). DOI: `10.1002/adfm.201907962`.

[344] M. Malekshahi Byranvand et al. “Chemical vapor deposited polymer layer for efficient passivation of planar perovskite solar cells”. In: *Journal of Materials Chemistry A* 8.38 (2020), pp. 20122–20132. DOI: `10.1039/d0ta06646j`.

[345] J. Peng et al. “Nanoscale localized contacts for high fill factors in polymer-passivated perovskite solar cells”. In: *Science* 371.6527 (2021), pp. 390–395. DOI: `10.1126/science.abb8687`.

[346] B. G. H. M. Groeneveld et al. “Stable Cesium Formamidinium Lead Halide Perovskites: A Comparison of Photophysics and Phase Purity in Thin Films and Single Crystals”. In: *Energy Technology* 8.4 (2019). DOI: `10.1002/ente.201901041`.

[347] D. Prochowicz et al. “Engineering of Perovskite Materials Based on Formamidinium and Cesium Hybridization for High-Efficiency Solar Cells”. In: *Chemistry of Materials* 31.5 (2019), pp. 1620–1627. DOI: `10.1021/acs.chemmater.8b04871`.

[348] W. Ke et al. “Narrow-Bandgap Mixed Lead/Tin-Based 2D Dion-Jacobson Perovskites Boost the Performance of Solar Cells”. In: *Journal of the American Chemical Society* 142.35 (2020), pp. 15049–15057. DOI: `10.1021/jacs.0c06288`.

[349] N. Yan et al. “Ligand-Anchoring-Induced Oriented Crystal Growth for High-Efficiency Lead-Tin Perovskite Solar Cells”. In: *Advanced Functional Materials* 32.27 (2022). DOI: `10.1002/adfm.202201384`.

[350] X. Zhang et al. “Orientation Regulation of Phenylethylammonium Cation Based 2D Perovskite Solar Cell with Efficiency Higher Than 11%”. In: *Advanced Energy Materials* 8.14 (2018). DOI: `10.1002/aenm.201702498`.

[351] T. Niu et al. “Spacer Engineering of Diammonium-Based 2D Perovskites toward Efficient and Stable 2D/3D Heterostructure Perovskite Solar Cells”. In: *Advanced Energy Materials* 12.2 (2021). DOI: `10.1002/aenm.202102973`.

[352] S. Li et al. “Interfacial Structure and Composition Managements for High-Performance Methylammonium-Free Perovskite Solar Cells”. In: *Advanced Functional Materials* 30.52 (2020). DOI: `10.1002/adfm.202005846`.

[353] Z. Zhang et al. “Anti-solvent engineering for efficient and stable perovskite solar cells with preferentially orientated 2-dimensional/3-dimensional heterojunctions”. In: *Energy & Environmental Science* 18.7 (2025), pp. 3223–3234. DOI: `10.1039/d4ee05879h`.

[354] L. Zhang et al. “Surface Defect Passivation of Pb-Sn-Alloyed Perovskite Film by 1,3-Propanediammonium Iodide toward High-Performance Photovoltaic Devices”. In: *Solar RRL* 5.8 (2021). DOI: `10.1002/solr.202100299`.

[355] S. Sidhik et al. “Two-dimensional perovskite templates for durable, efficient formamidinium perovskite solar cells”. In: *Science* 384.6701 (2024), pp. 1227–1235. DOI: `10.1126/science.abq6993`.

[356] J. Wang et al. “Unraveling the Molecular Size Effect on Surface Engineering of Perovskite Solar Cells”. In: *Small Methods* (2024). DOI: `10.1002/smtd.202400043`.

[357] J. Heo et al. “Interfacial modification of wide-bandgap perovskite solar cell approaching 20% with organic hole transport material”. In: *Chemical Engineering Journal* 474 (2023), p. 145632. DOI: `10.1016/j.cej.2023.145632`.

[358] S. Teale et al. “Molecular cation and low-dimensional perovskite surface passivation in perovskite solar cells”. In: *Nature Energy* 9.7 (2024), pp. 779–792. DOI: `10.1038/s41560-024-01529-3`.

[359] B. Gogoi et al. “Understanding the crystallization of triple-cation perovskites assisted by mixed antisolvents for improved solar cell device performance”. In: *Journal of Materials Science: Materials in Electronics* 33.7 (2022), pp. 4415–4425. DOI: `10.1007/s10854-021-07633-4`.

[360] X. Zheng et al. “The Controlling Mechanism for Potential Loss in $CH_3NH_3PbBr_3$ Hybrid Solar Cells”. In: *ACS Energy Letters* 1.2 (2016), pp. 424–430. DOI: `10.1021/acsenergylett.6b00215`.

[361] S. Shao et al. “Efficient Perovskite Solar Cells over a Broad Temperature Window: The Role of the Charge Carrier Extraction”. In: *Advanced Energy Materials* 7.22 (2017). DOI: `10.1002/aenm.201701305`.

[362] R. Singh et al. “Danger in the Dark: Stability of Perovskite Solar Cells with Varied Stoichiometries and Morphologies Stressed at Various Conditions”. In: *ACS Applied Materials & Interfaces* 16.21 (2024), pp. 27450–27462. DOI: `10.1021/acsami.4c04350`.

[363] K. Frohna et al. “The impact of interfacial quality and nanoscale performance disorder on the stability of alloyed perovskite solar cells”. In: *Nature Energy* 10.1 (2024), pp. 66–76. DOI: `10.1038/s41560-024-01660-1`.

[364] F. Scheler et al. “Correlation of Band Bending and Ionic Losses in 1.68 eV Wide Band Gap Perovskite Solar Cells”. In: *Advanced Energy Materials* 15.16 (2024). DOI: `10.1002/aenm.202404726`.

[365] F. Scheler et al. “How do diammonium iodide surface treatments accelerate degradation in perovskite solar cells?” In: *EU PVSEC 2025*. 2025.

[366] C. Kan et al. “Efficient and stable perovskite-silicon tandem solar cells with copper thiocyanate-embedded perovskite on textured silicon”. In: *Nat. Photonics* 19.1 (2024), pp. 63–70. DOI: `10.1038/s41566-024-01561-5`.

[367] D. Hauschild et al. “Impact of n-Butylammonium Bromide on the Chemical and Electronic Structure of Double-Cation Perovskite Thin Films”. In: *ACS Applied Materials & Interfaces* 13.44 (2021), pp. 53202–53210. DOI: `10.1021/acsami.1c15707`.

[368] R. A. Kerner et al. “Amine additive reactions induced by the soft Lewis acidity of Pb^{2+} in halide perovskites. Part II: impacts of amido Pb impurities in methylammonium lead triiodide thin films”. In: *Journal of Materials Chemistry C* 7.18 (2019), pp. 5244–5250. DOI: `10.1039/c8tc04872j`.

[369] P. K. Basu et al. “The effect of front pyramid heights on the efficiency of homogeneously textured inline-diffused screen-printed monocrystalline silicon wafer solar cells”. In: *Renewable Energy* 78 (2015), pp. 590–598. DOI: `10.1016/j.renene.2015.01.058`.

[370] P. K. Basu et al. “Liquid silicate additive for alkaline texturing of mono-Si wafers to improve process bath lifetime and reduce IPA consumption”. In: *Solar Energy Materials and Solar Cells* 113 (2013), pp. 37–43. DOI: `10.1016/j.solmat.2013.01.037`.

[371] S. C. Baker-Finch et al. “Reflection distributions of textured monocrystalline silicon: implications for silicon solar cells”. In: *Progress in Photovoltaics: Research and Applications* 21.5 (2012), pp. 960–971. DOI: `10.1002/pip.2186`.

[372] A. Farag et al. “Mitigation of Open-Circuit Voltage Losses in Perovskite Solar Cells Processed over Micrometer-Sized-Textured Si Substrates”. In: *Advanced Functional Materials* 33.3 (2022). DOI: `10.1002/adfm.202210758`.

[373] M. Jošt et al. “21.6%-Efficient Monolithic Perovskite/Cu(In,Ga)Se2 Tandem Solar Cells with Thin Conformal Hole Transport Layers for Integration on Rough Bottom Cell Surfaces”. In: *ACS Energy Letters* 4.2 (2019), pp. 583–590. DOI: `10.1021/acsenergylett.9b00135`.

[374] M. Roß et al. “Co-Evaporated Formamidinium Lead Iodide Based Perovskites with 1000 h Constant Stability for Fully Textured Monolithic Perovskite/Silicon Tandem Solar Cells”. In: *Advanced Energy Materials* 11.35 (2021). DOI: `10.1002/aenm.202101460`.

[375] B. Chen et al. “Blade-Coated Perovskites on Textured Silicon for 26%-Efficient Monolithic Perovskite/Silicon Tandem Solar Cells”. In: *Joule* 4.4 (2020), pp. 850–864. DOI: `10.1016/j.joule.2020.01.008`.

[376] A. Alasfour et al. “Sub-micrometer random-pyramid texturing of silicon solar wafers with excellent surface passivation and low reflectance”. In: *Solar Energy Materials and Solar Cells* 218 (2020), p. 110761. DOI: `10.1016/j.solmat.2020.110761`.

[377] K. Wang et al. “Efficiencies of perovskite hybrid solar cells influenced by film thickness and morphology of $CH_3NH_3PbI_{3-x}Cl_x$ layer”. In: *Organic Electronics* 21 (2015), pp. 19–26. DOI: `10.1016/j.orgel.2015.02.023`.

[378] J. Chen et al. “High-Performance Thickness Insensitive Perovskite Solar Cells with Enhanced Moisture Stability”. In: *Advanced Energy Materials* 8.23 (2018). DOI: `10.1002/aenm.201800438`.

[379] M. Rai et al. “Effect of Perovskite Thickness on Electroluminescence and Solar Cell Conversion Efficiency”. In: *The Journal of Physical Chemistry Letters* 11.19 (2020), pp. 8189–8194. DOI: `10.1021/acs.jpclett.0c02363`.

[380] C.-H. Hsieh et al. “Analysis of two-terminal perovskite/silicon tandem solar cells with differing texture structure, perovskite carrier lifetime, and tunneling junction quality”. In: *Journal of Applied Physics* 135.11 (2024). DOI: `10.1063/5.0193641`.

[381] L. Cojocaru et al. “Detailed Investigation of Evaporated Perovskite Absorbers with High Crystal Quality on Different Substrates”. In: *ACS Applied Materials & Interfaces* 10.31 (2018), pp. 26293–26302. DOI: `10.1021/acsami.8b07999`.

[382] M. Kroll et al. “Insights into the evaporation behaviour of FAI: material degradation and consequences for perovskite solar cells”. In: *Sustainable Energy & Fuels* 6.13 (2022), pp. 3230–3239. DOI: `10.1039/d2se00373b`.

[383] J. Borchert et al. “Impurity Tracking Enables Enhanced Control and Reproducibility of Hybrid Perovskite Vapor Deposition”. In: *ACS Applied Materials & Interfaces* 11.32 (2019), pp. 28851–28857. DOI: `10.1021/acsami.9b07619`.

[384] I. Levchuk et al. “Deciphering the Role of Impurities in Methylammonium Iodide and Their Impact on the Performance of Perovskite Solar Cells”. In: *Advanced Materials Interfaces* 3.22 (2016). DOI: `10.1002/admi.201600593`.

[385] K. P. S. Zanoni et al. “Photovoltaic Devices Using Sublimed Methylammonium Lead Iodide Perovskites: Long-Term Reproducible Processing”. In: *Solar RRL* 7.7 (2023). DOI: `10.1002/solr.202201073`.

[386] Q. Luo et al. “Combined evaporation-solution methodology for high-efficiency perovskite solar cells with exceptional reproducibility”. In: *Journal of Materials Chemistry A* (2025). DOI: `10.1039/d5ta03304g`.

[387] V. Škorjanc et al. “Seed Layers for Wide-Band Gap Coevaporated Perovskite Solar Cells: CsCl Regulates Band Gap and Reduces Process Variability”. In: *ACS Energy Letters* 9.11 (2024), pp. 5639–5646. DOI: `10.1021/acsenergylett.4c02173`.

[388] X. Liu et al. “Dominating (111) facets with ordered stacking in perovskite films”. In: *Energy & Environmental Science* 17.16 (2024), pp. 6058–6067. DOI: `10.1039/d4ee01863j`.

[389] K. Meng et al. “In Situ Observation of Crystallization Dynamics and Grain Orientation in Sequential Deposition of Metal Halide Perovskites”. In: *Advanced Functional Materials* 29.35 (2019). DOI: `10.1002/adfm.201902319`.

[390] B. Li et al. “Unraveling the Degradation Pathway of Inverted Perovskite Solar Cells Based on ISOS-D-1 Protocol”. In: *Small Methods* 8.2 (2023). DOI: `10.1002/smtd.202300223`.

[391] J. Petry et al. “Industrialization of perovskite solar cell fabrication: strategies to achieve high-throughput vapor deposition processes”. In: *EES Solar* 1.3 (2025), pp. 404–418. DOI: `10.1039/d5el00069f`.

[392] Erkan Aydin et al. “Pathways toward commercial perovskite/silicon tandem photovoltaics”. In: *Science* 383.6679 (2024), eadh3849. DOI: `10.1126/science.adh3849`.

[393] X. Zheng et al. “Solvent engineering for scalable fabrication of perovskite/silicon tandem solar cells in air”. In: *Nature Communications* 15.1 (2024). DOI: `10.1038/s41467-024-49351-5`.

[394] V. S. Nguyen et al. “Solvent-vapor assisted conversion process for hybrid perovskites coupling thermal evaporation and slot-die coating”. In: *Materials Science in Semiconductor Processing* 158 (2023), p. 107358. DOI: `10.1016/j.mssp.2023.107358`.

[395] X. Yu et al. “Interface modification effect on the performance of $Cs_xFA_{1-x}PbI_yBr_{3-y}$ perovskite solar cells fabricated by evaporation/spray-coating method”. In: *The Journal of Chemical Physics* 153.1 (2020). DOI: `10.1063/5.0012803`.

[396] L. Cojocaru et al. “Hybrid Evaporation/Spray-Coating Process for a Simplified and Controllable Production of Perovskite Solar Cells”. In: *IEEE Journal of Photovoltaics* 10.1 (2020), pp. 276–286. DOI: `10.1109/jphotov.2019.2949763`.

[397] O. Er-raji et al. “Coating dynamics in two-step hybrid evaporated/blade-coated perovskites for scalable fully-textured perovskite/silicon tandem solar cells”. In: *EES Solar* 1.3 (2025), pp. 419–430. DOI: `10.1039/d5el00073d`.

[398] A. Mahboubi Soufiani et al. “Sequentially Evaporated Wide Bandgap Perovskite Absorber for Large-Area and Reproducible Fabrication of Solar Cells”. In: *Solar RRL* 9.19 (2025). DOI: `10.1002/solr.202500412`.

[399] H. Luo et al. “Inorganic Framework Composition Engineering for Scalable Fabrication of Perovskite/Silicon Tandem Solar Cells”. In: *ACS Energy Letters* 8.12 (2023), pp. 4993–5002. DOI: `10.1021/acsenergylett.3c02002`.

[400] Y. Li et al. “CsCl induced efficient fully-textured perovskite/crystalline silicon tandem solar cell”. In: *Nano Energy* 122 (2024), p. 109285. DOI: `10.1016/j.nanoen.2024.109285`.

[401] Z. Xiong et al. “Constructing tin oxides Interfacial Layer with Gradient Compositions for Efficient Perovskite/Silicon Tandem Solar Cells with Efficiency Exceeding 28%”. In: *Small* 20.15 (2024), p. 2308024. DOI: `https://doi.org/10.1002/smll.202308024`.

[402] T. Yang et al. “Efficient and Stable Perovskite/Silicon Tandem Solar Cells Modulated with Triple-Functional Passivator”. In: *Advanced Energy Materials* 14.7 (2023), p. 2303149. DOI: `https://doi.org/10.1002/aenm.202303149`.

[403] Y. Sun et al. “Ionic Liquid Modified Polymer Intermediate Layer for Improved Charge Extraction toward Efficient and Stable Perovskite/Silicon Tandem Solar Cells”. In: *Small* 20.21 (2024), p. 2308553. DOI: `https://doi.org/10.1002/smll.202308553`.

[404] J. Chen et al. “Surface Molecular Engineering for Fully Textured Perovskite/Silicon Tandem Solar Cells”. In: *Angewandte Chemie International Edition* 63.36 (2024). DOI: `10.1002/anie.202407151`.

[405] A. A. Said et al. “Sublimed C_{60} for efficient and repeatable perovskite-based solar cells”. In: *Nature Communications* 15.1 (2024). DOI: `10.1038/s41467-024-44974-0`.

[406] Q. Wei et al. “Fusing Science with Industry: Perovskite Photovoltaics Moving Rapidly into Industrialization”. In: *Advanced Materials* 36.39 (2024). DOI: `10.1002/adma.202406295`.

[407] J. A. Steele et al. “How to GIWAXS: Grazing Incidence Wide Angle X-Ray Scattering Applied to Metal Halide Perovskite Thin Films”. In: *Advanced Energy Materials* 13.27 (2023). DOI: `10.1002/aenm.202300760`.

[408] W. Lee et al. “Spin-orbit effects on the electronic and optical properties of lead iodide”. In: *Applied Physics Letters* 122.21 (2023). DOI: `10.1063/5.0146397`.

[409] T. M. Brenner et al. “Conversion of Single Crystalline PbI_2 to $CH_3NH_3PbI_3$: Structural Relations and Transformation Dynamics”. In: *Chemistry of Materials* 28.18 (2016), pp. 6501–6510. DOI: `10.1021/acs.chemmater.6b01747`.

[410] S. Kumar et al. “Topotactic, Vapor-Phase, In Situ Monitored Formation of Ultrathin, Phase-Pure 2D-on-3D Halide Perovskite Surfaces”. In: *ACS Applied Materials & Interfaces* 15.19 (2023), pp. 23908–23921. DOI: `10.1021/acsami.3c01881`.

[411] E. C. Pettit et al. “Controlling Preferred Grain Orientation in Vapor-Deposited Metal-Halide Perovskite Thin Films”. In: *The Journal of Physical Chemistry C* 129.23 (2025), pp. 10643–10651. DOI: `10.1021/acs.jpcc.5c00165`.

[412] M. A. A. Mahmoud et al. “Tuning Perovskite Crystal Growth Dynamics Using Additives on Textured Silicon Substrates”. In: *Solar RRL* 8.24 (2024). DOI: `10.1002/solr.202400471`.

[413] M. M. Tavakoli et al. “Synergistic Crystal and Interface Engineering for Efficient and Stable Perovskite Photovoltaics”. In: *Advanced Energy Materials* 9.1 (2018). DOI: `10.1002/aenm.201802646`.

[414] M. M. Byranvand et al. “Defect Passivation of Perovskite Films for Highly Efficient and Stable Solar Cells”. In: *Solar RRL* 5.8 (2021). DOI: `10.1002/solr.202100295`.

[415] Z. Liang et al. “Homogenizing out-of-plane cation composition in perovskite solar cells”. In: *Nature* 624.7992 (2023), pp. 557–563. DOI: `10.1038/s41586-023-06784-0`.

[416] S. Li et al. “High-efficiency and thermally stable $FACsPbI_3$ perovskite photovoltaics”. In: *Nature* 635.8037 (2024), pp. 82–88. DOI: `10.1038/s41586-024-08103-7`.

[417] P. Fassl et al. “Fractional deviations in precursor stoichiometry dictate the properties, performance and stability of perovskite photovoltaic devices”. In: *Energy & Environmental Science* 11.12 (2018), pp. 3380–3391. DOI: `10.1039/c8ee01136b`.

[418] A. Diercks et al. “Particle Size Matters – Impact of Particle Size and Crucible Geometry on Sublimation Behavior of Formamidinium Iodide”. In: *Advanced Materials Technologies* (2025). DOI: `10.1002/admt.202501549`.

[419] L. Zhang et al. “Crystallization kinetics-driven defect landscape in wide-bandgap perovskite solar cells: Mechanistic elucidation and multiscale regulation strategies”. In: *Information & Functional Materials* 2.3 (2025), pp. 234–250. DOI: `10.1002/ifm2.70003`.

[420] Y. Li et al. “Open-Circuit Voltage Loss Management for Efficient Inverted Wide-Bandgap Perovskite Photovoltaics”. In: *Advanced Functional Materials* 35.7 (2024). DOI: `10.1002/adfm.202415331`.

[421] S. P. Harvey et al. “Investigating the Effects of Chemical Gradients on Performance and Reliability within Perovskite Solar Cells with TOF-SIMS”. In: *Advanced Energy Materials* 10.26 (2020). DOI: `10.1002/aenm.201903674`.

[422] N. Li et al. “Unveiling the role of halide mixing in the crystallization kinetics and charge transfer mechanisms of wide-bandgap organic-inorganic halide perovskites”. In: *Energy & Environmental Science* 18.24 (2025), pp. 10460–10472. DOI: `10.1039/d5ee05540g`.

[423] Z. Li et al. “Scalable fabrication of perovskite solar cells”. In: *Nature Reviews Materials* 3.4 (2018). DOI: `10.1038/natrevmats.2018.17`.

[424] H. Eggers et al. “Inkjet-Printed Micrometer-Thick Perovskite Solar Cells with Large Columnar Grains”. In: *Advanced Energy Materials* 10.6 (2019). DOI: `10.1002/aenm.201903184`.

[425] R. Patidar et al. “Slot-die coating of perovskite solar cells: An overview”. In: *Materials Today Communications* 22 (2020), p. 100808. DOI: `10.1016/j.mtcomm.2019.100808`.

[426] Y. Deng et al. “Scalable fabrication of efficient organolead trihalide perovskite solar cells with doctor-bladed active layers”. In: *Energy & Environmental Science* 8.5 (2015), pp. 1544–1550. DOI: `10.1039/c4ee03907f`.

[427] J. Yang et al. “Ink Engineering in Blade-Coating Large-Area Perovskite Solar Cells”. In: *Advanced Energy Materials* 12.28 (2022). DOI: `10.1002/aenm.202200975`.

[428] J. Liu et al. “Perovskite/silicon tandem solar cells with bilayer interface passivation”. In: *Nature* 635.8039 (2024), pp. 596–603. DOI: `10.1038/s41586-024-07997-7`.

[429] Z.-Y. Pan et al. “Comprehensive device modeling and a performance analysis of perovskite-silicon tandem solar cells through light management”. In: *Applied Optics* 63.22 (2024), p. 5820. DOI: `10.1364/ao.524036`.

[430] Y. Shi et al. “Perovskite/Silicon Tandem Solar Cells: Insights and Outlooks”. In: *ACS Energy Letters* 9.3 (2024), pp. 1305–1330. DOI: `10.1021/acsenergylett.4c00172`.

[431] A. K. Abbasi et al. “Silicon-Perovskite Tandem Solar Cells: An Alternative to the Market-Dominated Silicon-Based Solar Cell Technology”. In: *ACS Applied Materials & Interfaces* 17.37 (2025), pp. 51552–51577. DOI: `10.1021/acsami.5c09599`.

[432] F. Laufer et al. “Deep learning for augmented process monitoring of scalable perovskite thin-film fabrication”. In: *Energy & Environmental Science* 18.4 (2025), pp. 1767–1782. DOI: `10.1039/d4ee03445g`.

[433] H. Zhu et al. “Long-term operating stability in perovskite photovoltaics”. In: *Nature Reviews Materials* 8.9 (2023), pp. 569–586. DOI: `10.1038/s41578-023-00582-w`.

[434] K. T. Tanko et al. “Stability and reliability of perovskite photovoltaics: Are we there yet?” In: *MRS Bulletin* 50.4 (2025), pp. 512–525. DOI: `10.1557/s43577-025-00863-5`.

[435] L. Duan et al. “Stability challenges for the commercialization of perovskite-silicon tandem solar cells”. In: *Nature Reviews Materials* 8.4 (2023), pp. 261–281. DOI: `10.1038/s41578-022-00521-1`.

[436] A. Brand et al. “Beyond authorship: attribution, contribution, collaboration, and credit”. In: *Learned Publishing* 28.2 (2015), pp. 151–155. DOI: `10.1087/20150211`.

[437] Dotmatics. *GraphPad: T Test Calculator*. https://www.graphpad.com/quickcalcs/ttest1/?format=C. accessed: January, 2026.

[438] W. Soltanpoor et al. “Hybrid Vapor-Solution Sequentially Deposited Mixed-Halide Perovskite Solar Cells”. In: *ACS Applied Energy Materials* 3.9 (2020), pp. 8257–8265. DOI: `10.1021/acsaem.0c00686`.

List of Publications and Conference Contributions

Journal Articles

Authors marked with * have contributed equally.

Peer-Reviewed Publications (First Author)

R. Pappenberger, A. Diercks, J. Petry, S. Moghadamzadeh, P. Fassl, and U. W. Paetzold. Bandgap Engineering of Two-Step Processed Perovskite Top Cells for Perovskite-Based Tandem Photovoltaics. *Adv. Funct. Mater.*, 34:2311424, 2024. doi: 10.1002/adfm.202311424.

R. Pappenberger, R. Singh, A. Diercks, T. Zhao, R. Pesch, J. Petry, D. Baumann, X. Liu, and U. W. Paetzold. Versatile Two-Step Process for Perovskite-Based Tandem Photovoltaics. *Sol. RRL*, 9:2500193, 2025. doi: 10.1002/solr.202500193.

R. Pappenberger*, J. Petry*, A. Welle, T. Zhao, A. Diercks, R. Pesch, M. Krause, P. Fassl, and U. W. Paetzold. Benchmarking Inorganic Deposition Routes for Hybrid Two-Step Processed Perovskite Solar Cells: A Materials Perspective. *Sol. RRL*, 10:2500698, 2026. doi: 10.1002/solr.202500698.

Peer-Reviewed Publications (Co-Author)

B. Hacene, F. Laufer, S. Ternes, A. Farag, **R. Pappenberger**, P. Fassl, S. Moghadamzadeh, B. Abdollahi Nejand, T. Feeney, I. Howard, and U. W. Paetzold. Intensity Dependent Photoluminescence Imaging for In-Line Quality Control of Perovskite Thin Film Processing. *Adv. Mater. Technol.*, 9:2301279, 2023. doi: 10.1002/admt.202301279.

R. Pesch, A. Diercks, J. Petry, A. Welle, **R. Pappenberger**, R. Schackmar, H. Eggers, J. Sutter, U. Lemmer, and U. W. Paetzold. Hybrid Two-Step Inkjet-Printed Perovskite Solar Cells. *Sol. RRL*, 8:2400165, 2024. doi: 10.1002/solr.202400165.

B. Hacene, N. W. Rosemann, J. Roger, X. Liu, D. O. Baumann, **R. Pappenberger**, M. Gholipoor, H. Racky, P. Fassl, I. A. Howard, and U. W. Paetzold. Imaging of Recombination Rates and Lifetime in Perovskite Thin Film Processing. *Small Methods*, 9:2402119, 2025. doi: 10.1002/smtd.202402119.

K. Geistert, **R. Pappenberger**, P. Scharfer, P. Cavadini, W. Schabel, F. Sadegh, D. B. Ritzer, B. Abdollahi Nejand, and U. W. Paetzold. Spatially Regulated Gas Flow Control for Batch-Drying of Large Area Slot-Die-Coated Perovskite Thin Films. *Adv. Energy Mater.*, 15:2500923, 2025. doi: 10.1002/aenm.202500923.

R. Pesch, J. Petry, J. Petermann, **R. Pappenberger**, T. Kuechle, J. Schenk, L. P. Rothbauer, L. Fang, X. Liu, S. Rafizadeh, B. Abdollahi Nejand, J. Sutter, U. Lemmer, and U. W. Paetzold. Efficient Perovskite/Silicon Tandem

Solar Cells Using Hybrid Two-Step Inkjet Printing with Edge Isolation Precision. *Small Sci.*, 5:2500362, 2025. doi: 10.1002/smsc.202500362.

Conference Contributions

Talk and Poster Contributions (First Author Only)

Talk – DPG SKM 2023
R. Pappenberger, A. Diercks, A. Farag, P. Fassl, and U. W. Paetzold. Bandgap Engineering of Two-Step Processed Perovskite Top Cells for Application in Perovskite-Based Tandem Photovoltaics. *DPG Spring Meeting of the Condensed Matter Section 2023*, Dresden, Germany, 26.03.-31.03.2023.

Poster – tandemPV Workshop 2023
R. Pappenberger, A. Diercks, S. Moghadamzadeh, A. Farag, P. Fassl, and U. W. Paetzold. Bandgap Engineering of Two-Step Processed Perovskite Top Cells for Application in Perovskite-Based Tandem Photovoltaics. *tandemPV Workshop 2023*, Chambéry, France, 06.06.-08.06.2023.

Poster – PSCO 2023
R. Pappenberger, A. Diercks, S. Moghadamzadeh, A. Farag, P. Fassl, and U. W. Paetzold. Bandgap Engineering of Two-Step Processed Perovskite Top Cells for Application in Perovskite-Based Tandem Photovoltaics. *International Conference on Perovskite Solar Cells and Optoelectronics 2023*, Oxford, Great Britain, 18.09.-20.09.2023.

Talk – DPG SKM 2024
R. Pappenberger, A. Diercks, J. Petry, P. Fassl, and U. W. Paetzold. Improving Performance of Two-Step Processed Perovskite Top Cells for Tandem Photovoltaic Applications. *DPG Spring Meeting of the Condensed Matter Section 2024*, Berlin, Germany, 17.03.-22.03.2024.

Talk – tandemPV Workshop 2024
R. Pappenberger, A. Diercks, J. Petry, P. Fassl, and U. W. Paetzold. Wide-Bandgap Two-Step Processed Perovskite Top Cells for Perovskite-Based Tandem Photovoltaics. *tandemPV Workshop 2024*, Amsterdam, the Netherlands, 25.06.-27.06.2024.

Talk – DPG SKM 2025
R. Pappenberger, R. Singh, A. Diercks, T. Zhao, and U. W. Paetzold. Versatile Two-Step Process for Enhanced Stability and Efficiency in Perovskite Top Cells for Tandem Photovoltaics. *DPG Spring Meeting of the Condensed Matter Section 2025*, Regensburg, Germany, 16.03.-21.03.2025.

Talk – IEEE PVSC 2025
R. Pappenberger, R. Singh, A. Diercks, T. Zhao, and U. W. Paetzold. Versatile Two-Step Process for Enhanced Stability and Efficiency in Perovskite Top Cells for Tandem Photovoltaics. *IEEE Photovoltaic Specialists Conference 2025*, Montreal, Canada, 08.06.-13.06.2025.

Talk – EU PVSEC 2025
R. Pappenberger, R. Singh, A. Diercks, T. Zhao, and U. W. Paetzold. Optimized Solution-Based Two-Step Process for Perovskite-Based Tandem Photovoltaics. *European Photovoltaic Solar Energy Conference and Exhibition 2025*, Bilbao, Spain, 22.09.-26.09.2025.

Talk – DPG SKM 2026
R. Pappenberger, J. Petry, A. Welle, T. Zhao, A. Diercks, R. Pesch, P. Fassl, and U. W. Paetzold. A Materials Perspective on Sequential Inorganic Scaffold Deposition for Hybrid-Processed Perovskite Thin Films. *DPG Spring Meeting of the Condensed Matter Section 2026*, Dresden, Germany, 08.03.-13.03.2026.

Awards for Conference Contributions

Best Poster Award – KSOP Summer School 2022
R. Pappenberger. High-Efficiency Wide-Bandgap Perovskite Top Solar Cells for Tandem Photovoltaics. *Karlsruhe School of Optics and Photonics Summer School 2022*, Research Area V – Solar Energy, Bad Herrenalb, Germany, 29.09.-30.09.2022.

Acknowledgments

This PhD thesis would not have been possible without the support, guidance, and encouragement of my supervisor, colleagues, collaborators, friends, and family.

First and foremost, I would like to express my sincere gratitude to my PhD supervisor, Prof. Dr. Ulrich W. Paetzold, for his guidance and support throughout my doctoral studies. I am thankful for his scientific insights, constructive feedback, and the many valuable discussions we have had over the years. I would also like to thank Prof. Dr. Robby Peibst for kindly taking on the role of second reviewer.

My thanks go to all current and former members of the Perovskite Taskforce at KIT. The collaborative spirit, the scientific discussions, and the support I received were fundamental to this thesis. Special thanks go to all collaborators and co-authors of publications related to this work. I would especially like to thank Dr. Dirk Hauschild, Dr. Alexander Welle, and Dr. Tonghan Zhao for conducting measurements and experiments on my behalf, as well as for the enriching scientific discussions.

In addition, I would like to extend my thanks to Daniel Baumann, Dr. Alexander Diercks, Joshua Esteves, Kristina Geistert, Theresa Küchle, Dr. Felix Laufer, Hendrik Leutz, Raphael Pesch, Julian Petermann, Julian Petry, Dr. Julie Roger, and Dr. Roja Singh, with whom I shared not only productive workdays but also many wonderful moments at LTI.

My sincere thanks go to Christian Kayser, Reza Akbarzadeh Naseri and Julian Schickle for their invaluable technical support over the past years, particularly for their help with the gloveboxes.

Furthermore, I would like to thank the Karlsruhe School of Optics and Photonics (KSOP) for the opportunity to participate in their graduate program and for organizing numerous scientific and social events that enriched my doctoral studies. I am particularly grateful to my KSOP mentor Dr. Nils Rosemann for his thoughtful advice and guidance.

Special thanks go to Daniel Baumann, Theresa Küchle, Dr. Felix Laufer, Julian Pappenberger, Karlheinz Pappenberger, Julian Petry, Dr. Julie Roger and Marie Louise Schubert for kindly proofreading parts of this thesis.

Abseits des wissenschaftlichen Umfelds möchte ich mich außerdem bei zwei Lehrern bedanken, die mich inspiriert und meinen akademischen Weg nachhaltig geprägt haben: Herrn Dr. Weissenborn, der meine Begeisterung für Physik geweckt hat, und Herrn Heim, der mir gezeigt hat, dass ein Faible für logisches Denken und Schreiben durchaus kein Widerspruch ist.

Zum Schluss möchte ich mich herzlich bei meinen Freunden und meiner Familie bedanken, die mich während meiner Promotion – und darüber hinaus – bestärkt, unterstützt und motiviert haben.

Besonders danken möchte ich drei Arbeitskollegen, die meine Zeit am LTI in besonderem Maße geprägt haben: Daniel, für die morgendlichen Tee-Sessions und die unendliche Geduld bei sämtlichen Grafikfragen. Alex, für die vielen Gespräche und die gemeinsamen Reisen. Und Julian, für die vielen inspirierenden Diskussionen, die gemeinsamen Reisen und natürlich für P^2.

Ganz besonders möchte ich mich bei meinen Freundinnen Lara-Sophie, Nora und Carla bedanken, die mich schon den Großteil meines Lebens begleiten und mir stets mit einem offenen Ohr und gutem Rat zur Seite stehen.

Mein großer Dank gilt Sören – für die unermüdliche Unterstützung, die vielen schönen Unternehmungen, die für die nötigen Pausen während der Arbeit gesorgt haben, und für die Hilfe beim Python-Programmieren.

Ein besonderer Dank gilt meinem Opa Karl, der mit seinem Lebensmut und seiner Disziplin ein großes Vorbild für mich ist.

Schlussendlich möchte ich mich von ganzem Herzen bei meinem Bruder Juli und meinem Vater Charlie für die

unerschütterliche Unterstützung in allen Lebenslagen bedanken. Danke für alles!

Ich widme diese Arbeit all jenen, die nicht mehr sind und mir dennoch so viel bedeuten. Ihr habt mich zu dem Menschen gemacht, der ich heute bin. Ich vermisse euch.

> *“We often talk of saving the planet, but the truth is that we must do these things to save ourselves. With or without us, the wild will return.”*
>
> *Sir David Attenborough*